

REPORT DOCUMENTATION PAGE			Form Approved OMB NO. 0704-0188		
<p>The public reporting burden for this collection of information is estimated to average 1 hour per response, including the time for reviewing instructions, searching existing data sources, gathering and maintaining the data needed, and completing and reviewing the collection of information. Send comments regarding this burden estimate or any other aspect of this collection of information, including suggestions for reducing this burden, to Washington Headquarters Services, Directorate for Information Operations and Reports, 1215 Jefferson Davis Highway, Suite 1204, Arlington VA, 22202-4302. Respondents should be aware that notwithstanding any other provision of law, no person shall be subject to any penalty for failing to comply with a collection of information if it does not display a currently valid OMB control number.</p> <p>PLEASE DO NOT RETURN YOUR FORM TO THE ABOVE ADDRESS.</p>					
1. REPORT DATE (DD-MM-YYYY) 13-07-2014		2. REPORT TYPE Ph.D. Dissertation		3. DATES COVERED (From - To) -	
4. TITLE AND SUBTITLE IMPROVING THE DURABILITY OF METHANOL OXIDATION REACTION ELECTRO-CATALYSTS THROUGH THE MODIFICATION OF CARBON ARCHITECTURES			5a. CONTRACT NUMBER W911NF-09-1-0528		
			5b. GRANT NUMBER		
			5c. PROGRAM ELEMENT NUMBER 611103		
6. AUTHORS Kevin Wood			5d. PROJECT NUMBER		
			5e. TASK NUMBER		
			5f. WORK UNIT NUMBER		
7. PERFORMING ORGANIZATION NAMES AND ADDRESSES Colorado School of Mines 1500 Illinois St Golden, CO 80401 -1911			8. PERFORMING ORGANIZATION REPORT NUMBER		
9. SPONSORING/MONITORING AGENCY NAME(S) AND ADDRESS (ES) U.S. Army Research Office P.O. Box 12211 Research Triangle Park, NC 27709-2211			10. SPONSOR/MONITOR'S ACRONYM(S) ARO		
			11. SPONSOR/MONITOR'S REPORT NUMBER(S) 54646-CH-PCS.29		
12. DISTRIBUTION AVAILABILITY STATEMENT Approved for public release; distribution is unlimited.					
13. SUPPLEMENTARY NOTES The views, opinions and/or findings contained in this report are those of the author(s) and should not be construed as an official Department of the Army position, policy or decision, unless so designated by other documentation.					
14. ABSTRACT Carbon materials represent one of the largest areas of studied research today, having integrated applications stretching from energy production and storage to medical use and far beyond. One of these many intriguing applications is fuel cells, which offers the promise of clean electricity through a direct electrochemical energy conversion process. Unfortunately, at the present time the cost per watt-hour produced by fuel cells is more expensive than conventional methods of energy production/storage (i.e. combustion engines, batteries,					
15. SUBJECT TERMS Electrochemistry, direct methanol fuel cell, electrocatalysis, nitrogen-doped carbon					
16. SECURITY CLASSIFICATION OF:			17. LIMITATION OF ABSTRACT UU	15. NUMBER OF PAGES	19a. NAME OF RESPONSIBLE PERSON Ryan O'Hayre
a. REPORT UU	b. ABSTRACT UU	c. THIS PAGE UU			19b. TELEPHONE NUMBER 303-273-3952

Report Title

IMPROVING THE DURABILITY OF METHANOL OXIDATION REACTION ELECTRO-CATALYSTS THROUGH THE MODIFICATION OF CARBON ARCHITECTURES

ABSTRACT

Carbon materials represent one of the largest areas of studied research today, having integrated applications stretching from energy production and storage to medical use and far beyond. One of these many intriguing applications is fuel cells, which offers the promise of clean electricity through a direct electrochemical energy conversion process. Unfortunately, at the present time the cost per watt-hour produced by fuel cells is more expensive than conventional methods of energy production/storage (i.e. combustion engines, batteries, etc.). Under the umbrella of fuel cell systems, methanol is a promising fuel source because of its high energy density and convenience of direct liquid fuel operation. In this field, recent advancements are bringing direct methanol fuel cells (DMFCs) closer to commercial viability. However, just as in other fuel cell systems, further improvements are greatly needed, particularly in the area of catalyst durability. This need for improved durability has led to increased research activity focused on improving catalyst stability and utilization. This thesis explores one of the most promising areas of enhancing catalyst-support interactions; namely, modification of carbon support architectures. Through the use of heteroatom modifiers, such as nitrogen, fuel cell support systems can be enhanced in such a way as to improve metal nucleation and growth, catalyst durability and catalytic activity. To this end, this thesis employs advanced characterization techniques to study the changes in catalyst particle morphology before and after nitrogen modification of the support structure. These results clearly show the beneficial effects of nitrogen moieties on carbon structures and help elucidate the effects of nitrogen on the stability of supported catalytic nanoparticles systems. Similarly, the novel concept of post-modifying commercially available supported catalysts with nitrogen ion implantation gives further insight into the behavior of modified support structures. This result shows a method by which current industry leading benchmarks can be improved, in some cases by up to 100%. This thesis also explores the intriguing prospect of heteroatom modification beyond the effects of just nitrogen. Specifically, the consequences of halide functionalization are explored and shown to significantly improve durability, even to a greater extent than nitrogen modification. In total these results give great promise for the future of fuel cell technology and the field of carbon modification in general.

While the techniques and results presented in this thesis are employed to study durability in direct methanol fuel cells, the benefits of heteroatom modified carbon structures can be applied to other polymer electrolyte fuel cells and beyond. Many other devices and applications, including batteries, supercapacitors, hydrogen storage, and even biosensing and drug delivery can benefit from the work discussed within these pages.

IMPROVING THE DURABILITY OF METHANOL OXIDATION
REACTION ELECTRO-CATALYSTS THROUGH
THE MODIFICATION OF CARBON
ARCHITECTURES

by
Kevin N. Wood

© Copyright by Kevin N. Wood, 2014

All Rights Reserved

A thesis submitted to the Faculty and the Board of Trustees of the Colorado School of Mines in partial fulfillment of the requirements for the degree of Doctor of Philosophy (Materials Science).

Golden, Colorado

Date _____

Signed: _____

Kevin N. Wood

Signed: _____

Dr. Ryan P. O'Hayre
Thesis Advisor

Golden, Colorado

Date _____

Signed: _____

Chester Van Tyne
Professor and Interim Head
Department of Metallurgical and Materials Engineering

ABSTRACT

Carbon materials represent one of the largest areas of studied research today, having integrated applications stretching from energy production and storage to medical use and far beyond. One of these many intriguing applications is fuel cells, which offers the promise of clean electricity through a direct electrochemical energy conversion process. Unfortunately, at the present time the cost per watt-hour produced by fuel cells is more expensive than conventional methods of energy production/storage (i.e. combustion engines, batteries, etc.). Under the umbrella of fuel cell systems, methanol is a promising fuel source because of its high energy density and convenience of direct liquid fuel operation. In this field, recent advancements are bringing direct methanol fuel cells (DMFCs) closer to commercial viability. However, just as in other fuel cell systems, further improvements are greatly needed, particularly in the area of catalyst durability. This need for improved durability has led to increased research activity focused on improving catalyst stability and utilization.

This thesis explores one of the most promising areas of enhancing catalyst-support interactions; namely, modification of carbon support architectures. Through the use of heteroatom modifiers, such as nitrogen, fuel cell support systems can be enhanced in such a way as to improve metal nucleation and growth, catalyst durability and catalytic activity. To this end, this thesis employs advanced characterization techniques to study the changes in catalyst particle morphology before and after nitrogen modification of the support structure. These results clearly show the beneficial effects of nitrogen moieties on carbon structures and help elucidate the effects of nitrogen on the stability of supported catalytic nanoparticles systems. Similarly, the novel concept of post-modifying commercially available supported catalysts with nitrogen ion implantation gives further insight into the behavior of modified support structures. This result shows a method by which current industry leading benchmarks can be improved, in some cases by up to 100%. This thesis also explores the in-

triguing prospect of heteroatom modification beyond the effects of just nitrogen. Specifically, the consequences of halide functionalization are explored and shown to significantly improve durability, even to a greater extent than nitrogen modification. In total these results give great promise for the future of fuel cell technology and the field of carbon modification in general.

While the techniques and results presented in this thesis are employed to study durability in direct methanol fuel cells, the benefits of heteroatom modified carbon structures can be applied to other polymer electrolyte fuel cells and beyond. Many other devices and applications, including batteries, supercapacitors, hydrogen storage, and even biosensing and drug delivery can benefit from the work discussed within these pages.

TABLE OF CONTENTS

ABSTRACT	iii
LIST OF FIGURES	x
LIST OF TABLES	xix
LIST OF SYMBOLS	xx
LIST OF ABBREVIATIONS	xxi
ACKNOWLEDGMENTS	xxiv
DEDICATION	xxvi
CHAPTER 1 GENERAL INTRODUCTION	1
1.1 Thesis Outline	2
1.2 Research Statement	3
CHAPTER 2 DURABILITY OF ELECTROCATALYSIS IN DIRECT METHANOL FUEL CELLS	6
2.1 Principles of Operation	6
2.1.1 Oxidation Mechanism	9
2.1.2 PtRu Catalysts	10
2.1.3 Durability of PtRu Systems	10
2.2 Nitrogen Functionalization	14
2.2.1 Methods	14
2.2.2 Functionalities	16
2.2.3 Experimental Results of Nitrogen Modification	19

2.3	Other Functionalities	24
2.4	Conclusions	25
CHAPTER 3 THE EFFECTS OF NITROGEN MODIFICATION ON THE DURABILITY OF HIGH SURFACE AREA SYSTEMS		26
3.1	Experimental Information	27
3.1.1	Catalyst synthesis	27
3.1.2	Electrochemical Details	28
3.2	Results and Discussion	31
3.2.1	Surface Characterization	32
3.2.2	RDE Electrochemical Characterization	34
3.2.3	MEA Testing Analysis	34
3.2.4	Small Angle X-ray Scattering Analysis	39
3.2.5	X-ray Diffraction Results	45
3.3	Conclusions	47
CHAPTER 4 THE EFFECT OF POST NITROGEN MODIFICATION ON THE DURABILITY OF COMMERCIAL CATALYSTS		49
4.1	Experimental Information	50
4.1.1	Materials	50
4.1.2	Characterization	51
4.1.3	RDE Studies	51
4.1.4	MEA fabrication	52
4.2	Acidic Results and Discussion	53
4.2.1	Material characterization	53
4.2.2	Acid Media RDE Studies	57

4.2.3	Acidic MEA studies	62
4.2.4	Post-mortem TEM analysis	65
4.3	Alkaline Results and Discussion	66
4.3.1	Initial Alkaline MEA Study	74
4.4	Durability effects in Acid vs. Alkaline	74
4.5	Conclusions	76
CHAPTER 5 THE EFFECT OF NITROGEN ON DURABILITY OF GRAPHENE SUPPORTED CATALYSTS		79
5.1	Experimental Information	80
5.1.1	Materials Fabrication	80
5.1.2	Characterization and Testing Methods	81
5.1.3	Catalyst Ink formulation	82
5.2	Results and Discussion	83
5.3	Conclusions	89
CHAPTER 6 BEYOND NITROGEN: DO OTHER FUNCTIONALITIES OFFER IMPROVED DURABILITY?		94
6.1	Experimental	95
6.2	Results and Discussion	97
6.2.1	Support Modification with Iodine	97
6.2.2	Support Modification with Fluorine	100
6.2.3	Support Modification with Fluorine and Nitrogen	103
6.3	Conclusions	109
CHAPTER 7 CONCLUSIONS		110
7.1	Improved Active Site Retention	112

7.2	Retention of Most Active Catalyst Phases	114
7.3	Future Directions	116
APPENDIX A - RECENT PROGRESS ON NITROGEN/CARBON STRUCTURES DESIGNED FOR USE IN ENERGY AND SUSTAINABILITY APPLICATIONS		119
A.1	Introduction	119
A.2	Materials	121
A.2.1	Graphene	121
A.2.1.1	Direct Synthesis	122
A.2.1.2	Post-treatment	124
A.2.2	Carbon nanotubes	126
A.2.3	Activated Commercial Carbon Blacks	130
A.2.4	Highly Porous and Mesoporous Carbon	131
A.2.4.1	Ionic liquids	136
A.2.4.2	Hydrothermal Carbonization	137
A.2.5	Carbon nitride	138
A.2.6	Other Carbon Structures and Synthesis Methods	140
A.3	Theoretical Studies	143
A.3.1	Electronic Effects	143
A.3.2	Applications	145
A.3.2.1	Fuel Cells	145
A.3.2.2	Batteries	149
A.3.2.3	Hydrogen Storage	150
A.4	Applications	150

A.4.1	Fuel Cells	151
A.4.1.1	Precious metal N-containing catalyst systems for methanol electrooxidation	151
A.4.1.2	Precious metal N-modified catalyst systems for oxygen electrooxidation	157
A.4.1.3	Non-precious metal N-modified catalyst systems for oxygen electroreduction	159
A.4.1.4	Metal-free N-containing catalyst systems for oxygen electroreduction	165
A.4.2	Batteries	171
A.4.3	Supercapacitors	176
A.4.4	Hydrogen Storage	187
A.4.5	CO ₂ Capture	192
A.4.6	Other Applications	195
A.4.6.1	Chemical Production (H ₂ O ₂ , butyronitile, oxidized-cyclohexane)	195
A.4.6.2	Photocatalysis	198
A.4.6.3	Biosensing	200
A.5	Outlook and Conclusions	202
APPENDIX B - MEA TESTING EXPERIMENTAL/SUPPLEMENTARY INFORMATION		204
B.1	Acid Testing Information	204
B.2	Alkaline Testing Information	205
REFERENCES CITED		207

LIST OF FIGURES

Figure 2.1	A simplified conceptual view of the basic components needed for a direct methanol fuel cell. The backing, diffusion layer, catalyst layer with nitrogen doping tethering the metal sites and a proton exchange membrane.	8
Figure 2.2	A schematic of PtRu nanoparticles on a carbon supports, this illustrates the catalyst system which makes up most of the catalysts layer. The nanoparticles in this diagram are about 2–3 nm in diameter, while the size of the carbon particles is around 20–50 nm.	12
Figure 2.3	Proposed mechanisms for instability of metal nanoparticles in low-temperature fuel cells: (a): dissolved metal species from smaller particles diffuse through ionomer phase and redeposit onto the surfaces of larger particles (Ostwald ripening); (b): Metal nanoparticles migrate on the surface of carbon support and coalesce; (c): Metal nanoparticles detach from the carbon support and/or agglomerate due to carbon corrosion. Reprinted from reference	13
Figure 2.4	Structures of the various types of nitrogen functionalities commonly observed in the N-doped materials discussed throughout the literature. The three most common types are pyridinic, pyrrolic and graphitic. The other functionalities discussed are quaternary, triazine, pyridinic oxide and metal coordinated nitrogen. While these are common in literature, very little of my research deals with these types of functionalities. The figure also shows the different vacancy possibilities. This figure is your guide to the functionalities discussed in this thesis and in Appendix A.	18
Figure 2.5	TEM micrographs representative of sputtered PtRu deposited on HOPG substrates (1) pre-cycled, demonstrating coverage and range of nanoparticle sizes, and (2) post-cycled, demonstrating changes in the coverage, particle size, and formation of agglomerations. Shown for samples with dosages of (a) 0.0×10^{16} , (b) 0.4×10^{16} , (d) 1.3×10^{16} , (e) 4.7×10^{16} , and (f) 9.6×10^{16} ions cm^{-2} (0, 5, 15, 45, and 100 s). Reprinted from reference	22
Figure 3.1	Schematic of the vacuum chamber used for catalyst synthesis. Ion-implantation a) and Pt-Ru sputter deposition b) are carried out step-wise in the fabrication chamber.	29

Figure 3.2	a) The design of the custom in-situ electrochemical cell allowing for analysis of the same precise area on the electrode. b) A schematic of SLAC's beam line 1-4.	31
Figure 3.3	XPS N1s spectra acquired from the unmodified and 20mA N-modified sample after metal deposition. Nitrogen concentration in N-doped sample is (~2 at.%). The unmodified sample contains only trace amount of nitrogen (~.2 at.%).	33
Figure 3.4	CO stripping curves obtained for the undoped, doped, and commercial Pt-Ru materials.	37
Figure 3.5	CO stripping curves obtained after 0 (black), 100 x (red), and 5000 x (green) cycles for (a) JM5000, (b) Pt-Ru/C (undoped), and (c) Pt-Ru/N-C (N-doped).	38
Figure 3.6	CO stripping voltammograms for the MEAs as a function of ADT time; (a) JM5000, (b) PtRu/N-C, and (c) Relative anode ECSA loss vs. ADT time extracted from the CO stripping voltammograms.	41
Figure 3.7	TEM images of the nitrogen modified catalyst before cycling. a) and b) Low-magnification images demonstrating coverage of the sputtered PtRu/N-Carbon. Micrographs at higher magnification (c and d) show regions of less dense particle coverage demonstrating that nanoparticle size observed by TEM (~1-5nm) is in agreement with values determined by SAXS.	42
Figure 3.8	Modeled SAXS intensities shown with the collected experimental data for the unmodified (a) and nitrogen-modified (b) samples. The particle size distributions extracted from the SAXS modeling at various cycling times are shown in (c) and (d) for the unmodified and nitrogen-modified samples, respectively.	44
Figure 3.9	XRD difference spectra for the commercial catalyst (JM5000), implanted and sputtered (Pt-Ru/N-C), and the sputtered (Pt- Ru/C) materials obtained during in-situ potential cycling. Each spectrum is the mathematical difference between the cycling spectrum and the initial un-cycled spectrum.	46
Figure 4.1	High resolution N1s spectra, shown for three areas on each sample and their average.	56
Figure 4.2	High resolution C 1s+Ru 3d spectra, curve-fitted a) PtRu/C, b) PtRu/C-N1, and c) PtRu/C-N2.	57

Figure 4.3	TEM micrographs demonstrating three types of metal coverage for the catalysts a) PtRu/C, and b) PtRu/C-N2. b1 and b2 demonstrate morphology similar to the original catalyst. b3 shows areas with small well dispersed nanoparticles not observed in the original catalyst.	58
Figure 4.4	CO stripping data of unmodified JM 10000, PtRu/C-N1 and PtRu/C-N2 catalysts as a function of cycling.	60
Figure 4.5	The electrochemical surface area (ESCA) of unmodified JM10000, PtRu/C-N1 and PtRu/C-N2 catalysts as a function of cycling. The electrochemical surface area is shown on the left axis. The right axis is a figure-of-merit plot where the surface area is multiplied by the percent of cycles completed during that testing segment (i.e. $52.2 \times (50/5000)$ after 50 cycles and $24.7 \times (4000/5000)$ after 5000 cycles) and then accumulated over the lifetime of the electrode.	60
Figure 4.6	The ECSA of JM10000, PtRu/C-N1 and PtRu/C-N2 before and after cycling. The redistribution from implantation can clearly be seen before cycling as well as the enhancement in ECSA after 500 cycles. . . .	61
Figure 4.7	Initial electrochemical characterization of the MEAs. a) Anode CO stripping curves, 5 mV s^{-1} , b) Methanol:air polarization curves, 80°C	63
Figure 4.8	a) DMFC performance curves before and after 425 hours of durability. b) Anode ECSA as measured from anode CO stripping at 5 mV/s	64
Figure 4.9	TEM micrographs representative of anode material after durability testing: a) JM10000, and b) PtRu/C-N2. b1 and b2 demonstrate morphology similar to the undoped catalyst. b3 shows areas with different type of catalyst morphology than in the undoped catalyst	67
Figure 4.10	TEM images showing the effect of post doping. Images a-c show areas of redistribution, where the ion implantation removes metal from large cluster and forms small nanoparticles around the edges of the carbon particles. Images d-e show morphologies identical to those of unmodified JM10000.	68
Figure 4.11	Initial electrochemical results of the post modified (blue) and unmodified catalyst (black). a) shows initial un-cycled CO stripping and b) initial methanol performance curves.	69
Figure 4.12	Changes in electrochemical surface area as a function of cycle. The upper graph shows the shift toward higher kick off potential for the unmodified commercial catalyst. While the lower graph shows the limited changes in on set for the nitrogen modified catalyst.	70

Figure 4.13	Showing the change in electrochemical surface area before and after 5000 cycles in a solution of .5M NaOH and methanol. Results show a more improvement in a solution with methanol than in a pure NaOH solution.	71
Figure 4.14	Electrochemical surface area before and after cycling. The dotted lines indicate the error in the measurement. The nitrogen improves surface area retention by ~7%	72
Figure 4.15	MOR performance comparing the unmodified and nitrogen modified commercial catalysts. The upper graph shows the collected data and the lower graph shows the data normalized versus surface area. The data shows only a 15% loss in performance over the lifetime of the cell for the nitrogen modified catalyst, while nearly 60% of the unmodified catalyst performance is lost.	73
Figure 4.16	The effects of ADT testing on (a) PtRu/C in acid media (b) PtRu/C-N2 in acid media (c) PtRu/C in alkaline media (d) PtRu/C-N3 in alkaline media. Results show a change in mechanism for nitrogen modified catalyst in alkaline media.	76
Figure 5.1	SEM images of the morphology of a) JM5000 and b) PtRu/G. Dispersed nanoparticles can be seen for the JM5000 sample while a homogeneous covering of PtRu is observed for the PtRu/G sample. . . .	84
Figure 5.2	SEM images of the PtRu/G ink dropped on a glassy carbon electrode. Areas of clumping and poor dispersion can be seen in a) and good catalyst ink dispersion can be seen in b). Areas similar to b) are desirable.	85
Figure 5.3	Three areas of PtRu coverage can be seen. 1) Dense metal agglomeration 2) Film-like metal coverage 3) Nanoparticle coverage. This TEM images shows the three dominate types of metal coverage in the PtRu/G sample.	86
Figure 5.4	TEM images comparing the nanoparticle coverage of PtRu/G a) against the typical morphology observed for PtRu sputtered HOPG b). These types of morphologies could lead to incredibly high surface area and low metal loadings once sputtering and graphene conditions are optimized.	87

Figure 5.5	The effects of solvent on the methanol performance of PtRu/G catalyst samples. Samples normalized per metal loading shown in a) reveal an improvement in catalyst performance for DMF as time increases, while IPA performance decreases b) Shows samples normalized per active surface area. This underscores the role DMF has in improving catalyst performance via a mechanism other than surface area.	88
Figure 5.6	Initial performance before cycling of PtRu/G, PtRu/G-N, and JM5000 normalized (a) against metal loading (9wt%, 5wt%, 30wt%, respectively), (b) surface area (.313cm ² , .189cm ² , 2.8cm ² , respectively). .	90
Figure 5.7	The MOR performance of DMF and IPA graphene based electrocatalysts compared against JM5000. This figure shows that graphene has no intrinsic catalytic activity. Additionally, this figure is only normalized per geometric electrode surface area, which is identical for all samples. PtR/G only has 9wt% compared with the 30wt% JM5000.	91
Figure 5.8	ADT testing results of graphene support PtRu catalysts. a) shows the effect of 1000 cycles on PtRu/G and PtRu/G-N normalized vs. metal loading b) plots the effect of cycling vs. electrochemcially active surface area determined from CO stripping.	92
Figure 6.1	TEM images of pre- and post-cycled unmodified and N-modified samples. A) unmodified, pre-cycled, B) unmodified, post-cycled, C) N-modified, pre-cycled, D) N-modified, post-cycled	98
Figure 6.2	Raman spectra of I-modified HOPG samples compared to unmodified and N- modified reference samples.	99
Figure 6.3	XPS high-resolution spectra a) I 3d in iodine modified sample and b) F 1s in fluorine modified sample.	100
Figure 6.4	TEM images of pre- and post-cycled low and high-dose iodine modified samples. a) low dose I-modified, pre-cycled b) low dose I-modified, post-cycled c) high-dose I-modified, pre-cycled d) high-dose I-modified, post-cycled	101
Figure 6.5	Raman spectra of CF ₄ modified HOPG samples compared to unmodified and N-modified reference samples.	102
Figure 6.6	High-resolution C 1s XPS spectra of CF ₄ modified HOPG samples compared to unmodified and N-modified reference samples.	103

Figure 6.7	TEM images of the pre- and post-cycled low and high-dose CF ₄ -modified samples. a) low dose, pre-cycled b) low dose, post-cycled c) high-dose, pre-cycled d) high-dose, post-cycled.	104
Figure 6.8	Characterization of co-implanted samples with varying ratios of nitrogen vs. fluorine concentrations a) XPS elemental composition, b) average particle size obtained from analysis of TEM micrographs . . .	105
Figure 6.9	High-resolution C 1s XPS spectra of co-implanted samples a-d compared compared N-modified reference samples.	106
Figure 6.10	TEM images of post-cycled co-implanted HOPG samples a) 13% fluorine, 4% nitrogen, Sample b) 11.5% fluorine, 4.5% nitrogen, Sample c) 3% fluorine, 10.5% nitrogen, Sample d) 1.5% fluorine, 8.5% nitrogen	107
Figure 7.1	A schematic showing the differences between in-house modified catalysts and post doped catalysts. The In-house catalyst helps maintain Ru while post-modified catalyst loses Ru, this can be seen in the CO stripping results presented below the pictorial representation. .	113
Figure 7.2	The effect of acid and alkaline media on the nitrogen post-modified commercial catalyst. The CO stripping results show the Ru retention associated with ADT testing done in alkaline media	114
Figure 7.3	The synergistic effect of nitrogen and fluorine on PtRu nanoparticle durability.	115
Figure 7.4	A schematic representation of the effect of nitrogen on helping maintain the most active catalyst phases. After electrochemical cycling nitrogen modified samples have greater methanol performance per electrochemically active surface area.	116
Figure A.1	a) Direct synthesis route: Illustration of the treatment of graphene oxide by NH ₃ for simultaneous reduction and N-doping, followed by the loading of Pt nanoparticles (nanoparticles not-to-scale) Reprinted (adapted) with permission from Citation. Copyright (2013) Elsevier. (b) Post-modification route: Schematic illustration of synthesis of N-doped graphene using the pyrolysis of polypyrrole coated functionalized graphene, with subsequent deposition of SnO ₂ nanoparticles. Reprinted (adapted) with permission from Citation. Copyright (2013) Royal Society of Chemistry.	124

Figure A.2	TEM images of (a) CNT's, (b) CN_x (1.5 at.% N), (c) CN_x (5.4 at.% N), and (d) CN_x (8.4 at.% N) showing the effect of nitrogen on the structure of CNT's. Reprinted (adapted) with permission from Citation (Y. Chen et al., 2009). Copyright (2009) Elsevier	129
Figure A.3	(a) HAADF-STEM image and corresponding EELS oxygen, carbon, and nitrogen maps obtained from Graphitic Vulcan doped with nitrogen and decorated with Pt nanoparticles showing enrichment of the support surface with doped nitrogen. (b) XPS N1s spectrum of N-doped Graphitic Vulcan. Reprinted (adapted) with permission from Citation (Pylypenko et al., 2013). Copyright (2013) Royal Society of Chemistry.	132
Figure A.4	TEM images (a) polypyrrole nanospheres, 14.3 at% N, and carbon nanospheres carbonized at BET 45 m ² /g (b) 300°C, 14.1 at% N, BET 23 m ² /g (c) 600°C, 12.5 at% N, BET 36 m ² /g (d) 900°C, 7 at% N, BET 89 m ² /g (e) 1100°C, 5.9 at% N, BET 20 m ² /g (f) 1300°C, 4.3 at% N, BET 12 m ² /g and microporous carbon nanospheres (g) and (h) 2.2 at% N BET 1080 m ² /g. Reprinted (adapted) with permission from Citation (Su et al., 2011). Copyright (2011) Royal Society of Chemistry.	135
Figure A.5	Illustration for the synthesis process of ordered mesoporous-CN using (a) traditional method and (b) new method. Reprinted (adapted) with permission from Citation (Jinshui Zhang et al., 2013). Copyright (2013) Wiley-VCH.	141
Figure A.6	(a) Electron density of singly and triple doped nitrogen sites. (b)) Pt adsorption energy as a function of distance from the dopant atom. Reprinted (adapted) with permission from Citation (Muhich et al., 2013). Copyright (2013) American Chemical Society.	146
Figure A.7	Minimal energy paths of oxygen molecule dissociation on (a) a pure (8,0) SWNCT, (b) a one nitrogen atom substituted (8,0) SWCNT, (c) a two meta nitrogen atom substituted (8,0) SWCNT, (d) a two para nitrogen atom substituted (8,0) SWCNT, (e) a one nitrogen atom substituted (8,0) SWCNT with a stone-wales defect, and (f) a (8,0) SWCNT with pyridine-like nitrogen atoms. Gray dots, blue dots and red dots represent carbon, nitrogen and oxygen atoms respectively. Reprinted (adapted) with permission from Citation (Ni et al., 2012). Copyright (2013) Royal Society of Chemistry.	148

Figure A.8	TEM images and size distribution histograms (insets) of Pt electrocatalysts before and after ADT. (a) Pt/CNT's; (b) Pt/N-CNT's (1.5 at.% N); (c) Pt/N-CNT's (5.4 at.% N); (d) Pt/N-CNT's (8.4 at.% N) and (e) the comparison of the degradations of the five catalysts. on the structure of CNT's. Reprinted (adapted) with permission from Citation (Y. Chen et al., 2009). Copyright (2009) Elsevier (f) the effect of N-doping on performance of PtRu anode. Reprinted (adapted) with permission from Citation (Corpuz et al., 2014). Copyright (2014) Elsevier (g) the effect of N-doping on Ru crossover in DMFC made with PtRu anode. Reprinted (adapted) with permission from Citation (Joghee et al., 2012). Copyright (2012) The Electrochemical Society.	154
Figure A.9	Correlation between XANES, XPS, and BET data and ORR activity for PANI-Fe-C using principal component analysis. All catalysts after heat treatment, acid leach, and a second heat treatment. Reprinted (adapted) with permission from Citation(Ferrandon et al., 2012). Copyright (2012) American Chemical Society.	162
Figure A.10	Graphical Representation of Proposed ORR Mechanism at CNT versus N-CNT Electrodes with Representative Cyclic Voltammograms for CNT's and 6.3 at. % N-CNT's in 1 M Na ₂ HPO ₄ (V vs. NHE). Reprinted (adapted) with permission from Citation(Wiggins-Camacho & Stevenson, 2011). Copyright (2011) American Chemical Society.	169
Figure A.11	a) Electrochemical performance of graphene films grown on Cu foil, galvanostatically cycled in Li half cells. Variation in discharge capacity vs. cycle number for the pristine graphene and N-doped graphene cycled at a rate of 5 mA/cm ² between 3.2 and 0.02 V vs. Li/Li ⁺ in 1 M solution of LiPF ₆ in 1:1 (v/v) mixture of ethylene carbonate (EC) and dimethyl carbonate (DMC) as the electrolyte. Reprinted (adapted) with permission from Citation (Reddy et al., 2010). Copyright (2010) American Chemical Society. b) Reversible charge/discharge capacity verse cycle number of (i) graphene-nanosheets and (ii) N-graphene-nanosheets Reprinted (adapted) with permission from Citation (Xifei Li et al., 2011). Copyright (2011) Elsevier.	174
Figure A.12	Performance of 10 wt% PANi as a function of scan rate (from 2 to 100 mV/s) in 1M H ₂ SO ₄ electrolyte. Reprinted (adapted) with permission from Citation (Lai, Yang, et al., 2012). Copyright (2012) American Chemical Society.	180

Figure A.13	(1) Hydrogen adsorption mechanism schematic on Pd/N-graphene Reprinted (adapted) with permission from Citation(Z M Ao et al., 2012). Copyright (2013) Royal Society of Chemistry. (2) Scanning electron micrographs of (a) N-HEG and (b) Pd-N-HEG depicting the folds in graphene layers. Transmission electron micrographs of (c) N-HEG and (d) Pd-N-HEG. A uniform dispersion of Pd NPs on N-HEG support is clearly visible. Reprinted (adapted) with permission from Citation (Parambath et al., 2012). Copyright (2012) American Chemical Society.	190
Figure A.14	Relationships between the CO ₂ adsorption capacities (at 298 K and 1 atm) and BET surface area of nitrogen-doped carbons and undoped carbons. The N-doped carbons contain 6-7 wt % nitrogen. Reprinted (adapted) with permission from Citation (L. Wang & Yang, 2011). Copyright (2011) American Chemical Society.	194

LIST OF TABLES

Table 3.1	Quantification of Pt-Ru/Carbon materials demonstrating elemental composition, determined by XPS, distribution of ruthenium species obtained by curve-fitting Ru 3p spectra and ratio of ruthenium to platinum, determined by XPS and XRF.	35
Table 3.2	The values for ECSA as determined by MEA CO stripping, the MOR specific activities, and percentage of ECSA after 100× and 5000× cycles in the ADT protocol are tabulated.	36
Table 3.3	ECSA measured by CO stripping voltammetry for the anode of the MEAs with PtRu/N-C and JM5000.	40
Table 4.1	XPS analysis: elemental composition, and quantification of deconvoluted XPS spectra of Ru3d, and Pt 4f, reported as average of three areas per sample.	55
Table A.1	Recent reports on progress of supercapacitors	181
Table A.2	Research in the last 5 years on hydrogen storage	191
Table A.3	Recent Progress on CO ₂ Capture	196

LIST OF SYMBOLS

Contrast	$\Delta\rho$
Scattering form factor	$F(Q, r)$
Particle volume	$V(r)$
Number of scattering particles	N
Probability of scattering	$P(r)$
Minimum diameter size	Min
Standard deviation	$sdev$
Mean diameter subtracted from the minimum particle size	$mean$

LIST OF ABBREVIATIONS

Proton Exchange Membrane Fuel Cell	PEMFC
Direct Methanol Fuel Cell	DMFC
Colorado School of Mines	CSM
National Renewable Energy Laboratory	NREL
Membrane Electrode Assembly	MEA
Army Research Office	ARO
Polymer Electrolyte Membrane	PEM
Methanol Oxidation Reaction	MOR
X-ray Photoelectron Spectroscopy	XPS
X-ray Adsorption Spectroscopy	XAS
Triple Point Boundaries	TPB
Electrochemical Surface Area	ECSA
Reference Hydrogen Electrode	RHE
US Department of Energy	DOE
Chemical Vapor Deposition	CVD
Carbon Nanotubes	CNT
Density Functional Theory	DFT
Highly Oriented Pyrolytic Graphite	HOPG
Brunauer–Emmett–Teller Surface Area	BET
Rotating Disk Electrode	RDE

Small-Angle X-ray Scattering	SAXS
X-ray Diffraction	XRD
Methanol	MeOH
Johnson Matthey 30wt % PtRu	JM5000
In-House Unmodified PtRu Catalyst	Pt-Ru/C
In-House N-modified PtRu Catalyst	Pt-Ru/N-C
X-ray Fluorescence	XRF
Accelerated Electrochemical Degradation Tests	ADT
Energy Electron Loss Spectroscopy	EELS
Thermogravimetric Analysis	TGA
Transmission Electron Microscopy	TEM
Cyclic Voltammetry	CV
CO Stripping	COS
Saturated Calomel Reference Electrode	SCE
2-propanol	IPA
Gas Diffusion Electrode	GDE
Johnson Matthey PtRu 60 wt%	JM 10000
Post-Modified JM10000 12mA	PtRu/C-N1
Post-Modified JM10000 45mA	PtRu/C-N2 & PtRu/C-N3
Binding Energy	BE
Electrochemical Society	ECS
University of New Mexico	UNM
Unmodified graphene with PtRu	PtRu/G

N-modified graphene with PtRu	PtRu/G-N
Di-methlyformamide	DMF
Near Edge X-ray Adsorption Fine Structure	NEXAFS

ACKNOWLEDGMENTS

It seems that there is a trend among authors who write acknowledgements to thank every famous person (or thing) for inspiration, non-existent assistance, or maybe, if lucky, a casual reference. Authors do this to pump themselves up; especially scientists. Since our work isn't read for fun on a rainy night and requires several cups of coffee to focus on, we have to make ourselves feel good somehow. So, on the off chance that this trend is helpful, I wish to thank the following people: the Emperor of Japan and the Queen of England for promoting literacy; Julius Caesar, for showing the world that illiterate barbarians can be beaten; Albert Einstein, for some of those theories I should remember; string theorists, for reminding me I don't know anything; Mark Zuckerberg, for making sure that I didn't write my thesis any quicker; Jorge Cham, for putting my life into a comic strip; giardia, for making my time in Ethiopia an adventure; warm coffee, for keeping me from falling asleep while writing this; and the CCAC printer, for reminding me why scientists do what they do; to make things work.

But in all seriousness the research process can be a daunting task at times and I am so grateful to so many. Thanks to my parents who have had to put up with me speaking in words, like moieties and intercalation, for the last 4+ years. Your support has been such an encouragement and helped me keep going. Thanks to my close friends (Michael, TJ, Zaac, Trey, and Eric) who have prayed for me, gotten me out of the house, gone on adventures and played volleyball until the wee hours of the morning. Lindsay, thanks so much for your love, care, and support. You are truly a blessing and a gift from God. I don't think I would have made it through this last year without you! You're wonderful.

A special thanks to my thesis advisor Dr. Ryan O'Hayre for the guidance and direction that he has provided me. Somehow he has always seemed to see my potential even when I wasn't sure. Thanks to Dr. Svitlana Pylypenko for helping me so much over the last 4

years. This thesis would not have been anything like it is without your help. I would also like to thank Dr. Arrelaine Dameron, Dr. Tim Olson, Dr. Prabhuram Joghee, and Dr. April Corpuz for their help and collaboration. The results presented herein would not have been possible without their assistance. Also, the ion gun may have defeated me if Arrelaine had not supported me through that fight.

I would also like to thank Dr. Tom Gennett for putting up with the complicated site access issues and granting me privileges to the equipment at NREL. Thanks to Dr. Steven Christensen for writing the proposal to access SLAC National Accelerator Laboratory and teaching me how real scientists drink Mtn. Dew. A special thanks to my close friends Aaron Miller and Stefan Nikodmeski. Aaron for all the basketball breaks and still being my friend after a cactus went through his shoe; oh and the help in the lab too. Stefan for helping me study, pass my classes, and eat Chipotle...lots of Chipotle. There are so many others I owe a thanks to as well, Dr. Jianhua Tong, Dr. Brian Trewyn, Dr. Mike Sanders, Dan Clark, Amy Morrissey, Dr. Badri Narayanan, Dr. Meng Shang, Will Huddleson, Dr. Hongjun Liang's research group, and all the professors and teachers along the way that have inspired me.

But at the end of the day all of this is worthless unless there is the hope and promise of eternity. Without Christs death and resurection I would be like a boxer beating the air aimlessly. I am so blessed by the gifts and opporunities that God has given me. I am underserving.

Pure and undefiled religion before God the Father is this: to care for orphans and widows
in their misfortune and to keep oneself unstained by the world.

James 1:27

CHAPTER 1

GENERAL INTRODUCTION

The current insatiable demand for energy in today's society has put us on the brink of an energy shortage and crisis. Many efforts focused on meeting our global energy needs are being centered around hydrogen and liquid biofuels, such as methanol and ethanol, because of their potential sustainability and minimal environmental impact. Within the expanding range of energy conversion technologies, the fuel cell is one of the most environmentally friendly and sustainable solutions. In the last 30 years enormous improvements have been made in the area of proton exchange membrane fuel cells (PEMFC's), which has transformed these devices into viable candidates for stationary, transportation, and portable energy needs. Several types of fuel cells have shown great promise in reaching commercialization in the short term, and arguably the top candidate is direct methanol fuel cells (DMFCs).

The direct use of methanol as a fuel has several advantages to other alternative energy sources. When compared to hydrogen gas-based fuel cells, DMFCs are attractive because of the simple fuel feed strategy, the ease of fuel production and storage, and a simplified transportation infrastructure. In comparison to other energy storage devices, such as Li-ion batteries, DMFCs possess advantages such as higher energy density and a simple refueling process. This makes DMFCs great candidates for applications in portable electronics, such as computers and cellular telephones.

Unfortunately, several obstacles are still hindering the commercialization of DMFCs. The three components most to blame for current performance issues in these systems are sluggish reaction kinetics, high over potential losses associated with methanol crossover, and poor lifetime catalyst stability. Initially, high loadings of expensive precious metal catalysts are needed for DMFCs to operate at the power densities required for their intended application (a results of the sluggish reaction kinetics). Consequently, long term operation of these

systems results in very high material costs associated with the loss of active precious metal sites.

Therefore, in order to improve performance and mitigate the loss of expensive materials in fuel cells, the high surface area carbon architectures (utilized as the catalyst support) can be modified to enhance the metal-support interactions. To this end, the results and motivation of my project are to elucidate which support modification allows for improvement in catalytic utilization and reduction in material cost. This thesis attempts to answer the question:

- How and in what ways can modified carbon structures be used to improve the durability of methanol oxidation reaction catalysts?
- What can we say about the types of modification most beneficial for enhanced durability?
- Are there new frontiers for improved durability development?

Improving catalytic utilization and reducing material cost is a complicated and multifaceted process, which will remain the focus of research for the foreseeable future, however this work aims to elucidate some effective strategies for enhancing fuel cell lifetime and performance. To answer the questions above, I attempt to provide insight into areas in which the scientific community is already active as well as pursuing novel research topics. One avenue pursued in this work documents the effect of nitrogen modification on high surface area supports. Novel routes investigated include, nitrogen post-modification of industry leading commercial catalysts and a study on the durability effects of new support functional groups. Through these explorations this thesis aims to provide insight that will make sure commercial deployment of DMFCs will be a viable energy alternative in the future.

1.1 Thesis Outline

The body of this thesis contains 6 chapters, as follows:

- Chapter 2 covers the background and current state of research on modified carbon support systems. Readers interested in a more in-depth review of state-of-the-art nitrogen modified techniques and applications are referred to Appendix A. Here, a manuscript is provided which gives a broad overview and discusses the recent progress of nitrogen/carbon structures designed for use in energy and sustainability applications.
- Chapter 3 discusses the effects of nitrogen modification on the durability of high surface area catalyst support structures. These ‘in-house’ fabricated materials are characterized through a myriad of techniques to determine the effects of nitrogen modification on real fuel cell catalysts systems.
- Chapter 4 provides a detailed look at the durability effects of nitrogen post-modification of commercial catalysts in acid and alkaline media. This novel functionalization technique limits the location of functionalities present and provides a potential pathway for improving widely accepted industry-leading benchmarks.
- Chapter 5 explores the effect of nitrogen in relation to the durability of graphene-supported catalysts. Electrochemical analysis is combined with characterization to show the effect of nitrogen on a support that possesses many potential advantages over conventional carbon blacks.
- Chapter 6 discusses novel support functionalities beyond that of just nitrogen. Through characterization the effects of halide functional groups on electrochemical durability are discussed.
- Chapter 7 ties together the conclusions about durability, which can be made for PtRu catalysts supported on modified carbon structures, across the range of studied systems.

1.2 Research Statement

Due to the nature of scientific research in today’s day and age, this work presents data and analysis that was part of a collaborative effort. The Colorado School of Mines (CSM)

and the National Renewable Energy Laboratory (NREL) foster an environment conducive to teamwork and collaboration. This increases productivity and allows researchers to gain further insights into their research. As such I would like to thank, Dr. Svitlana Pylypenko, Dr. Tim Olson, Dr. April Corpuz, Dr. Arrelaine Dameron, Dr. Prabhuram Joghee, Dr. Guido Bender, Dr. Tom Gennett, Stefan Nikodemski, Dr. Jianhua Tong, Dr. Michael Sanders and Aaron Miller for there insightful conversation and contribution to parts of this work.

Assistance in materials fabrication was provided through a generous collaboration with NREL, Dr. Arrelaine Dameron and Dr. Tom Gennett. Electrochemical expertise and advice was provided through Dr. Tim Olson as well as members of NREL's hydrogen technologies sector. The author would also like to thank NREL for the use of electrochemical testing equipment at CSM.

I would also like to thank Dr. John Chandler, Gary Zito and the CSM electron microscopy facilities for access to equipment used to acquire the microscopy presented herein. XPS characterization shown throughout this work is thanks to the surface analysis facilities at NREL and Dr. Svitlana Pylypenko. Most other x-ray characterization provided throughout this paper was in collaboration with SLAC National Accelerator Laboratory and Dr. Steve Christensen at NREL.

Dr. Prabhuram Joghee and Dr. April Corpuz helped acquired the membrane electrode assembly (MEA) data provided in this thesis, various stages of this process were completed at both CSM and NREL. While this data is not the main focus of my research, it helps confirm the results of the materials I fabricated and characterized with various other techniques, giving validity to the statements I make within this work.

Near the beginning of each chapter I indicate the work done by the authors which helped me publish the work which makes up the body of this thesis.

My time at the Colorado School of Mines and all of the research presented in this document were funded thanks to the Army Research Office (ARO), under grant number W911NF-

09-1-0528. The research provided in this thesis has been presented at several conferences and published in multiple scientific journals. I take full responsibility for any inaccuracies printed in this document.

CHAPTER 2

DURABILITY OF ELECTROCATALYSIS IN DIRECT METHANOL FUEL CELLS

Liquid organic fuels are known for their relatively high energy density and the ability to generate enough energy, through electrochemical conversion into CO_2 , to be comparable to the combustion of hydrogen into water. Methanol is particularly attractive because of its low temperature reactivity, as well as its ease of storage and handling. Thus, a methanol-fed proton exchange membrane fuel cell (PEMFC) utilizing this potentially inexpensive fuel, would provide a sustainable and renewable energy source[1].

Unfortunately, the reality isn't that simple. There are several key factors preventing the commercialization of direct methanol fuel cells (DMFCs), including slow reaction kinetics, fuel crossover, and poor durability. Durability is a key issue in the overall DMFC picture because it affects the ultimate commercialization litmus test; cost per watt-hour. Currently Li-ion batteries, and other similar applications, perform better on a cost bases. However, these applications have disadvantages such as recharging, cycle length, and poor energy density that continue to drive researchers toward other solutions.[2]

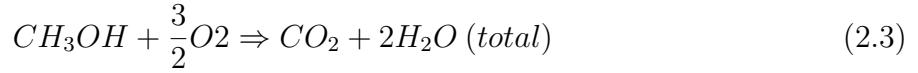
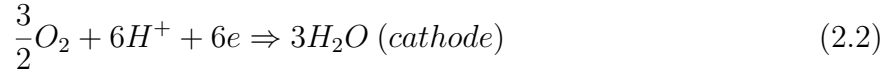
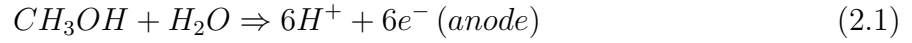
This chapter deals with the history, challenges, and current state of research on durability in DMFC studies. The basic aspects of DMFC operation are reviewed first, specifically with regard to reaction mechanisms, catalysts, and durability. Nitrogen is then discussed as a possible avenue for enhancing durability of fuel cell supports and the current status of study in this field is also discussed. Finally, the potential of other durability enhancing functionalities is considered.

2.1 Principles of Operation

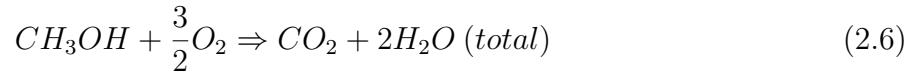
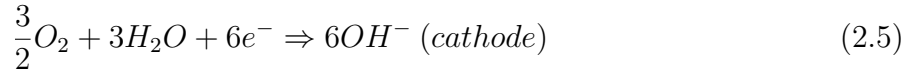
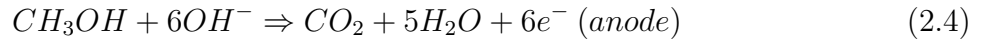
At the very core of current DMFCs is a polymer electrolyte membrane (PEM), used for ion exchange. This membrane is in complete contact with an electrode on each side (anode and cathode) of the membrane[3]. These electrodes are made up of three major components:

a catalyst layer, a diffusion layer, and some type of backing, see Figure 2.1. Within the catalyst layer, a combination of conductive carbon, electroactive species, and an ionomer is present. This combination allows for the mixed ionic and electronic conduction properties needed at the fuel interface for energy generation. When integrated with a diffusion layer and stacked together in series, the DMFC can be operated to deliver power to an external load.

PEM-based DMFCs are directly fed via a liquid methanol mixture (typically containing water) at the anode side. The methanol is then oxidized to CO_2 , although other reaction intermediates can form (i.e. formic acid and other organic molecules). The typical methanol oxidation reaction (MOR) in an acid electrolyte can be seen as follows:



A similar formulation can be written for the MOR in an alkaline solution:



E. Muller first studied this electro-oxidation process in 1922 [4], but it was not until the 1950's that the concept of methanol fuel cells was considered[5–7]. During this period it was determined that the reaction kinetics in alkaline media were superior to those in acid. However, at the time, the actual implementation of alkaline methanol fuel cells required a liquid electrolyte. Unfortunately, this type of electrolyte undergoes a chemical reaction with CO_2 (an MOR bi-product) and forms a carbonate, inhibiting performance.

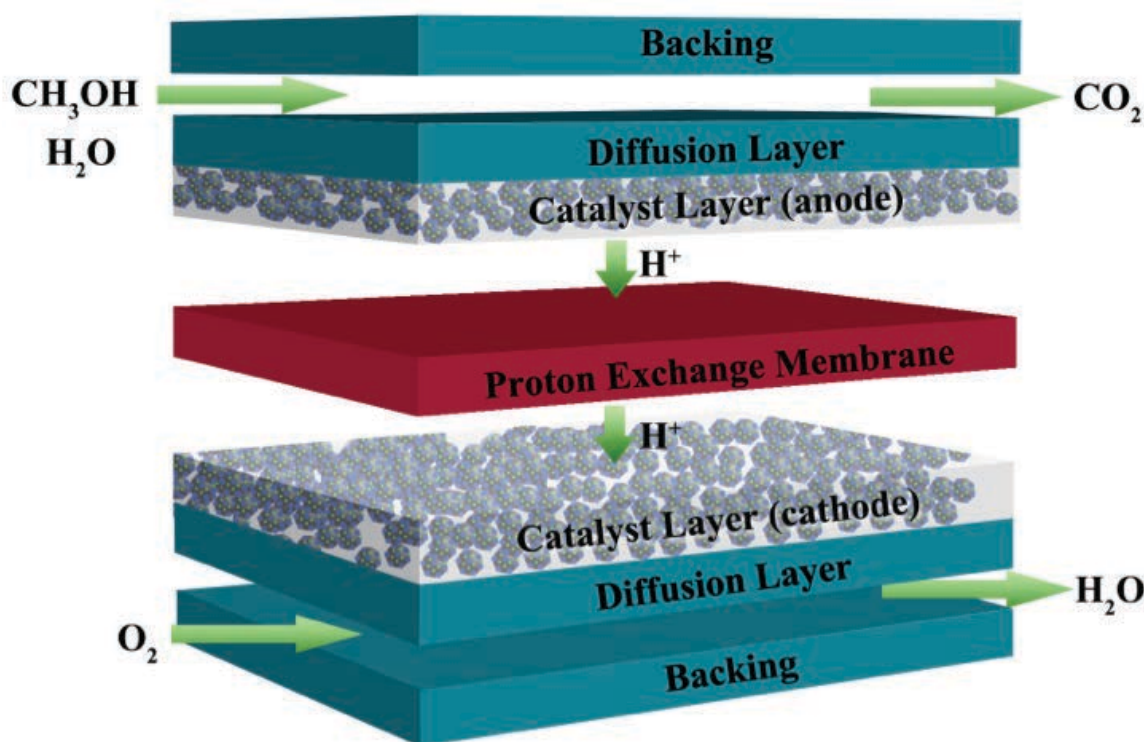


Figure 2.1: A simplified conceptual view of the basic components needed for a direct methanol fuel cell. The backing, diffusion layer, catalyst layer with nitrogen doping tethering the metal sites and a proton exchange membrane.

Therefore, revolutionary studies on methanol oxidation catalysts began in acid media. It was quickly found that Pt-based electro-catalysts performed the best, and Pt-Ru and Pt-Sn were labeled as the most promising candidates [8]. It appeared that Pt-Sn was a better intrinsic catalyst, however, a study by Watanabe [9] in the 1970's showed the improved potential of PtRu when alloyed with the proper ratio.

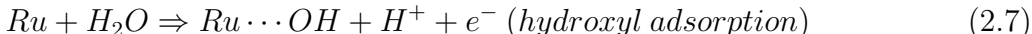
Early attempts to understand the MOR mechanism were carried out on pure Pt electrodes by Bagotzky and Vassiliev [10]. Their results led to the idea that a sort of methanolic residue and an oxygen species were adsorbing onto the Pt electrode and restricting performance. Based on these results researchers formed a bi-functional theory for bimetallic catalysts, in which two reactions were needed to proceed in combination with each other to create a synergistic effect. It became apparent that Pt had to be supplemented with an ad-atom or

alloyed metal that, modified the physical structure, changed the electronic structure of the surface, or allowed for the adsorption of species that participated in the oxidation reaction. Finally, in the later part of the century, through the use of various spectroscopic techniques and specifically in situ mass spectrometry, it was finally determined that CO was the cause of deleterious performance in Pt methanol oxidation[11–13].

The 1980’s and 90’s proved to be an important time for understanding the surface, electronic, and structural properties of Pt-based, bimetallic catalysts. Much of this work was completed through the use of advanced characterization techniques like X-ray photoelectron spectroscopy (XPS), ion scattering spectroscopy, and X-ray adsorption spectroscopy (XAS) [14–17]. This opened the door for researchers to begin studying catalyst behavior in single cell configurations (i.e. membrane electrode assemblies) rather than in just half-cell studies[18, 19]. These works reiterated the importance of bi-functional catalysts, but also revealed new challenges, like anodic to cathodic Ru crossover[19]. Ultimately, it was predicted that the Ru sites enhanced performance because they adsorbed oxygen species at low potentials.

2.1.1 Oxidation Mechanism

There has been much work in recent years to better understand the methanol oxidation reaction[20, 21]. As eluded to before, the MOR reaction on Pt proceeds through a series of intermediate steps, namely the dehydrogenation of methanol, the adsorption of CO, the chemisorption of OH like species, and the reaction of CO with the oxygen containing species to generate CO₂. Today, state-of-the-art DMFC catalysts are supported on high surface area carbon materials and the electrochemical performance is promoted through the alloying of Pt with Ru. According the bifunctional theory discussed above, the Ru sites help CO₂ evolution by removing the poisoning CO species through the adsorption of hydroxyl groups.



2.1.2 PtRu Catalysts

For these reasons the binary alloy of PtRu is the most promising DMFC catalyst to date. In this system Pt facilitates the dehydrogenation of methanol and strongly adsorbs the reaction intermediates. Although some debate still exists, many studies have shown that the optimal Pt:Ru ratio is 1:1[22]. From this it is easy to assume that the surface reaction between the CO and OH species is the rate-determining step. This is true at higher operating temperatures ($\sim 90^\circ\text{C}$), however, as operation temperature decreases, the adsorption of methanol requires more Pt sites[23]. Meaning that methanol adsorption becomes the rate-determining step and at low temperatures a more Pt-rich catalyst is beneficial.

Studies showing the synergistic effects of Pt and Ru through XAS revealed that the number of vacancies in the d-band of Pt increases when alloyed with Ru. This suggests that the benefit of PtRu may extend beyond the bi-functional mechanism into an electronic perturbation caused through alloying[16]. The performance of these electrodes is also impacted by their metal-support interactions. This is most easily seen through a study done by Arico et al. in which various metal/carbon ratios (85%, 60% and 30% Pt-Ru/C) were studied[24]. Their results showed 30% Pt-Ru/C to have the largest active surface area per weight. XPS analysis on these samples revealed a larger positive binding energy shift for the Pt4f spectra as the carbon content was increased. In the lower wt% samples the spectra showed larger concentrations of oxidized species, meaning that the carbon support could play a role in affecting the electronic structure of the active catalyst, if even just through an increase in surface area[24]. More directly, the carbon support also plays an essential role in effecting the durability and lifetime of these catalyst systems.

2.1.3 Durability of PtRu Systems

PEM fuel cells typically consist of catalytic nanoparticles on the order of 2–3 nm in diameter, which are dispersed across the surface of high surface area carbon particles, typically 20–50 nm in size (Figure 2.2). This maximizes the area-to-mass ratio of Pt and allows for im-

proved reaction kinetics due to an increased number of triple point boundaries (TPB's)[25]. This dispersion is also essential in reducing initial cost, but it must be maintained over the lifetime of a cell to decrease the cost per watt-hour.

Unfortunately, the coarsening of these nanoparticles decreases the number of catalytic surface sites and increases the number of bulk atoms. This creates a loss of TPB's, increasing the activation overpotential and resulting in the decrease of cell voltage, efficiency and lifetime. Coarsening occurs because the dispersion of nanoparticles is thermodynamically unstable and the formation of agglomerates reduces surface energy. Therefore, well-designed catalyst supports should stabilize nanoparticles through enhanced binding.

Coarsening can occur through two different mechanisms. The first mechanism is Ostwald ripening based. Ostwald ripening of individual nanoparticles precipitates through the dissolution of smaller particles. The dissolved metal then diffuses through the ionomer phase and re-deposits onto a larger catalytic-metal particle. This happens on the nanometer-scale (see Figure 2.3a). This process is analogous to the conventional definition of Ostwald ripening, which involves the transport of atoms or molecules from small particles to large particles. The reduction of surface energy is the driving force for this process, which causes the "larger particles to grow at the expense of the smaller ones." This process is one of the ways in which electrochemical surface area (ECSA) is lost during fuel cell operation.

Nanoparticle migration and coalescence is another mechanism for particle coarsening. This process involves the motion of nanoparticles across the support and their coalescence where they meet on the carbon surface, as shown in Figure 2.3b. This type of crystallite migration has been observed in the absence of an electrolyte through gas-phase sintering studies. However, this process is insignificant at temperatures below 500 °C for Pt-based catalysts. Although there is still a lack of conclusive experimental evidence for the migration of nanoparticles in low-temperature fuel cells, this proposed theory is widely accepted[26, 27] as responsible for surface area loss when fuel cells are operated at low voltages. This is hypothesized due to the fact that the solubility of Pt is negligible at voltages lower than 0.7

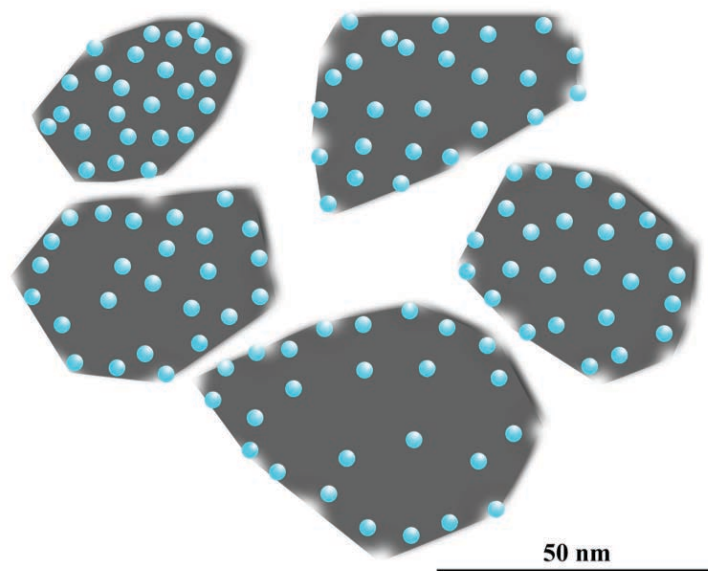


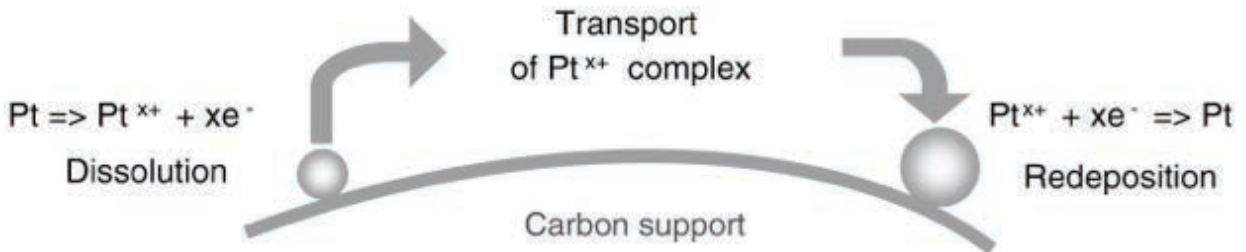
Figure 2.2: A schematic of PtRu nanoparticles on a carbon supports, this illustrates the catalyst system which makes up most of the catalysts layer. The nanoparticles in this diagram are about 2–3 nm in diameter, while the size of the carbon particles is around 20–50 nm.

V vs. RHE[28].

Detachment of Pt nanoparticles is another form of degradation in which active metal sites are removed from the support surface during operation. This can be seen in Figure 2.3c. The extent to which this process affects the loss of ECSA in fuel cell electrodes is dependent on cell voltage, as well as the nature of interactions between the metal sites and the support. These interactions can be changed through a variety of methods, including changing the graphiticity of the support or through heteroatom functionalization. Although corrosion of conventional carbon supports, such as Vulcan, is considered negligible at cell voltages lower than 0.8 V in low-temperature fuel cells, carbon corrosion and weight loss has been shown to be significant at voltages higher than 1.1 V vs. RHE [29].

Complicating this, current DMFC catalysts typically employ PtRu loading levels between 0.05–0.1 mg/cm² which needs to be lowered below 0.03 mg/cm² to achieve US Department of Energy (DOE) targets [2]. This ultimately means that fuel cells need to maintain more

(a) Growth via Modified Ostwald Ripening



(b) Coalescence via Crystal Migration



(c) Detachment from carbon support

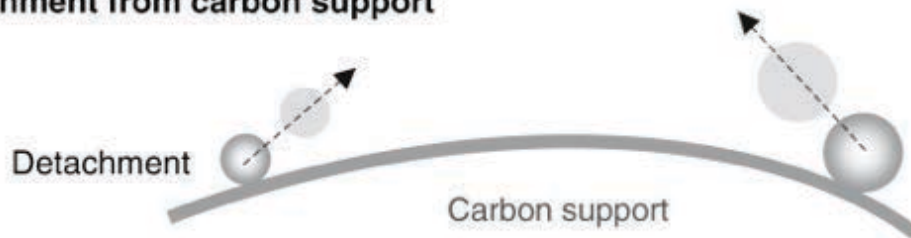


Figure 2.3: Proposed mechanisms for instability of metal nanoparticles in low-temperature fuel cells: (a): dissolved metal species from smaller particles diffuse through ionomer phase and redeposit onto the surfaces of larger particles (Ostwald ripening); (b): Metal nanoparticles migrate on the surface of carbon support and coalesce; (c): Metal nanoparticles detach from the carbon support and/or agglomerate due to carbon corrosion. Reprinted from reference [29]

active ECSA with less metal loading over their lifetime. Therefore, since thousands of hours of consistent energy production are required for commercial implementation of fuel cells, metal-support stability is a crucial issue.

If fuel cells are to have a share of our energy future, the area of catalyst stability must be addressed. Several approaches have been explored to enhance catalyst durability, including changing the carbon structure, porosity, or even the use of extended surfaces; however, one of the most promising techniques is surface functionalization.

2.2 Nitrogen Functionalization

Within the last two decades an emerging body of literature has begun to suggest that carbon-based catalyst supports can be intentionally modified with nitrogen to form strong, beneficial catalyst-support interactions. This doping effect substantially enhances catalytic activity and stability while allowing for decreased metal loadings. The concept of ‘doping’ was made familiar in the semiconductor industry decades earlier, however Shukla et al., first demonstrated observations focused on fuel cell enhancement, in 1994[30]. Their results showed that the MOR reaction was enhanced through a nitrogen activation process. Since then, nitrogen modification has been suggested to provide up to a 10-fold increase in catalytic enhancement for the MOR reaction in Pt-based carbon systems. This potential has elevated fuel cells, and specifically DMFCs, closer to commercialization. As such there has been a significant effort placed on understanding and improving current knowledge of nitrogen modified carbon supports for fuel cells applications.

2.2.1 Methods

Carbon can be nitrogen modified through two primary methods: 1) direct synthesis or 2) post-treatment. In principle, direct synthesis strategies have the potential to induce homogeneous modification throughout the entirety of the material, however current efforts have not conclusively demonstrated this potential. The major direct synthesis routes of N-carbon structures include chemical vapor deposition (CVD) and pyrolysis. While these

direct synthesis methods have shown success, post-treatment nitrogen modification methods (including bombardment, thermal annealing, or solution treatment) are more widely used. In comparison to direct synthesis methods, post treatment methods generally lead only to surface doping, leaving the interior (bulk) of the treated carbon material unchanged.

Depending on the carbon allotrope, pyrolysis of various nitrogen containing organic compounds is arguably the simplest intrinsic doping route. Pyrolysis, which is the thermal decomposition of organic molecules in the absence of oxygen, has been demonstrated by several studies to be an effective manner through which to incorporate nitrogen heteroatoms. This process has led to nitrogen functionalization in carbon materials like graphene, carbon nanotubes (CNT's), mesoporous carbons, and activated carbon blacks. The simplicity of this technique has also lent itself to use in templating strategies.

CVD has been used for decades to synthesize a variety of carbon structures[31–35], most commonly graphene and nanotubes. Frequently gas mixtures are used to create both the n-modified and unmodified carbon structures, although liquid precursors have been used as well. In these processes, a simple hydrocarbon (i.e. CH_4) is used as the carbon source, while ammonia (or similar) is typically used as the nitrogen source. Importantly, the doping level can be controlled through flow rate adjustments and gas precursor ratios. Using this technique N concentration levels can be controlled between 1-9 at%.[31, 35–40] However, the CVD processes can be relatively expensive and difficult to scale. Therefore, motivation exists to explore more facile techniques that have the ability to scale easily and create large volumes of material.

Post synthesis modification of carbon is a well-documented field of study having been explored for the last 4 decades. These types of methods typically introduce nitrogen into the carbon matrix by energetic thermal treatment routes or ion bombardment. As early as the late 1970's Evans and Kuwana had explored ammonia plasma processing on a glassy-carbon electrode as a method of nitrogen doping[41, 42]. Around the same time ion implantation was also implemented on carbon based materials like amorphous carbon, diamond, and

graphite. In 1976 researchers documented the effects of thermal processing on carbon electrodes, however it was not until the thermal processing study by Shukla et al. that nitrogen functionalities were first explored in fuel cell environments[30].

A comprehensive comparison of literature studies investigating the effect of nitrogen modification on catalyst support interactions with Pt-alloy catalyst activity shows that it is still unclear whether certain N-doping methods are more effective than others. Studies do show that nearly all N-doping methods offer positive benefits. In some cases, specific N functionalities are correlated as primary contributors to catalytic enhancement. Current research suggests that doping methods as well as processing conditions can strongly influence the composition and distribution of nitrogen sites. Therefore, careful studies are still needed to clearly understand which specific functional groups and processing methodologies can enhance catalytic activity with the most effectiveness[2]. Appendix A gives more insight into this area[43].

2.2.2 Functionalities

Regardless of the modification technique used, a wide variety of nitrogen functional groups are created after treatment. The most common of these functionalities are pyridinic, pyrrolic, and graphitic; however, other functionalities can exist depending on precursor, driving force, and other such parameters. Examples of these functionalities are graphically presented in Figure 2.4. Although inconclusive, literature has shown certain N functionalities strongly implicated as main contributors in the durability and catalytic enhancement of fuel cells. Pyridinic sites are frequently listed as beneficial, due to observations that appear to stabilize catalyst nanoparticles. Similarly, graphitic (or substitutional) nitrogen is also frequently reported as having an encouraging effect on nucleation sites.

To better understand the complicated contribution of various functionalities, density functional theory (DFT) has been employed by many research groups. This quantum mechanical modeling technique can provide invaluable insight into the energetic shifts of carbon as a function of nitrogen modification and help elucidate the role of specific functional groups

on stability and performance for specific applications. These insights can help direct future study, give validity to current hypotheses and/or raise valuable questions. To this end, theory can give insight into properties such as structure, absolute and relative (interaction) energies, reactivity or other spectroscopic quantities, dipoles and higher multipole moments, vibrational frequencies, and electronic charge distributions. Computational chemistry frequently involves a delicate dance between residual error minimization and computation time. As such, all computational chemistry approaches, including both *ab initio* and semi-empirical approaches involve approximations. These range anywhere from simplified forms of first-principle equations, which are easier/faster to solve, to approximations limiting the system size (i.e. periodic boundary conditions). Because of these limitations, the carbon allotropes, graphene and graphene’s cylindrical analog, CNT’s, are typically the best suited for computational study.

In 2012, Schiros et al. used x-ray adsorption spectroscopy combined with DFT to show the overall electronic effect of the different bond structures in N-doped graphene[44]. In this study, the extra electron from the single N defect was shown to be distributed in the local network (electron donation) of carbon π -states and create an n-type effect. However, multi-defects such as pyridinic species have the opposite effect, insomuch as the two electrons fill the σ -bonds of the carbon neighbors, two electrons form a lone pair in the graphene plane, and the remaining electron occupies the N π -state. Thus, the pyridine-like defect has the equivalent occupation of a nominal carbon in graphene, however a π -electron is missing due to the vacancy site. Therefore the system is p-doped, leading to the conclusion that pyridinic nitrogen has an electron withdrawing nature.

More recently, Muhich et al. studied singly and triply bound N-substituted graphene using DFT[45]. Their results indicated that both n-type singly N-doped graphene and p-type triply N-doped graphene gain electron density; these results were contrary to the study by Schiros[44]. This behavior was attributed to unequal charge sharing in the C-N sp^2 sigma bond and the necessity of occupation for the orthogonal p orbital to maintain the

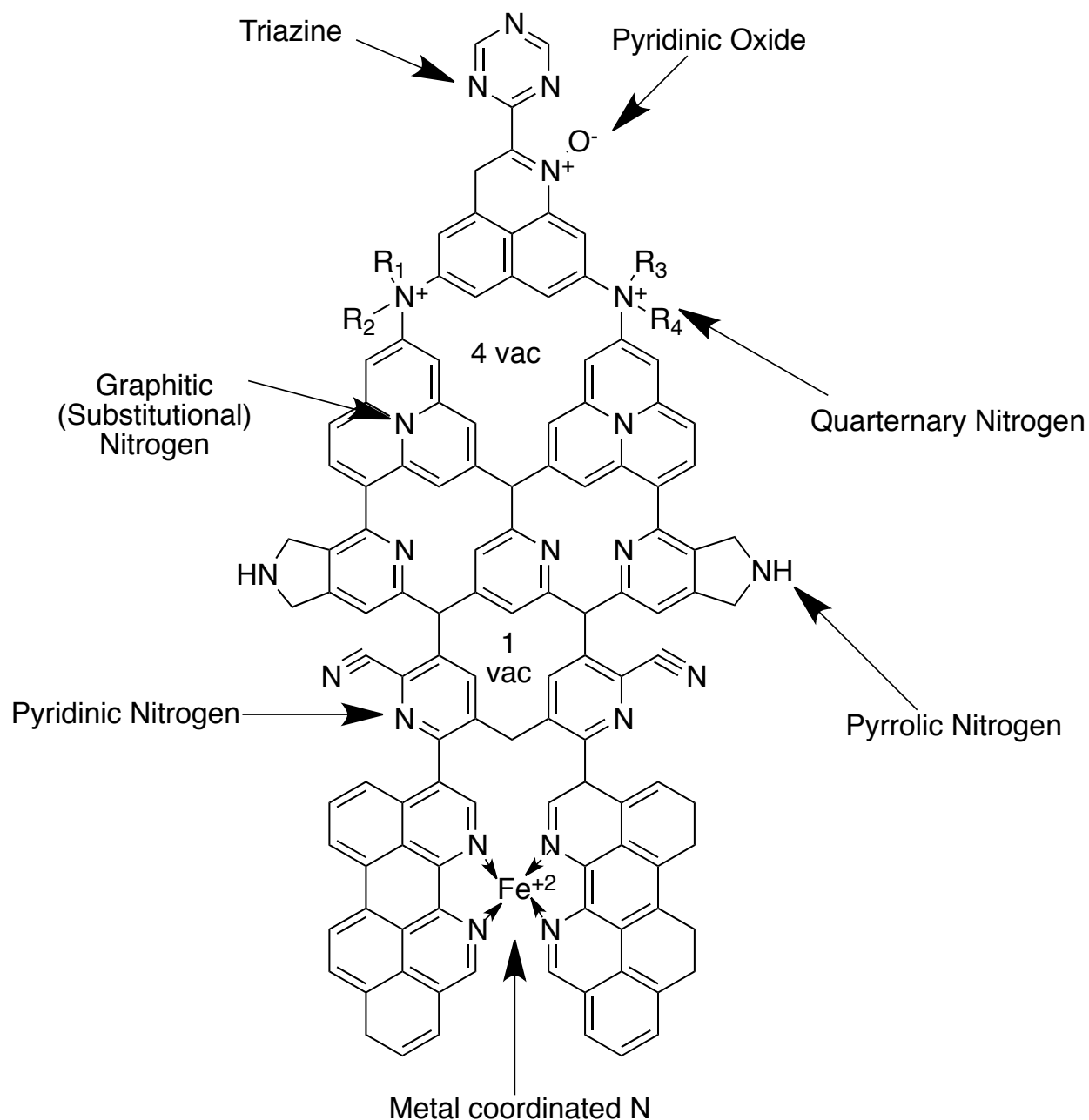


Figure 2.4: Structures of the various types of nitrogen functionalities commonly observed in the N-doped materials discussed throughout the literature. The three most common types are pyridinic, pyrrolic and graphitic. The other functionalities discussed are quaternary, triazine, pyridinic oxide and metal coordinated nitrogen. While these are common in literature, very little of my research deals with these types of functionalities. The figure also shows the different vacancy possibilities. This figure is your guide to the functionalities discussed in this thesis and in Appendix A.

aromaticity of graphene. This work also showed a strong enhancement in adsorption of Pt even at distances well away from the nitrogen site while revealing that migration over the nitrogen atom is unlikely due to the increased energy barrier. This phenomena has also been supported through experimental studies using STM mapping[46]and motivates the use of N-doped carbon materials as Pt catalyst supports to mitigate catalyst migration and agglomeration. Muhich et al. also showed that metal sites adsorbed on a pyridine ring are trapped by the strong Pt-N bonds having a greater stabilizing effect than the single N defect[45].

A 2009 study combining DFT theoretical applications with experimental results using highly oriented pyrolytic graphite (HOPG) highlighted the fact that Pt binding energy modification due to N-doping is likely the principal reason for the improved Pt catalytic activity and metal site ‘tethering’ in N-doped carbon fuel cell support systems[47, 48]. Similar studies investigating the effects of PtRu on nitrogen-modified systems reveal the complicated nature of the bi-functional system and indicate that the behavior is greatly affected by the specific nitrogen functionality employed. Simulations revealed that graphitic N defects consistently improve resistance to dissolution in all considered cases, (dissolution of Pt from Pt, dissolution of Pt from Ru_2Pt_2 and dissolution of Ru from Pt_2Ru_2). However, DFT analysis shows that the effect of pyridinic nitrogen is conflicting. It helps improve resistance to dissolution for Pt from Ru_2Pt_2 , but makes dissolution of Ru from Pt_2Ru_2 more likely. Therefore, current literature states that the stability of PtRu catalysts can be improved through a well-balanced mix of pyrrolic, pyridinic and graphitic N[49].

2.2.3 Experimental Results of Nitrogen Modification

While a few authors have examined the role of nitrogen-doping on the enhancement of performance for carbon-supported Pt-Ru catalysts, most papers have discussed the effects of nitrogen doping on carbon-supported Pt catalysts[47, 48, 50–59] even though these pure Pt-based catalysts are not optimal for methanol oxidation applications. A review paper published in 2010 highlighted the effects of nitrogen doping on the performance of methanol

electro-oxidation catalysts. This study concluded that regardless of the nitrogen precursor or doping method, N-modified systems generally showed improved MOR performance when compared against unmodified analogs[2]. Specifically, N-doped catalyst systems showed improved catalyst dispersion[47, 49–51, 53, 54, 57], earlier onset potential[47, 53–55, 60, 61], increased current produced per catalyst surface area (specific activity)[54, 60] or per metal catalyst mass (mass activity)[53, 57, 62] and exhibited improved stability. The evidence that nitrogen modification improves dispersion of carbon-supported precious metal nanoparticles and enhances their durability is strong. Figure 2.5 shows the effect of nitrogen concentration on the pre- and post-cycled Pt particle size distribution and the respective benefit to the electrochemical surface area. Unfortunately, the evidence that nitrogen modification enhances intrinsic catalytic activity is less clear-cut.

It is well documented that the nucleation and dispersion of metal nanoparticles on carbon materials with high graphitic content is quite poor and typically requires surface pretreatment. Studies on the incorporation of nitrogen into CNT’s shows that nitrogen creates sites for preferential nucleation, without need for pretreatment[50]. Generally, catalyst nanoparticles supported on undoped and N-doped carbon differ in their initial density, dispersion, size and composition. This is especially the case when colloidal or wet chemistry methods are used. It has been observed that N-doping alters the nucleation and growth of nanoparticles in a beneficial way, by leading to improved dispersion and smaller particle sizes[47, 49–51, 53–55]. Guo et al. showed that incorporation of nitrogen into ordered mesoporous carbon enables dense dispersions of Pt nanoparticles at dramatically increased Pt loading[51]. Lei et al. performed a similar study by comparing a series of nitrogen-containing ordered mesoporous carbons synthesized in the temperature range of 600-950 °C. Their results showed that the nitrogen concentration was critical to the dispersion of the Pt nanoparticles[53]. Within this set of materials, the authors reported BET surface areas from 988 to 1166 m²/g, pore sizes from 2.7 to 3.3 nm and nitrogen concentrations from 9.6 to 4.8 at.%. The authors found that despite relatively comparable BET surface areas, the increase in nitrogen

concentration from 4.8 % to 9.6 % led to a systematic decrease in the Pt nanoparticle size, from 4.0 to 2.4 nm. The interplay between the N concentration and particle size in terms of their effect on the CO stripping peak was also discussed. Typically, materials synthesized at lower temperatures possess the higher N contents and exhibited the higher CO tolerance, while the materials synthesized at the highest temperatures showed lower nitrogen content, but larger pore size. These materials synthesized at the higher temperatures frequently show lower charge transfer resistance and demonstrated the best mass activities for methanol oxidation. Lei et al. explored this effect of nitrogen by using a series of nitrogen-doped carbon shells pyrolyzed in the temperature range of 400-950 °C. Their results showed that materials synthesized at 900°C have the best-combined catalytic performance towards oxidation of methanol. Meaning that an optimum nitrogen/particle size ratio exists.

Pt and PtRu supported on N-doped porous carbon nanospheres show enhanced dispersion and particle size as well as improved onset and mass activities[55]. Authors also reported that N-supported PtRu retained better performance even after durability cycling. For bimetallic precious metal nanoparticles such as PtRu, nitrogen functionalization of the carbon support can change the Pt-to-Ru composition due to altered nucleation and growth kinetics. For example, PtRu nanoparticles grown on ammonia-treated N-containing CNT's also contained an unalloyed hexagonal Ru phase that appeared to be at least partially responsible for enhanced activity[60].

In addition to the typical catalyst degradation mechanisms (i.e. dissolution/precipitation, migration/coalescence, support detachment) experienced by carbon-supported Pt-based catalysts, PtRu/C anode catalysts experience an additional degradation mechanism associated with the dissolution of ruthenium, which crosses over the electrolyte and contaminates the cathode. A few recent studies have indicated that N modification of the catalyst-support interactions could improve PtRu catalyst nanoparticle stability while also mitigating Ru crossover and particle-growth mechanisms[63]. This topic will be the focus of chapter 3 in this dissertation.

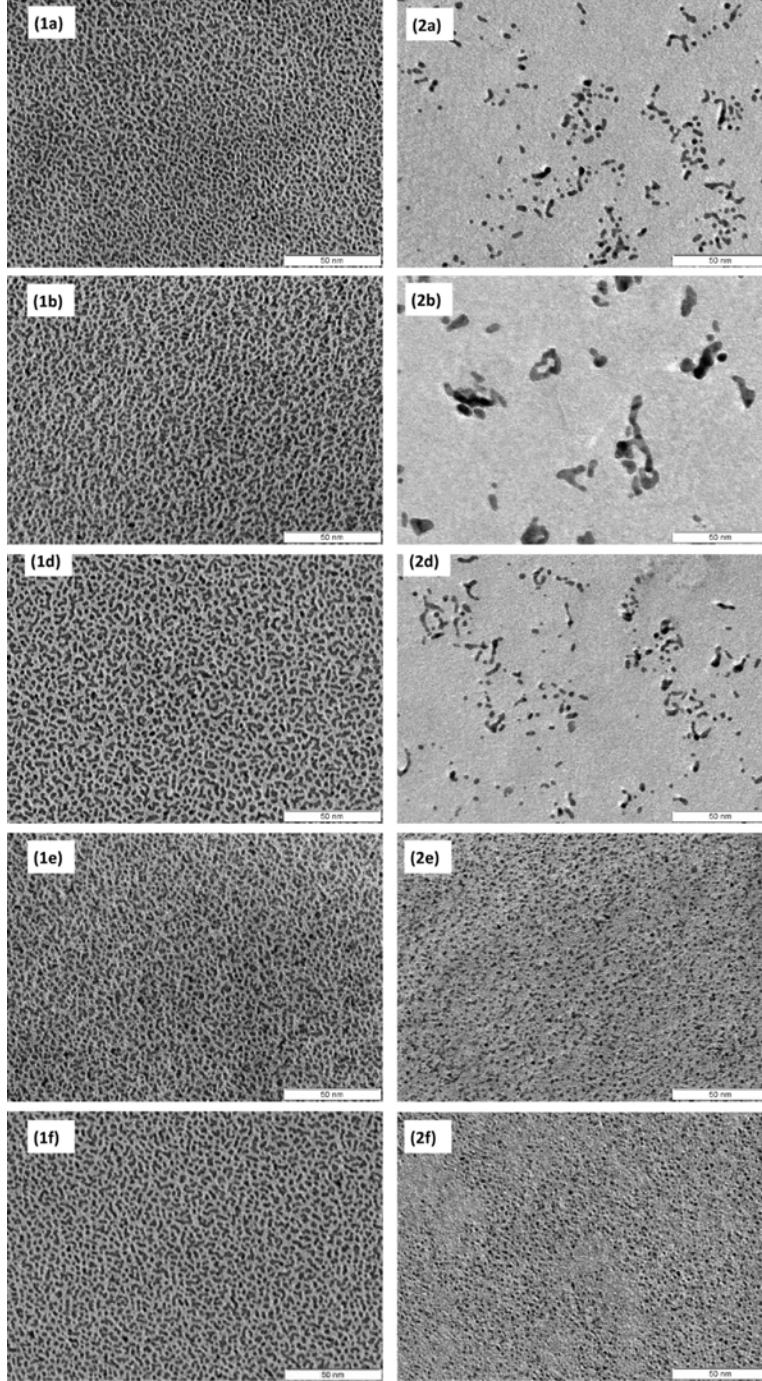


Figure 2.5: TEM micrographs representative of sputtered PtRu deposited on HOPG substrates (1) pre-cycled, demonstrating coverage and range of nanoparticle sizes, and (2) post-cycled, demonstrating changes in the coverage, particle size, and formation of agglomerations. Shown for samples with dosages of (a) 0.0×10^{16} , (b) 0.4×10^{16} , (d) 1.3×10^{16} , (e) 4.7×10^{16} , and (f) 9.6×10^{16} ions cm^{-2} (0, 5, 15, 45, and 100 s). Reprinted from reference[63]

Since N-doping alters the metal nanoparticle nucleation dynamics, changing the initial particle size, it is difficult to assess the effect of N-doping on catalyst durability. In order to address this issue, the experiments documented in this thesis isolate the effect of nitrogen functionalization on the stability of PtRu nanoparticles by utilizing catalysts sputtered from a single-alloyed target. This experimental design was introduced by the O’Hayre research group in 2009 [47, 48, 63–65] and leads to initial PtRu nanoparticle coverage, dispersion, and particle size distributions that are nearly identical for nitrogen-modified and unmodified carbon supports. Using catalysts fabricated in this manner nanoparticle stability can be probed through accelerated degradation testing. This was first explored by Pylypenko et al. using a series of model HOPG substrates with varying nitrogen concentrations (controlled via ion implantation dosage). These samples had identical starting PtRu nanoparticle composition, size and coverage[63]. It was found that low implantation dosages had an overall negative effect on catalyst stability, presumably due to the presence of implantation-induced physical defects and oxygen groups associated with the nitrogen functionalities present at low dosages. These samples were similar in their stability to those exposed to Ar^+ irradiation, which introduced physical defects that had a beneficial effect on nucleation, but a detrimental effect on durability[47]. Samples implanted at higher nitrogen dosage, however, possessed a mixture of physical defects, oxygen functionalities and significantly higher amounts of nitrogen (up to 8 at% N prior to metal deposition). The high nitrogen concentrations led to the formation of clustered multi-nitrogen defects and also led to great improvement in PtRu nanoparticle stability (specifically preventing nanoparticle agglomeration from migration/coalescence). During my time at Mines I contributed to further investigations of this system. In this study, electron energy spectral images were analyzed to reveal that only regions with the highest nitrogen concentration offered improved stability after accelerated degradation testing[49]. Within the areas of best stability, PtRu nanoparticles appeared to be surrounded by nitrogen defects, suggesting that the incorporation of nitrogen next to the catalyst nanoparticles is of utmost importance in preventing migration[49]. Experimental

results presented in chapter 4 of this thesis confirm these results and provide further insight.

In a similar vein, nitrogen modified graphene based electrocatalysts have been studied by multiple research groups mostly investigating ORR performance[37, 66–70]. A few groups have also investigated the effect of N-graphene on Pt catalysts systems[58], however, to my knowledge, no research has been done investigating PtRu catalyst systems on N-graphene. Chapter 5 provides an initial look into this promising field, documenting the challenges and benefits.

2.3 Other Functionalities

While doping carbons with nitrogen atoms has experienced great progress and yielded promising material throughout the past couple decades, other doping strategies could provide a bright future for fuel cell related carbon supports. Within the last five years, heteroatom dopants such as boron, sulfur, and phosphorus have been shown to effectively modify the physical, chemical, and electronic properties of bulk carbon materials[71]. The chemistry of other heteroatoms might not be as conducive for incorporation into a carbonaceous backbone, as is the case for nitrogen; nevertheless the electronic structure of halide elements could provide exciting functionalization opportunities.

In conducting polymers, iodine has been widely accepted as an important dopant that improves the electrical conductivity[72]. Since graphene can be compared with the conjugated structure of polymers, recent studies have confirmed that the charge transfer doping of iodine in a few-layers of graphene can be achieved through a post deposition process that leads to intercalation[73]. Yao et al. investigated these iodine intercalated graphene structures for use in the ORR and showed performance greater than that of commercial Pt/C[72]. These above-mentioned factors motivated me to explore the use of PtRu/HOPG doped with iodine as electrocatalysts for MOR. While some studies have recently investigated iodine doping, fuel cell research into this type of carbon modification is undocumented.

In chapter 6 alternative functionalities are discussed. Iodine is explored as well as fluorine. To date little literature exists on the effect of fluorine modification of carbon, however the

chemistry is limited because of the electronic structure of fluorine. This work is the first to discuss the effect of fluorine modification on fuel cell based supports.

2.4 Conclusions

A large research effort has been placed on understanding DMFC systems and functionalized carbon architectures. While these are not always studied in conjunction with each other, the convergence of these topics has proved a synergistic avenue of research with great possibilities for commercial application and future scientific research. Many of these insights provided on carbon functionalized materials for DMFCs can be applied to applications far and wide. This thesis provides an exciting avenue for future study in the realm of fuel cells as well as batteries, supercapacitors, hydrogen storage, drug delivery, and microelectronic applications.

CHAPTER 3

THE EFFECTS OF NITROGEN MODIFICATION ON THE DURABILITY OF HIGH SURFACE AREA SYSTEMS

As discussed in the previous chapter, alloyed PtRu catalysts supported on high surface area carbon powders are the current state-of-the-art DMFC catalyst system. Unfortunately, any nanoparticle interface is plagued by the loss of active catalyst surface area over time. This can be due to particle growth mechanisms such as migration/coalescence and Oswald ripening, which contribute to overall performance degradation. Additionally, another side-effect of utilizing Pt-Ru based anode catalyst materials, is Ru-crossover; this also leads to performance losses[74–76]. Developing material-based solutions to mitigate the effect of Ru-crossover and limit particle growth processes are highly desired. In this chapter I demonstrate that the enhanced catalyst particle stability provided by tuning catalyst-support interactions through nitrogen modification of high surface area carbon supports can mitigate particle-growth degradation mechanisms and Ru crossover.

This chapter focuses on the N-functionalization of high surface-area carbon powders relevant to integration in fuel cell membrane electrode assemblies (MEA's) through a two-step synthesis procedure. First, nitrogen heteroatoms are incorporated into a commercial high surface area carbon support via a N-ion implantation technique, followed by Pt-Ru incorporation via magnetron sputtering. Both ion-implantation and sputtering processes are performed in a single chamber without breaking vacuum. Rotating disk electrode (RDE) electrochemical testing, membrane electrode assembly (MEA) testing, microscopy, X-ray photoelectron spectroscopy (XPS), small-angle X-ray scattering (SAXS), and X-ray diffraction (XRD) experimentation was conducted. This work illustrates the unique electrochemical performance of these new materials. Overall, nitrogen-functionalized high surface-area catalyst materials demonstrate similar enhancements in stability to what was previously

described for the model HOPG[47, 48] and outperform benchmark commercial catalyst in terms of both activity and stability.

3.1 Experimental Information

I co-author all three papers [77–79] presented in part throughout this chapter. Dr. Tim Olson performed a majority of the electrochemical analysis, while Dr. Prabhuram Joghee performed the MEA testing. Dr. Arrelaine Dameron analyzed the XRD and provided material synthesis. I helped analyze and draw correlation between all parts of the results presented herein. I was also the main party responsible for the SAXS data presented in this chapter.

3.1.1 Catalyst synthesis

Powder catalyst samples were fabricated in a custom sputter chamber described in detail elsewhere[64]. The chamber, consisting of vacuum components and backed by a 520 L/s turbo molecular pump (Balzers TMP 520, Pfeiffer Vacuum GmbH, Asslar, Germany), housed a rotating barrel type powder sample holder rotated with a DC gear motor (Leeson Electric Corporation, Graphon, WI), an ion source (3 cm DC (ITI) ion gun, Veeco, Santa Barbara CA) and an orthogonally-oriented 2" sputter gun (Onyx Mag 2, Angstrom Sciences, Duquesne, PA). The ion gun was positioned a distance of 9 inches at 35 degrees from normal to the powder surface. The retractable sputter gun was at a sample-to-target distance of 2.6". (Figure 3.1). During implantation and deposition, the barrel was rotated at 30 rpm in order to achieve uniform modification of the samples. During ion-implantation, the sputter gun was retracted to be clear of the incident ion beam (Figure 3.1a). For sputtering, the sputter gun head was positioned inside the wheel to allow for free rotation. (Figure 3.1b). Sputter process gases were introduced through a MFC controlled manifold while implantation gases were introduced directly via a separate leak valve directly through the ion gun. During an experiment, 500–1000 mg of commercially available carbon powder (Cabot Vulcan XCR72R) was placed into the barrel and the chamber was evacuated to approximately

1×10^{-6} Torr. Implantation was performed prior to sputtering at a chamber pressure of 8×10^{-4} Torr N_2 . The beam current and implantation times were held constant for a particular sample in the range of 12mA to 45 mA, and 15 mins to 120 mins, respectively. Discharge and acceleration voltage were held constant at 55 V and 100 V, respectively, for all samples. Following implantation, sputter depositions were performed at 25 mTorr with 10 mol% $O_2:Ar$ at DC power of 45W for 60 mins. The chamber was not opened between implantation and sputtering, which limited any oxidation of the modified support surface. Optimization of the Pt-Ru sputter parameters we completed before I started work on this project and is discussed in detail[64].

The composite inks of the electrode materials for half-cell electrochemical testing consisted of 10 mg of catalyst powder, 7.96 mL of DI water, 2 mL of isopropyl alcohol and 40 μ L of 5wt% Nafion solution (total catalyst concentration of 1 mg/mL). The ink was bath-sonicated in ice water for 20 minutes to generate a stable homogeneous catalyst ink solution. A 10 μ L aliquot of the dispersed ink solution was placed on a 0.196 cm^2 glassy carbon electrode and dried in air. The electrochemical 3-electrode half-cell was completed with a Pt-mesh counter electrode and a calomel reference electrode (235 mV vs. RHE) separated from the main cell via a salt bridge.

3.1.2 Electrochemical Details

Carbon monoxide (CO) stripping experiments were performed in 0.5 M H_2SO_4 by saturating the electrolyte with CO and holding the working electrode at a potential of 0.2 V vs. RHE for 10 minutes at 25 $^{\circ}C$ (room temp). The cell was then purged with N_2 for 15 minutes while the electrode potential was maintained at 0.2 V vs. RHE. The potential was then scanned in the positive direction to 0.9 V at 20 mV/s. The upper potential limit of 0.9 V was implemented for Accelerated Degradation Testing (ADT). This ADT protocol allows us to obtain data in a short amount of time and correlate DMFC catalyst stability and degradation with the results of the ADT. Two subsequent full potential sweeps (0 to 0.9 V vs. RHE) were collected and used as the background for determination of CO stripping area.

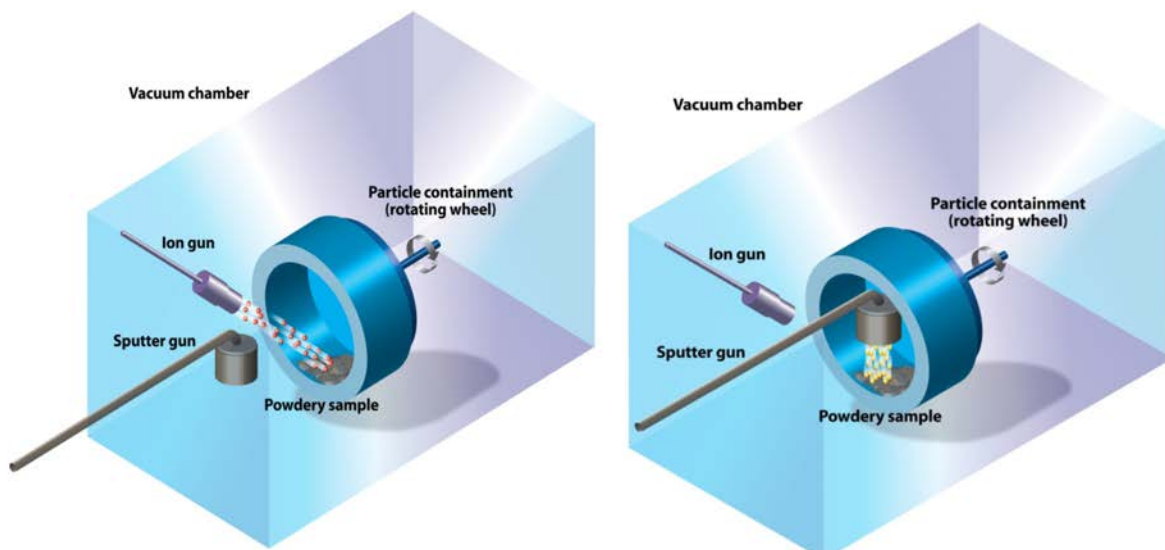


Figure 3.1: Schematic of the vacuum chamber used for catalyst synthesis. Ion-implantation a) and Pt-Ru sputter deposition b) are carried out step-wise in the fabrication chamber.

Methanol oxidation testing was performed in N_2 saturated 0.5 M H_2SO_4 /0.5 M methanol solution (room temp). The potential was swept from 235 mV to 800 mV vs. RHE at 10 mV/s. X-ray Characterization Details

The electrodes for the in-situ Small Angle X-ray Spectroscopy (SAXS) and X-ray diffraction (XRD) experiments were prepared by applying catalyst ink drop-wise to SGL Group company Carbon 25BA gas diffusion backing paper. The inks were prepared to produce electrode catalyst layers with 1:1 carbon:Nafion ratios and total metal loadings of approximately 5 mg.

XRD was performed on the 11-3 beam line at the Stanford Synchrotron Radiation Light source (SSRL) at SLAC National Accelerator Laboratory. The beam line employs a side-deflecting, bent Si (311) monochromator to select X-rays at 12.724 keV off an insertion device. No calibration of the flux was performed. The data were collected on an image plate (MAR345) and reduced using the WxDiff software platform. Data are plotted as intensity versus magnitude of the momentum transfer vector, $q=4\pi/\lambda \sin(\theta)$, where λ is the X-ray wavelength and θ the angle between the incident X-rays and sample surface. The q calibration was performed during data reduction using the diffraction rings from lanthanum

hexaboride powder.

SAXS was conducted on beam line 1–4 of SSRL at SLAC National Accelerator Laboratory. Data was collected at incident photon energy of 8.33 keV using a Rayonix 165 CCD detector. The collected data was then analyzed with the Igor Pro (v. 6.22, Wavemetrics) plug-in, Irena (v. 2.40). Samples were subjected to approximately 3000 electrochemical cycles, while the X-ray spot remained in the same location. This data was then analyzed with the Igor Pro (v. 6.22, Wavemetrics) plug-in, Irena (v. 2.40). By subtracting the blank carbon backing data from the catalyst spectrum of interest, and normalizing the background noise, a proper comparison of the intensities was made. This process was completed for each sample shown here. The intensities were then modeled using the following equation using the Irena software package for SAXS[80].

$$I(Q) = |\Delta\rho|^2 \int_0^{\infty} |F(Q, r)|^2 V^2(r) NP(r) dr \quad (3.1)$$

Where $\Delta\rho$ is contrast, $F(Q, r)$ is scattering form factor, $V(r)$ is the particle volume, N is the total number of scattering particles, and $P(r)$ is the probability of occurrence of scattering site size r . In this experiment the probability was fit using a log-normal distribution, shown in (3.2), adopted from the NIST engineering statistics handbook[81]

$$P(r) = \frac{1}{r - (\min mean \sqrt{2\pi})} \frac{\exp(-\ln(\frac{r - \min}{sdev})^2)}{2sdev^2} \quad (3.2)$$

In this equation Min is the minimum diameter size, $sdev$ is the standard deviation of the size distribution, and $mean$ is the mean diameter subtracted from the minimum particle size.

The X-ray experiments were conducted using a custom-built cell specifically designed for in-situ measurements. The cell operates in transmission mode with a working electrode constructed of carbon paper modified with catalyst material suspended in solution. The window materials consisted of 6 μm Kapton (Chemplex Industries, Inc). The transmission path for an empty cell included $\sim 12 \mu\text{m}$ of Kapton and $\sim 0.5 \text{ mm}$ of electrolyte solution. The

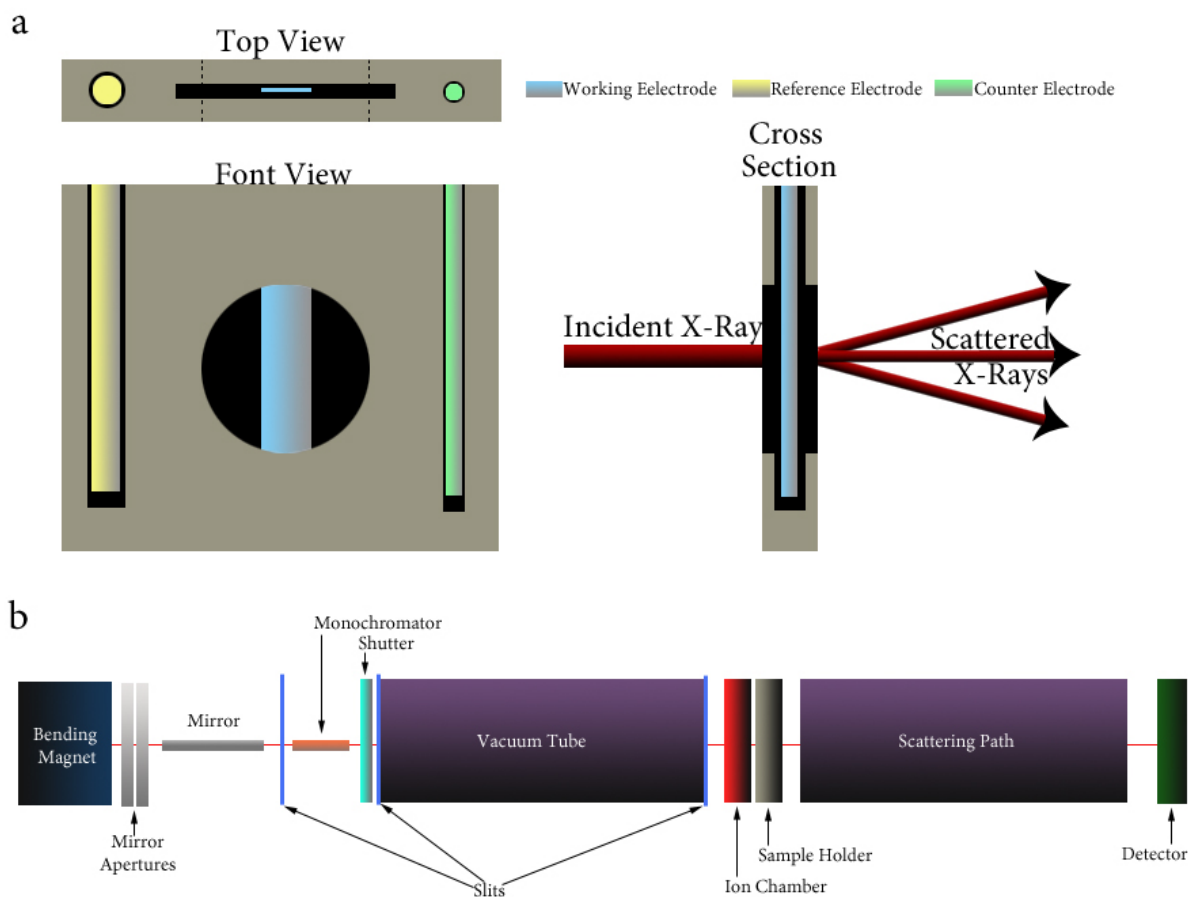


Figure 3.2: a) The design of the custom in-situ electrochemical cell allowing for analysis of the same precise area on the electrode. b) A schematic of SLAC's beam line 1-4.

cell also had a small reservoir (approx. 50mL) for solution and spaces to hold a platinum mesh counter electrode. Another compartment in the cell allowed for connection to the $\text{Ag}^+/\text{AgCl}_2$ reference electrode (BASi, Part No. MF2052) via a salt bridge. Figure 3.2 shows a detailed schematic of the cell used. I used a 0.1 M perchloric acid solution (GSF Chemicals). Typical waveforms consisted of cyclic sweeps from 0 to 0.9 V vs. RHE with a 0.5 V/s scan rate.

3.2 Results and Discussion

In this chapter the characterization and electrochemical performance of three sets of Pt-Ru based fuel cell catalyst materials were investigated. The materials included: commercially

available Johnson Matthey Pt-Ru/C catalyst (JM 5000); an in-house material utilizing a non-modified carbon support (Pt-Ru/C); and two in-house materials fabricated with a N-modified carbon support (Pt-Ru/N-C).

3.2.1 Surface Characterization

XPS analysis of the three catalyst materials showed that the elemental concentration of nitrogen ranged from 0.2 at% for the undoped in-house support, to 0.5 at% for the JM 5000 commercial benchmark, to 1.3 at% for the in-house N-doped sample implanted at 14 mA. Another N-modified in-house sample, implanted at 20 mA, is also discussed in the SAXS section, this sample has ~2 at% nitrogen. The increase in N concentration for the N-doped samples were also accompanied by the broadening of the C 1s spectra caused by the formation of various C-N as well as C-O bonds[65]. The small amounts of nitrogen detected in the undoped and JM5000 materials are related to the presence of a single nitrogen peak attributed to amine, cyano or pyrrolic nitrogen. Meanwhile, the N 1s spectrum for implanted samples is much broader, indicative of the likely presence of various nitrogen functionalities, including pyrrolic, pyridinic, amine and graphitic N, as shown in Figure 3.3.

The bulk Ru:Pt ratio was also measured with X-ray fluorescence (XRF). The results showed the sputtered materials to be consistently, slightly more rich in platinum when compared versus the commercial catalyst benchmark. However, the surface Ru:Pt ratio, as measured by XPS, indicates more enrichment in ruthenium with the N-modified samples as compared to the non-implanted commercial and in-house sputtered samples. Overall the major difference between commercial and sputtered samples was with respect to their ruthenium compositions. In the commercial catalyst, surface ruthenium is distributed between metallic ruthenium (Ru(0), Ru(II), Ru(IV), ruthenium oxide RuO_2 and hydrous ruthenium oxide RuO_xH_y [63, 82]. By contrast all in-house catalysts show significantly greater amounts of hydrous ruthenium oxide RuO_xH_y and significantly lower amounts of Ru(0), Ru(II), and RuO_2 .

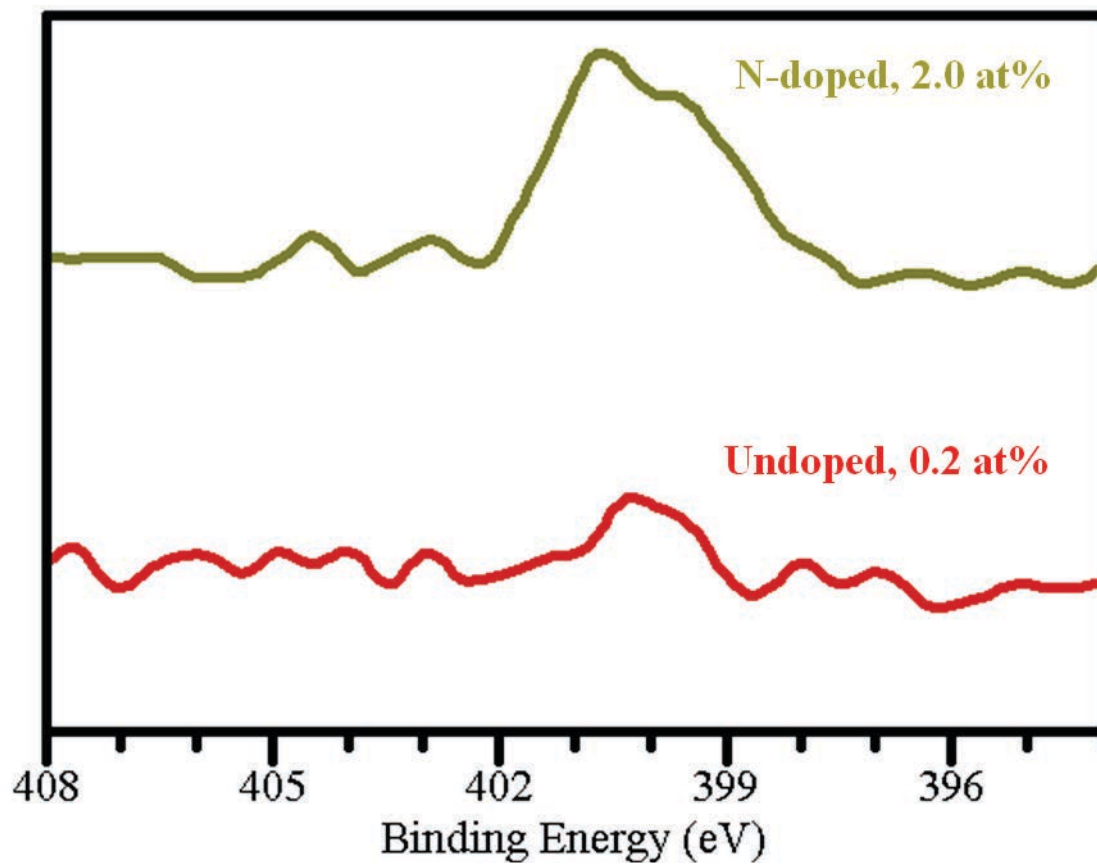


Figure 3.3: XPS N1s spectra acquired from the unmodified and 20mA N-modified sample after metal deposition. Nitrogen concentration in N-doped sample is (~ 2 at.%). The unmodified sample contains only trace amount of nitrogen ($\sim .2$ at.%).

3.2.2 RDE Electrochemical Characterization

Determination of the electrochemical surface area (ECSA) for the various Pt-Ru/C and Pt-Ru/N-C materials was accomplished with standard CO stripping analysis ($420 \mu\text{C}/\text{cm}^2$). Figure 3.4 shows the CO stripping curves for two of the in-house fabricated materials, as well as commercially available 30 wt% Pt-Ru/C (JM 5000). All in-house materials show a more negative “kick-off” potential for the removal and oxidation of the adsorbed CO as compared to the commercial benchmark. The N-modified carbon supported catalysts indicate lower ECSA ($55 \text{ m}^2/\text{g}$) as compared to the non-modified carbon supported catalysts ($69\text{--}73 \text{ m}^2/\text{g}$). Based on this data and the overall Pt-Ru metal contents of the respective catalyst materials, the mass-specific surface areas (m^2/g) were calculated and the values are shown in Table 3.1.

Accelerated electrochemical degradation tests (ADT) were performed by cycling the electrode potential from 0 to 0.9V vs. RHE. To determine the ECSA as a function of cycle number the CO stripping areas were measured after 0, 100, and 5000 electrochemical potential cycles. Since a DMFC anode is rarely brought to potentials higher than 0.7 V during typical fuel cell operation and because an increased rate of Ru dissolution at potentials greater than 0.9 V is common, this limited potential cycling window was chosen for accelerated durability testing[83]. Figure 3.5 shows the stripping curves for the materials while the calculated percent of remaining ECSA after $100\times$ and $5000\times$ cycles are shown in Table 3.2. Compared to the unmodified catalysts, the N-modified Pt-Ru/N-C catalyst shows a higher retention of metal surface area after the ADT. Even though the initial ECSA is lower for the n-modified samples, upon electrochemical cycling, improved durability is obtained for PtRu nanoparticles associated with nitrogen defect clusters in the N-modified catalyst.

3.2.3 MEA Testing Analysis

To further understand the effects of nitrogen treatment on anode catalyst materials in a real fuel cell environment, the same materials were also subjected single cell testing. For the JM5000 anode (Figure 3.6a) before testing, a narrow peak associated with the CO oxidation

Table 3.1: Quantification of Pt-Ru/Carbon materials demonstrating elemental composition, determined by XPS, distribution of ruthenium species obtained by curve-fitting Ru 3p spectra and ratio of ruthenium to platinum, determined by XPS and XRF.

Sample	Elemental Conc. XPS (rel. conc.%)					Ru:Pt Ratio		Distribution of Ru, XPS (rel. Conc. %)			
	C	O	Pt	Ru	N	XPS	XRF	Ru ₁ , Ru	Ru ₂ , RuO ₂ (Screened)	Ru ₃ , RuO _x H _y	Ru ₄ , RuO ₂ (unscreened)
JM5000	89.3	7.8	1.2	1.3	0.5	1.1	.99	10.7	32.1	38.7	18.6
PtRu/C	85.9	9.9	1.9	2.0	0.2	1.1	.91	0.0	10.1	50.6	39.3
PtRu/N-C	88.3	7.4	1.4	1.6	1.3	1.2	.93	0.0	6.8	52.9	40.3

Table 3.2: The values for ECSA as determined by MEA CO stripping, the MOR specific activities, and percentage of ECSA after 100× and 5000× cycles in the ADT protocol are tabulated.

Sample	ECSA ($\frac{m^2}{g}$)	Specific Activity @.4V ($\frac{A}{cm^2}$)	Mass Activity@.4V($\frac{A}{mg_{metal}}$)	% of ECSA after 100 cycles	% of ECSA after 5000 cycles
JM5000	69	3.0×10^{-5}	20	48	17
PtRu/C	73	3.0×10^{-5}	24	51	10
PtRu/N-C	55	2.9×10^{-5}	17	60	40

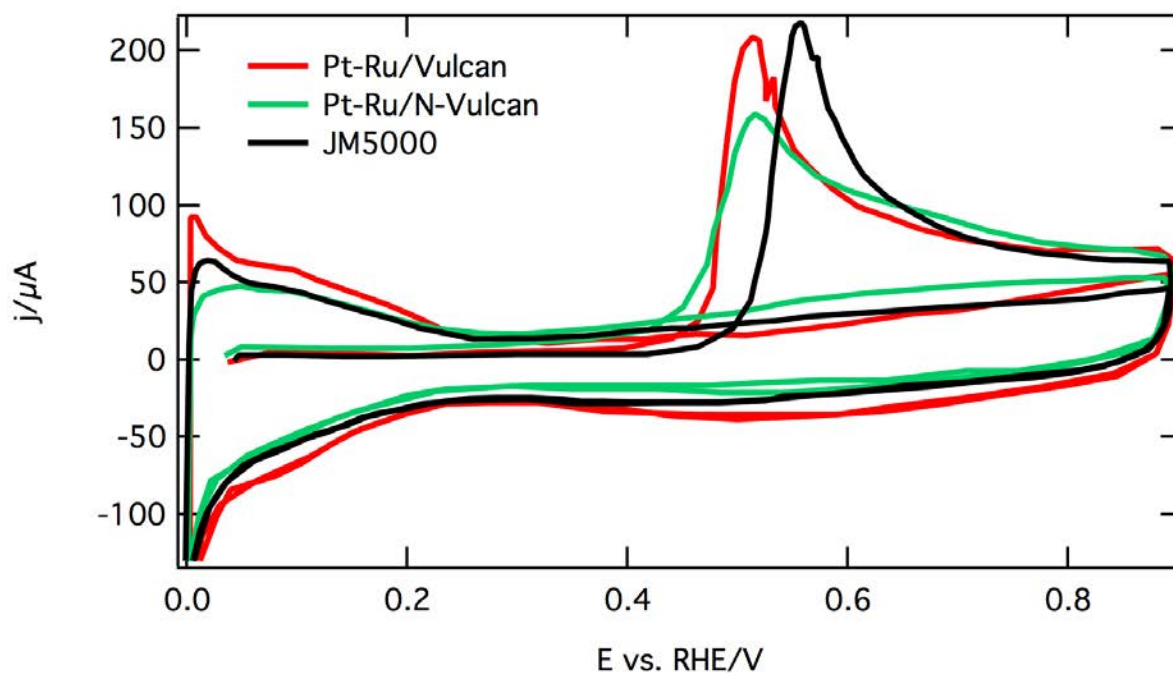


Figure 3.4: CO stripping curves obtained for the undoped, doped, and commercial Pt-Ru materials.

was observed at a peak potential of 0.47 V. After 200h ADT, this CO oxidation peak shifted positively by ~ 20 mV (0.49 V). For the N-modified PtRu/N-C anode (Figure 3.6b), the CO oxidation peak was initially located at ~ 0.44 V and after 200h ADT the peak potential only shifted by ~ 10 mV. Additionally, the PtRu/N-C anode peak height and width shows less reduction as a result of the ADT protocol. These results indicate a smaller loss of ECSA for PtRu/N-C when compared with JM5000 over the course of the ADT study. This point is further quantified by the relative ECSA loss curves depicted in Figure 3.6c. These outcomes suggests that less RuO_xH_y dissolution[84] may occur for the PtRu/N-C anode (which consists largely of RuO_xH_y species), during the initial stages of the ADT. It is hypothesized that the higher initial amounts of metallic Ru in JM5000 preferentially dissolve during the initial stages of the ADT, thereby leading to the more rapid initial ECSA losses observed for this catalyst.

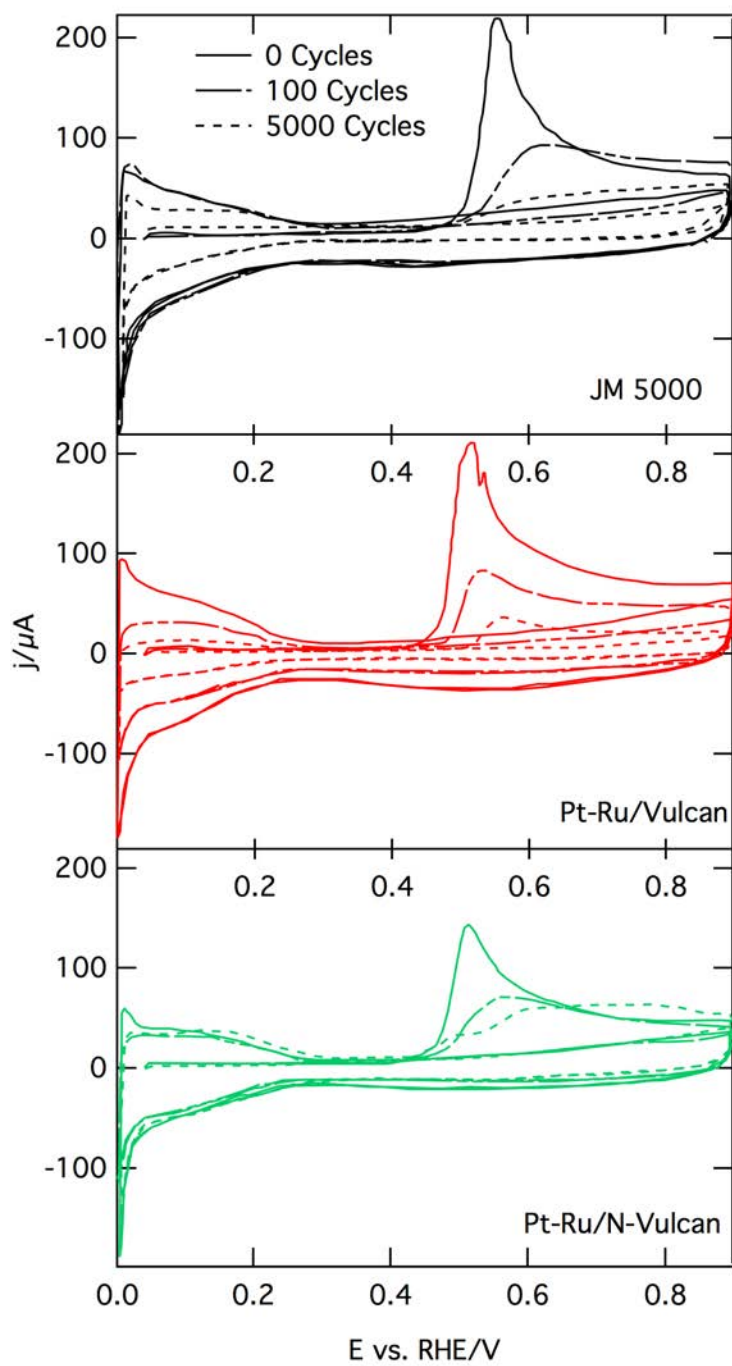


Figure 3.5: CO stripping curves obtained after 0 (black), 100 x (red), and 5000 x (green) cycles for (a) JM5000, (b) Pt-Ru/C (undoped), and (c) Pt-Ru/N-C (N-doped).

After 400 and 640h ADT there are no further shifts in the CO oxidation peak onset potential. This is most likely due to the electrochemical formation and conversion of mainly RuO₂ to higher oxide species during ADT at 0.8 V, which helps to mediate CO oxidation at an early potential[85–87]. Because of the formation of these higher Ru-oxides, further ECSA loss in both catalysts is mostly mitigated at the longer 400 and 640h ADT intervals. The absolute values of the ECSA for both the catalysts after different intervals of ADT are given in Table 3.3. After completion of the full 640h ADT study, the loss in ECSA for the PtRu/N-C and JM5000 anodes was found to be ~21 and ~26%, respectively. Even though the ECSA loss is largely attributed to Ru dissolution in these MEA studies, additional ECSA loss from the particle agglomeration processes is likely.

3.2.4 Small Angle X-ray Scattering Analysis

In high surface area systems it can be difficult to show with convincing evidence, the mitigation/change of morphological behavior of the catalyst particles. As can be seen from the TEM images, Pt-Ru nanoparticles obtained with sputtering (Figure 3.7) have different morphologies from those obtained via other synthesis routes (i.e. colloidal deposition) and can have many nanoparticles located in close proximity to each other making estimation of the particle size challenging. It has previously been shown that particle size and particle size distribution estimated by TEM, XRD and SAXS closely match [88–90] although TEM has been shown to sometimes overestimate particle size because measured particles can easily contain several primary crystallites[89]. Therefore, in order to tackle this challenging problem SAXS was employed as a method of assesses the changes that occur to the catalysts during potential cycling.

This in-situ technique enabled specific, identical regions of the electrodes to be compared before and after potential cycling in order to eliminate the variability issues associated with the heterogeneous nature of the materials at different regions of the electrodes. The collected experimental intensities are shown in Figure 3.8a/b and modeled data is shown in Figure 3.8c/d. In Figure 3.8c SAXS scattering diameters for the pre-cycled unmodified cata-

Table 3.3: ECSA measured by CO stripping voltammetry for the anode of the MEAs with PtRu/N-C and JM5000.

Sample	Before ADT ($\frac{m^2}{g}$)	After 160 hours ADT ($\frac{m^2}{g}$)	After 400 hours ADT ($\frac{m^2}{g}$)	After 640 hours ADT ($\frac{m^2}{g}$)
PtRu/N-C	56.1	51.9	47.0	44.1
JM5000	126.6	109.0	98.0	94.1

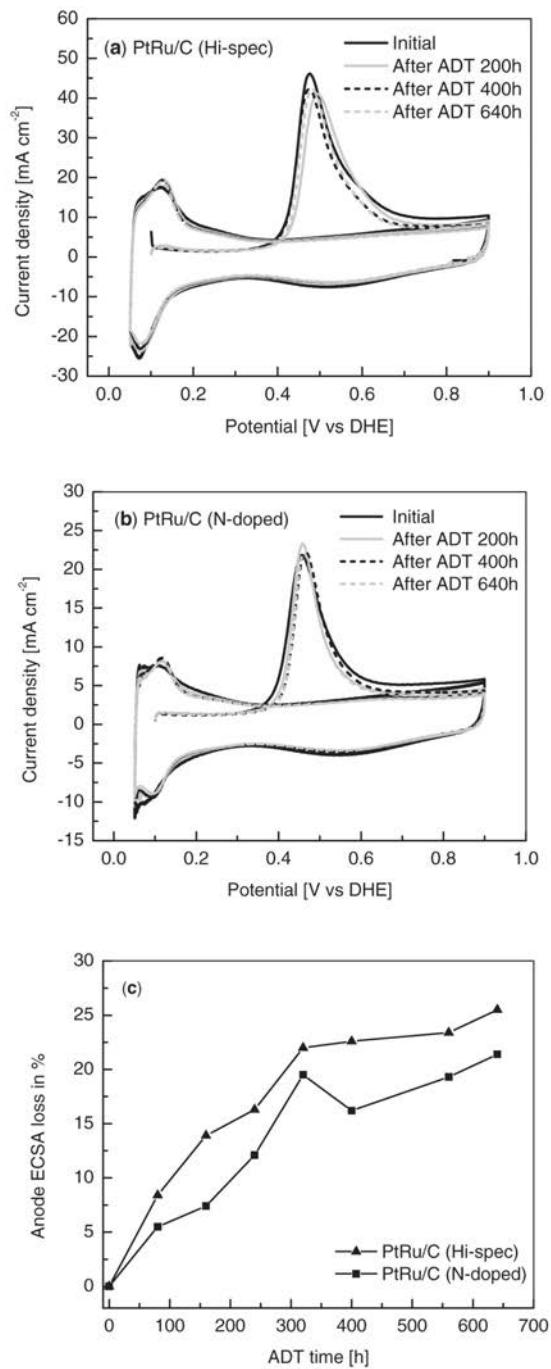


Figure 3.6: CO stripping voltammograms for the MEAs as a function of ADT time; (a) JM5000, (b) PtRu/N-C, and (c) Relative anode ECSA loss vs. ADT time extracted from the CO stripping voltammograms.

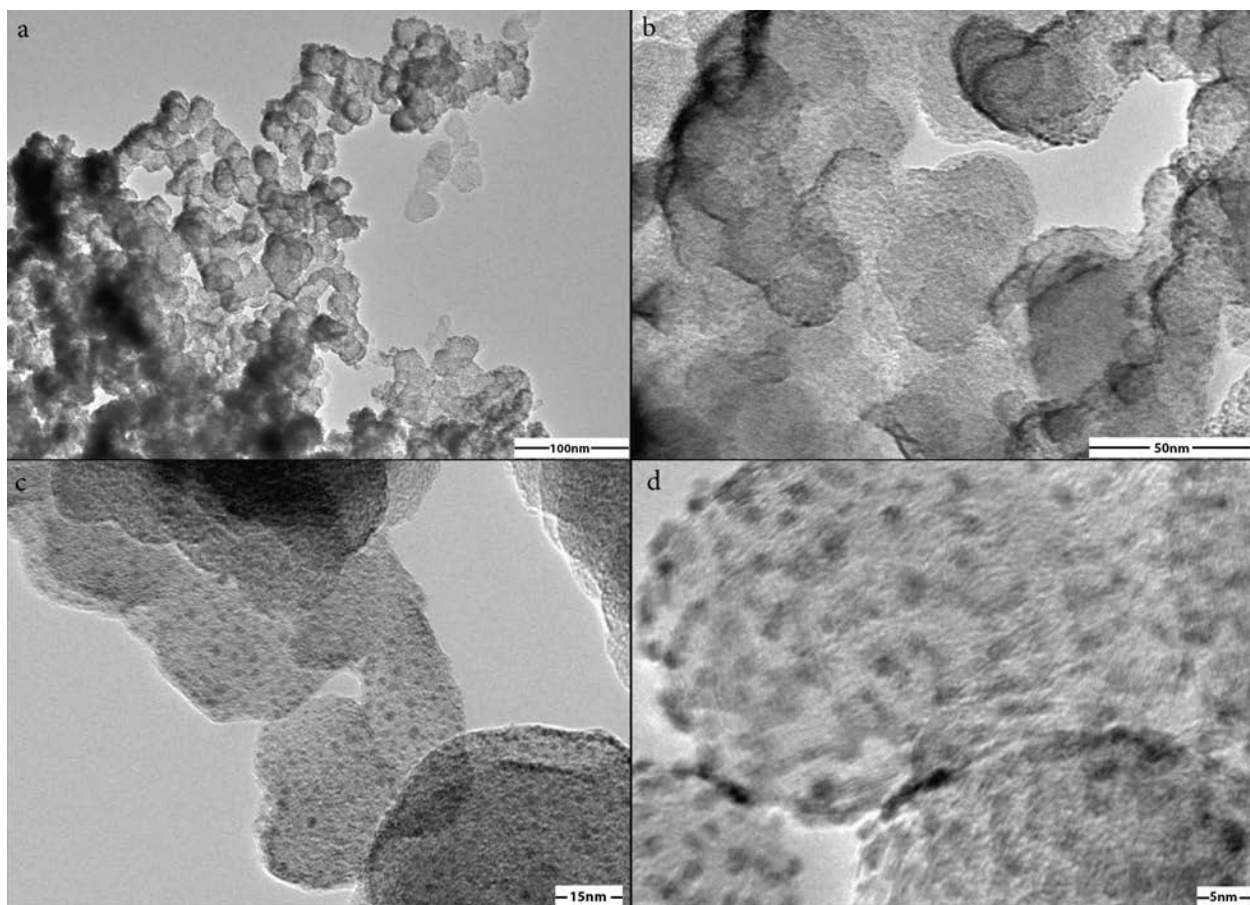


Figure 3.7: TEM images of the nitrogen modified catalyst before cycling. a) and b) Low-magnification images demonstrating coverage of the sputtered PtRu/N-Carbon. Micrographs at higher magnification (c and d) show regions of less dense particle coverage demonstrating that nanoparticle size observed by TEM ($\sim 1\text{-}5\text{nm}$) is in agreement with values determined by SAXS.

lyst are shown. In general, the particle size distribution for this unmodified electrode shows a relatively wide bi-modal range of particles from $\sim 1.8\text{nm}$ to 5nm in size. The particles can be roughly divided into two Gaussian distributions (as indicated on the plot): one distinct particle distribution at $\sim 1.9\text{nm}$ and another more broad distribution at 3.5 nm tailing toward higher particle sizes. After in-situ accelerated degradation testing, the catalyst shows significant changes in particle size distribution, Figure 3.8c (red line). The changes are most clearly seen in the increasing size and changing volume of the 5nm size distribution, indicating the formation of large agglomerations. These agglomerates are likely caused by migration/coalescence and modified Ostwald ripening mechanisms. The leftwards shift on the small particle size end of the distribution, which occurs simultaneously with the appearance of this peak change, is indicative of Ostwald ripening processes occurring through dissolution/reprecipitation.

For the nitrogen-modified support, Figure 3.8d shows the initial particle distribution. Again two distinct particle sizes are observed, however there are marked differences from the unmodified sample. The N-modified material shows a much narrower, more distinct and slightly smaller set of particle size distributions compared to the unmodified material (initial mean particle sizes are $\sim 1.5\text{nm}$, and 2.7nm). The narrower widths and lower mean sizes associated with the bimodal Pt-M particle distribution on the nitrogen-modified carbon support are consistent with previous studies of Pt-M on carbon systems which show smaller average particle size and narrower particle size distributions for metal nanoparticles deposited on nitrogen-modified surfaces compared to unmodified surfaces[90]. These observations may show that nitrogen modification dramatically increases the ease of Pt-M nucleation on the carbon surface, thereby leading to smaller average particle size and a tighter particle size distribution. However, this result is surprising in some ways, because sputtering was chosen to limit morphological differences created from preferential nucleation. Therefore, this indicates 1) the incredible preference of nucleation on or near nitrogen sites or 2) the changes to the carbon structure associated with N-modification leads to less metal deposited

on the surface under identical sputtering conditions.

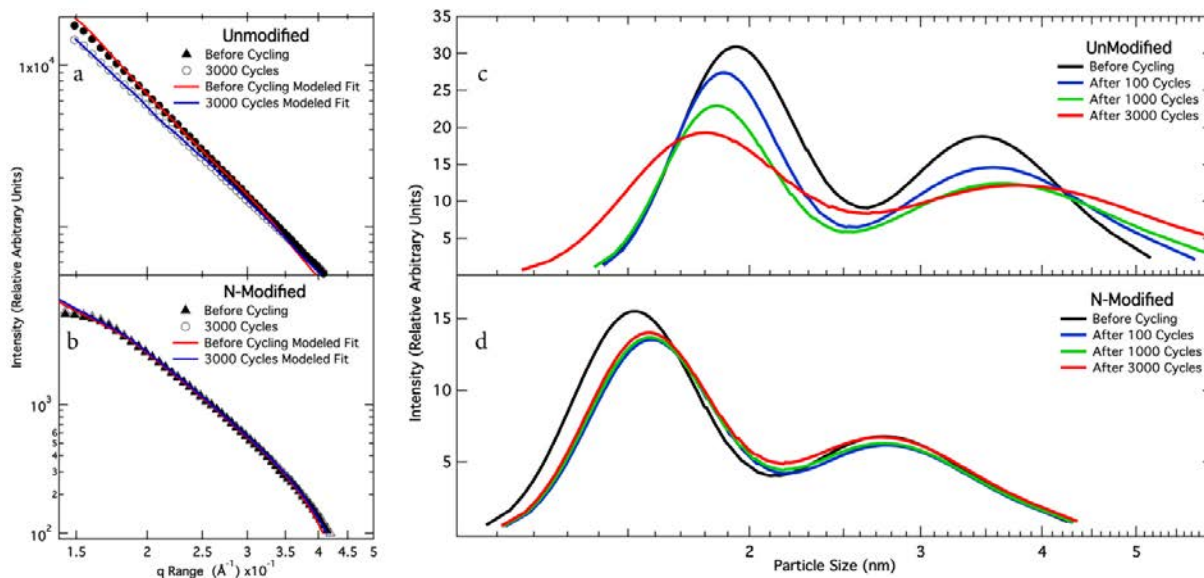


Figure 3.8: Modeled SAXS intensities shown with the collected experimental data for the unmodified (a) and nitrogen-modified (b) samples. The particle size distributions extracted from the SAXS modeling at various cycling times are shown in (c) and (d) for the unmodified and nitrogen-modified samples, respectively.

After cycling, a small amount of particles near the 1.5nm distribution were dissolved in-solution. Meaning this process still occurred, but at a much slower rate than observed in the unmodified system. The absence of significant changes to the 2.7nm particle size peak is important, indicating an improved binding interaction between catalyst and support (minimization of migration). Furthermore, most of the changes in the N-modified sample's particle distribution occurs in the first 100 electrochemical cycles, after which the distribution stabilizes and remains virtually unchanged out to 3000 cycles. This is in marked contrast to the unmodified sample, which shows significant continued changes in particle size distribution with increasing cycling, even out to 3000 cycles. These results suggest that nitrogen modification strongly mitigates the particle size growth observed in the unmodified sample, which facilitates significantly longer catalyst lifetime and increased catalyst performance over time due to the increased retention of catalyst surface area. It is also of interest to point out that

the commercial catalyst (not shown) decreases in the volume distribution across the entire 1–5 nm particle range, which is most likely due to dissolution. This is in agreement with the electrochemical results presented above. (Although the manufacturer does not provide information, the JM5000 catalyst is believed to be fabricated via an industrial standard colloidal deposition technique to achieve the small particle size.)

3.2.5 X-ray Diffraction Results

A comparison of the SAXS vs. XRD provides data that can help distinguish between agglomeration and dissolution/re-deposition particle growth mechanisms. If the re-deposition of the dissolved metal phase is the primary particle growth mechanism, then growth of crystalline peaks in the XRD spectrum is expected. The XRD data can be seen in Figure 3.9, this data is presented as the difference between a spectrum acquired after a certain number of electrochemical cycles vs. the initial un-cycled material spectrum. These difference spectra can be computed because exactly the same area of the sample is examined before and after cycling in the synchrotron using the in-situ electrochemical cell setup (Figure 3.2a). For all samples, the initial spectra lacked any peak structure, meaning that the metal catalyst phases are non-crystalline and more amorphous in nature.

As a function of cycling, the undoped in-house catalyst (red spectra) developed several crystalline peaks indicative of a Pt-Ru alloy material. The crystalline peaks grew quickly, within the first 150 cycles, and then remained unchanged for the duration of the cycling experiments. This data suggests a growth and stabilization mechanism with dissolution of particles balanced by growth through re-deposition, migration and coalescence processes. By contrast, the commercial catalyst (black spectra) changed minimally, and discernible crystalline peaks were only apparent after ~1000 cycles. The doped in-house catalyst (blue spectra), at initial cycling times, appears much more stable than the undoped in-house catalyst. At 100 cycles, no appreciable peak signature can be discerned from the noise. These data demonstrate that N-doping within the catalyst-carbon matrix blocks or delays the degradation of the sputtered catalyst materials by increasing the catalyst support interactions.

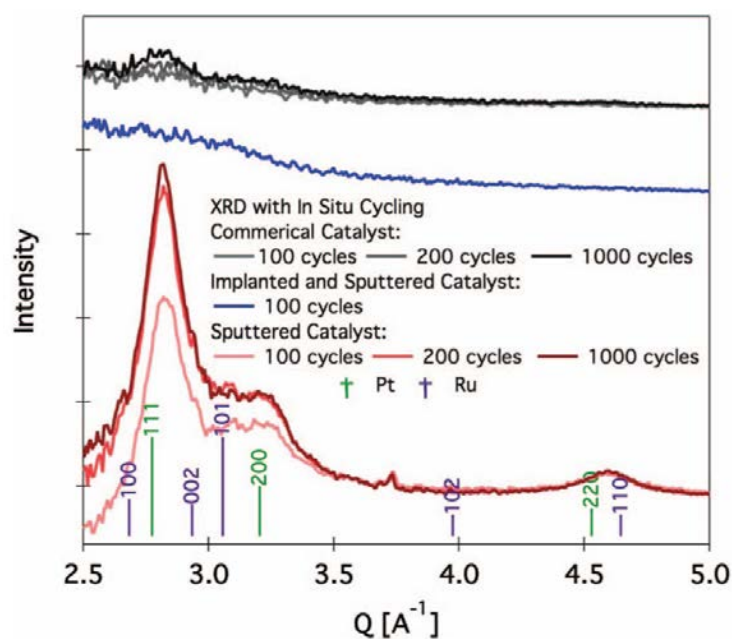


Figure 3.9: XRD difference spectra for the commercial catalyst (JM5000), implanted and sputtered (Pt-Ru/N-C), and the sputtered (Pt-Ru/C) materials obtained during in-situ potential cycling. Each spectrum is the mathematical difference between the cycling spectrum and the initial un-cycled spectrum.

3.3 Conclusions

In this chapter I have compared the durability of Pt-Ru nanoparticle catalysts through the use of SAXS and other combined characterization techniques, such as RDE, MEA, TEM, and XRD. The results showed that nitrogen modification significantly increased the durability of the supported catalyst material over the course of an ADT protocol involving thousands of electrochemical cycles. Additionally, comparing a commercial catalyst against in-house fabricated unmodified and N-modified PtRu catalysts allows for the investigation of particle growth processes that result in loss of active ECSA. The emergence of the crystalline phase on the un-doped in-house material supports the dissolution/re-deposition particle growth process. In comparison, the SAXS/XRD analysis for N-modified material does not show the emergence of a new particle size regime or crystalline phase. As documented in Chapter 2 there is strong DFT evidence that suggests that the incorporation of N-species on the carbon support surface results in improved catalyst-support interactions. Combining these insights it can be said that the enhanced interactions from nitrogen are likely to increase resistance to dissolution and migration.

The positive shift in the CO stripping “kick-off” and peak potentials shown in Figure 3.5 indicate that a large portion of the surface area losses can be attributed to the loss of Ru phases for all materials tested. This was confirmed by MEA testing, which associated performance degradation with RuO_xH_y dissolution. It was shown that nitrogen modification can also change the metallic phase, of the Ru specifically. These results show that the modified support interactions play a key role in changing and stabilizing the phases of nanoparticle catalysts, creating a positive impact on the dissolution of metal-based nano-particle catalyst phases. This effect will be discussed in more detail in the next chapter.

As supported by the SAXS and CO stripping results, nitrogen appears to help maintain Ru, because of the more negative kick-off potentials and constant particle size. Unfortunately, it is still difficult to discriminate between the effects of select N surface species. DFT analysis suggests that the specific roles of pyridinic, pyrrolic, cyano, and graphitic N are com-

plex in nature and that the presence of two or more N-species may be needed to stabilize bi-metallic catalyst systems such as Pt-Ru[91].

While stabilization of fuel cell catalyst particles during fuel cell operation is a materials engineering challenge that must continue to be addressed, it has been demonstrated that the manipulation of catalyst-support interactions via N-modification of support chemistry can result in improved retention of Pt-Ru particle surface area after electrochemical cycling. Based on a combined electrochemical, structural, and morphological analysis of doped vs. undoped support materials, observations suggest that N-modified support materials mitigate catalyst surface area loss from catalyst phase dissolution and re-deposition processes in particular. This work focused on the stabilization of catalyst phases and materials for utilization in DMFC anodes; however the concept/process of chemically modifying fuel cell catalyst supports to fabricate highly functionalized materials for energy conversion and storage technology platforms can be extended to other systems as well. Implementation of the fuel cell catalyst fabrication techniques and routes described in this work can be directly applied to material synthesis approaches for Pt-based cathode catalyst materials.

CHAPTER 4

THE EFFECT OF POST NITROGEN MODIFICATION ON THE DURABILITY OF COMMERCIAL CATALYSTS

As discussed in Chapter 2, recent theoretical DFT work and experimental studies conducted on model supports (highly oriented pyrolytic graphite; HOPG) have provided additional insight into the effect of nitrogen on nanoparticle catalyst durability([49, 92–94]. These studies have identified the importance of nitrogen concentration and nitrogen defect clustering on overlying catalyst nanoparticle activity and durability. In a 2013 study, by the O’Hayre research group, an understanding of nitrogen-modified materials through the use of energy electron loss spectral (EELS) imaging was provided. This study showed that there was a spatial correlation between the most stable nano-particles and higher amounts of nitrogen in the carbon support[93–95]. Within the areas of best stability, the PtRu nanoparticles appeared to be surrounded by nitrogen defects, suggesting that the incorporation of nitrogen next to the catalyst nanoparticles was of utmost importance in preventing migration. It was also suggested that this correlation was likely due to both a reduction in nanoparticle dissolution and a reduction in nano-particle agglomeration/coarsening facilitated by the dopant, as was demonstrated in the previous chapter for high surface area materials.

The current work further examines the effects of nitrogen modification by studying the performance of a pre-existing state-of-the-art commercial catalyst implanted with nitrogen. In this case, nitrogen doping (via nitrogen ion implantation) is conducted on a commercial 60 wt% PtRu/C catalyst, consisting of PtRu nano-particles already deposited onto a high surface area carbon support. Due to the shadowing effect caused by the pre-existence of the PtRu nanoparticles during the N-implantation process, the nitrogen heteroatom incorporation is expected only in regions of the carbon structure unshielded by PtRu nanoparticles. This work therefore helps to further advance fundamental understanding of the way in which

nitrogen improves the stability of the nanoparticle catalysts while exploring a facile pathway for the enhancement of current industry leading products.

To assess the effects of post-doping on state-of-the-art carbon supported PtRu catalysts, unmodified and post-modified samples are characterized and compared using both RDE experiments and MEA tests. These studies are carried out in both acid and alkaline media and demonstrate that after durability testing, the post-modified state-of-the-art commercial catalysts outperform the unmodified benchmark catalyst.

4.1 Experimental Information

This chapter has or will be published in three different journal articles[96–98]. Dr. April Corpuz helped provided MEA analysis in acidic media, while Dr. Prabburam Joghee did the MEA testing in alkaline media. I did a majority of the experimental work with help from Dr. Arrelaine Dameron. I am also responsible for all of the half-cell electrochemistry discussed in this chapter; Dr. Tim Olson provided some assistance in this area.

4.1.1 Materials

The commercial anode catalyst used in these studies is nominally 60 wt% PtRu supported on carbon black (Johnson Matthey HiSpec® 10000). Specifically, the platinum weight loading is 39.39% and the ruthenium weight loading is 18.91%, as given by the company specifications for the specific lot used.

For the modification of samples with nitrogen, approximately 500 mg of PtRu/C catalyst was placed into a rotating sample holder (rotating wheel), and the chamber was evacuated to less than 5×10^{-6} Torr [64, 99]. Prior to nitrogen ion implantation, powders were out-gassed by heating to above 180 °C for 15 min. Samples were then implanted with a 3 cm DC ion source (Veeco) at a pressure of 1×10^{-3} Torr (N_2) at two different dosages by changing the beam current between 12mA and 45mA, while maintaining a constant discharge voltage (55 V) and acceleration voltage (100 V) for 60 min.

4.1.2 Characterization

Thermogravimetric analysis (TGA) was done using the TA Q600 (TA Instruments, New Castle, DE) by feeding 100 mL/min of synthetic air (80% N₂, 20% O₂) with a heating rate of 5 °C/min to a temperature of 850 °C. The total metal content of the catalyst powders was determined based on the assumption that the final mass at 850 °C is composed of RuO₂ and Pt. The Transmission Electron Microscopy (TEM) micrographs of undoped and post-modified PtRu/Carbon were obtained on a Philips CM200 TEM. In addition to initial evaluation of catalyst powders, samples were also collected from the anode surface of the cycled MEA's.

XPS analysis was performed on a Kratos Nova X-ray photoelectron spectrometer using pass energies of 160 eV for the survey spectra and 20 eV for the high-resolution spectra of C1s/Ru3d, O1s, N1s, Ru3p, and Pt4f. Data processing was carried out using Casa XPS software and involved background subtraction, charge calibration, and curve fitting. A linear background was applied to O1s and N1s regions, while Shirley background was used for C1s/Ru3d, Pt4f and Ru3p regions. Charge referencing was done to the carbon peak at 284.8 eV. Consistent fitting parameters and constraints were applied to the C1s/Ru3d region to obtain the distribution of ruthenium species. The Ru3d region was fitted with 4 peaks, each containing 3d5/2 and 3d3/2 components separated by 4.2 eV, as shown in Table 4.1. Elemental quantification of ruthenium was performed using the Ru3p region.

4.1.3 RDE Studies

Initial electrochemical studies of post-modified PtRu/C catalyst powders included rotating disk electrode (RDE), cyclic voltammetry (CV), and CO stripping voltammetry. Electrochemical measurements were conducted at room temperature in a standard three-electrode configuration that utilized either a saturated calomel reference electrode (SCE) in acid media or a Hg/HgO electrode in alkaline, as well as a Pt mesh counter electrode and a thin-film layer of the catalyst (applied from an ink) as the working electrode. RDE electrodes were

prepared using 1 mg/mL solutions of catalyst inks made with 10 mg of the catalyst powder, 7.96 mL of water, 2 mL of 2-propanol (IPA), and 40 μ L of 5 wt % Nafion solution. For alkaline testing a newly fabricated Tokuyama ionomer was used. These mixtures were bath sonicated for 20 min and 10 microliters of the ink was then applied to the glassy carbon RDE tip. The electrodes were then dried at 40 °C for 30 min.

In acid media, prior to performing CO stripping voltammetry, the working electrode was electrochemically cleaned in a solution of 1M H₂SO₄ by cycling 5 times from 0.05 to 0.80 V versus RHE. Then, pure CO gas was bubbled into 1M H₂SO₄ for 10 min while the working electrode was held at 0.1 V versus RHE. While the working electrode was still held at 0.1 V versus RHE, pure N₂ was bubbled for 10 min to purge excess CO from the electrolyte. The potential was then swept to 0.9 V versus RHE at 20 mV s⁻¹ to strip the adsorbed CO from the surface of the working electrode. Two subsequent sweeps from 0 to 0.9 V were then performed to ensure that all the bulk CO had indeed been removed from the electrode.

In alkaline media a very similar process was followed, with the electrolyte being .5M NaOH. A 5-cycle breakin, from 0 to .985V vs. RHE, was used on each sample. The CO stripping experiments were completed in a related approach while being held at .285V. Cycles were run between 0 and .985V vs. RHE. Everything else was performed in a similar manner as to what was described above.

4.1.4 MEA fabrication

For testing in acid media, two MEA's with a geometric area of 5 cm² each were fabricated for single-cell fuel cell studies. The anode ink was made by mixing 40 mg of anode catalyst (either the unmodified commercial PtRu/C or the PtRu/C post-modified with nitrogen at beam current 45 mA, PtRu/C-N2) with 320 mg 5 wt% Nafion in alcohol and 300 mg water. Subsequently, the anode ink was then hand-painted onto a Nafion 117 membrane over a vacuum table at 70 °C using a 5 cm² mask. The catalytic ink painted on the membrane was dried over the vacuum table. Then, the anode-coated membrane was hot-pressed at 130 °C with 294 lbs for 10 min. The approximate catalyst (total metal) loading was maintained to

3 mg cm⁻² for each anode. During MEA assembly into the fuel cell hardware, 5 cm² carbon paper with a microporous layer (SGL GDL 25BC) was placed on PtRu/Carbon anode to facilitate fuel distribution to the anode. For the cathode side, a commercial Pt-coated (0.4 mg cm⁻²) gas diffusion electrode (GDE), ELE062, (procured from Johnson Matthey) was placed directly opposite to the anode, with the Nafion 117 membrane sandwiched in-between the electrodes. As MEA data is not the main focus of this thesis, I refer readers to Appendix B where a more detailed description of MEA testing methods is provided, especially alkaline.

4.2 Acidic Results and Discussion

In this chapter the electrochemical performance of three sets of Pt-Ru based fuel cell catalyst materials are investigated. The materials included: commercially available Johnson Matthey PtRu/C catalyst (JM 10000); post-modified JM10000 ion implanted at 12mA (PtRu/C-N1); and another JM10000 sample modified at 45mA (PtRu/C-N2 & PtRu/C-N3).

4.2.1 Material characterization

Table 4.1 summarizes changes to the elemental composition of the commercial PtRu/C catalyst after doping with nitrogen as a function of ion implantation conditions. XPS shows that nitrogen was successfully incorporated into the materials with concentration between 1 and 2 at.% as compared to levels of 3-5 at.% for the same implantation condition without metals.[100] Figure 4.1 shows high-resolution N1s spectra for the catalyst powder samples as a function of implantation dosage, demonstrating that there is some variation within each sample, as evaluated by analyzing three areas per sample. The high level of noise in the N1s spectra obtained on PtRu/C-N1 is due to the presence of multiple functionalities (pyridinic, pyrrolic, amine, graphitic, amine, etc.) spreading over a large range of binding energies (BE), with each being present in relatively small amounts. Increase in the implantation dosage resulted in an increase in the total amount of nitrogen, while still producing a wide spectrum. The shape of the nitrogen spectrum however, appears to change with the increase in the nitrogen dosage indicating that the ratio of nitrogen species at lower binding

energy (pyridinic, amine) to species at higher binding energy (graphitic, pyrrolic) is different. Specifically, higher implantation dosages appear to favor the formation of a greater percentage of lower-binding energy nitrogen species. These results are reproducible and have been duplicated with different JM10000 catalyst lots.

Since HOPG studies have found a correlation between the most improved stability and higher amounts of low binding energy species such as pyridinic nitrogen (albeit in the presence of other species such as pyrrolic and graphitic nitrogen) [63]. I hypothesized that the electronic effects of nitrogen post-doping are likely to be similar to those of nitrogen pre-doping, where higher amounts of lower binding energy species (corresponding to longer implantation times) may be more favorable for improving stability.

TGA analysis confirmed that materials before and after nitrogen implantation have the same metal loading, ~60 wt%. Based on XPS analysis, the ratio of surface Pt to Ru was also maintained at 1:1 for all samples, but the total amount of surface Pt and Ru was changed from the original catalyst, especially for the sample modified at a higher dosage (PtRu/C-N₂) (Table 4.1). In addition, ion implantation also affected the distribution of the ruthenium and platinum species, decreasing the relative amount of metallic components and increasing the oxide components (Table 4.1 and Figure 4.2).

TEM images in Figure 4.3 show three areas representative of the three different types of nanoparticle distribution and coverage, typical for 60 wt% PtRu/C before (Figure 4.3, a1-a3) and after modification with nitrogen (Figure 4.3, b1-b3). Analysis of these (unmodified and post-modified PtRu/C) images shows that a large fraction of catalyst is agglomerated, complicating analysis of individual nanoparticles (Figure 4.3 a1 and b1). Figure 4.3 a2 and b2 show regions of carbon black with more disperse nanoparticles. Figure 4.3 a3 demonstrates that regions with high metal coverage often neighbor regions with little to no metal on the carbon support. While images of PtRu/C-N₂ in Figure 4.3 b1 and b2 are similar to those found in undoped PtRu/C, areas such as shown in Figure 4.3 b3 are only found in the post-doped materials (including materials post-modified at low implantation dosages).

Table 4.1: XPS analysis: elemental composition, and quantification of deconvoluted XPS spectra of Ru3d, and Pt 4f, reported as average of three areas per sample.

Sample	PtRu/C	PtRu/C-N1	PtRu/C-N2
Implantation Beam Current, mA	0	12	14
Elemental Concentration, at%			
Carbon, C 1s	82.6	80.5	77.5
Oxygen, O 1s	10.1	10.8	11.4
Nitrogen, N 1s	.02	1.1	1.7
Platinum, Pt 4f	3.3	3.7	4.5
Ruthenium, Ru 3p	3.8	3.9	4.9
Pt+Ru	7.2	7.6	9.3
Pt/Ru	1.1	1.1	1.1
Quantification of Ru 3d, relative Concnetration%			
Ru metallic: Ru1(280.6 eV) and Ru5 (284.8eV)	34.0	29.9	24.4
RuO ₂ , screened state: Ru2 (281.4 eV) and Ru6 (285.6 eV)	38.3	38.3	42.8
RuOxHy: Ru3 (282.5 eV) and Ru7 (286.7 eV)	10.7	12.7	18.9
RuO ₂ , unscreened final state and/or RuO ₃ : Ru4 (283.7 eV) and Ru8 (287.9 eV)	17.1	19.1	13.9
Quantification of Pt 4f, relative concentration, %			
Pt metallic: Pt1 (72.2 eV) and Pt4 (75.5 eV)	53.1	51.6	48.6
Pt in Oxide and hydroxide states: Pt2 (73.1 eV) and Pt5 (76.4 eV) and Pt2 (75.1 ev) and Pt5((78.3 eV)	47.0	48.4	51.4

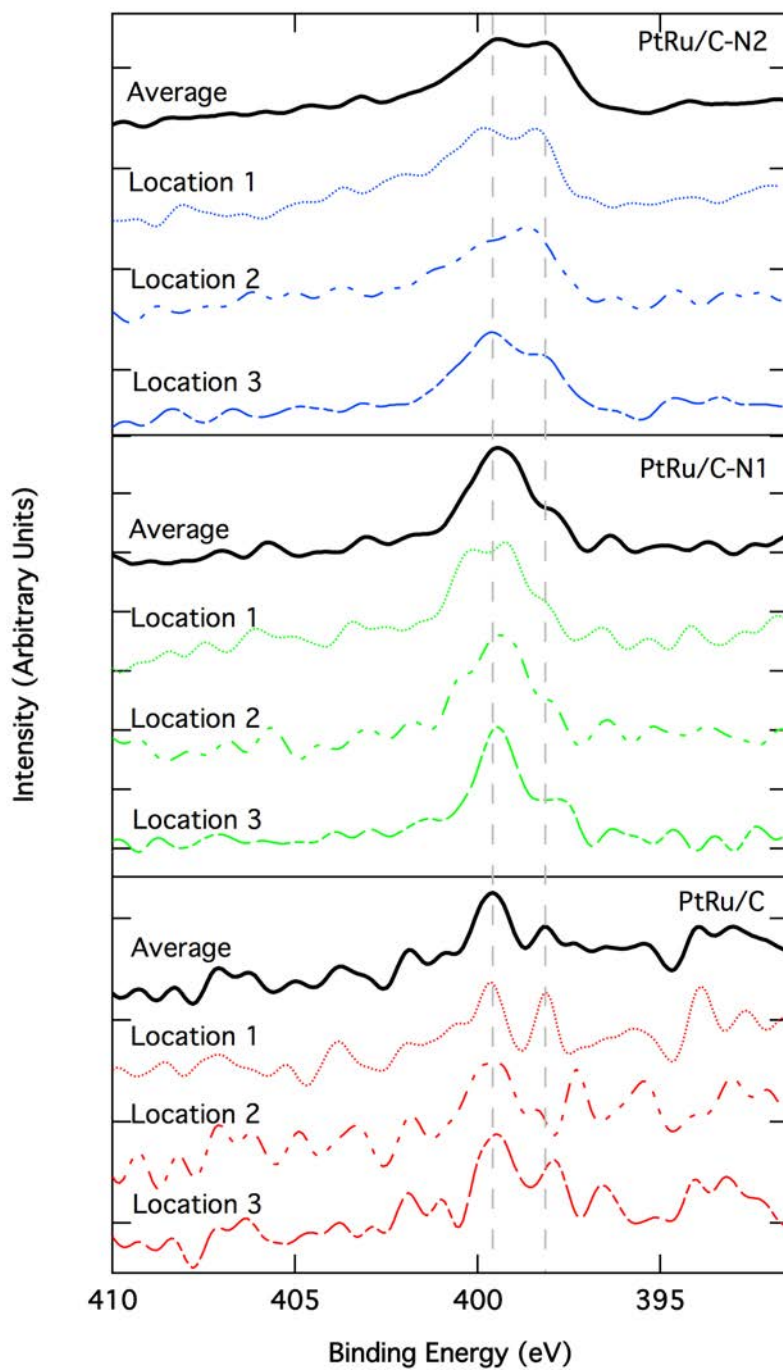


Figure 4.1: High resolution N1s spectra, shown for three areas on each sample and their average.

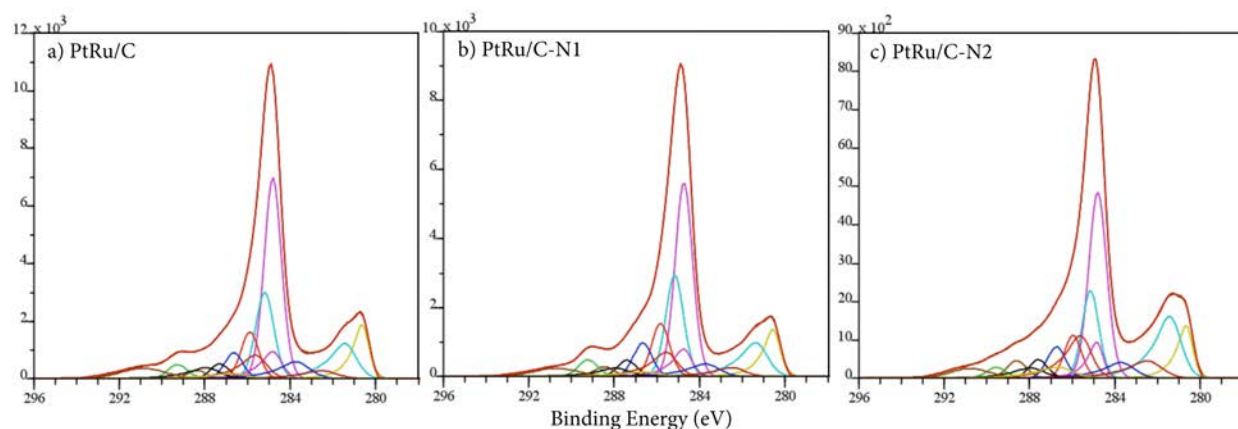


Figure 4.2: High resolution C 1s+Ru 3d spectra, curve-fitted a) PtRu/C, b) PtRu/C-N1, and c) PtRu/C-N2.

These regions have small PtRu nanoparticles evenly distributed on the surface of the carbon support and it is hypothesized that their appearance results from ion-implantation-induced redistribution of the PtRu nanophase from regions with high metal coverage to regions with low metal coverage. Appearance of areas such as those shown in Figure 4.3 b3 are expected to increase the relative concentration of platinum and ruthenium to carbon detected with XPS, consistent with our experimental data (Table 4.1). In summary, XPS and TEM experiments showed a fraction of PtRu reorganizes on the surface of the carbon support, after ion implantation, to form small well-dispersed nanoparticles that are richer in hydrous and anhydrous oxides than the original catalyst (particularly at high doses).

4.2.2 Acid Media RDE Studies

Electrochemical surface area (ECSA) for the unmodified PtRu/C catalyst powder and post-modified PtRu/C catalyst powders was determined using standard CO stripping analysis (assuming a stripping charge of $420 \mu\text{C}/\text{cm}^2$). Initial CO stripping curves obtained for the unmodified and post-modified materials (Figure 4.4) indicate that the post-modified catalysts showed a more positive “kick-off” potential for the removal and oxidation of the adsorbed CO as compared to the commercial unmodified benchmark. As mentioned before, while XPS shows that the platinum to ruthenium ratio (including both metallic and oxide

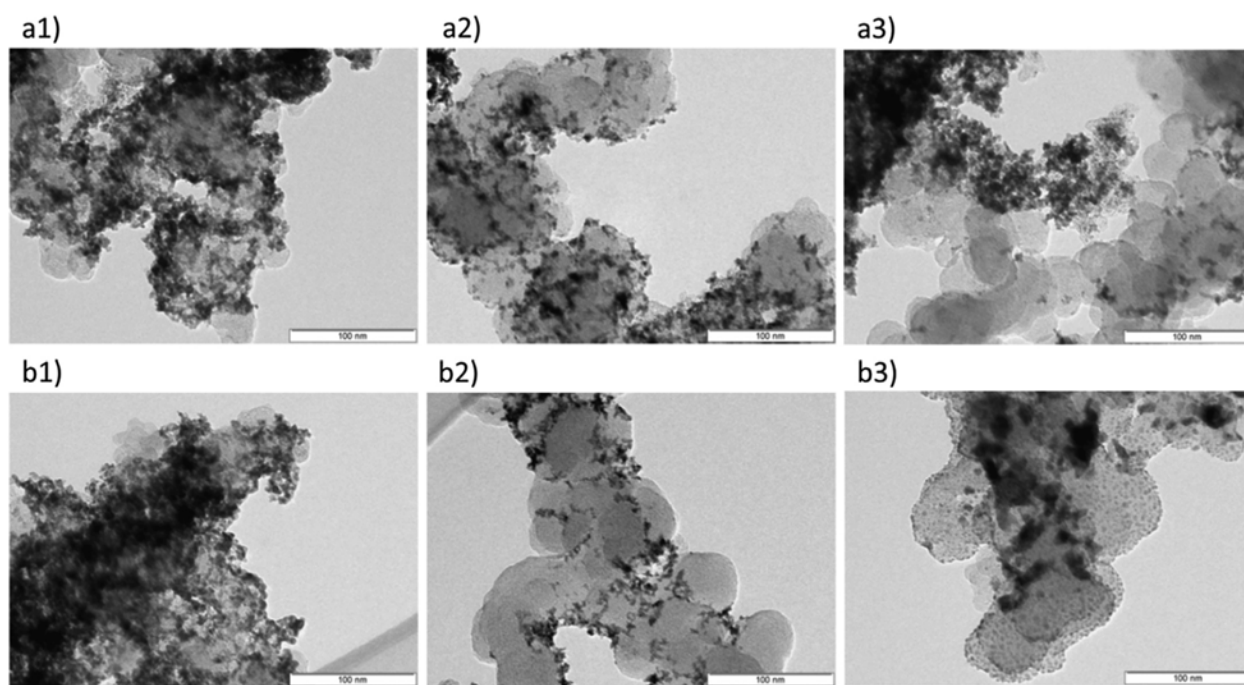


Figure 4.3: TEM micrographs demonstrating three types of metal coverage for the catalysts a) PtRu/C, and b) PtRu/C-N₂. b1 and b2 demonstrate morphology similar to the original catalyst. b3 shows areas with small well dispersed nanoparticles not observed in the original catalyst.

species) stayed the same for all samples, there were differences in the metallic and oxide species due to ion implantation. The PtRu phase in post-modified samples showed a somewhat higher concentration of ruthenium and platinum oxide species. XPS also showed that the post-doped materials are more deficient in metallic Ru components when compared to the unmodified material. This suggests that the shift in CO stripping onset potential might be related to redistribution of surface Pt and Ru species.

The material modified using a low implantation dosage (PtRu/C-N1) has a lower ECSA ($39.1 \text{ m}^2/\text{g}$) than the unmodified catalyst ($56.3 \text{ m}^2/\text{g}$). In contrast, the material modified using a high implantation dosage (PtRu/C-N2) exhibited a higher ECSA ($65.2 \text{ m}^2/\text{g}$) than the unmodified material. This is consistent with XPS results, which showed the sample implanted at higher dosage has higher combined surface concentrations of Pt and Ru (Table 4.1). TEM observations also suggest that PtRu is reorganized on the surface in such a way that active PtRu surface area increases, as explained earlier. After initial surface area tests, each sample electrode was subjected to accelerated degradation testing (ADT) through potential cycling from 0 to 0.9 V vs. RHE. Detailed graphs showing the CO stripping curves as a function of cycles (measured after 0, 50, 100, 1000 and 5000 electrochemical potential cycles) are included in Figure 4.4, while the resultant CO stripping areas are shown in Figure 4.5. For all samples, upon initial cycling (after 50 and 100 cycles), the onset potential slightly shifted towards more negative values. Then after 1000 cycles onset potential significantly shifted towards more positive values (approx. 0.2V), which was subsequently maintained through 5000 cycles. The initial and final (after 5000 cycles) curves of all samples are compared in Figure 4.6.

After 5000 cycles (Figure 4.4), a significant decrease in current density was observed for every sample, and the peak positions shifted toward more positive onset potentials (as described above, this shift appeared after 1000 cycles) indicating changes to the catalyst composition, possibly resulting from Pt enrichment originated from dissolution of ruthenium. Plotting the ECSA values for the all samples as a function of cycling allows the beneficial

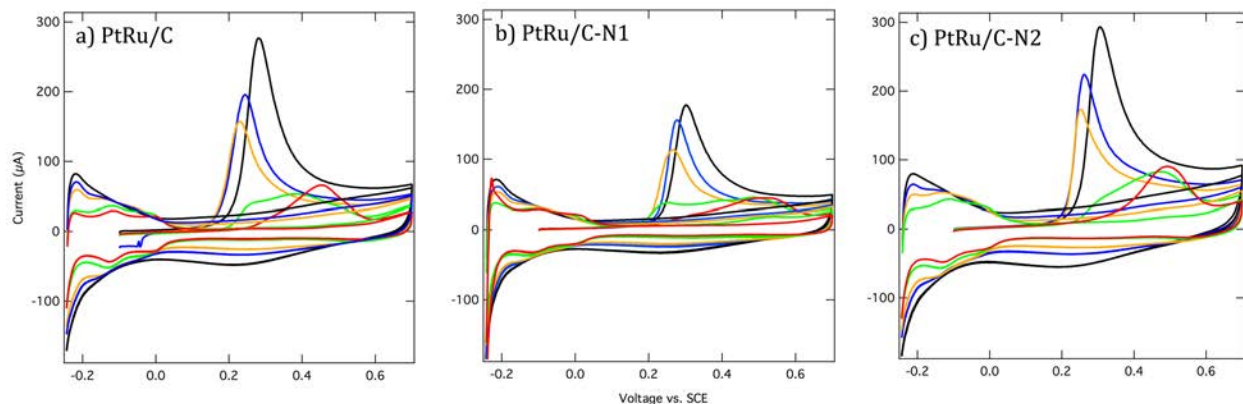


Figure 4.4: CO stripping data of unmodified JM 10000, PtRu/C-N1 and PtRu/C-N2 catalysts as a function of cycling.

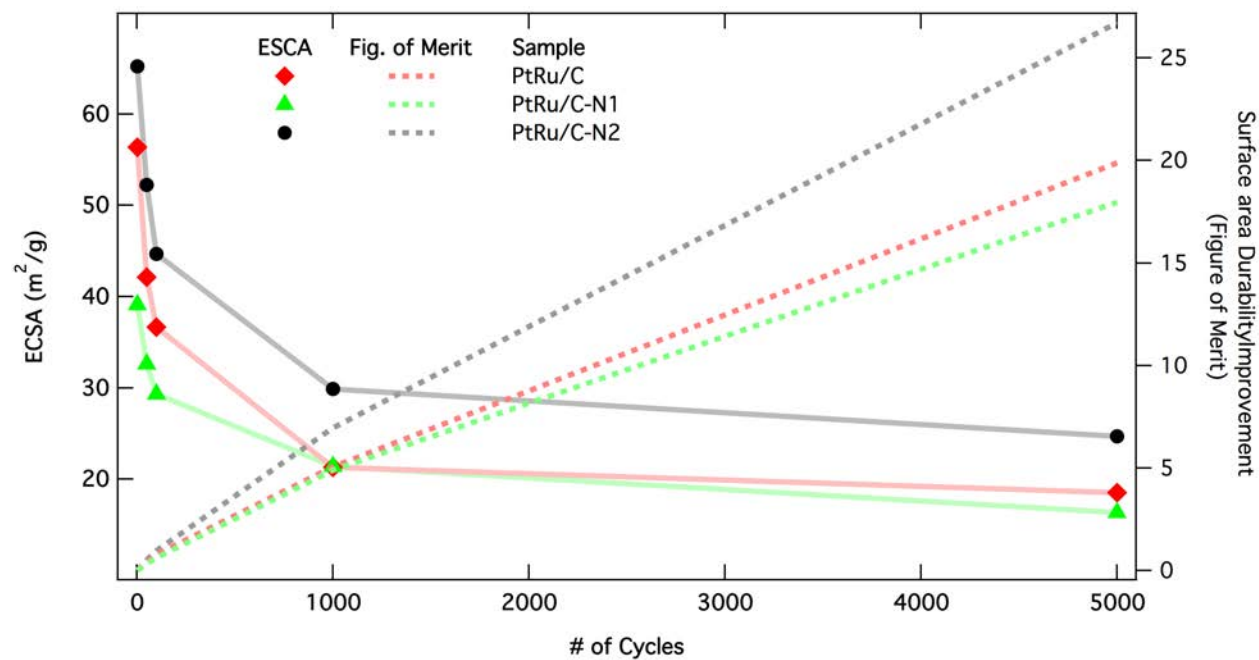


Figure 4.5: The electrochemical surface area (ESCA) of unmodified JM10000, PtRu/C-N1 and PtRu/C-N2 catalysts as a function of cycling. The electrochemical surface area is shown on the left axis. The right axis is a figure-of-merit plot where the surface area is multiplied by the percent of cycles completed during that testing segment (i.e. $52.2 \times (50/5000)$ after 50 cycles and $24.7 \times (4000/5000)$ after 5000 cycles) and then accumulated over the lifetime of the electrode.

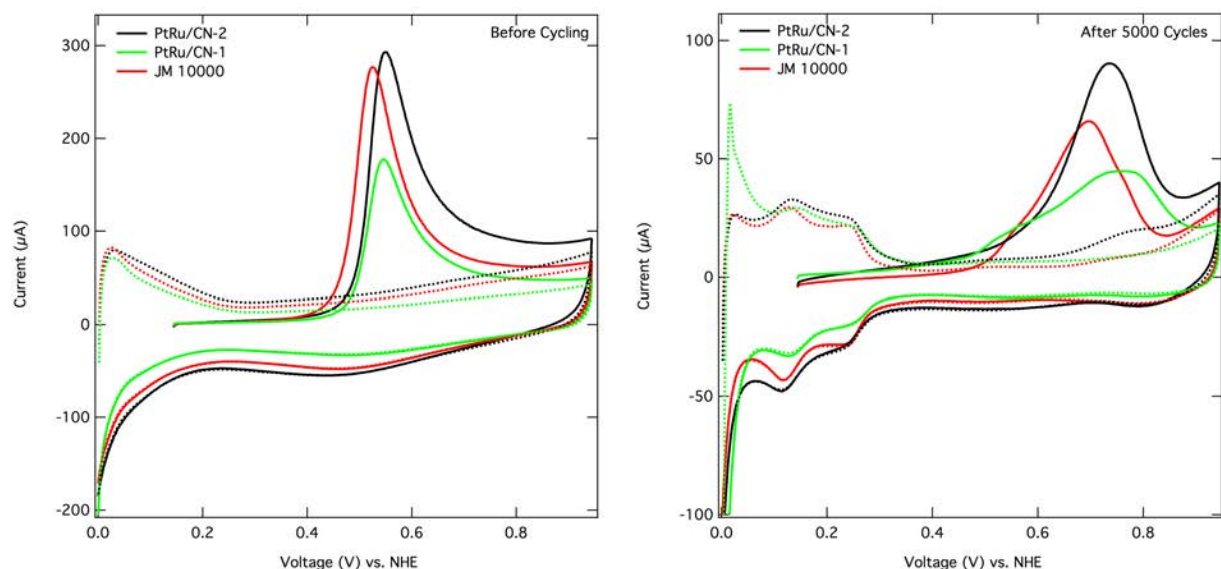


Figure 4.6: The ECSA of JM10000, PtRu/C-N1 and PtRu/C-N2 before and after cycling. The redistribution from implantation can clearly be seen before cycling as well as the enhancement in ECSA after 500 cycles.

effects of post-modification to be clearly observed (Figure 4.5). Before cycling, the ECSA of PtRu/C-N2 was 16% higher than the unmodified PtRu/C. After each ADT segment the difference in ECSA between the two samples further widens, so that after 5000 cycles the PtRu/C-N2 sample maintains 34 % higher ECSA than that of its unmodified counterpart.

It is interesting that despite differences in initial surface areas between unmodified JM10000 and PtRu/C-N1, their surface areas are almost identical after the first 1000 cycles and even after 5000 cycles. Meanwhile, PtRu/C modified at high implantation dosage starts with and, most importantly, maintains higher surface area throughout the entire cycling range. In these experiments, it is difficult to conclusively show that improved durability results from nitrogen incorporation and not simply from changes to the PtRu phase, but it is highly suggestive that both of these factors impacted the performance. Reorganization of the PtRu phase becomes evident even at low dosages, but does not result in better preservation of active surface area. Also, advantages of the implantation at higher dosages over low dosages and unmodified samples follow the trend observed in previous work, where samples were modified with nitrogen prior to metal deposition [63, 77, 78, 99, 101, 102]. Based on work

with model HOPG substrates, more aggressive dosages are expected to lead to the formation of multi-clustered nitrogen defects [63, 65] that may act as effective trapping states to mitigate the migration of the catalyst nanoparticles.

4.2.3 Acidic MEA studies

In order to make comparisons under conditions closer to those used commercially, the post-doped material implanted at high implantation dosage (PtRu/C-N2) and the unmodified commercial catalyst were compared in MEA DMFC studies. An MEA made with a PtRu/C-N2 anode and a standard cathode (Pt/C GDE, 0.4 mg/cm²) was compared to another MEA made with the unmodified PtRu/C and a standard cathode over the course of a long-term (425h) durability test. The initial electrochemical characterization of the two MEAs is provided in Figure 4.7. As shown by the anode CO stripping voltammograms in Figure 4.7a, both anode catalysts show a narrow, single CO stripping peak, indicating a narrow distribution in the PtRu alloy[103]. For the PtRu/C and the PtRu/C-N2 anodes respectively, the corresponding ECSA was 40 m²/g and 48 m²/g respectively when normalized by the metal mass-loadings of the two MEAs. This corresponds to about 20% increase in the ECSA for the nitrogen modified anode, a result which is well supported by RDE measurements of the catalyst powders that indicated about 16% increase in the ECSA for the PtRu/C-N2 powder relative to the unmodified control. The higher ECSA of the MEA anode employing the post-doped catalyst also correlates with the higher amount of surface platinum and ruthenium species detected with XPS (Table 4.1). Similar to the RDE studies, these observations suggest that ion implantation results in the exposure of more surface Pt and Ru, likely due to reorganization of PtRu on the surface evident from TEM analysis. Similar to what was observed in the RDE experiments, PtRu/C has a slightly more negative CO oxidation onset peak than PtRu/C-N2; shown in Figure 4.7a. Again, this can be explained by comparison to the XPS studies. Table 4.1 shows that PtRu/C-N2 has more Pt and Ru than PtRu/C, while maintaining an almost identical overall Pt:Ru ratio; however, the ratio of metallic species (Pt and Ru) is not the same after post-doping. Table 4.1 also

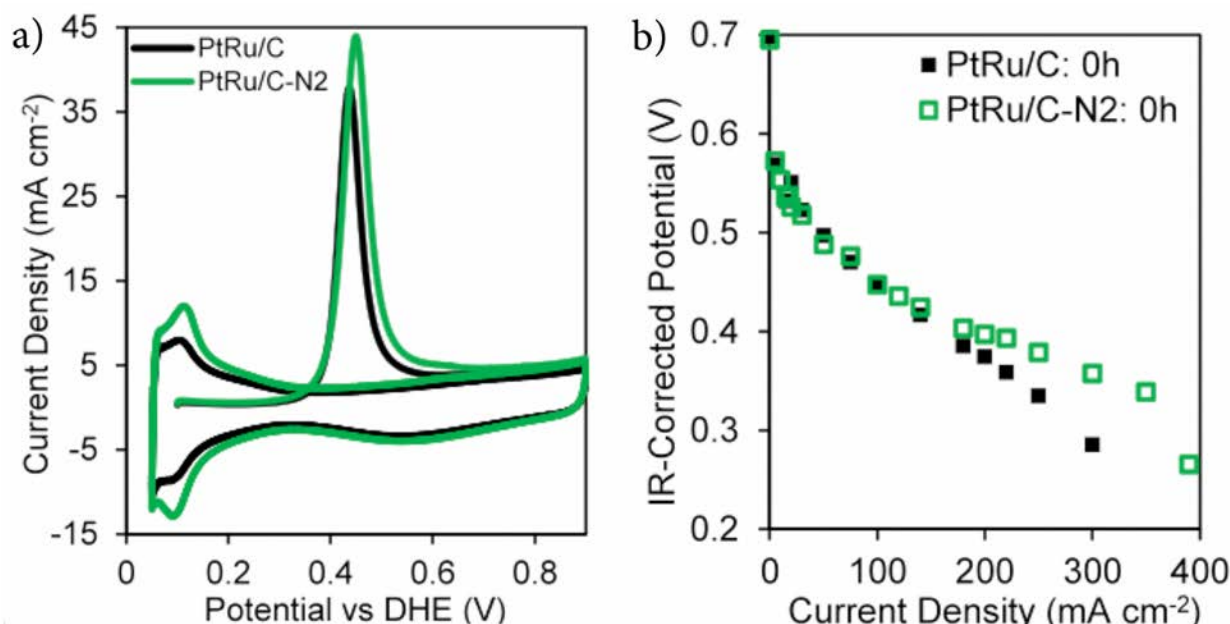


Figure 4.7: Initial electrochemical characterization of the MEAs. a) Anode CO stripping curves, 5 mV s⁻¹, b) Methanol:air polarization curves, 80 °C.

shows that PtRu/C-N2 is more deficient in its metallic ruthenium component than PtRu/C (and respectively more enriched in its metallic Pt component). Gasteiger, et al. determined that a Pt:Ru ratio with 46% atomic Ru produces the lowest CO oxidation peak potentials in comparison to other ratios, and predicted that a 1:1 Pt-to-Ru ratio would be the most favorable for CO oxidation[104].

As shown in Figure 4.7b, both MEAs show similar initial direct methanol fuel cell (DMFC) performance. At 0.4V, a standard operating voltage, the MEA made with PtRu/C-N2 generates approximately 190 mA/cm², and the MEA made with PtRu/C generates approximately 161 mA/cm². Also, the MEA made with PtRu/C-N2 performs slightly better in the mass-transport regime. This may be related to the higher ECSA of PtRu/C-N2, particularly if higher ECSA is due to better dispersions and higher accesibility of the active sites. [105, 106]

Durability testing on the two MEAs was conducted by holding each fuel cell at 0.4 V under standard DMFC operating conditions (70 °C, 0.70 mL/min 1M MeOH, 3.3 air stoichiometry

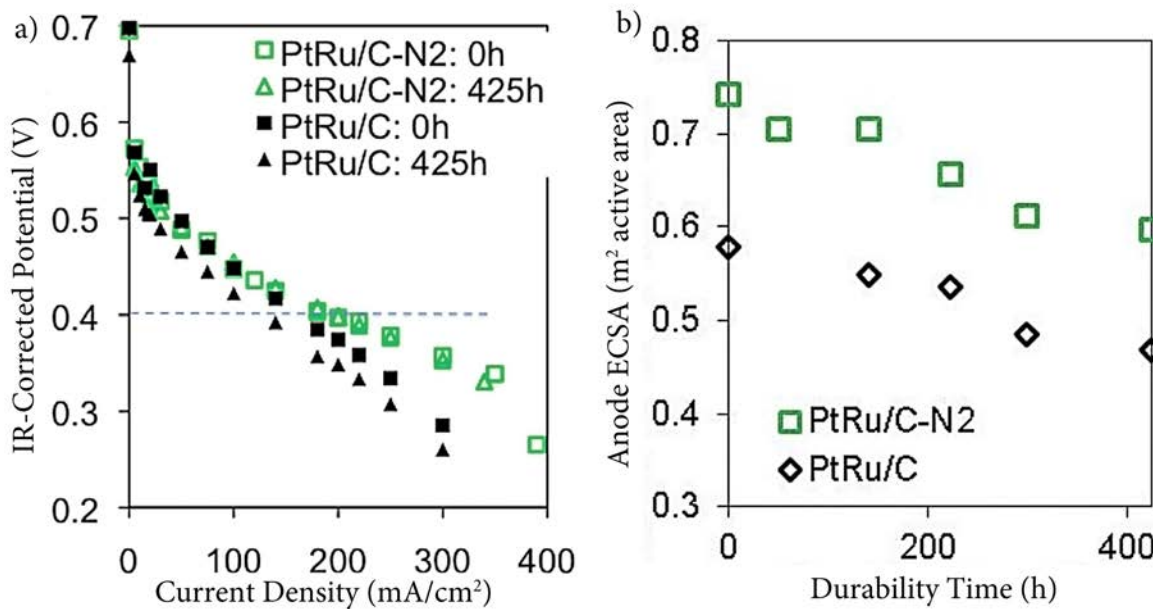


Figure 4.8: a) DMFC performance curves before and after 425 hours of durability. b) Anode ECSA as measured from anode CO stripping at 5 mV/s.

at 100%RH). The two MEAs were each tested for 425 hours of total durability time, with intermittent electrochemical measurements. Figure 4.8 shows DMFC performance curves before and after the durability test period. After 425 hours of durability testing, the MEA made with the undoped commercial anode shows an observable loss in performance across the entire operating range (e.g. ~33% loss in performance at 0.4V). This is not the case for the MEA made with the post-doped anode catalyst, which fully retains its DMFC performance without any losses, thereby confirming the remarkable DMFC durability advantages provided by the nitrogen post-doping treatment.

From Figure 4.8a, the MEA fabricated with the post-doped PtRu/C-N2 anode catalyst retains most of its anode performance (90% or greater) during the 425 hours of durability testing. This is not the case with the undoped PtRu/C anode, which drops to 85% of its initial performance after durability testing when considering the current drawn at 0.4V. Also, for the undoped PtRu/C, the onset potential shifts positively with operating time, suggesting changes in PtRu alloy ratio[107].

CO stripping on the anode, for both MEAs, was used to determine the active surface area for each sample (Figure 4.8b). The potential of the CO stripping peak and the onset for the unmodified PtRu/C anode shifts significantly during durability testing as was shown with RDE. It shifts positively after 141 and 223 hours of durability testing, then negatively after 300 and 425 hours of durability (data not shown). These shifts are indicative of changes in catalyst composition, i.e. the ratio between platinum and ruthenium species[103]. The CO stripping peak of the PtRu/C-N₂ anode shifts less during durability testing, which is evidence of a more stable catalyst, although this was not observed in the RDE studies. It is also worth mentioning that after 425 hours of durability testing, neither anode exhibits new peaks other than that of the PtRu alloy, indicating that there has been no formation of separate Pt or Ru phases[103]. However, the nitrogen post-doped PtRu/C-N₂ anode has higher ECSA than its unmodified counterpart (as measured by the area under the CO stripping curve) throughout durability testing. Remarkably, after 425 hours of durability, ECSA of the post-doped PtRu/C-N₂ is close to that of undoped PtRu/C before durability testing (as can be seen in Figure 4.8b). CO stripping of the cathode revealed that after 425 hours of durability testing, the apparent amount of Ru crossover substantially increases for both MEAs, with the MEA made with post-doped PtRu/C (PtRu/C-N₂) having a slightly higher and narrower Pt peak than the MEA made with the unmodified PtRu/C.

4.2.4 Post-mortem TEM analysis

Figure 4.9 shows TEM micrographs that were obtained from the powder extracted from the anode side of both MEAs after 425 hrs of durability testing. Similar to the materials before durability testing, the powders evaluated after MEA testing also had a large fraction of PtRu in agglomerations (Figure 4.9 a1 and b1). Despite the limitations in using TEM to analyze metal nanoparticles supported on carbon particles as described in 3, overall inspection of the both anode catalysts after durability testing does indicate that both materials lost significant amount of PtRu with a clear loss in particle density accompanied by particle coarsening/agglomeration (Figure 4.9 a2, a3, b2 and b3). Analysis of less agglomerated re-

gions, however, suggests that the surface coverage and distribution of nanoparticles on the surface are distinctively different on the unmodified and post-modified anode catalysts. Significantly, analysis of PtRu/C-N2 reveals that some fraction of nanoparticles appear to have strong interaction with the surface, apparent from the formation of worm-like nanoparticles covering the carbon surface (Figure 4.9 b2 and b3). The worm-like morphology suggests that the post-doped material does provide the additional carbon-support interaction that the undoped material does not possess. These observations directly support the electrochemical surface area results (from the anode CO stripping experiments) that the post-modified anode catalyst material has higher surface areas than its unmodified counterpart. It is likely that higher active surface area of the post-modified anode catalyst observed after 425 hours of durability results from the stronger catalyst-substrates interactions due to nitrogen defects that mitigate catalyst migration and coalescence. However, without performing an *in situ* technique like SAXS it is difficult to draw definitive conclusions about changes in particle morphology.

4.3 Alkaline Results and Discussion

Based on the performance results of studies in acid media, another sample set was made (PtRu/C-N3) imitating the conditions used for PtRu/C-N2. TEM images acquired from this batch of post-modified catalyst samples are shown in Figure 4.10. These reveal that a large majority of areas were similar to what was observed for PtRu/C-N2. Some areas around the edges of the carbon particles possess small nanoparticles, likely redistributed from the bulk PtRu during the implantation process, and, as shown on for the acid data set, a large portion of the catalyst was still very similar to the unmodified JM10000.

The ESCA, determined from CO stripping of PtRu/C-N3 in alkaline media, is shown in Figure 4.11a. This graph clearly indicates that the nitrogen-modified catalyst has a slightly higher ESCA than its unmodified counterpart. Once again this was attributed to the formation of the small nanoparticles, shown in Figure 4.10. To further study the effect of nitrogen in this environment, the catalyst performance was in a solution of .5M NaOH and

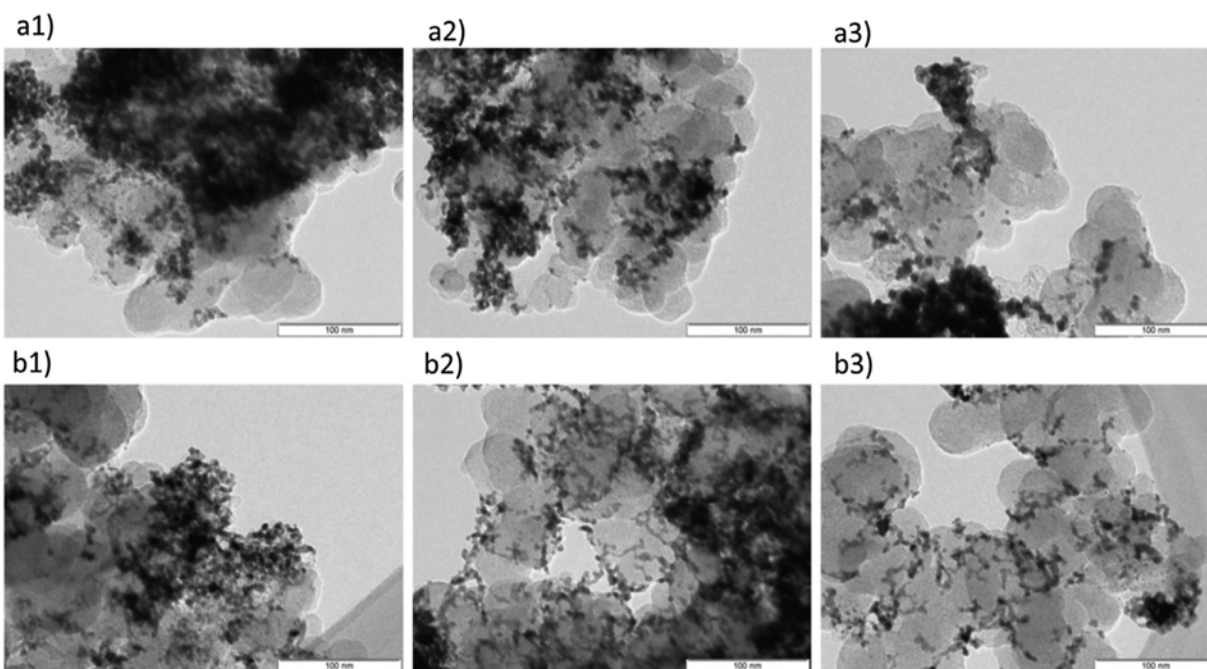


Figure 4.9: TEM micrographs representative of anode material after durability testing: a) JM10000, and b) PtRu/C-N2. b1 and b2 demonstrate morphology similar to the undoped catalyst. b3 shows areas with different type of catalyst morphology than in the undoped catalyst .

.5 M methanol before and after ADT testing. Before cycling this study revealed only a slight increase in MOR performance, indicating that the initial change in surface morphology had a limited effect on methanol oxidation. It is possible that this was because of an enrichment of Pt surface sites and/or a suboptimal metal composition after implantation redistribution. This hypothesis is supported by the more positive kick off potential observed during MeOH performance. It is worth noting however, that the peak potential of this material was still slightly improved, before any cycling occurred.

The graphs in Figure 4.12 show the effects of ADT on the unmodified and N-modified catalysts in a pure .5M NaOH environment. After a set number of cycles, the same as in acid media, the electrochemical surface area of the catalyst was tested. For the unmodified catalyst, as the number of cycles increases, the onset potential trends toward more positive values, likely resulting from a loss of Ru, Figure 4.12a. However, the N-modified commercial

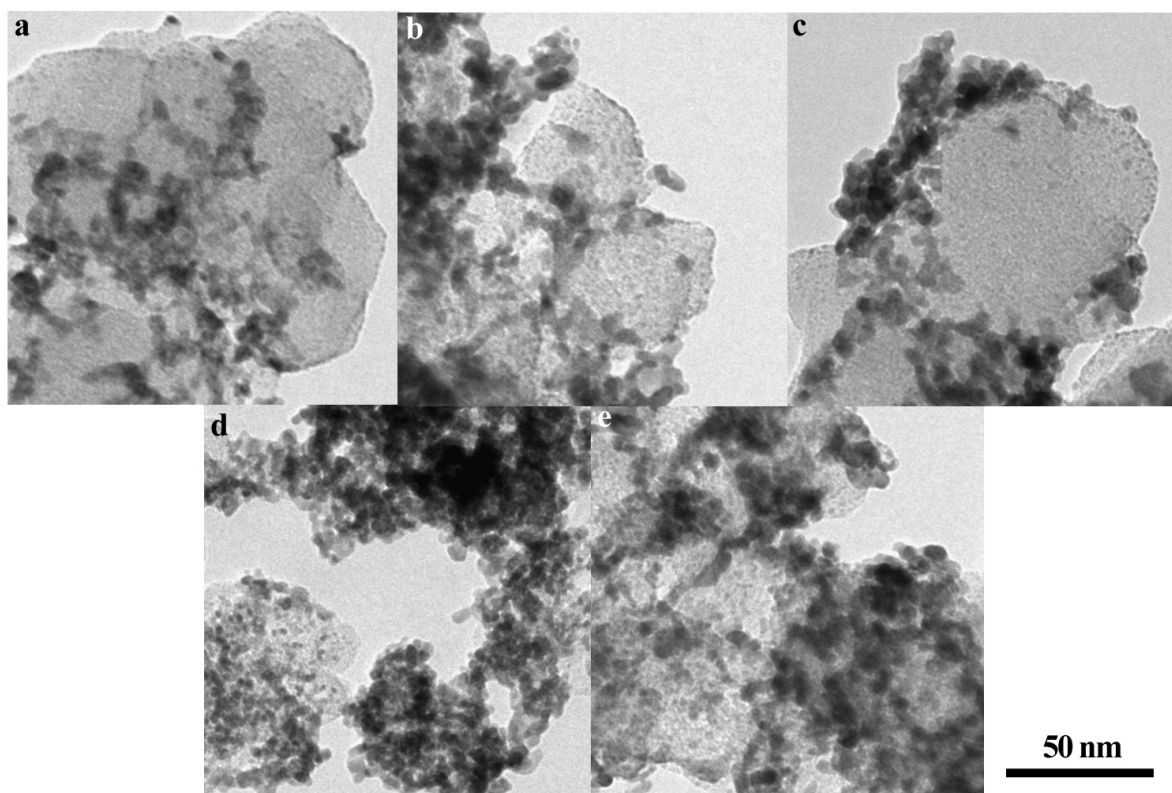


Figure 4.10: TEM images showing the effect of post doping. Images a-c show areas of redistribution, where the ion implantation removes metal from large cluster and forms small nanoparticles around the edges of the carbon particles. Images d-e show morphologies identical to those of unmodified JM10000.

catalyst appears to maintain its active Ru phase as evident by the relatively consistent onset potential. For this sample on a slight shift toward more negative values is observed after 50 cycles (Figure 4.12b). This initial instability may again be due to the change in metal phase after implantation, alluding to the instability of the redistributed phase. Even so, the overall stability of PtRu/C-N3 is significantly enhanced over JM10000.

An experiment, similar to that shown in Figure 4.12, was used to examine the effects of the ADT testing in a methanol environment. These results shown in Figure 4.13 indicate this type of testing to be harsher on the catalyst and as a result the PtRu/C-N3 shows a greater improvement over PtRu/C. It is worth mentioning that in comparing cycle 0 to cycle 5000, identical trends are observed for the catalysts tested in either environment

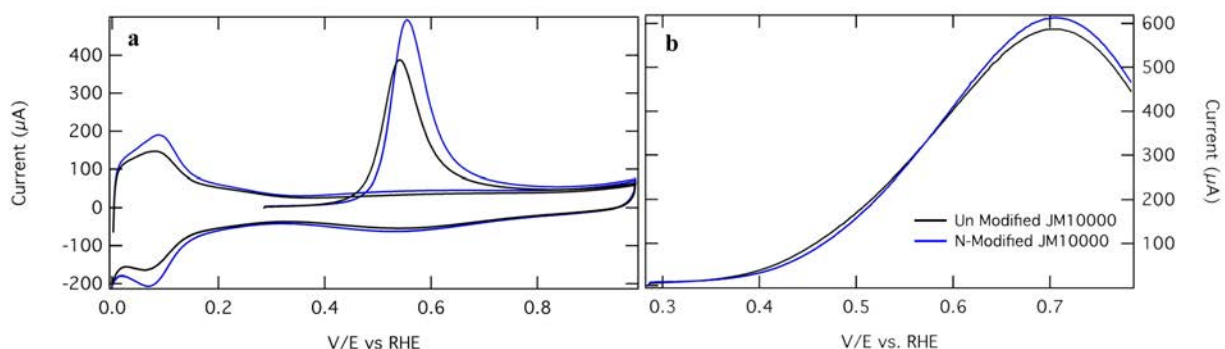


Figure 4.11: Initial electrochemical results of the post modified (blue) and unmodified catalyst (black). a) shows initial un-cycled CO stripping and b) initial methanol performance curves.

(pure NaOH, Figure 4.12, or with methanol, Figure 4.13). PtRu/C-N3, in both Figure 4.12 and Figure 4.13, shows a stabilized kick off and peak potential throughout all parts of the ADT process, while the data for PtRu/C reveal significant shifts toward more positive values after 5000 cycles. These results highlight the improved Ru dissolution resistance and enhanced retention of electrochemical surface area attainable through post modification. Reproducibility experiments shown in Figure 4.14 indicate that the ECSA is consistent and reproducible. For PtRu/C an average of 40% of the initial surface area was maintained after cycling, this was improved to 47% with the post-modified PtRu/C-N3 catalyst.

The effect of nitrogen post-modification is even more clearly articulated by the MOR performance after ADT testing. As was mentioned in the discussion of Figure 4.13, the initial MOR performance was only slightly improved after nitrogen modification, despite the significantly larger enhancement in surface area. After cycling, the unmodified catalyst performed poorly, retaining 41% of the initial methanol performance (.55V). Meanwhile, PtRu/C-N3 showed significant improvement maintaining 85% of the initial current response (see Figure 4.15). Based on this improvement in methanol oxidation, there are two possible benefits to nitrogen post modification of commercial catalysts in alkaline media. First, it could be possible, as proposed by other groups, that nitrogen participates in the MOR reaction. If this was the case one might expect the initial materials to provide a greater

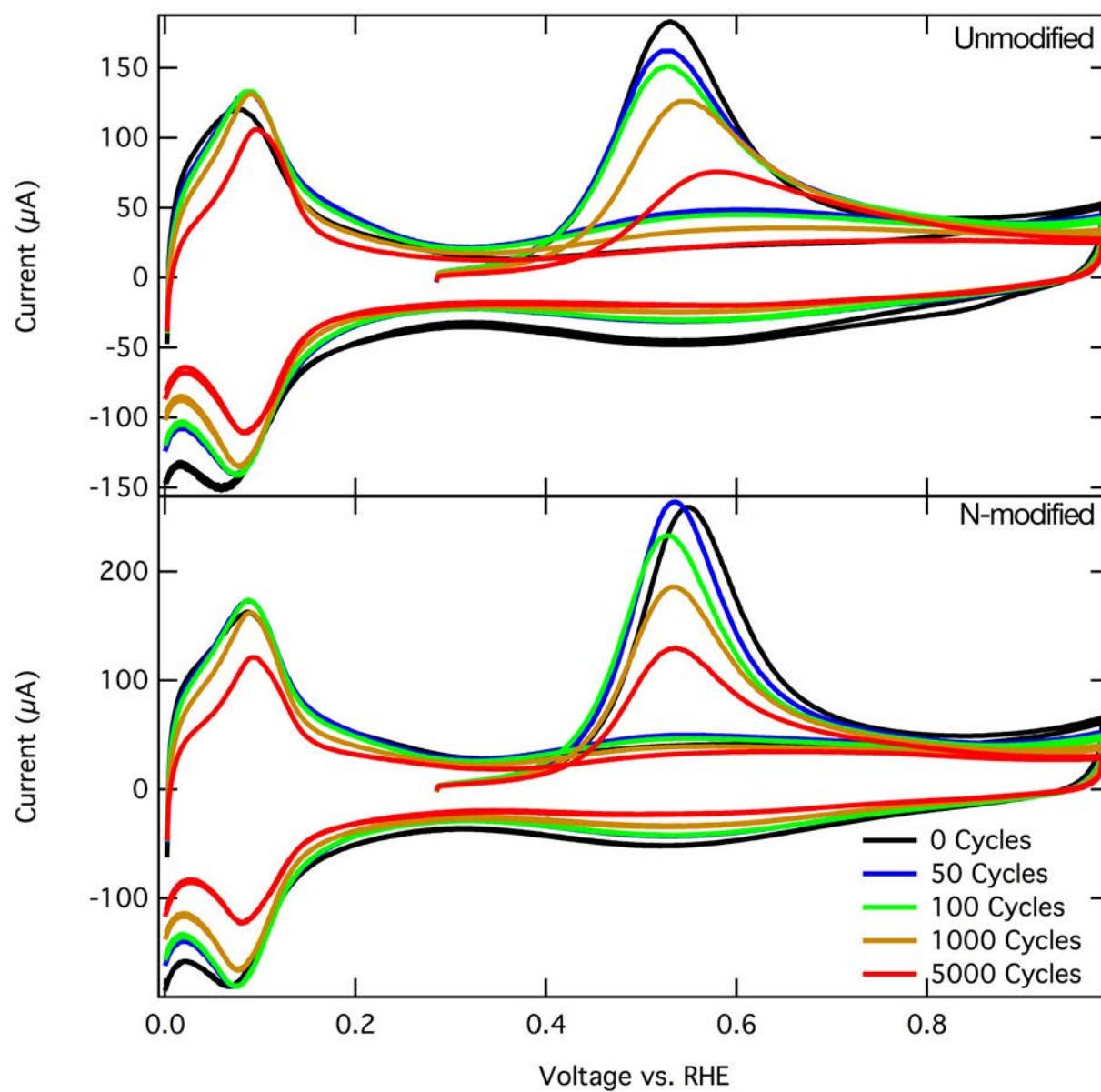


Figure 4.12: Changes in electrochemical surface area as a function of cycle. The upper graph shows the shift toward higher kick off potential for the unmodified commercial catalyst. While the lower graph shows the limited changes in on set for the nitrogen modified catalyst.

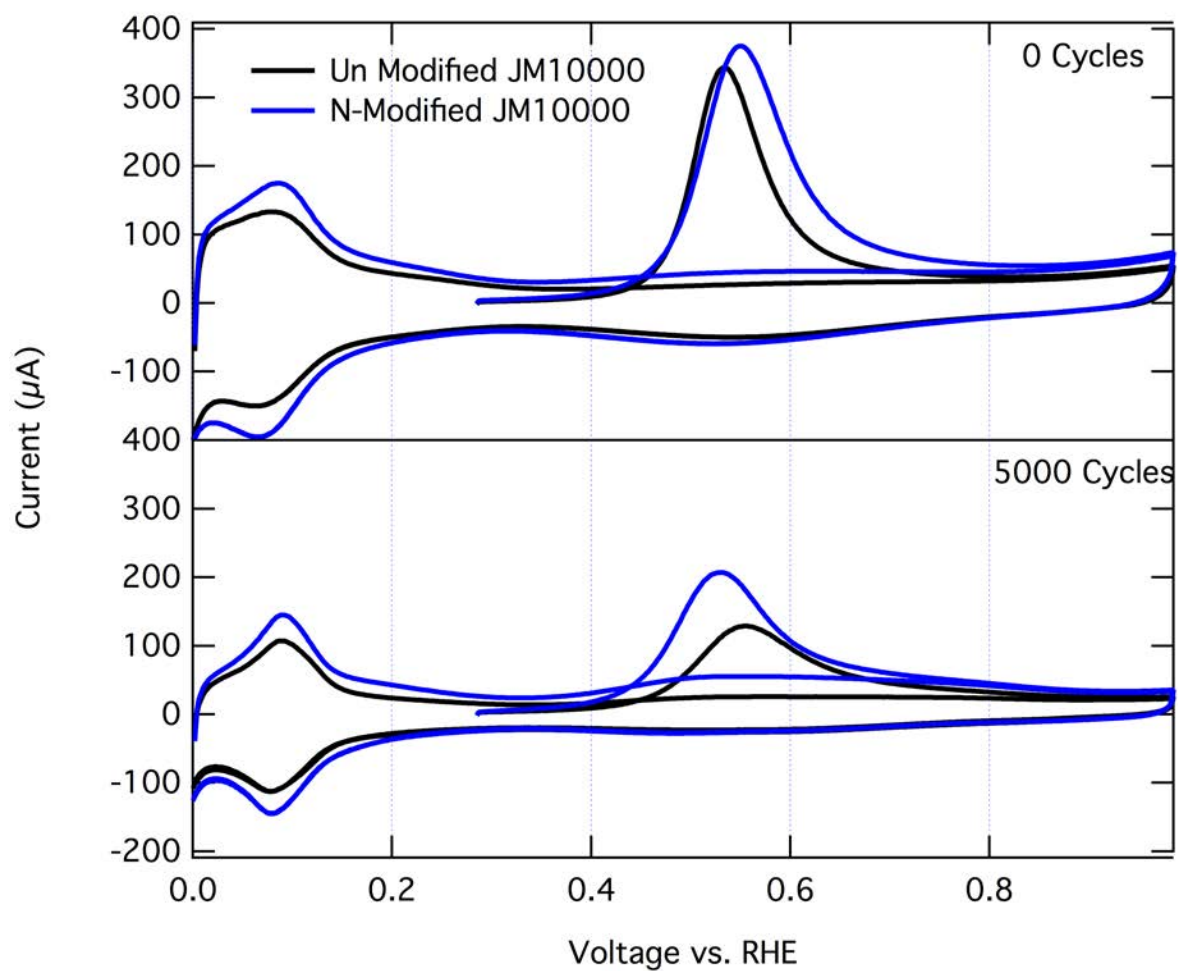


Figure 4.13: Showing the change in electrochemical surface area before and after 5000 cycles in a solution of .5M NaOH and methanol. Results show a more improvement in a solution with methanol than in a pure NaOH solution.

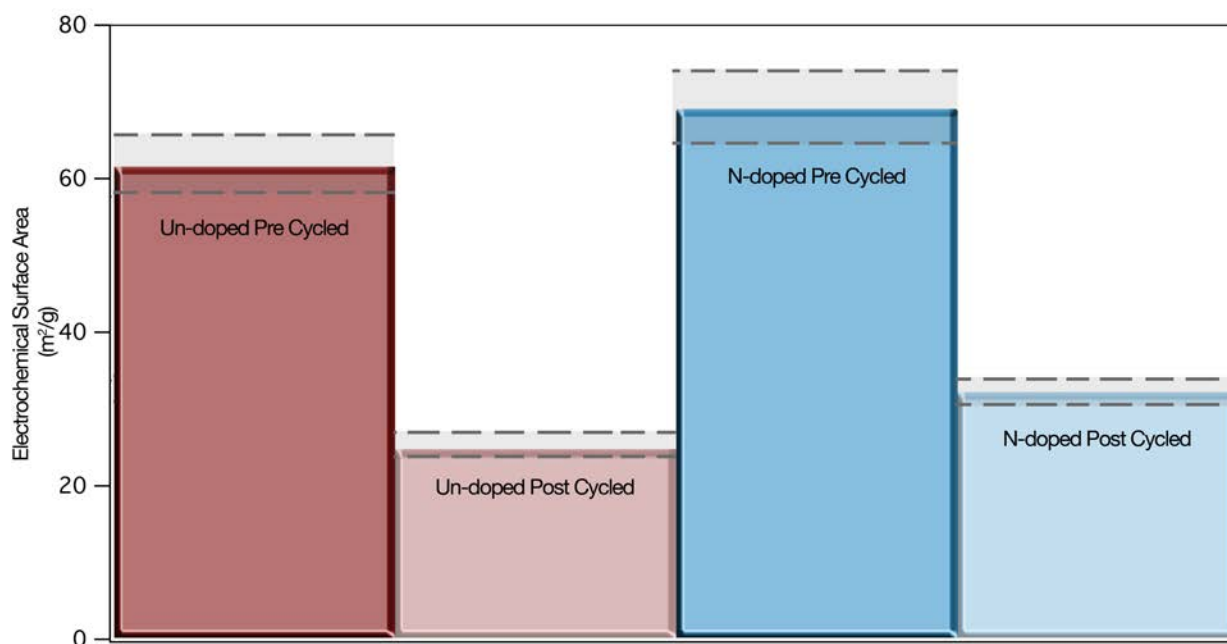


Figure 4.14: Electrochemical surface area before and after cycling. The dotted lines indicate the error in the measurement. The nitrogen improves surface area retention by ~7% .

enhancement in MOR performance. However, this hypothesis is supported by the fact that after cycling the nitrogen modified sample significantly out performed its un-cycled-self on a per surface area basis. This improvement appears to be greater in alkaline media than it does in acid. Secondly, this data indicates that nitrogen helps maintain the important composition necessary for efficient methanol oxidation. This point can be clearly seen by the shift in peak potential toward more positive values for the PtRu/C catalyst. Based on initial performance metrics this possibility seems more likely.

Together these results provide convincing evidence that nitrogen is an effective agent at helping improve catalyst performance and durability over the lifetime of a fuel cell. Initially, ion implantation of the modified commercial catalyst increases the electrochemical surface area through a re-sputtering process, confirmed by TEM and CO stripping. This effect shifted the onset potential of the modified catalyst toward a more Pt active phase. During the accelerated degradation process this initial shift was then reversed and the composition of the

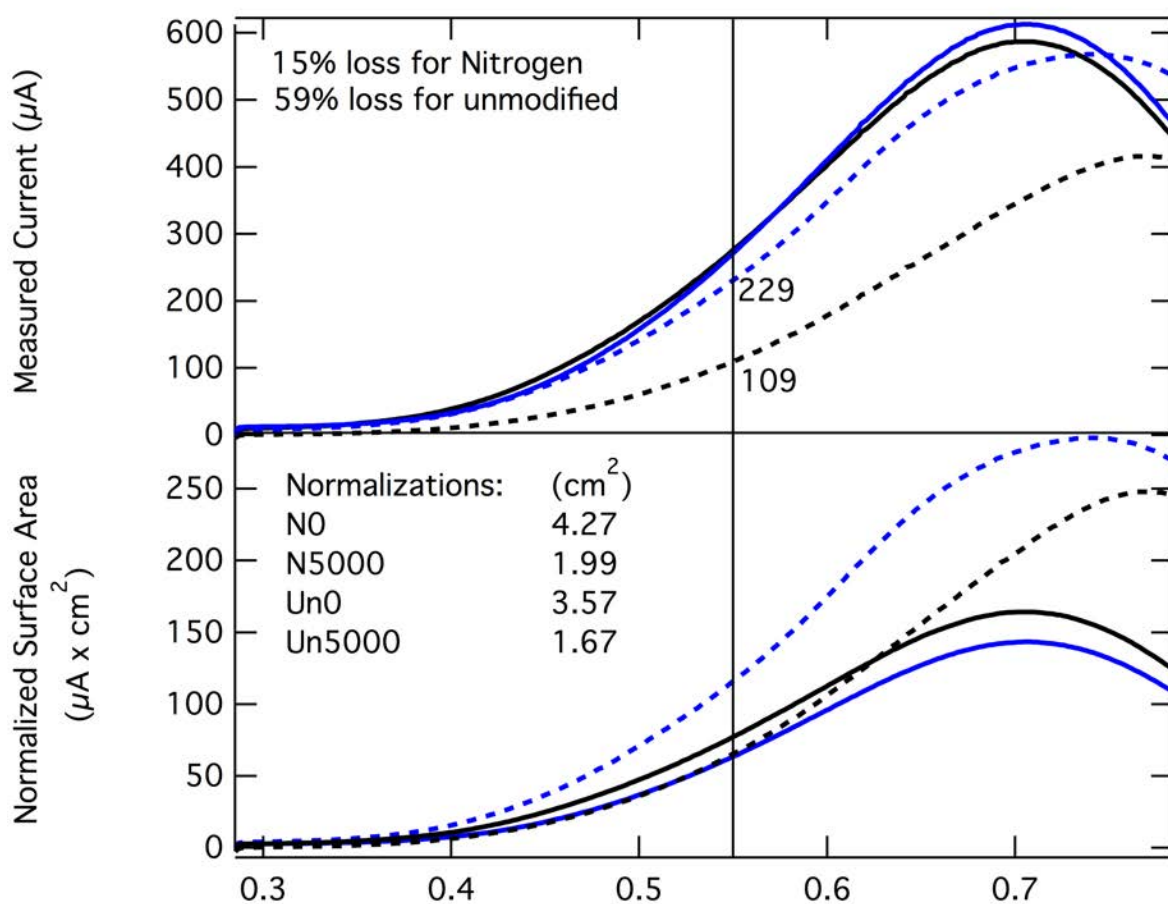


Figure 4.15: MOR performance comparing the unmodified and nitrogen modified commercial catalysts. The upper graph shows the collected data and the lower graph shows the data normalized versus surface area. The data shows only a 15% loss in performance over the lifetime of the cell for the nitrogen modified catalyst, while nearly 60% of the unmodified catalyst performance is lost.

active phase appeared to become stabilized. For the PtRu/C catalyst the intermediate CO stripping experiments indicated that Ru loss was a significant problem causing a positive shift in onset potential, an effect not observed during the testing of PtRu/C-N3. As evident by the position of the CO stripping peak, the nitrogen-modified catalyst maintained a more optimal Pt:Ru ratio, closer to 50:50. While the CO stripping results only showed a slight improvement in surface area retention for PtRu/C-N3 after ADT. MOR performance metrics after the degradation process indicated that the nitrogen post-modification improving durability from 41% to 85%. These results indicate that the retained surface area in the N-doped material appears to be more active than retained surface area in undoped samples.

4.3.1 Initial Alkaline MEA Study

To help confirm these results MEA testing was performed in alkaline media. Similar to what was observed in the half-cell studies, MEA's utilizing PtRu/C-N3 demonstrated an ECSA increase of 32%. While RDE studies showed a minimal effect of increased surface area on the methanol oxidation reaction for PtRu/C-N3, MEA results revealed a significantly higher alkaline DMFC performance when compared against an unmodified version of the same catalyst. In initial tests the MEA made from PtRu/C-N3 showed a 10-17% increase in the power density, which was greater than what RDE measurements would have predicted. However, it should be noted that based on the results seen in acid media, MEA testing leads to larger improvements in performance; as a result this is not unexpected. Currently, durability studies are being completed on PtRu/C-N3 in alkaline media, however these initial results show great promise for a highly durable alkaline DMFC anodic catalyst. Early indications appear to suggest that this catalyst could have a relatively greater improvement in alkaline media than in acid.

4.4 Durability effects in Acid vs. Alkaline

The ADT results of both acid and alkaline environments can be compared side-by-side to provide further revelation on the effect of nitrogen in these systems. It can be clearly seen in

Figure 4.16a/b that nitrogen plays little role in effecting CO stripping peak potentials or on-set potentials. However, Figure 4.16c/d shows that nitrogen modification in alkaline media leads to a change in peak positions as well as on-set potentials. This is significant because nitrogen appears to have a different effect on degradation mechanisms in alkaline media. As alluded to in the previous section, Figure 4.16a/b/c all show dissolution of Ru, evident by peak shifts toward higher potentials. For the acidic results a dramatic effect occurs after 100 cycles indicating a significant change in catalyst composition. Throughout the whole ADT process in the acidic environment, catalyst instability is clearly evident, even for the nitrogen modified sample. Due to the similar results for the PtRu/C and PtRu/C-N₂ sample, it is concluded that beneficial effect of nitrogen comes from maintaining active surface area and/or maintaining the most electrochemically active phases. In other words nitrogen helps slow down the degradation of the catalyst, but it doesn't eliminate a specific mechanism, it simply reduces the combined effects of modified Ostwald ripening, migration/coalescence, and carbon corrosion.

The un-modified sample in alkaline media shows some consistent instability as well, however when compared with the acidic results, the PtRu/C catalyst in alkaline is remarkably stable. This is expected because the reaction kinetics in alkaline media are more facile and less harsh toward the catalyst. Intriguing results come during ADT cycling of PtRu/C-N₃. Here, it is clearly observed that a change in the degradation mechanisms has occurred. It can be hypothesized that dissolution has been nearly completely stopped, however migration/coalescence is still occurring. As was shown in 3, this process is significantly reduced through the addition of nitrogen. Therefore, if dissolution is stopped and migration/coalescence is mitigated, the outstanding half-cell performance of PtRu/C-N₃ makes sense. This dramatic point was highlighted in Figure 4.15.

Since alkaline media provides accessible OH groups, CO poisoning on Pt is reduced regardless of Ru. Several studies have shown that PtRu catalysts still outperform Pt catalyst for methanol oxidation in alkaline solutions, however this benefit is less substantial than it

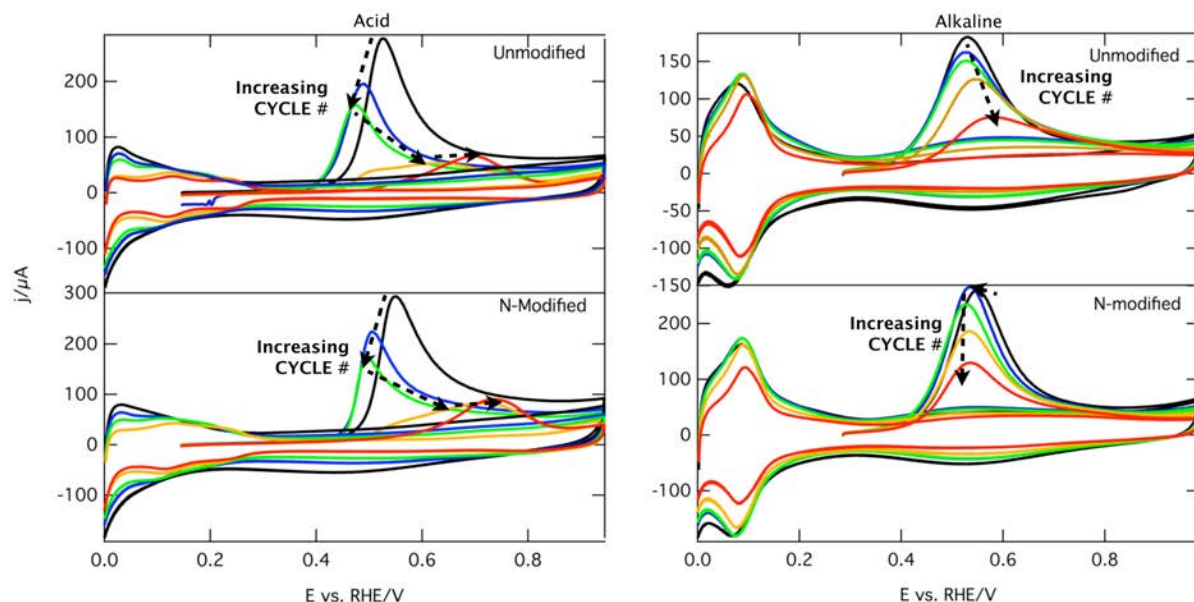


Figure 4.16: The effects of ADT testing on (a) PtRu/C in acid media (b) PtRu/C-N2 in acid media (c) PtRu/C in alkaline media (d) PtRu/C-N3 in alkaline media. Results show a change in mechanism for nitrogen modified catalyst in alkaline media.

was for acid. The results provided in this chapter show the significant effects nitrogen functional groups and the retention of Ru have on catalytic performance of alkaline DMFCs. It is difficult to deconvolute these effects and further studies should look at examining the outcome of nitrogen on Pt catalysts in alkaline media.

4.5 Conclusions

The results observed in this chapter using post-modified commercial anode catalysts show increased performance after durability in comparison to its undoped counterpart, regardless of electrolyte media. This was similar to what was observed with the in-house synthesized, pre-doped catalysts tested in acid, discussed in chapter 3. For the pre-doped catalysts, the greatest improvement in durability was attributed to reduced catalyst migration and coalescence on the nitrogen-modified support. These pre-doped materials included nitrogen in the carbon structure underneath and around the nanoparticles themselves. In the post-modified sample, nitrogen heteroatoms are expected to incorporate only into the

carbon regions that are unshielded by nanoparticles without altering the carbon structure directly under the nanoparticles themselves (due to shadowing during implantation). Nevertheless, as was clearly shown, post-metal nitrogen-modification effectively improves anodic durability. As previously mentioned, a DFT study on Pt interactions with nitrogen-doped HOPG showed that most nitrogen defects in carbon are negatively charged, attracting electron density and making the surrounding nearest-neighbor carbon atoms more positive. It was suggested that these nearest-neighbor carbons have attractive interactions with Pt and therefore likely restrict Pt migration. Since nitrogen acts as a negative defect it actually repels Pt[48, 93], making it reasonable to assume that it is energetically unfavorable for Pt to migrate over nitrogen defects. Thus nitrogen-doping, whether it is performed before or after metal deposition, has the potential to create a trapping state which make it energy energetically unfavorable for metal particles to migrate.[45] This also creates adjacent sites (the more positively charged nearest neighbor carbons) where it is more energetically favorable for the metal to adsorb.

In this chapter it has been shown that nitrogen implantation reorganizes the PtRu composition and its spatial distribution on the surface, which can result in a higher density of active sites. In acidic media it was shown that the initial improvement in surface area and performance was maintainable even after hundreds of hours of operation, highlighting the effectiveness of this technique for commercial applications. For alkaline media a similar trend was observed, with the initial increase in performance being less pronounced, but leading to greater durability after ADT, even when compared to an identical nitrogen modified catalyst in acid media.

A detailed investigation of the differences between nitrogen post modification in acid and alkaline media leads to the hypothesis that nitrogen modification in alkaline media prevents the dissolution degradation mechanism. Nitrogen also helps reduce migration/coalescence, as seen in acid studies, however the synergistic effect of dissolution prevention and migration mitigation lead the nitrogen modified catalyst in alkaline media to have a great improvement

effect than in acid. Overall, no matter the environment, post modification has a significant beneficial effect.

Incorporating nitrogen into the carbon support before adding metal nanoparticles is likely the most efficient way to gain all of the positive effects attributed to nitrogen-doping, including smaller nanoparticles and higher ECSA due to preferential nucleation,[53, 62, 108–110] increased Pt immobilization,[111] increased electrochemical activity,[62, 108–110] and increased durability.[48, 55, 63, 112] However, modifying the carbon support after metal deposition allows for a reduction in the complexity associated with the nitrogen effects. As shown in this chapter, immediate improvement to already highly optimized benchmark commercial catalyst materials is possible by after-the-fact support modification. These findings have important implications for electrocatalysis and a wide range of other applications utilizing carbon-supported catalysts. It is through a variety of studies such as this, that the scientific community can underscore nitrogen’s unequivocal role in modifying catalyst performance.

CHAPTER 5

THE EFFECT OF NITROGEN ON DURABILITY OF GRAPHENE SUPPORTED CATALYSTS

Carbon blacks are common catalysts supports used in current fuel cells, but their properties are not completely satisfactory. Some recent effort has been placed on developing alternative materials such as nanostructured carbons, ceramic and polymer materials to improve fuel cell catalyst support interactions. One of the most interesting next-generation fuel cell supports is graphene, due to high surface area, high conductivity, unique graphitized basal plane structure and potential low manufacturing cost. In this chapter I explore the effects of catalyst-support interactions on nitrogen-modified graphene supports decorated with PtRu nanoparticles.

Graphene is a single sheet of carbon atoms arranged in a hexagonal lattice. Due to its many unique physical and electronic properties, it has been dubbed by many as a ‘dream material’. Since the first report of its synthesis via the “Scotch tape”[113] method in 2004, the field of graphene research has witnessed extraordinary activity. While pure graphene by itself has many intrinsic benefits, chemical doping provides an important route to further tailor its properties for specific applications. For instance, the spin density and charge distribution of the carbon atoms will be influenced by neighboring nitrogen dopants[35]. This charge localization can help participate in catalytic reactions directly, as in the ORR, or can help tether metal nanoparticles to the graphene support[114].

Graphene can be nitrogen modified through two primary methods: 1) direct synthesis or 2) post-treatment. While these direct synthesis methods have shown success, post-treatment nitrogen modification methods, are more widely used. By comparison, post treatment methods generally lead only to surface doping, leaving the interior (bulk) of the treated carbon material unchanged.

Here I discuss the effects of nitrogen ion implantation on the performance of PtRu supported on graphene. In order to show the effect of nitrogen modification on performance of graphene-supported PtRu catalyst, unmodified and N-modified in-house PtRu catalyst systems were fabricated and tested in half-cell experiments. These samples were characterized by TEM, SEM, RDE, XPS, and TGA and compared against commercial JM5000 (50:50 Pt:Ru, 30wt%). Due to issues discussed later, this discussion is limited to alkaline media.

5.1 Experimental Information

The work presented in this chapter is part of an article that is in preparation and has been presented at an electrochemical society (ECS) meeting[95]. This work was done in collaboration with Dr. Alexey Serov and Dr. Plamen Atanasov, at the University of New Mexico (UNM). UNM provided undoped graphene samples used in this work. I completed the ion implantation and metal deposition process at the National Renewable Energy Laboratory, under the supervision of Arrelaine Dameron. Electrochemical testing and microscopy was completed at the Colorado School of Mines.

5.1.1 Materials Fabrication

Graphene oxide was synthesized via a modified Hummer’s method[115]. Further reduction of the graphene oxide was performed through means of a hydrazine reduction process at room temperature. This material was then fabricated into a DMFC catalyst through the use of the custom sputter chamber described in chapter 3 and chapter 4.[64] During an experiment, 500mg of the graphene fabricated at UNM was placed into the barrel and the chamber was evacuated to approximately 1×10^{-6} Torr. For PtRu/G-N Implantation was performed prior to sputtering at a chamber pressure of 1×10^{-4} Torr N_2 . The beam current and implantation times were held constant at 14 mA for 60min. Discharge and acceleration voltage were held constant at 55 V and 100 V, respectively, for all samples. For both PtRu/G and PtRu/G-N, sputter depositions were performed at 25 mTorr with 10 mol% $O_2:Ar$ at DC power of 45W for 60 mins. The chamber was not opened in-between implantation and

sputtering, which limited any oxidation of the modified support surface. These procedures have not been optimized for a graphene-based catalyst. Further work could document the optimum parameters for increasing metal loadings and increasing nitrogen incorporation. In a similar fashion to that shown elsewhere Dameron *et al.* [64]. In this chapter the fabricated graphene catalysts, unmodified graphene with PtRu (PtRu/G) and N-modified (14mA) graphene (PtRu/G-N), are compared against 30 wt% JM5000.

5.1.2 Characterization and Testing Methods

Thermogravimetric analysis (TGA) was used to verify the loading of the catalysts before and after implantation. TGA was completed using the TA Q600 (TA Instruments, New Castle, DE) by feeding 100 mL/min of synthetic air (80% N₂, 20% O₂) with a heating rate of 5 °C/min to a temperature of 850 °C. Quantification of the total metal content on the catalyst powders was based on the assumption that the final mass at 850 °C is composed of RuO₂ and Pt.

Transmission electron microscopy (TEM) images were collected on a Philips CM200 TEM. These images were used to determine morphological differences between unmodified and post-modified catalysts.

XPS analysis was performed using a Kratos Nova X-ray photoelectron spectrometer with pass energies of 160 eV for the survey spectra and 20 eV for the high-resolution spectra of C 1s/Ru 3d, O 1s, N 1s, Ru 3p, and Pt 4f. XPS spectra were analyzed using Casa XPS software. A linear background was applied to O 1s and N 1s regions, while Shirley background was used for C 1s/Ru 3d, Pt 4f and Ru 3p regions. Charge referencing was done to the carbon peak at 284.8 eV. Elemental quantification of ruthenium was performed using the Ru 3p region. Analysis of ruthenium species was performed using C 1s/Ru 3d region, employing consistent fitting parameters and constraints for all analyzed areas/samples. The Ru 3d region was fitted with 4 peaks, each containing 3d 5/2 and 3d 3/2 components separated by 4.2 eV.

Electrochemical studies of JM5000, PtRu/G and PtRu/G-N catalyst materials included rotating disk electrode (RDE), cyclic voltammetry (CV), CO stripping voltammetry, and methanol performance. The measurements were conducted in a standard three-electrode configuration that utilized a Hg/HgO, a Pt mesh counter electrode and a thin-film layer of the catalyst (applied from an ink) as the working electrode. All experiments were carried out at room temperature and pressure. The preparation of catalyst inks varied and will be discussed in a later section. These mixtures were bath sonicated in ice for 20 min and the ink was then applied to the glassy carbon RDE tip. The electrodes were dried at 40 °C for 30 min. Prior to performing any electrochemical testing, the working electrode was cleaned in a solution of 1M NaOH by cycling 10 times from 0. to 0.985 V versus RHE. Then, pure CO gas was bubbled into .5M NaOH for 10 min while the working electrode was held at 0.2 V versus RHE. While the working electrode was still held at 0.2 V versus RHE, pure N₂ was bubbled for 10 minutes to purge excess CO from the electrolyte. The potential was then swept to 0.985 V versus RHE at 20 mV/s to strip the adsorbed CO from the surface of the working electrode. Two subsequent sweeps from 0 to 0.985 V were then performed to ensure that all the bulk CO had indeed been removed from the electrode.

Methanol experiments were completed in a .5M NaOH and .5M MeOH environment. The measurements were acquired at 10mV/s to limit the faradic capacitance. The sweep started at .2V vs. RHE and was cycled through .985V. Accelerated durability testing was completed in MeOH/NaOH environments.

5.1.3 Catalyst Ink formulation

Unfortunately, many of the properties that allow graphene to be resistant to corrosion and durable also make graphene hard to disperse. Currently this is one of the largest hurdles preventing the widespread use of graphene in many applications. Due to its high degree of graphiticity and strong energetic potential to bond with itself, mutli-layer graphene clumps make dispersion and deposition of high metal loadings difficult (discussed later). To improve the dispersion for these samples as much a possible a series of experiments were completed

to insure an optimized ink formulation.

Testing initially began with an ink fabrication process involving Nafion. Several Nafion ionomer ratios were varied within reasonable quantities, but all solutions showed visibly poor suspensions. As such, the Tokuyama A-201 alkaline ionomer was tested, in place of the Nafion. Results showed a visible dispersion and prompted further investigations. Initial electrochemical testing was performed on inks similar to those previously reported (79.6% IPA, 20%water, .4% ionomer). From SEM images it was observed that dispersion was not as desirable for the graphene supported catalyst as it was for the commercial catalyst. In an attempt to improve dispersion other solvents were explored. During these studies it was determined that IPA and dimethylformamide (DMF) allowed for the most homogeneous catalyst suspensions. The inks were optimized and electrochemically tested. For DMF the inks made in a ratio of 1mg/ml in 4.96mL of DMF with .4mL of alkaline ionomer showed the best performance while the best IPA formulation followed the protocol given before (79.6% IPA, 20%water, .4% ionomer).

5.2 Results and Discussion

After material fabrication, TGA was completed on the graphene samples. Results showed low metal loadings for both PtRu/G and PtRu/G-N, 8wt% and 5wt% respectively. JM5000 was also tested and confirmed at 30wt%. XPS analysis was completed on both the nitrogen doped and undoped PtRu catalysts. Interestingly, the data showed extremely high metal contents, similar to what is expected of metal black sample (i.e. PtRu black, JM6000). To understand this unexpected result, SEM images were collected on the graphene samples and the JM5000. Figure 5.1a shows the typical morphology of a commercial catalyst, where small nanoparticles and agglomerates decorate the carbon surface. In Figure 5.1b, the morphology of the PtRu/G sample shows a complete coating of PtRu over the surface of the graphene, resembling surfaces similar to those employed in extended surface studies. These exciting results show the potential for this type of material to have low load metal loadings and large surface areas. Therefore, to better understand these materials further SEM images of the

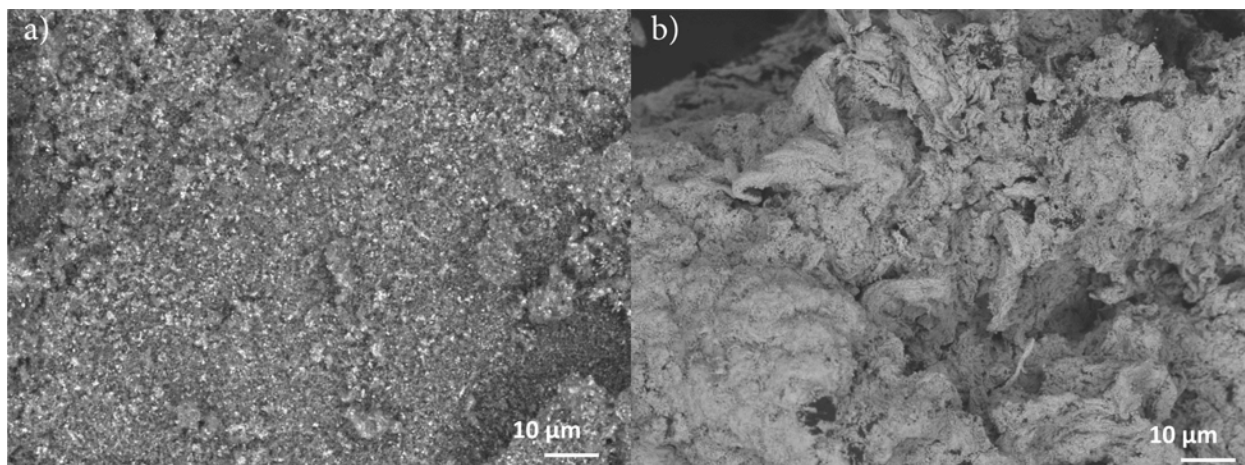


Figure 5.1: SEM images of the morphology of a) JM5000 and b) PtRu/G. Dispersed nanoparticles can be seen for the JM5000 sample while a homogeneous covering of PtRu is observed for the PtRu/G sample.

catalyst inks we taken. These images shown in Figure 5.2, reveal areas of bare graphene and areas of dense coating-like coverages. This is likely due to the clumping of graphene during the sputtering process, which prevents large areas from being coated because of the line-of-sight technique. Indicating, significant improvements can be made in the performance of this material through the use of fabrication methods that reduce clumping and improve metal coverage.

The suspended catalyst samples were investigated in TEM as well. Once again areas of complete metal coverage and bare carbon were observed, however areas with well-dispersed PtRu were also seen. Figure 5.3 shows the three possible metal coverages, thick areas of PtRu, film-like PtRu, and nanoparticle PtRu. The nanoparticle regions show the extreme attractiveness of this support materials and its potential utility. The highly dispersed nanoparticle coverage is similar to that observed on model system studies and provides the potential for extremely high surface areas per metal loading, see Figure 5.4. However, the current clustering of the graphene samples during the sputtering process prevents the deposition of homogeneously well-dispersed PtRu throughout and instead leads to low metal loadings (Figure 5.4).

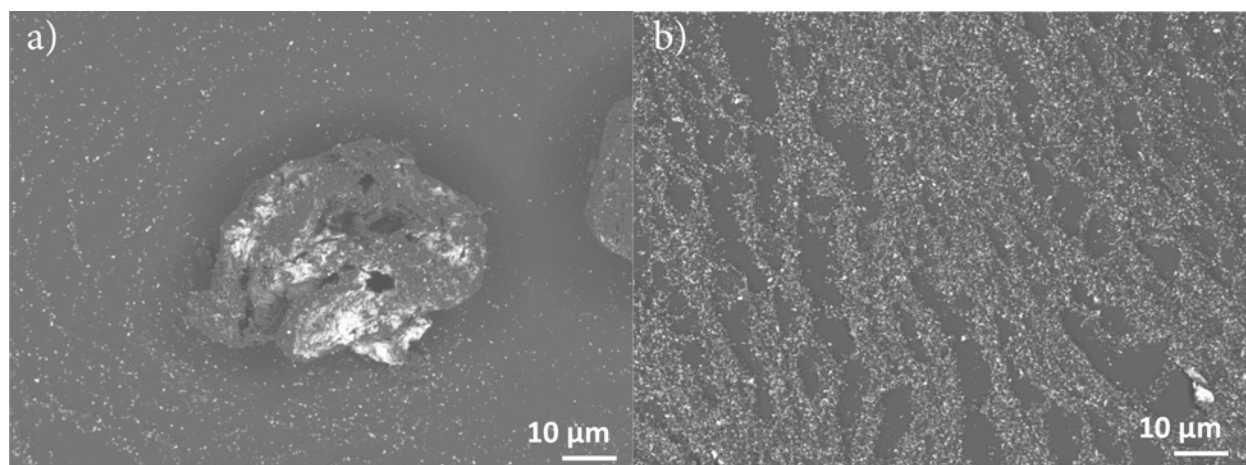


Figure 5.2: SEM images of the PtRu/G ink dropped on a glassy carbon electrode. Areas of clumping and poor dispersion can be seen in a) and good catalyst ink dispersion can be seen in b). Areas similar to b) are desirable.

Initial ink optimization was done on PtRu/G. These results, shown in Figure 5.5, reveal that inks made with DMF outperform the traditional IPA-based inks when normalized vs. active surface area. Figure 5.1 also shows that after 2 months of standing the ink formulation with DMF performs better than IPA-based inks, after 2 weeks and 2 months. Evaluation of IPA-based inks after 2 months revealed a decrease in their performance, as compared to that after 2 weeks, however the time series of IPA inks performed the same when normalized vs. active surface. This indicates that over time the PtRu/G catalyst loses surface area, either through dissolution, migration, or detachment, and the decrease in surface area results in decreased performance. The DMF sample however, increases the surface area and increases methanol performance as the sample is aged. Interestingly, the methanol performance increases to a larger degree than the surface area, indicating that over time the DMF starts to assist in the precipitation of the reaction. This could be attributed to the fact that DMF contains nitrogen functional groups and as the ink ages the DMF may modify the support with nitrogen in a beneficial way. Unfortunately, more studies need to be completed to elucidate the mechanism by which DMF improves performance over time. It is worth mentioning that the CO stripping area for the IPA samples is, in general, higher than the

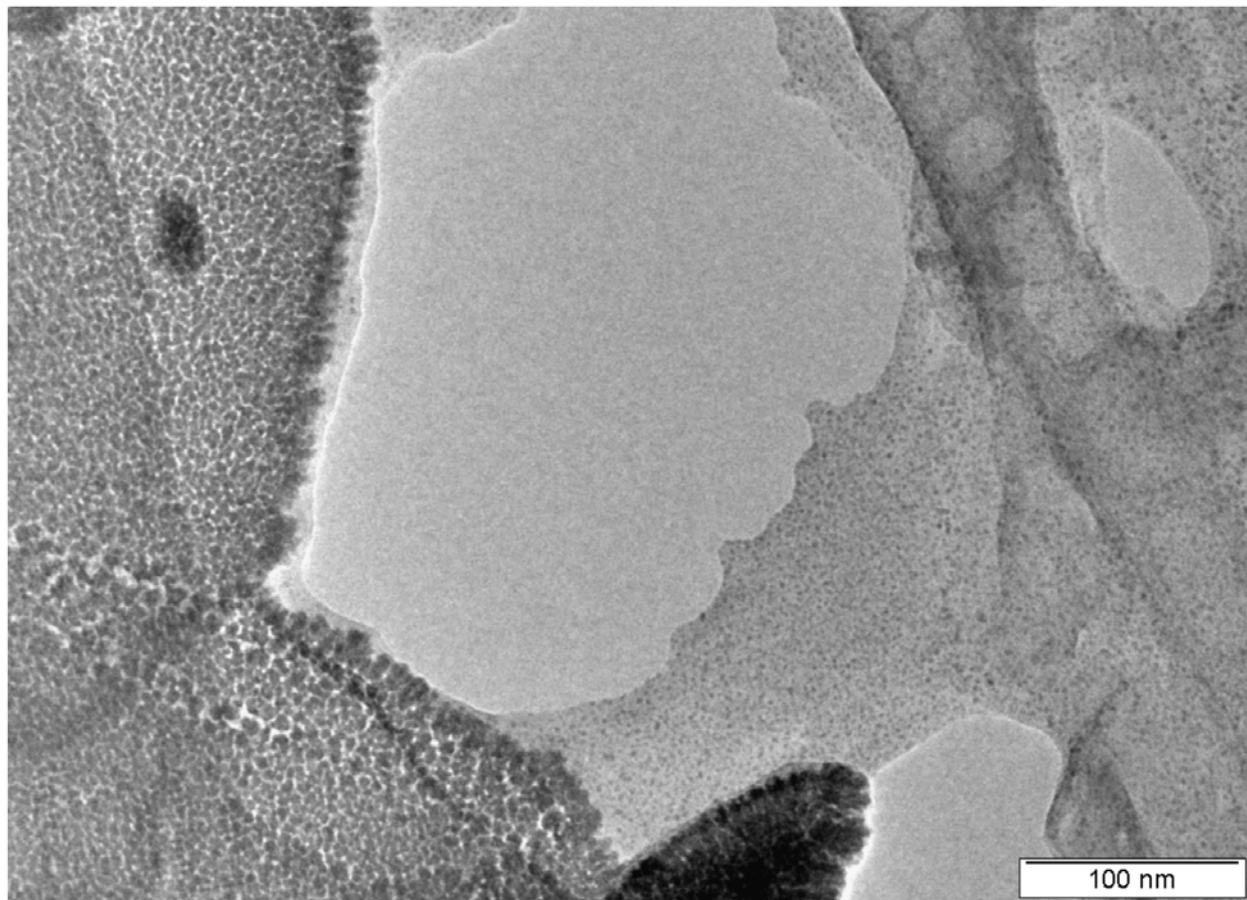


Figure 5.3: Three areas of PtRu coverage can be seen. 1) Dense metal agglomeration 2) Film-like metal coverage 3) Nanoparticle coverage. This TEM images shows the three dominate types of metal coverage in the PtRu/G sample.

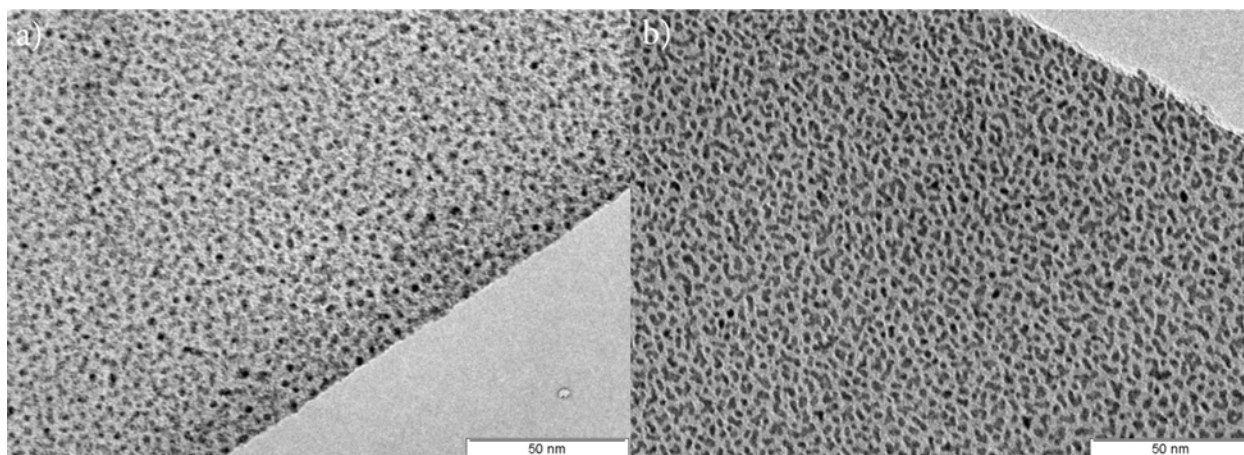


Figure 5.4: TEM images comparing the nanoparticle coverage of PtRu/G a) against the typical morphology observed for PtRu sputtered HOPG b). These types of morphologies could lead to incredibly high surface area and low metal loadings once sputtering and graphene conditions are optimized.

DMF samples, but the DMF sample's performance is significantly greater. For this reason the DMF ink formulation will be used for the graphene samples through the remainder of this chapter. Contrary to graphene-based materials, the DMF had a negative effect on the performance of the JM5000 samples. More information on the ink formulation and procedures can be found in the paper to be published and was discussed in detail at the 2013 fall ECS conference.

The graphene samples and JM5000 sample were tested before accelerated degradation testing to obtain a baseline performance. These results can be seen in Figure 5.6 and provide some interesting insight into the performance of graphene based catalysts. In Figure 5.6a the MOR performance is normalized per metal weight loading, demonstrating mass-activity of the metal present. It is easy to observe that the nitrogen-modified graphene outperforms both the PtRu/G and JM5000 samples. The PtRu/G-N catalyst has notable improvement throughout the entire reaction regime. However, PtRu/G performs worse in the kinetic region and greater at the peak potential than JM5000. At .55V vs RHE PtRu/G performs nearly identical to the commercial benchmark. In Figure 5.6b the same data is normalized against active surface area determined through CO stripping. Comparing active surface area

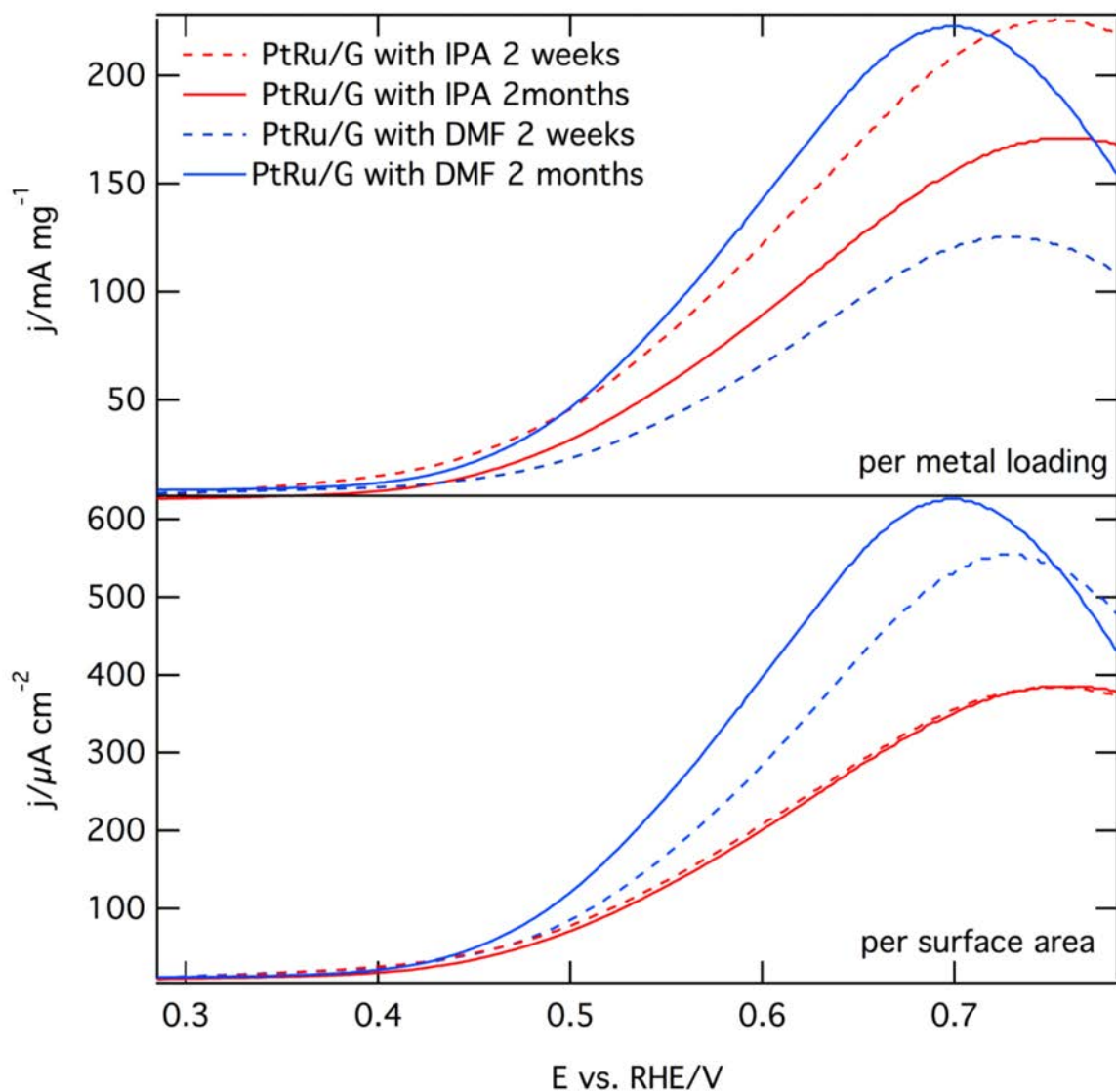


Figure 5.5: The effects of solvent on the methanol performance of PtRu/G catalyst samples. Samples normalized per metal loading shown in a) reveal an improvement in catalyst performance for DMF as time increases, while IPA performance decreases b) Shows samples normalized per active surface area. This underscores the role DMF has in improving catalyst performance via a mechanism other than surface area.

per metal wt% shows that JM5000 has the greatest metal utilization in terms of surface area ($.034 \text{ cm}^2/\text{wt}\%$, $.038 \text{ cm}^2/\text{wt}\%$, $.093 \text{ cm}^2/\text{wt}\%$, PtRu/G, PtRu/G-N, JM5000). The fact that PtRu/G-N shows better metal utilization than PtRu/G indicates that either the nitrogen sites help participate in the reaction or improve metal nucleation. However, this current study cannot deconvolve which effect nitrogen plays in the observation. Raw data normalized versus electrode geometric surface area can be seen in Figure 5.7. While increasing metal loadings is essential, this figure helps show that even the 8wt % catalysts in DMF have respectable current responses compared with the 30wt% JM5000. This figure also shows that graphene has no intrinsic catalytic activity.

The accelerated durability testing, as seen in Figure 5.8, was completed for 1000 electrochemical cycles. Initially, as documented previously, PtRu/G-N shows slightly better electrochemical performance than PtRu/G. After cycling, per metal loading, the improved performance is slightly greater than before cycling. When this data is normalized per active surface area a huge increase in electrochemical performance is observed. This indicates that nitrogen helps retain the most electrochemically active metal species. These results are identical to that which was observed in chapter 4 for the nitrogen post-modified catalyst system. It is likely that the magnitude of performance enhancement is greater in this experiment because of the low surface area for PtRu/G-N, however the beneficial effects of nitrogen modification are clearly undeniable. For the PtRu/G, the decrease in performance (Figure 5.8a) can be attributed to a loss in surface area, due to the nearly identical results before and after cycling when normalized per active surface area, Figure 5.8b. PtRu/G-N increases by nearly 4x when compared vs. the same metric. This significant increase shows the great potential for the nitrogen modification in these types of systems.

5.3 Conclusions

Graphene is a promising support material for many reasons. However, many challenges stand between the scientific community's current knowledge of graphene as a catalyst support and the level of understanding needed for commercialization. In this chapter I investigated

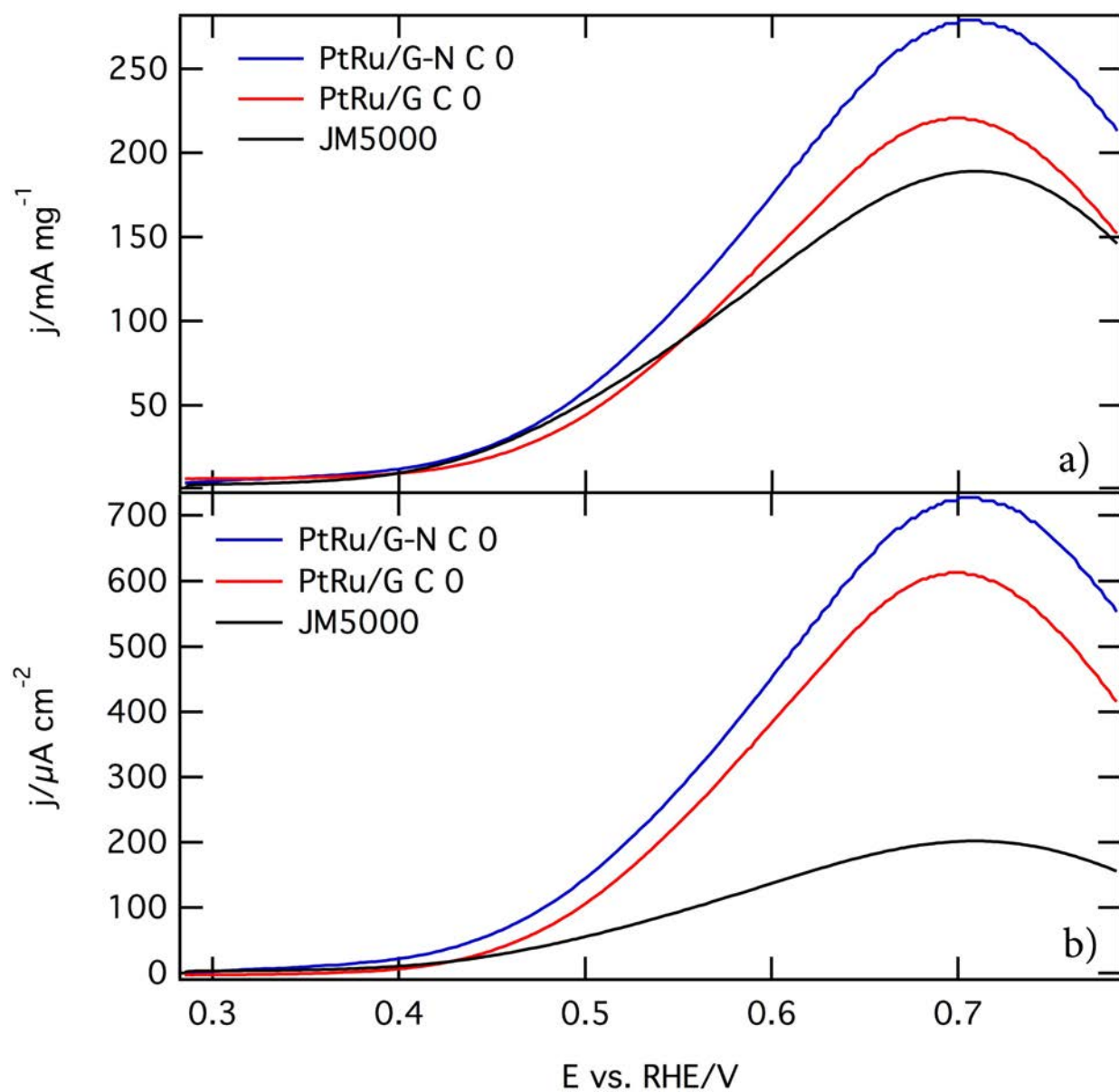


Figure 5.6: Initial performance before cycling of PtRu/G, PtRu/G-N, and JM5000 normalized (a) against metal loading (9wt%, 5wt%, 30wt%, respectively), (b) surface area (.313cm², .189cm², 2.8cm², respectively).

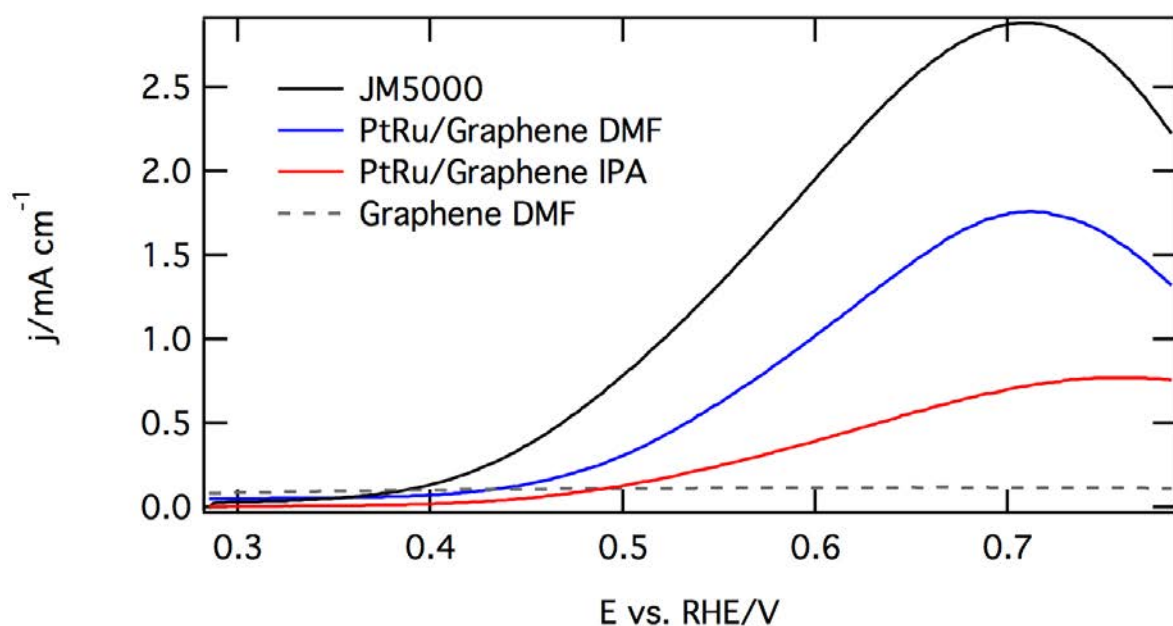


Figure 5.7: The MOR performance of DMF and IPA graphene based electrocatalysts compared against JM5000. This figure shows that graphene has no intrinsic catalytic activity. Additionally, this figure is only normalized per geometric electrode surface area, which is identical for all samples. PtR/G only has 9wt% compared with the 30wt% JM5000.

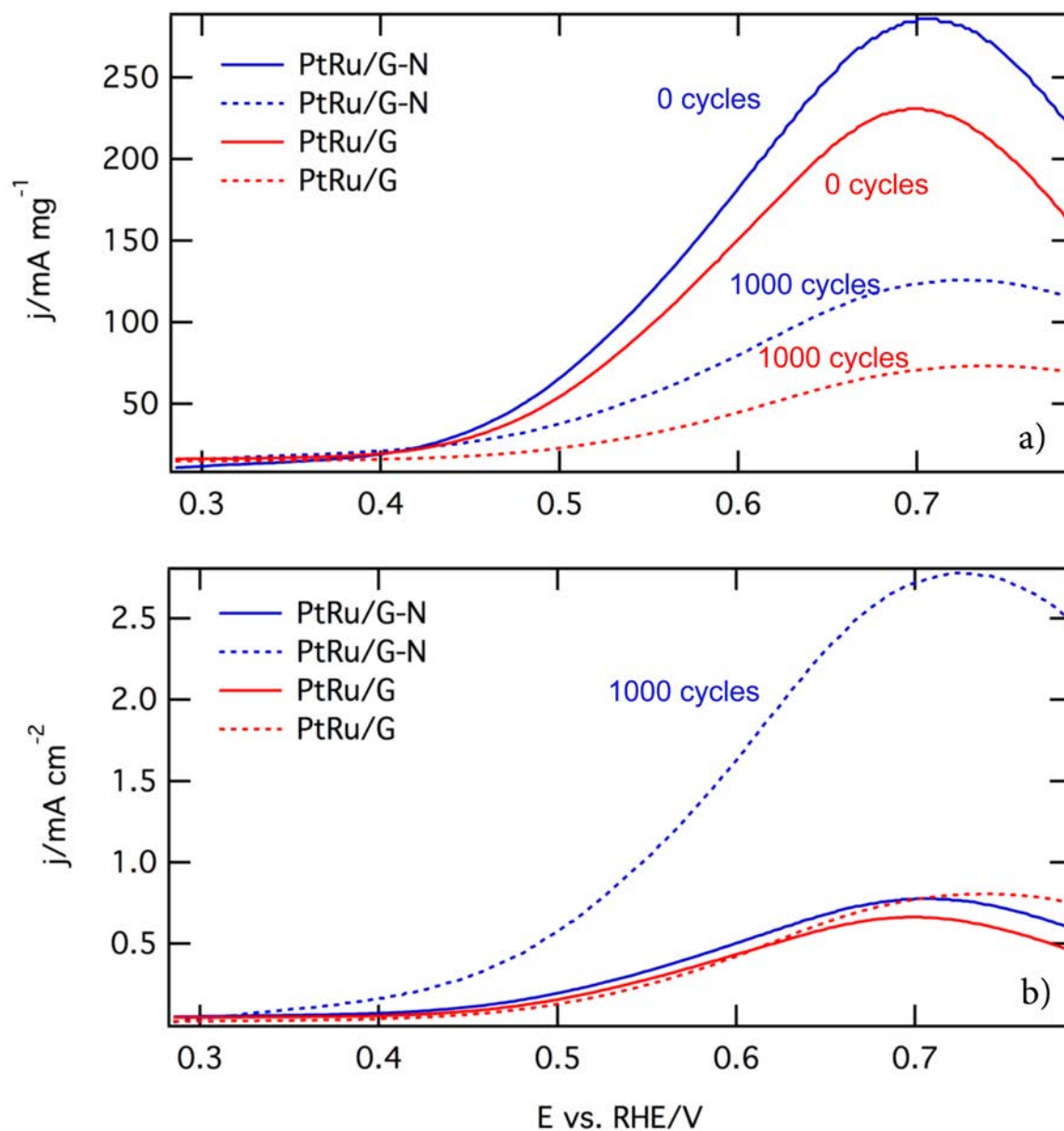


Figure 5.8: ADT testing results of graphene support PtRu catalysts. a) shows the effect of 1000 cycles on PtRu/G and PtRu/G-N normalized vs. metal loading b) plots the effect of cycling vs. electrochemically active surface area determined from CO stripping.

the role of graphene and nitrogen modified graphene as a catalyst supports for the anodic reaction of a DMFC.

Due to the strong energetic feasibility of graphene bonding with itself, metal loadings for these catalyst supports were 3-4 times lower than that of current commercial catalysts. While these loadings are lower than desired, comparisons of the PtRu/G, PtRu/G-N, and JM5000 show that per metal loading PtRu/G-N is the best performing catalyst. More importantly, accelerated durability testing on the graphene catalysts revealed that PtRu/G-N shows the largest increase in durability. This result, similar to that which was shown in chapter 4, gives further credence to the hypothesis that nitrogen helps maintain the most active PtRu phases. However, possibly the most promising results are shown in the TEM images of these materials, where it can be clearly seen that the sputter deposition process can lead to dense nanoparticle coverages, nearly identical to materials fabricated for model studies. This potential for a dispersed alloyed catalyst on a corrosive resistant, highly electrically conductive support is highly desirable.

While these initial findings are very promising and have great potential for future study, much work still needs to be completed to continue this study. The first significant hurdle is increasing the metal loading of the graphene catalysts. This task is already underway as we are conducting research on a new class of graphene that will hopefully reduce clumping and result in higher metal loadings. Additionally, a better understanding of ink formulation is also needed to determine the optimum solute and solution age. Once these topics have been researched in more depth, more conclusive statements can be made about the overall effect of nitrogen on graphene catalyst support systems.

CHAPTER 6

BEYOND NITROGEN: DO OTHER FUNCTIONALITIES OFFER IMPROVED DURABILITY?

As briefly discussed in chapter 2, early studies (circa 2009) on N-modification effects were done using model substrates to investigate the effects of the adatoms with limited effects from inhomogeneity and/or edge defects. Due to the fact that it has been proposed that edge defects and surface roughness generated by the implantation process could be partially responsible for the improved durability on heteroatom-functionalized supports, studies were also conducted using inert gases. These studies showed that implantation of HOPG with gases such as Ar, which do not incorporate into the matrix, created defects that lead to detrimental effects on support stability[47]. Similarly, low dosage levels of nitrogen introduced into HOPG have been observed to have negative effects on catalyst durability. This was attributed to the substantial physical damage and small amount of nitrogen functionalization. In these studies sputtering was also used to decorate the model substrates in such a way as to prevent preferential nucleation.

Within the last five years, heteroatom dopants such as nitrogen, boron, sulfur, and phosphorus have been shown to effectively modify the physical, chemical, and electronic properties of bulk carbon materials. To a similar end, this study focuses on the modification of the model HOPG substrates through the ion-implantation of halides, specifically fluorine and iodine. Based on the effects observed previously (in N and Ar implanted samples) and the use of sputtering, the observed effects presented in this chapter can be deconvoluted to determine the effect of functionalization. Raman spectroscopy and X-ray photoelectron spectroscopy (XPS) were used to determine the structural and chemical modifications of the HOPG substrates as a function of dopant and implantation conditions. Through the use of magnetron sputtering based deposition we were able to produce consistent, repro-

ducible, non-preferential Pt-Ru catalyst coverages, which were subsequently subjected to electrochemical durability cycling. Transmission electron microscopy (TEM) was used to evaluate the changes in the coverage and particle size distribution before and after cycling, and correlate them with specific structural effects and chemical functionalities associated with the different modifications. This chapter demonstrates that incorporation of iodine, fluorine and nitrogen into the graphitic structure of HOPG modifies the substrate surface chemistry and changes catalyst-substrate interactions. In iodine-modified samples, improved durability is most likely associated with the presence of polyiodide species. The improved durability observed with fluorine modification is co-dependent on the presence of nitrogen. In this co-implanted system it is hypothesized that the enhanced durability is due to 1) the charge difference between nitrogen and carbon, 2) nitrogen's incorporation into the carbon ring structure, and 3) the electron withdrawing nature associated with the formation of C-F bonds.

6.1 Experimental

Highly oriented pyrolytic graphite (HOPG, grade 2, 10x10x1mm, SPI inc.) was used as the model carbon substrate material. Ion implantation of HOPG substrates was performed with a 3cm DC (ITI) Ion Source (Veeco) at room temperature using an ion beam of N₂, I₂, CF₄, or a mix of N₂ and CF₄ directed to the surface at an incident angle of 35 degrees. CF₄ was chosen instead of fluorine gas due to its relative benign nature. For all precursors, ion beam energy was kept constant at 100 eV, and ion current and time of implantation were in the range of 13-42 mA and 45-120 s respectively. These conditions correlate to an estimated ion dosage in the range of 10¹⁶-10¹⁷ ions/cm². It was observed that the chemical nature and surface concentration of the inherent nitrogen heteroatoms varied with the CF₄ implantation parameters. The CF₄ process gas did not contain nitrogen, as was determined by mass spectroscopy.

Raman spectra were collected using a Nd:YAG laser with an excitation wavelength of 532 nm in conjunction with a double grating UHTS300 spectrometer set to the 600 g/mm option

with a center wavelength of 598 nm. The setup also included a 100X Nikon objective lens and an Andor iDus CCD camera. Each single Raman spectrum resulted from 25 scans with each scan having an integration time of 0.5 s. The D/G ratio was calculated by subtracting the background from both peak intensities and then dividing the D band (defect) peak intensity by the G band (graphitic carbon) peak intensity.

XPS survey and high-resolution spectra were collected on a Kratos Nova XPS using a monochromatic Al K-alpha source operated at 300 W. Data analysis was performed using CasaXPS software and included subtraction of the linear background and charge referencing using the graphitic peak at 284.6 eV.

Pt_{1-x} Ru_x nanoparticles were sputtered onto the modified and unmodified HOPG substrates from a single composition Pt_{0.5} Ru_{0.5} (ACI Alloys) alloyed target with a 2" Onyx magnetron sputter gun (Angstrom Sciences). Direct current (DC) magnetron sputtering was performed using an MDX 1.5 kW DC power supply (Advanced Energy). The samples were positioned at a distance of 1.5" directly above the target, and the deposition was done after establishing a base pressure below 4 x10⁻⁶ Torr. Nanoparticles were deposited by sputtering for 5 s in an inert Argon environment at a constant power of 20 W and a constant pressure of 20 mTorr Ar. Material flux was limited to very short time frames (few seconds) by the use of a shutter between the sample and source.

After sputtering deposition, electrochemical cycling of HOPG substrates was performed using the three-electrode configuration in acid media. In a special aqueous cell, the HOPG acted as the working electrode, while Ag/AgCl was used for the reference electrode and a Pt wire counter electrode completed the circuit. The modified HOPG substrates were cycled this way 300x in an acidic 1M H₂SO₄:1M MeOH solution, from 0 to 1.2V vs. Ag/AgCl at 250 mV/s.

TEM images the Pt-Ru nanoparticles on HOPG substrates were obtained using a Philips CM200 Transmission Electron Microscope. The samples were prepared by peeling off a thin surface layer of the HOPG sample and positioning it between the two grids of a Cu double

grid (Electron Microscopy Sciences). Evaluation of the coverage and particle size analysis was conducted using Photoshop and Igor following methods reported on elsewhere[2, 47, 63]. The coverage was determined by applying both high pass and threshold filters to separate the background HOPG from the Pt-Ru particles. These particles were then analyzed by converting black Pt-Ru particles to a ratio versus total area of the image. A representative number of single nanoparticles were then measured to obtain average particle size. This allowed for size resolution down to ~ 1 nm.

6.2 Results and Discussion

The relationship between the chemical and structural effects caused by ion implantation to the stability of overlying PtRu catalyst nanoparticles supported on HOPG substrates was established through TEM analysis of catalyst coverage and particle size variations. First results were obtained for the two reference samples, unmodified and N-modified HOPG, shown in Figure 6.1. Initial TEM images show the substrates to have consistent PtRu particle size and coverage (Figure 6.1a/c). For the post-cycled, unmodified sample (Figure 6.1b), poor coverage and larger particle size were observed, indicating degradation of the catalyst through dissolution and migration/coalescence of the metal phase. However, doping the carbon support with nitrogen at a dosage of 10^{16} ions/cm² (Figure 6.1d) resulted in better coverage retention and smaller changes in the particle sizes. These findings are consistent with the previous reports for unmodified and nitrogen modified HOPG and will be used to compare stability of PtRu nanoparticles on iodine and fluorine modified HOPG samples[94].

6.2.1 Support Modification with Iodine

Figure 6.2 compares the Raman spectra of iodine modified HOPG at two dosages to the spectra acquired for the unmodified and nitrogen modified reference samples. The major change in the Raman spectra associated with implantation is the appearance of a defect peak (D-band) near 1350 rel. cm⁻¹. In the iodine sample modified with 10^{16} ions/cm² (low dose), the spectrum reveals the presence of this defect peak, but no response in the

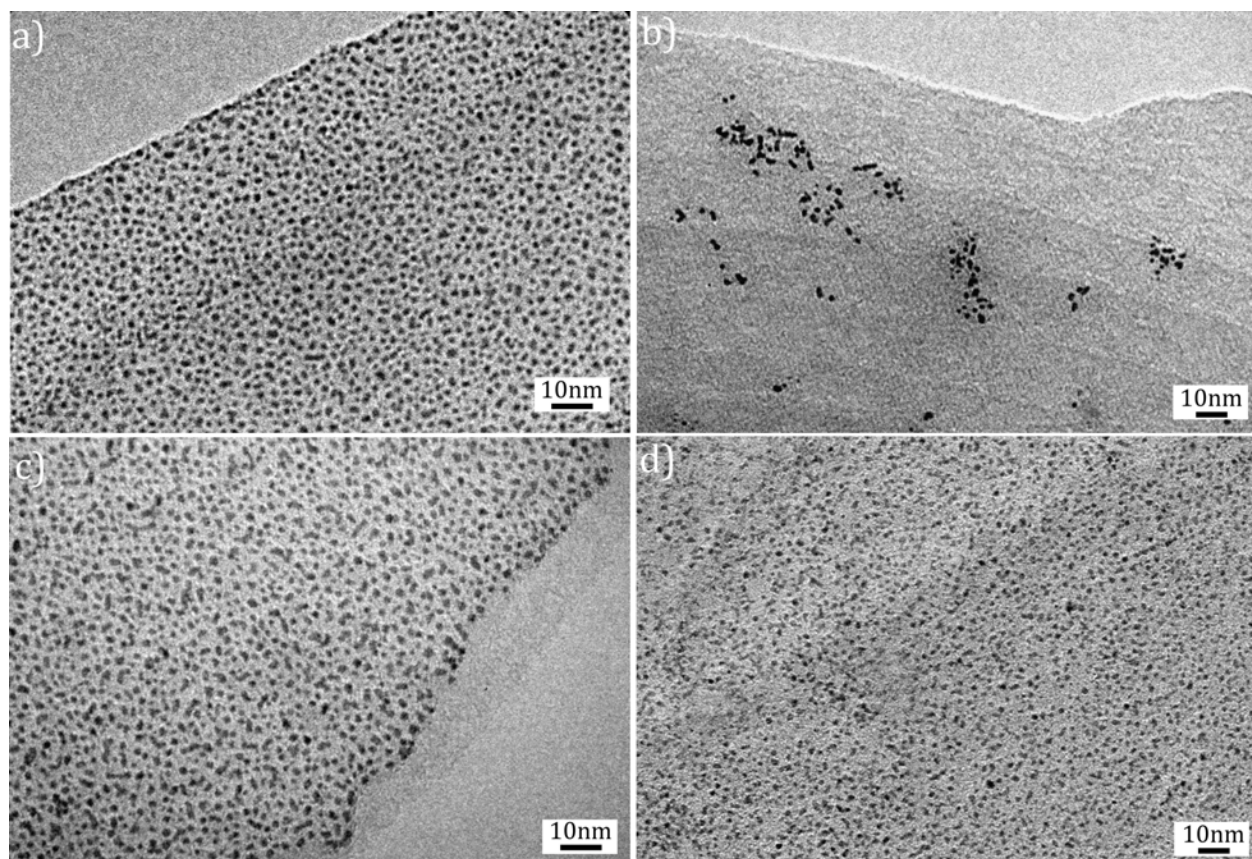


Figure 6.1: TEM images of pre- and post-cycled unmodified and N-modified samples. A) unmodified, pre-cycled, B) unmodified, post-cycled, C) N-modified, pre-cycled, D) N-modified, post-cycled .

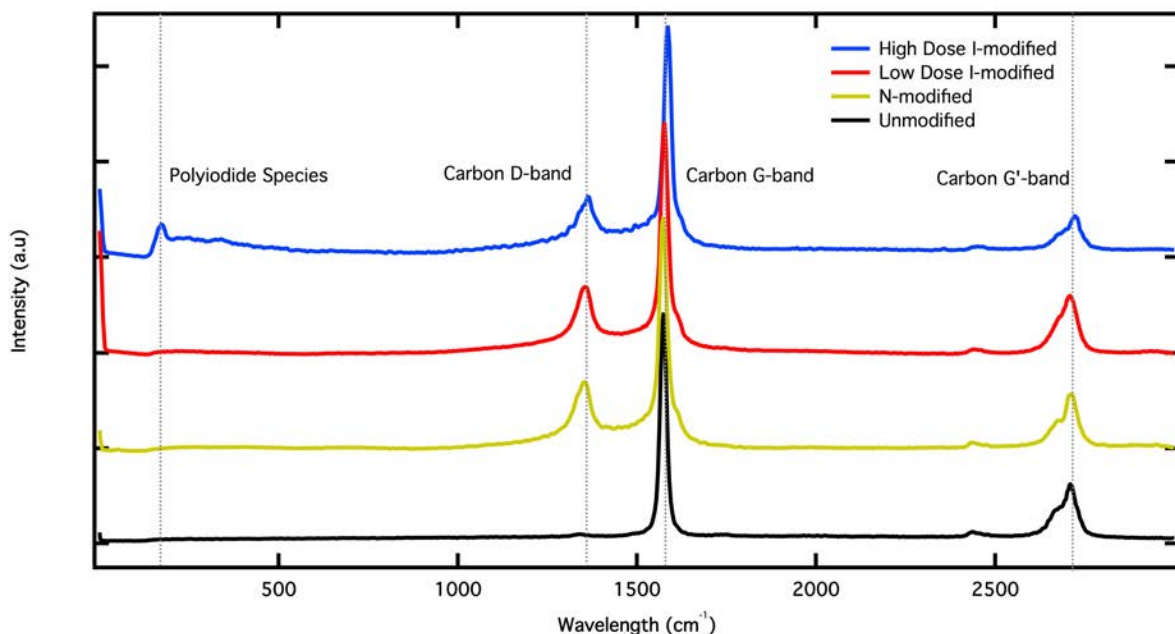


Figure 6.2: Raman spectra of I-modified HOPG samples compared to unmodified and N-modified reference samples.

range expected for polyiodide species ($100\text{--}200\text{ rel. cm}^{-1}$)[72, 73]. This suggests that low dose implantation of iodine creates structural damage to the carbon, but does not provide sufficient driving force to create extended iodine structures. In the sample modified by 10^{17} ions/ cm^2 (high-dose), the intensity of the D-band remains fairly consistent to that of the low dose sample, but the appearance of an iodine resonance peak around $\sim 170\text{ rel. cm}^{-1}$ was observed. The lack of further change to the D-band indicates that structural damage to the carbon did not increase with dose. Appearance of an iodine resonance peak however, suggests incorporation of iodine into support material[48, 116]. XPS analysis also suggested the presence of polyiodide species at binding energies of ~ 619 and 620 eV (Figure 6.3)[72].

For the iodine modified samples (Figure 6.4) the pre-cycled catalyst morphology is consistent with the previous samples shown in Figure 6.1. TEM images of the post-cycled low dose I-modified sample suggest a significant loss of catalyst coverage indicative of poor stability (Figure 6.4b). In particular, the formation of large agglomerates on this sample is strong evidence of insufficient modification to improve catalyst stability on the surface, even

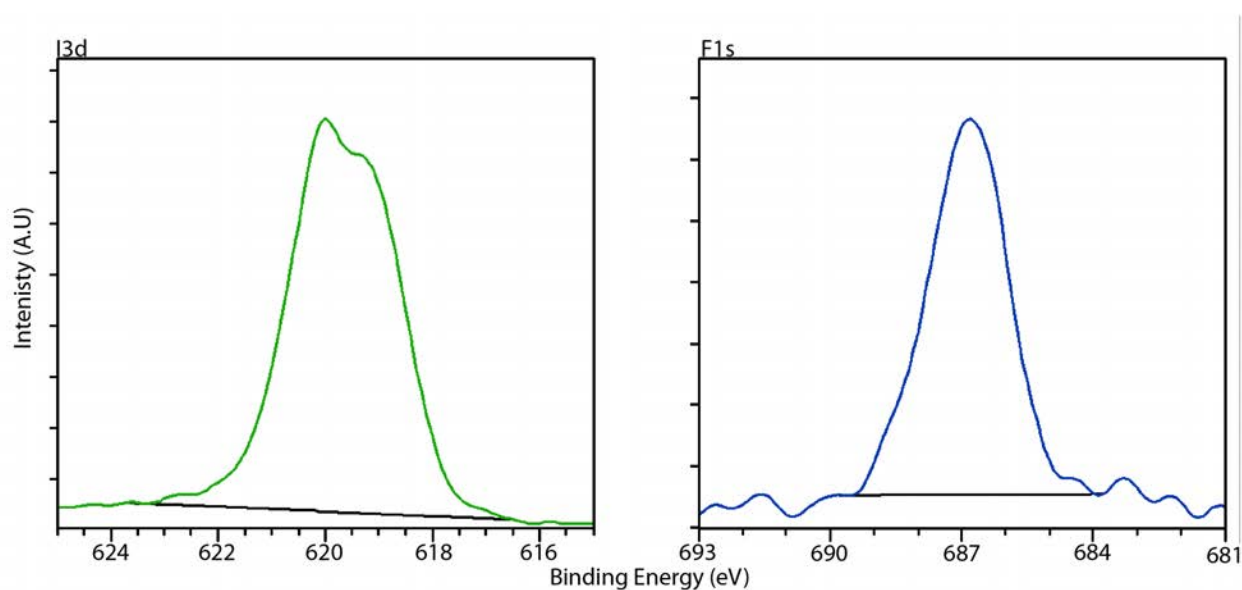


Figure 6.3: XPS high-resolution spectra a) I 3d in iodine modified sample and b) F 1s in fluorine modified sample.

though the durability of this low-dosage I-modified sample showed slight improvement over the unmodified baseline (Figure 6.1b). Figure 6.4c/d show TEM micrographs for the pre and post-cycled, high-dose I-modified sample; analysis of which shows $\sim 40\%$ retention in particle coverage and an approximate 0.4 nm decrease in particle size. These results are a significant improvement over the unmodified sample, and about equivalent to the beneficial effect observed for N-modified samples. Significant improvement in durability of the high-dose I-modified sample as compared to the low dose I-modified sample is most likely related to formation of polyiodide species. Polyiodide species have shown to have beneficial effects on catalytic activity of the carbon-based materials used in batteries[72].

6.2.2 Support Modification with Fluorine

Figure 6.5 compares the Raman spectra of HOPG modified with fluorine at two dosages vs. the spectra acquired for the unmodified and nitrogen modified reference samples. This data shows very small changes in the carbon defect peak for the CF_4 modified samples compared against the N-modified reference, indicating that there are few structural differences

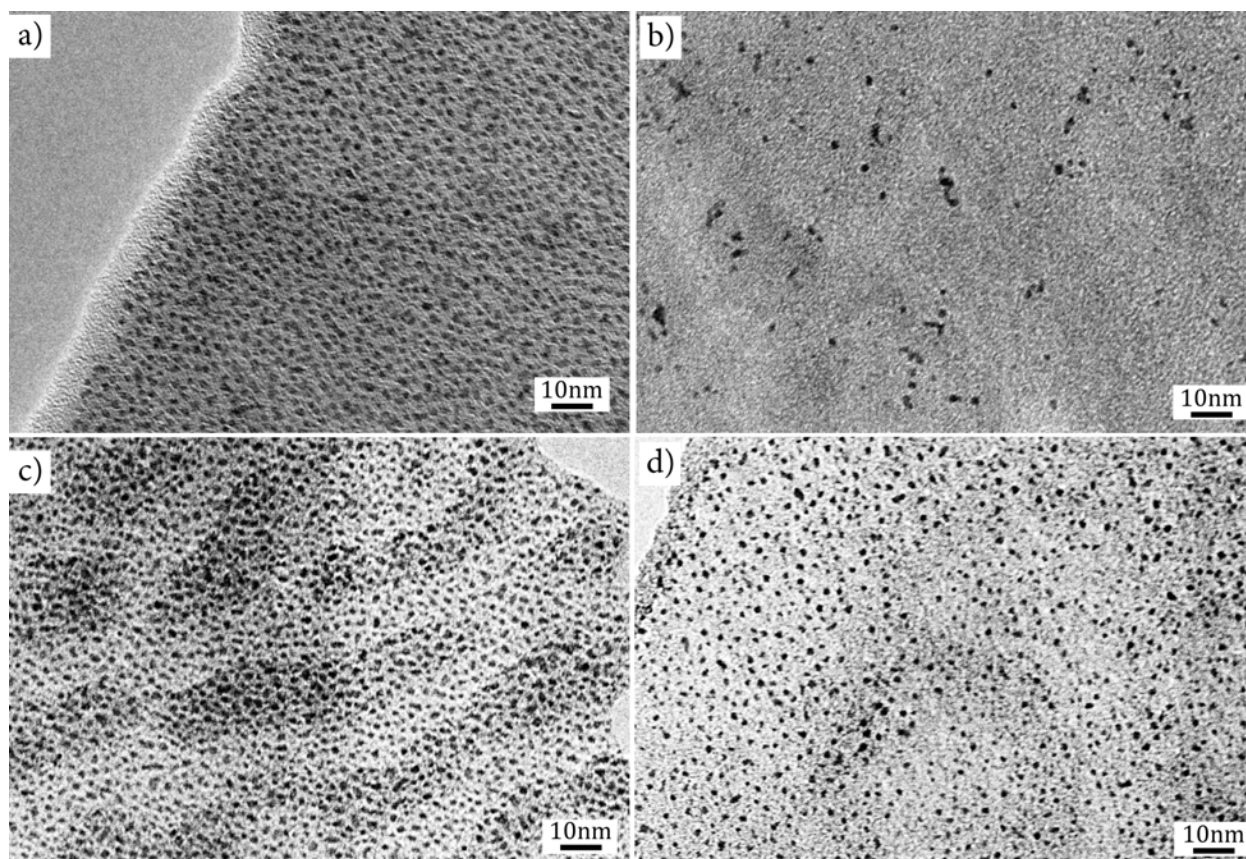


Figure 6.4: TEM images of pre- and post-cycled low and high-dose iodine modified samples. a) low dose I-modified, pre-cycled b) low dose I-modified, post-cycled c) high-dose I-modified, pre-cycled d) high-dose I-modified, post-cycled

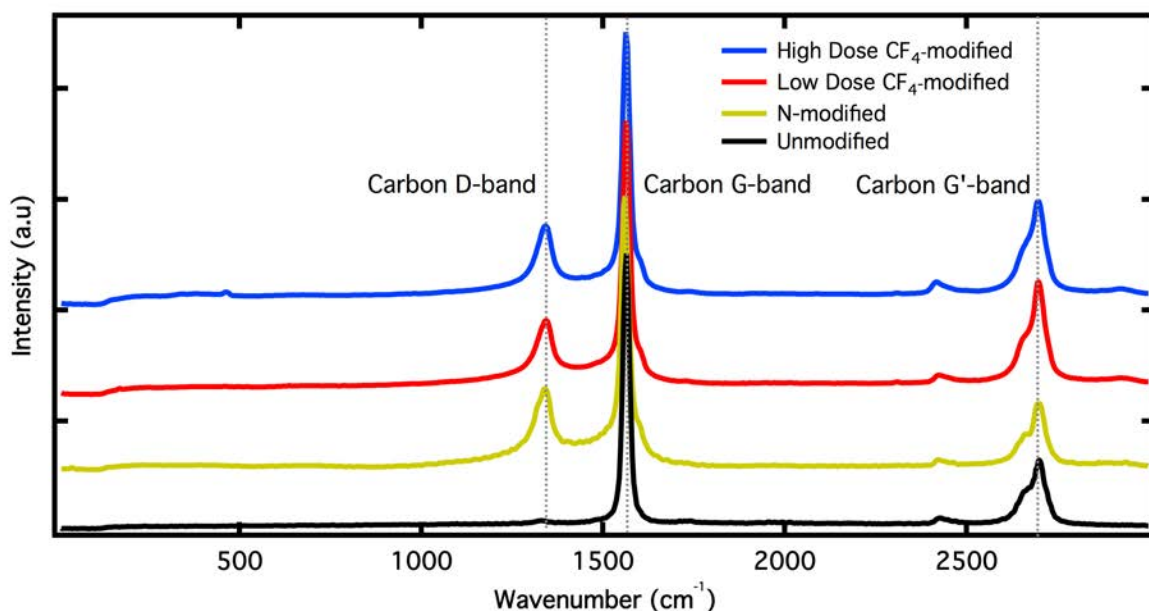


Figure 6.5: Raman spectra of CF_4 modified HOPG samples compared to unmodified and N-modified reference samples.

between the N-modified sample and the CF_4 modified samples at either dose.

Figure 6.6 shows XPS spectra for both CF_4 modified samples against unmodified and N-modified reference samples. These spectra illustrate significant differences between the N-modified and high-dose CF_4 modified sample resulting from incorporation of fluorine. Incorporation of fluorine into graphitic carbon is supported by observations of C-F species at BE 288-290 eV, and C*-C-F species at BE 285-286 eV. Equally significant is the fact that peaks above BE 291 eV, which correspond to fragmented precursor species such as CF_3 and CF_2 , are not observed. In addition, along with fluorine incorporation, CF_4 -modified samples also showed significant incorporation of nitrogen. XPS analysis indicated ~ 2 at.% and ~ 8 at.% nitrogen in the low and high-dose CF_4 modified samples, respectively. The increase in nitrogen concentration and C-N species at 286 eV appears to be dose-dependent.

TEM images for the low and high-dose CF_4 modified pre and post-cycled samples are shown in Figure 6.7. The micrograph for the post-cycled lower dose CF_4 modified sample (Figure 6.7b) shows a significant reduction in the frequency and size of agglomerates when

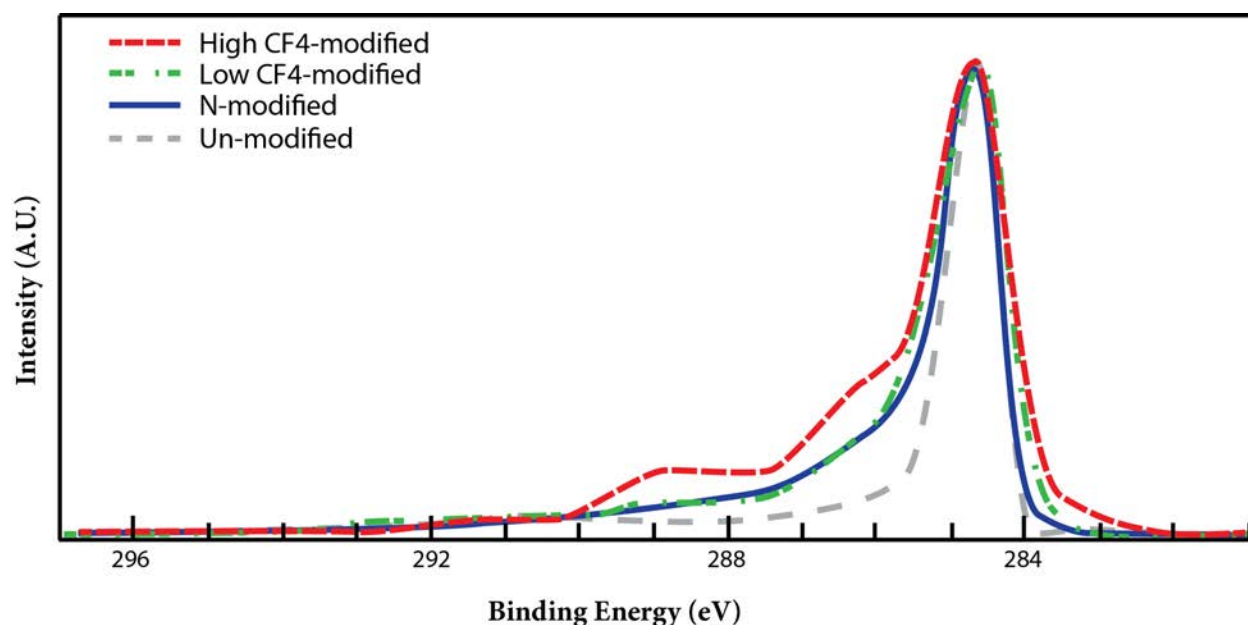


Figure 6.6: High-resolution C 1s XPS spectra of CF_4 modified HOPG samples compared to unmodified and N-modified reference samples.

compared with the unmodified and lower dose I-modified samples, but a substantial loss of catalyst coverage when compared with the N-modified sample. Similar to the iodine-modification, fluorine modification at higher dose also yielded an enhancement in durability, as demonstrated by improved retention of both catalyst particle size and coverage (Figure 6.7d). These results show that the high-dose CF_4 modified sample actually outperforms the N-modified samples. The best results obtained with optimized N-modified samples have previously showed reduction in coverage $\sim 60\%$ and decrease in the particle size $\sim 0.4\text{nm}$. By comparison, the presence of fluorine functionalities included with nitrogen moieties showed dramatic improvement over the N-modified results, minimizing coverage loss to $\sim 20\%$ and retaining the particle size to within approximately $\sim 0.2\text{ nm}$ of the pre-cycled value.

6.2.3 Support Modification with Fluorine and Nitrogen

In light of the finding that along with fluorine incorporation, CF_4 modification resulted in incorporation of significant amounts of nitrogen, a further set of experiments utilizing intentional mixing of relative amounts of nitrogen and fluorine precursors (N_2 and CF_4) was

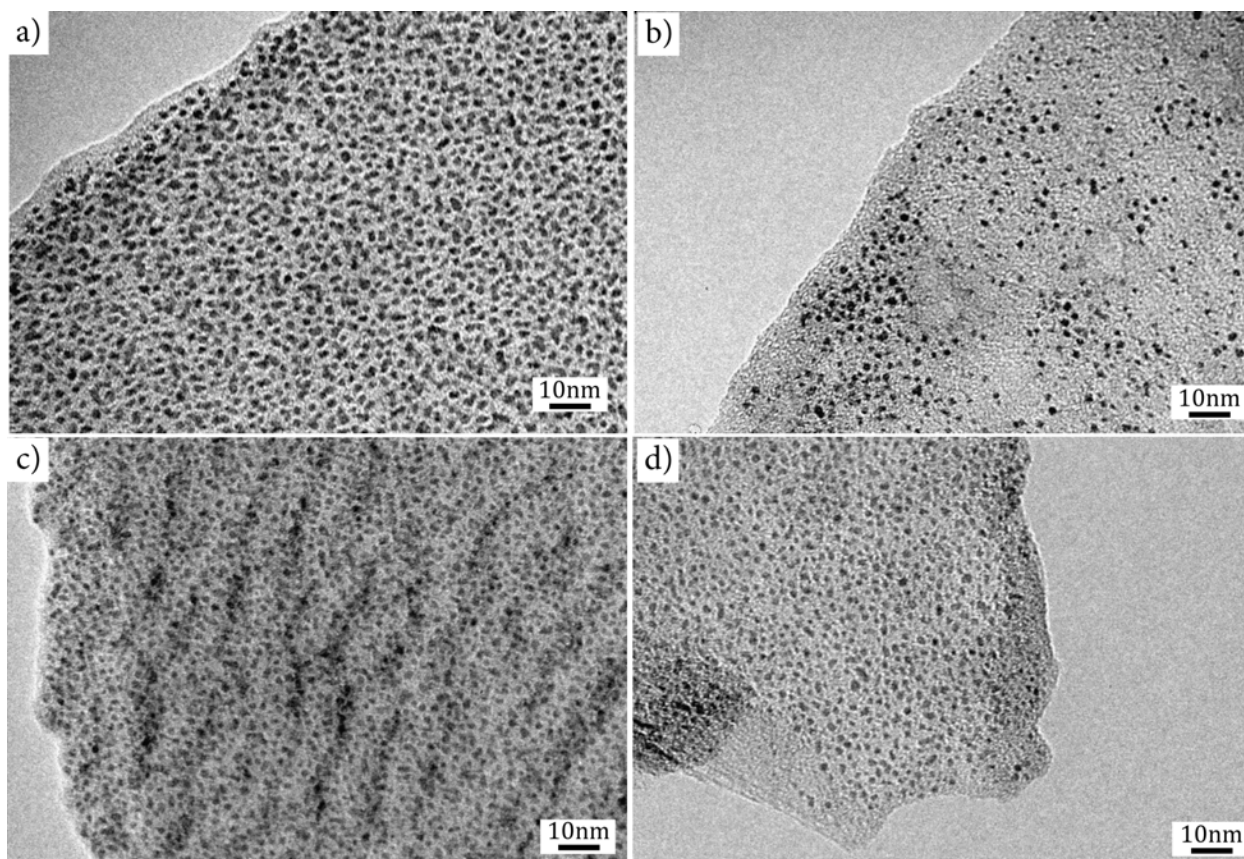


Figure 6.7: TEM images of the pre- and post-cycled low and high-dose CF_4 -modified samples. a) low dose, pre-cycled b) low dose, post-cycled c) high-dose, pre-cycled d) high-dose, post-cycled.

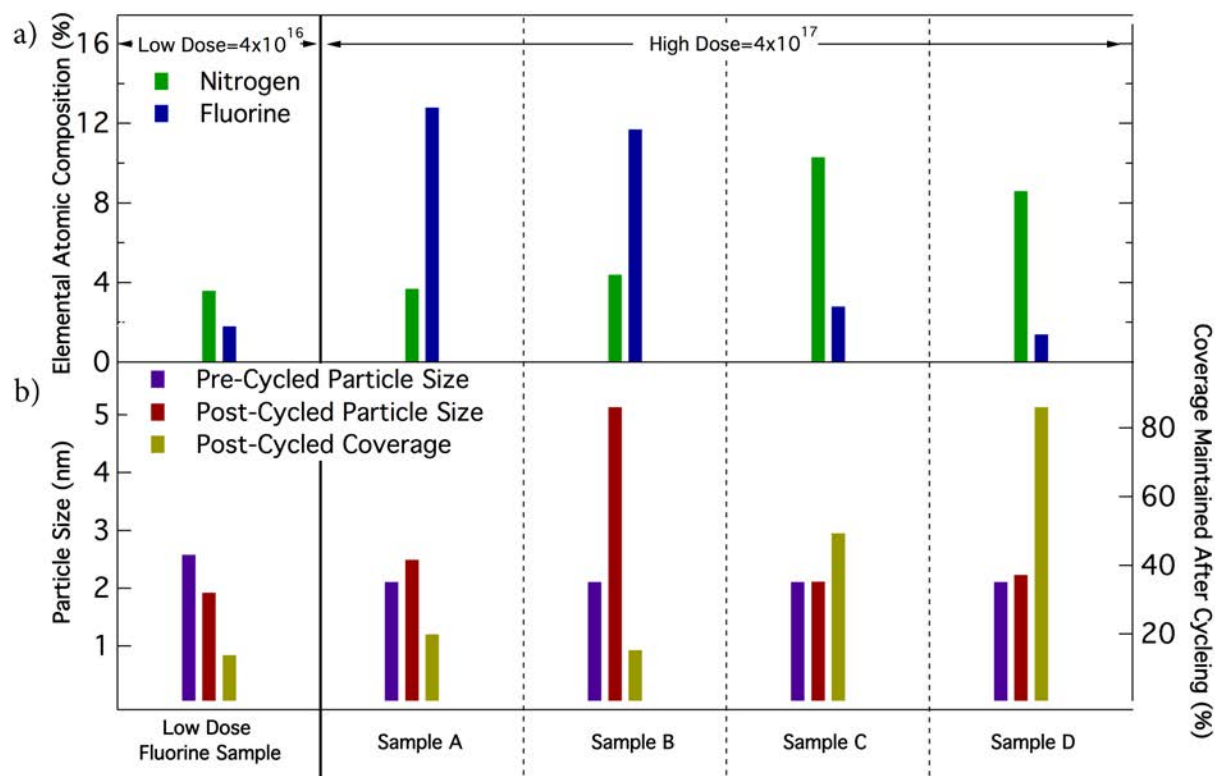


Figure 6.8: Characterization of co-implanted samples with varying ratios of nitrogen vs. fluorine concentrations a) XPS elemental composition, b) average particle size obtained from analysis of TEM micrographs

used to understand the relative importance of the contributions from nitrogen vs. fluorine on the catalyst stability. Figure 6.8a shows the elemental composition of a series of HOPG samples functionalized with fluorine and nitrogen. For reference, the samples are labeled a-d, where the sample with the most fluorine is labeled as “a” and the lowest as “d”. Figure 6.9 compares C1s spectra from this set of samples to that of the solely N-doped reference sample.

Comparing C1s spectra of co-implanted sample a vs. the N-modified reference sample, we see pronounced peaks at approx. 288, 290.5 and 293 eV, caused by carbon species bound to one, two and three fluorine atoms, respectively. CF_2 and CF_3 species are most likely fragments of precursor that adsorbed on the surface. Sample b, although containing slightly less fluorine, also exhibits a similar, slightly less defined shoulder in the binding energy range 287-295 eV. This result again indicates associatively adsorbed precursor fragments, but in a

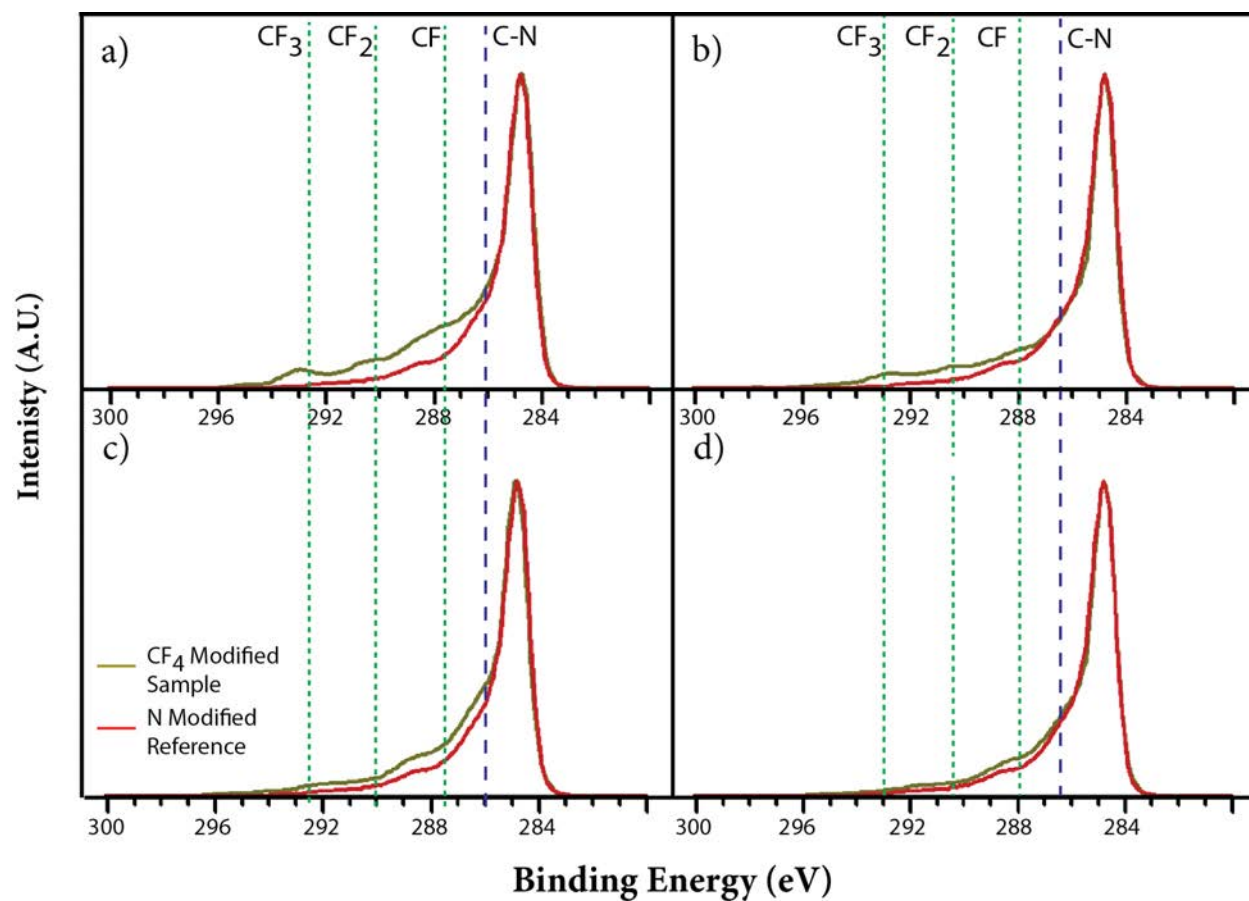


Figure 6.9: High-resolution C 1s XPS spectra of co-implanted samples a-d compared compared N-modified reference samples.

smaller concentration than observed for sample a. Representative TEM images of the post-cycled catalyst morphology for the four co-doped samples are provided in Figure 6.10. After cycling, samples with the highest fluorine content and lowest nitrogen content (a and b) suffer significant particle coverage loss along with evidence of particle aggregation. We attribute this poor stability performance to the presence of precursor fragments loosely attached to the surface (associative adsorption).

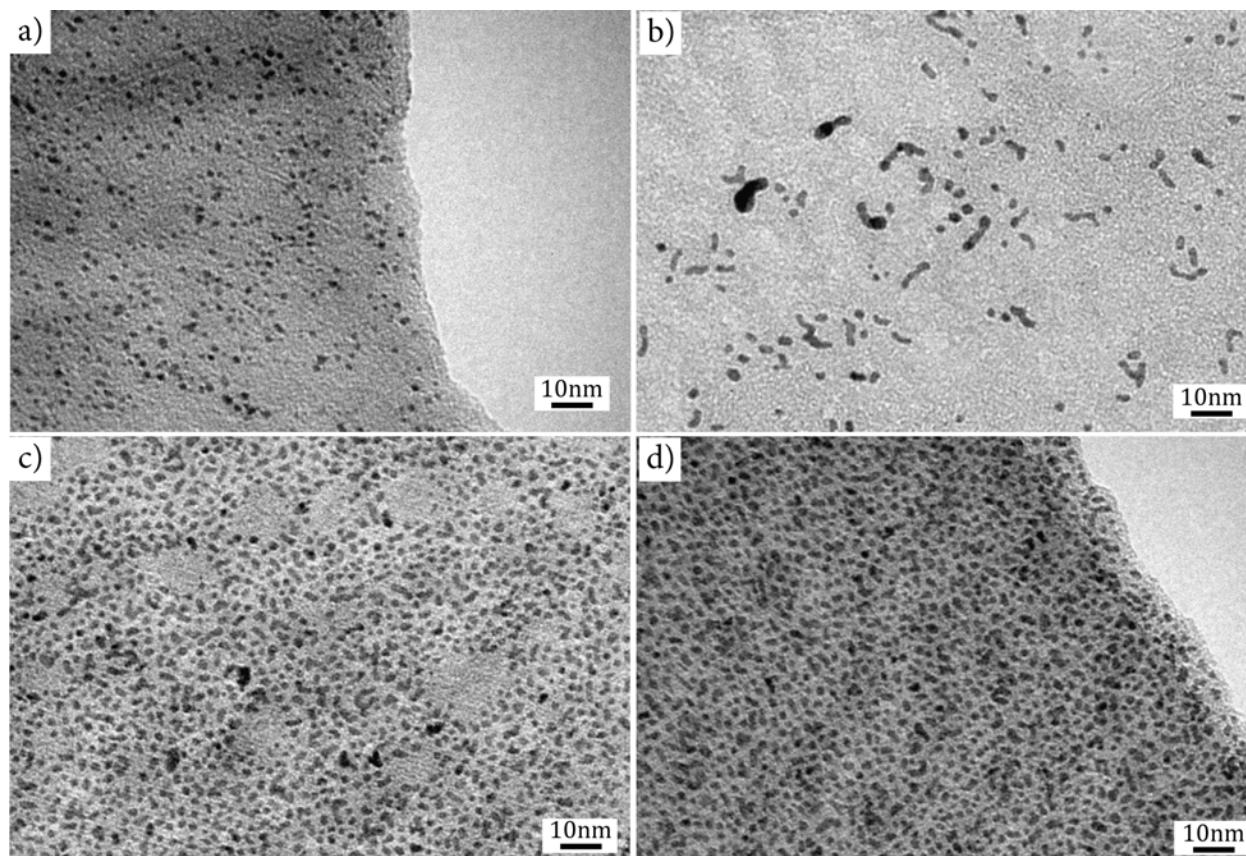


Figure 6.10: TEM images of post-cycled co-implanted HOPG samples a) 13% fluorine, 4% nitrogen, Sample b) 11.5% fluorine, 4.5% nitrogen, Sample c) 3% fluorine, 10.5% nitrogen, Sample d) 1.5% fluorine, 8.5% nitrogen

Sample c (Figure 6.9) showed a significant decrease in fluorine content ($\sim 3\text{at.}\%$) compared to samples a and b and an increase in nitrogen content to $\sim 10.5\text{at.}\%$, which is higher than the nitrogen concentration in the N-modified reference sample. The C1s XPS spectrum of sample C shows an increase in the amount of C-N species at BE 286 eV when compared with the

nitrogen baseline. Additionally, we see a significant increase in the amount of species around BEs of 288-290eV indicating presence of C-F bonds. TEM micrographs of post-cycled sample c (Figure 6.10c) reveal inconsistent behavior, where some areas manifest excellent durability (good coverage and consistent particle size) while other areas suffer significant coverage loss (albeit without much change in particle size or particle morphology). Sample d shows a chemical composition closest to the previously discussed high-dose CF₄ modified sample; nitrogen approx. 8.5 at.% and fluorine ~1.5 at.%. Comparing the C1s XPS spectrum to that of the best performing N-modified sample, we see a slight increase in C-F species (~288 eV) and a similar concentration of C-N species (~286 eV). Most notably, however, fragmented precursor species, such as CF₂ and CF₃ are not observed. Analysis of the TEM micrograph of the post-cycled sample d (Figure 6.10d) confirms that elimination of the of precursor fragments associatively bonded to the surface, while still providing direct incorporation of fluorine and nitrogen functionalities into the graphitic network. A comparison of Figure 6.10d vs. Figure 6.1d clearly reveals the improved coverage and particle stability of this co-doped sample surpasses the positive effects of nitrogen doping by itself.

Nitrogen dopants in carbon have been shown to have an electron-withdrawing nature that is hypothesized to improve the strength of metal carbon interactions and act as a trapping state that helps prevent catalyst migration[48]. It is most likely that the role of nitrogen in the co-implanted systems is same as in N-implanted systems. Fluorine cannot be directly incorporated into the ring structure of the carbon support and therefore cannot act as a trapping site. Addition of fluorine to the support however, may stabilize catalyst particle size by decreasing the dissolution of the metal phase more significantly than by nitrogen modification alone due to the strong electronegative character of fluorine. Complicating the incorporation of active fluorine species into the catalyst support system is the fact that high precursor concentrations of CF₄ are difficult to completely ionize, leading to large amounts of associative bonding and catalyst detachment (as observed in our highly concentrated fluorine samples). However, the combined fluorine/nitrogen studies suggest that if the correct ratio

of nitrogen and fluorine is incorporated into the support, associatively bound C-F precursor species can be eliminated and the resulting catalyst stabilization effects are significant.

6.3 Conclusions

The results shown above demonstrate the potential to tune catalyst/support interactions using carbon support structures modified with halide functionalization. It was shown that iodine modification improves catalyst durability compared to unmodified structures. This improvement was associated with the presence of polyiodide species, and minimal C-I interactions. In the nitrogen/fluorine system both C-F and C-N bonds are formed, the electronic properties of fluorine improve resistance to metal dissolution while the nitrogen sites mitigate migration and coalescence through incorporation into the carbon ring structure. This co-incorporation of nitrogen and fluorine appears to have the potential to improve the interactions between the carbon support and the overlying metal nanoparticles, beyond the effects observed for just nitrogen, as long as the heteroatoms are incorporated into the support and the surface remains free from precursor fragments. The results presented in the work provide a framework for the selection of catalyst/support functionalization and offer new directions for fuel cell electrocatalyst optimization in order to reach DOE targets for durability and reliability.

CHAPTER 7

CONCLUSIONS

Current state-of-the-art fuel cell systems utilize a catalyst layer supported on high surface area carbon architectures. The durability and lifetime of this layer is essential as it provides a place for the electrochemical reaction to occur as well as electron conduction and proton diffusion. As we have seen throughout this thesis, the performance and durability of this layer can be greatly enhanced through the use of support functionalization. To better understand the mechanisms and effects of functionalization I have collaborated with many scientists and institutions to pursue novel research that probes the fundamental effects of a variety of functionalities, with the an emphasis on nitrogen dopants.

In chapter 3, nitrogen-ion implantation of high surface area carbon supports yielded superior Pt-Ru catalyst particle stability and performance as compared to industry standards. Specifically, these results showed an improvement of electrochemical activity and the number of Ru metal catalyst sites after accelerated electrochemical degradation testing. Through detailed characterization techniques, it was shown that ADT testing of nitrogen modified systems did not lead to the emergence of a new particle size regime or crystalline phase, suggesting that dissolution and migration were mitigated. Additionally, it was observed that the initial Ru phases were different for the nitrogen modified sample, which could be attributed to the improved kick-off potential after cycling.

This study was then expanded in chapter 4 to show the improvement capabilities of after-the-fact nitrogen modification of commercially available catalyst systems. In these post-modified samples, nitrogen heteroatoms were expected to be incorporated only into the carbon regions unshielded by nanoparticles without altering the carbon structure directly under the nanoparticles themselves (due to shadowing during implantation). After implantation these materials again, showed a shift in Ru phase composition as well as an

increase in surface area, leading to initially enhanced performance. For studies conducted in acid media, the accelerated degradation testing procedure revealed the nitrogen modified samples maintained the increased surface area initially observed, however Ru dissolution occurred unlike the results in chapter 3. Similar testing of these post modified materials in alkaline media demonstrated that nitrogen-modified materials significantly enhance the catalytic performance of PtRu systems and changed the degradation mechanisms by preventing Ru dissolution.

In chapter 5 graphene functionalization with nitrogen was also investigated as a novel support structure due to its interesting properties (ie. high conductivity, high corrosion resistance). The preliminary results showed improvement in performance of the nitrogen-doped samples per metal loading before and after cycling, with the greatest enhancement being observed after cycling. Further studies on this PtRu catalyst system could lead toward commercialization of fuel cell systems.

The final chapter of this thesis explored alternative dopants/functionalizations. These studies utilized model substrates to show that both fluorine and iodine have the potential to enhance durability. By combining nitrogen and fluorine functionalities, it was shown that these novel systems retain a significantly greater percentage of the initial particle size when compared to nitrogen modified materials without fluorine. Iodine showed a slight enhancement in durability and has been shown to improve electrocatalytic activity in ORR studies. These results show that in addition to nitrogen, other functionalities also have the potential to improve durability in real systems and future work in this area could provide a functionalization scheme similar to that observed with nitrogen.

Combining the results from the different sections of this thesis we can see that nitrogen has many benefits on improving electrochemical surface area and performance after an accelerated degradation testing procedure.

7.1 Improved Active Site Retention

Through out this culmination of studies it has been shown that heteroatoms can improve the durability of methanol oxidation reaction electrocatalysts. Specifically chapters 3, 4, and 6 have shown that improved catalyst support interactions lead to improved catalytic nanoparticle surface areas in DMFC systems. Comparing the results from the ‘in house’ nitrogen modified materials (chapter 3) to those of the post-doped system (chapter 4) we can glean further understanding into the way nitrogen improves durability. In systems fabricated ‘in-house’ it appears that nitrogen atoms beneath the metal sites improve resistance to Ru dissolution more effectively than systems where nitrogen was limited to sites around pre-existing catalytic nanoparticles, i.e. post-modification (see Figure 7.1). These studies, completed in acid media, indicate the possibility of in-house catalyst samples forming nitrogen-metal coordinated sites that lead to a reduction in Ru dissolution. Further studies, utilizing near edge x-ray adsorption fine structure spectroscopy (NEXAFS), that I have completed (not presented in this thesis) indicate that nitrilic species could be present in the in-house samples. These types of species have been known to have an affinity for metallic interactions. As can be seen in Figure 7.1, the more negative onset potential of in-house catalysts indicates an enhancement of Ru retention, however both samples result in improved durability when compared to their unmodified counterpart. These results suggest that clustered nitrogen defects (i.e. pyridinic type) appear to prevent migration by acting as a trapping state, while other functionalities, specifically those under metallic sites, might be attributed to a reduction in metal dissolution.

In the latter part of Chapter 4 the effect of the electrolyte solution was discussed. It was shown that the Ru stability of post-modified samples was greatly increased by testing in alkaline solutions, Figure 7.2. The results indicate one of two possibilities for the enhancement in durability. 1) the nitrogen sites act as a location for OH adsorption (the main function of the Ru site), this could occur in alkaline solutions more effectively than acidic ones, because of the accessibility of OH groups in alkaline environments. 2) the improvement in Ru

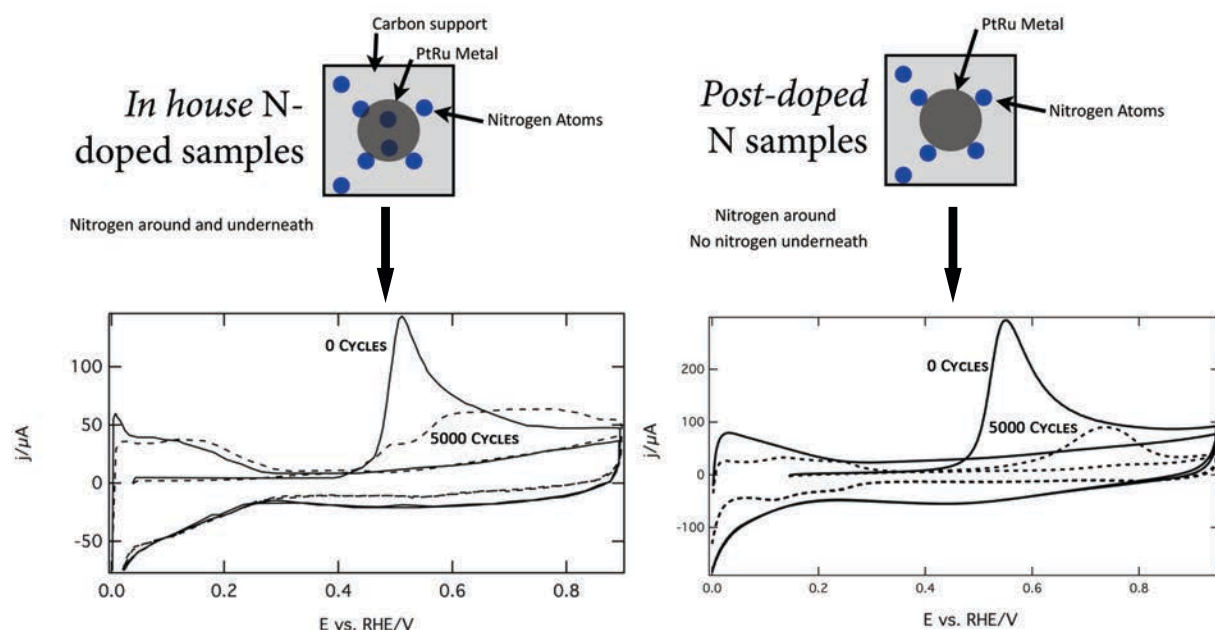


Figure 7.1: A schematic showing the differences between in-house modified catalysts and post doped catalysts. The In-house catalyst helps maintain Ru while post-modified catalyst loses Ru, this can be seen in the CO stripping results presented below the pictorial representation.

retention could be related to the enhanced binding of catalyst to the support in combination with the more benign environment of alkaline solutions. This means that the increase in energetic attraction of metal to the support requires a driving force greater than what is applied through durability testing in alkaline media. Along with the fact that alkaline based fuel cells allow for inexpensive ORR catalyst materials and nitrogen modification can greatly improve anode electrocatalysts, this type of environment appears to have great promise.

In chapter 6 it was also discussed that the addition of fluorine sites combined with nitrogen can provide a synergistic effect. Similar to the in-house samples discussed in chapter 3, the incorporation of the fluorine and nitrogen is likely beneath the metal sites. It is also likely that the increased electron-withdrawing nature of the fluorine atoms, which replace the carbon sites in the graphitic network, create an effectively positive charge on the carbon atoms neighboring the fluorine. This increases the bonding strength between the now positive carbon site and the negative platinum atoms. In a similar manner, migration could be prevented in these systems due to the unfavorable possibility of a negative Pt atom

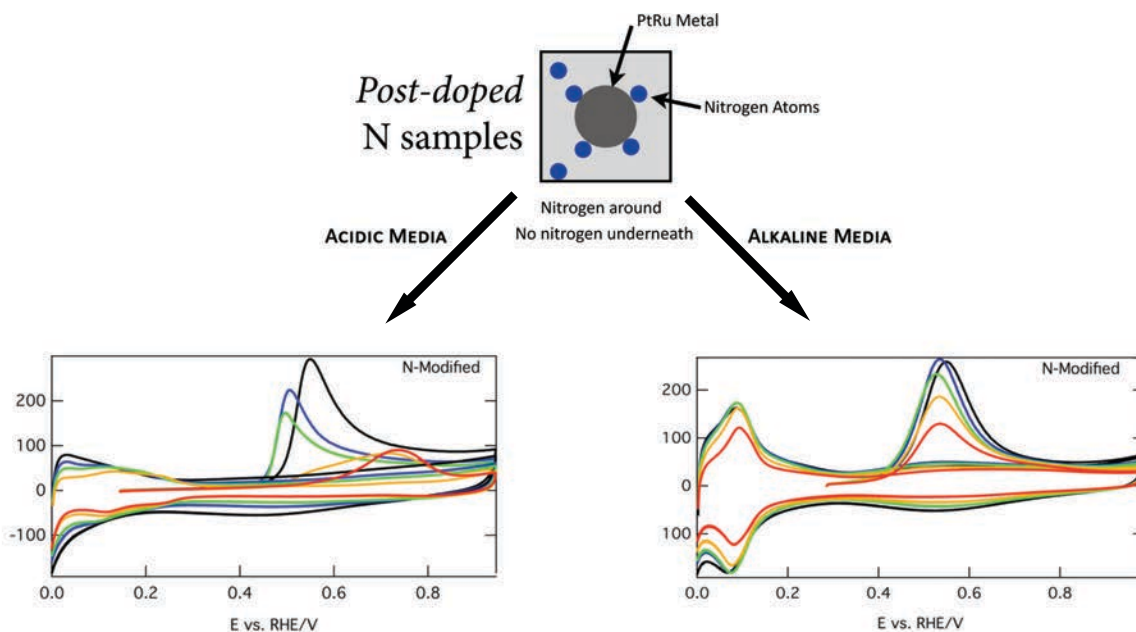


Figure 7.2: The effect of acid and alkaline media on the nitrogen post-modified commercial catalyst. The CO stripping results show the Ru retention associated with ADT testing done in alkaline media

migrating over an electron rich fluorine site, Figure 7.3. These hypotheses still need extensive testing as there are other mechanisms possible, which could be more unfavorable. One such possibility is that fluorine changes the hydrophobicity of the surface, preventing the aqueous electrolyte from interacting with the electro-active catalyst species. This possibility would lead to the significantly improved durability of nanoparticles, but is also likely to lead to a significant loss of electrochemical oxidation efficiency.

7.2 Retention of Most Active Catalyst Phases

It was also shown in chapters 4 and 5 that nitrogen helps retain the most active catalyst phases. In chapter 4 the methanol oxidation performance in nitrogen modified samples was greater after cycling when normalized per electrochemically active surface area. This indicates that even though the surface area was higher than before durability testing, the amount of current generated per cm^2 increased. This was not the case for the unmodified commercial catalyst. Ultimately, the amount of active surface area present in these samples

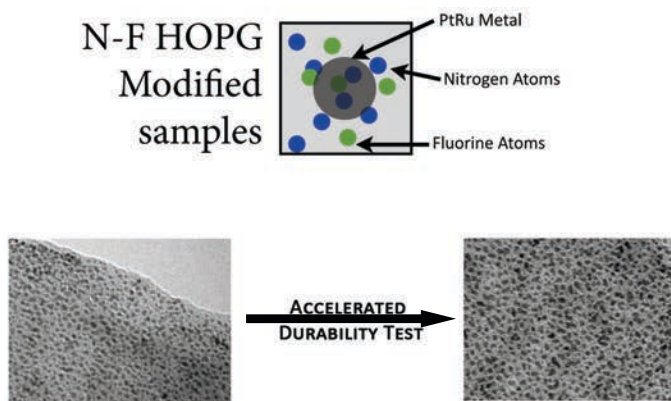


Figure 7.3: The synergistic effect of nitrogen and fluorine on PtRu nanoparticle durability.

is only part of the most important kinetic metric, the exchange current density. Therefore, other parameters which effect the exchange current density may be enhanced by the addition of nitrogen, mainly the activation barrier of the reaction (although the symmetry factor of the reaction could also be effected, which would improve overpotential losses). This means that nitrogen either reduces the activation barrier of the reaction by participating in the reaction, or nitrogen modified supports maintain catalyst phases which allow the reaction to proceed with a smaller activation barrier. Since the results in both chapters 4 and 5 show limited improvements in initial oxidation performances normalized per electrochemically active surface area, the latter mechanism is more likely. It is worth mentioning that this effect was observed for samples in which nitrogen is likely located beneath metal sites (chapter 5) and samples where nitrogen is limited to areas surrounding the metal phases (chapter 4), see Figure 7.4.

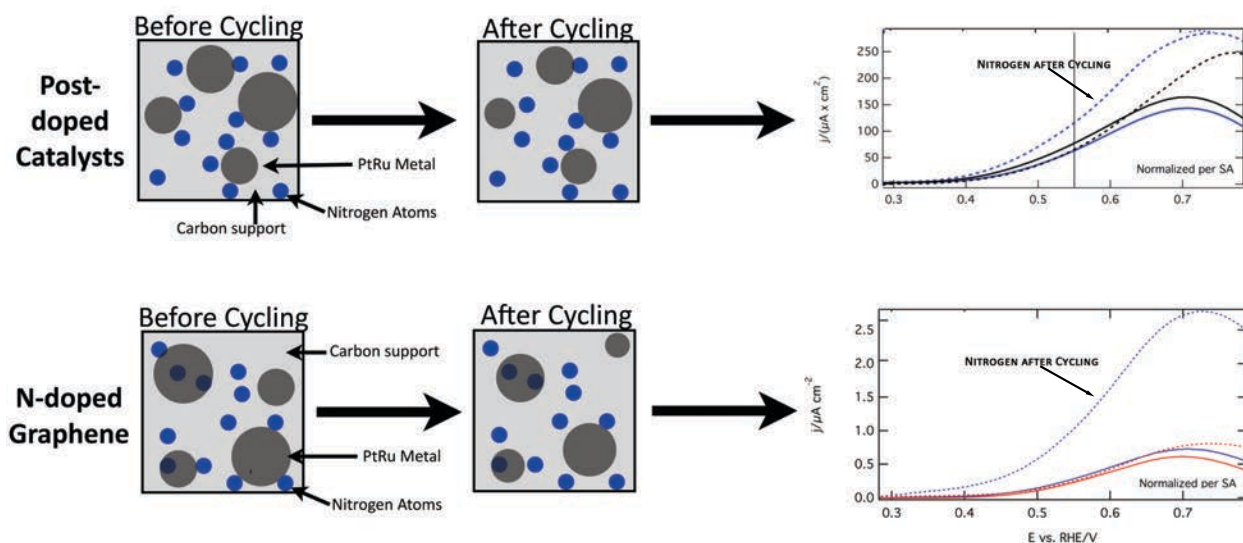


Figure 7.4: A schematic representation of the effect of nitrogen on helping maintain the most active catalyst phases. After electrochemical cycling nitrogen modified samples have greater methanol performance per electrochemically active surface area.

7.3 Future Directions

Due to complexity of the modified carbon systems, the reasons for some of the effects discussed in this these are still not understood. As over 800 papers have been published in the field of just nitrogen modified carbon structures in the last 5 years, this is not an easy task and new creative approaches must continue to be developed to help the scientific community's understanding. More in-depth characterization studies are needed to help confirm the effects of specific functional groups. In a similar vein the design of material fabrication techniques that create isolated functional groups will help conclusively show the effect of these functionalities on catalytic activity and durability. More specifically however, this thesis has raised several questions that remain to be answered:

- How does nitrogen underneath the metal site improve the Ru retention? What functionalities are present (nitrilic)? Some of these questions are currently being addressed through the careful correlation of NEXAFS and XPS. More DFT studies investigating

the dissolution of Ru are also needed to better understand this complex effect.

- How does nitrogen post-modification in alkaline media prevent Ru dissolution? Is this because nitrogen participates in the reaction or because of nitrogens enhanced binding effect? Studies could look at this effect through studying Pt/C, Pt/C-N, PtRu/C and PtRu/C-N in an alkaline solution to look at the effect of poisoning and Ru dissolution. Alkaline media is also of key interest in future studies because of low cost ceramic ORR catalysts which degrade in acidic solutions. Therefore, understanding and improving anodic alkaline reactions is in demand.
- Can the PtRu metal loadings of graphene based catalyst systems be increased? What strategies can prevent clumping? Studies investigating a templated graphene structure are currently underway.
- How does fluorine improve the durability of these systems? Is nitrogen essential or are there specific fluorine groups that enhance durability without the presents of nitrogen? In previous HOPG studies it appeared that nitrogen reached a saturation limit, however through co-implantation nitrogen incorporation reached greater levels than previously observed. Therefore is the increase in nitrogen content the reason for enhanced durability? If a fluorinated catalyst support is used, will the hydrophobic nature of such a support prevent the fuel from being catalyzed effectively? Some of these questions could be answered by investigating the effect on a high surface area system, however fabrication challenges make this task more complicated than it sounds.
- What is the future of iodine modification? While some studies have indicated that iodine is good for ORR reactions and tolerant toward methanol, the improved durability observed in anodic durability testing requires future high surface area studies.

All of these questions will require more detailed studies than those presented herein and would be highly beneficial for the community. As heteroatom modification of carbon

continues to expand into a wider breadth of applications, a more complete and deeper understanding of these material effects will be developed. The potential benefit of understanding heteroatom functionalization of carbon architectures as it relates to fuel cells is likely a key component in their commercialization. The utility of surface functionalization does not stop there however, as nearly every renewable energy application has a component, which can be enhanced through heteroatom modification.

APPENDIX A - RECENT PROGRESS ON NITROGEN/CARBON STRUCTURES DESIGNED FOR USE IN ENERGY AND SUSTAINABILITY APPLICATIONS

An invited review paper published in *Energy and Environmental Science*

Kevin N. Wood^{*,1}, Ryan O’Hyare¹, Svitlana Pylypenko^{†,1}

Abstract: Heteroatom modification represents one of the largest studied areas of research related to nanostructured carbon materials, with integrated applications stretching from energy production and storage to sustainability and medical uses. While a wide variety of dopants (boron, phosphorus, iodine, fluorine, etc.) have been studied, doping carbon structures with nitrogen ad-atoms has arguably experienced the greatest progress and brought the most attention over the last several years. Research in this field has conclusively demonstrated that nitrogen doping is an effective way to tailor the properties of carbon and tune the material for various applications of interest. This review provides a comprehensive overview of advances in the last 5 years on state-of-the-art carbon modification with nitrogen heteroatoms. Improvements in well-established fabrication/modification processes are discussed as well as novel strategies. Additionally, recent theoretical and experimental findings related to the benefits and effects of nitrogen medication for specific applications in the energy and environmental fields are reviewed.

A.1 Introduction

Carbon remains one of the most attractive and well-studied materials systems in the scientific community due to its amazing variety and versatility in combination with low cost, availability, and wide ranging properties[117–121]. The physical, chemical, optical

*Primary author and editor. Direct correspondence to kevin.n.wood@gmail.com.

†Corresponding author. Email: Spylypen@mines.edu.

¹Department of Metallurgical & Materials Engineering, Colorado School of Mines, 1500 Illinois Street, Golden, Colorado 80401, United States

and electronic properties of carbon, varies according to its allotropic form and also greatly depends on its structure, morphology and surface composition. High surface area carbon materials have been extensively used for sorption, sensing, photovoltaic, catalysis and storage applications. In many catalytic and hydrogen-storage applications, carbon materials are also used as supports to facilitate dispersion of noble and non-noble catalysts. Among the various carbon materials, carbon blacks and activated carbons are the most traditional, with various nanostructured carbons such as graphene, fibers, nanotubes, and mesoporous morphologies emerging in recent decades. Functionalization of carbon-based materials can modify their surface, interfacial, and electronic properties, thereby further increasing their utility across a wide range of applications.

Among possible chemical choices for carbon modification, nitrogen functionalization has long been a natural and widely studied option. Nitrogen-containing carbon structures have attracted great attention in large part because of their abundance, accessibility, and low health risk. As far back as the early 1800's nitrated carbon structures in various polymorphs were extensively examined for their thermal conductivity, low compressibility, and high strength[122–124]. In more recent years, the study of carbon and nitrogen has expanded into the sub-stoichiometric regime of nitrogen-modified carbons. This modification allows for the beneficial properties of the carbon to be utilized while finely tuning the final electrical, morphological, and chemical properties of the functionalized carbon network.

Nitrogen is the natural choice for efficient and beneficial modification due to three specific reasons. Firstly, N is one neighbor away from C on the periodic table and by replacing one C with N in the carbon network the total number electrons in the system can be tailored one electron at a time. Secondly, N has an atomic radius similar to that of C, thereby preventing significant lattice mismatch. Thirdly, N-doping can induce an n-type electronic modification to the carbon structure, in analogy to typical semiconducting materials, which enables the potential use of these C-N structures in multiple important nanoelectronic applications.

Due to the width and breadth of this field, it is almost impossible to fully review and cover all aspects of study. As such, in this review we try focusing on the work done within the last 5 years (2009-2013). Starting from a foundational review of recent findings on the synthesis, characterization, and theory of nitrogen modified carbon materials; we then focus primarily on the use of these materials in energy conversion, storage, and sustainability applications.

A.2 Materials

Increasingly sophisticated requirements for sustainability and energy applications drive the need for new inexpensive and environmentally friendly materials. To this end, researchers have increasingly pursued nitrogen modification of many types of well-studied carbon nanostructures in addition to “from-scratch” fabrication of entirely new types of C-N structures. In this section, we review the recent work on N-modification of graphene, carbon nanotubes (CNT’s), porous carbon structures, and carbon nitride as well as novel covalent-triazine frameworks, carbon nanospheres, and onion-like C-N structures. To start the discussion, Figure 2.4 shows the various functionalities referred to throughout this manuscript.

A.2.1 Graphene

Graphene is a single sheet of carbon atoms arranged in a hexagonal lattice. Due to its many unique physical and electronic properties, it has been dubbed by many as a ‘dream material’. Since the first report of its synthesis via the “Scotch tape” [113] method in 2004, the field of graphene research has witnessed extraordinary activity. While pure graphene by itself has many intrinsic benefits, chemical doping provides an important route to further tailor its properties for specific applications. Typically, there are two main approaches to chemically dope graphene: 1) the adsorption of gas, metal, or organic molecules onto the graphene surface and/or 2) substitutional doping, which introduces heteroatoms into the graphene lattice. In the context of nitrogen modification, both of these methods can modulate the electronic properties of graphene and they typically result in the combination of three common bonding configurations within the carbon lattice; graphitic N, pyridinic N,

and pyrrolic N[39] (Figure 2.4).

N-modified graphene shows different properties compared with pristine graphene. For instance, the spin density and charge distribution of the carbon atoms will be influenced by neighboring nitrogen dopants[35]. This charge localization can help participate in catalytic reactions directly, as in the ORR, or can help tether metal nanoparticles to the graphene support [114]. Furthermore, monolayer DFT studies reveal that nitrogen doping suppresses the density of states near the Fermi level and shifts the Fermi level above the Dirac point[125, 126]. This increases the band gap of graphene making it feasible for n-type semiconducting applications. Additionally, N-graphene also has beneficial properties for use in batteries, sensors, and supercapacitors, furthering its appeal across research disciplines[39].

Graphene can be nitrogen modified through two primary methods: 1) direct synthesis or 2) post-treatment. In principle, direct synthesis strategies have the potential to induce homogeneous modification throughout the entirety of the material, however current efforts have not conclusively demonstrated this potential. The major direct N-graphene synthesis routes include chemical vapor deposition, solvothermal fabrication, layer separation growth, and arc-discharge. While these direct synthesis methods have shown success (particularly direct CVD synthesized N-graphene), post-treatment nitrogen modification methods, which include bombardment, thermal annealing, or solution treatment are more widely used. In comparison to direct synthesis methods, post treatment methods generally lead only to surface doping, leaving the interior (bulk) of the treated carbon material unchanged.

A.2.1.1 Direct Synthesis

Chemical vapor deposition (CVD) has been used for decades to synthesize a variety of carbon structures[31, 34, 35, 37]. Recently, a number of CVD variations have been explored to prepare N-graphene. In several instances, liquid organic molecules have been used as graphene precursors, however this process requires careful choice of the precursor structure. Even if nitrogen moieties are included in the liquid, only double bonded C=N species lead to the formation of N-graphene. Because of this issue, liquid pyridine has proven to be the

most favorable liquid organic for creating nitrogen functionalized graphene. Alternatively, gas mixtures can also be used to create both pristine and N-modified graphene. In these processes, a simple hydrocarbon (i.e. CH_4) is used as the carbon source, while ammonia is typically used as the nitrogen source. Importantly, the graphene doping level can be controlled through flow rate adjustments and gas precursor ratios. Using this technique N concentration levels can be controlled between 1-9 at% (See Figure A.1a).[31, 35–37, 40, 127] However, CVD processes can be relatively expensive and difficult to scale. The wide range of potential applications has therefore motivated the exploration of more facile techniques that have the ability to scale easily and create large volumes of material.

Solvothermal processing is potentially one such approach. Although it has been less extensively investigated, it has several attractive advantages including a simple operation method, mild synthesis conditions, and the capability to deliver relatively large quantities of N-graphene[128]. Deng et al. demonstrated this novel technique based on the reaction of tetrachloromethane with lithium nitride below 350°C . This reaction allows for gram-scale production and synthesis can be easily scaled for commercial use. Their results suggest that nitrogen moieties can be successfully incorporated into the graphene structure using this approach with contents ranging from 4.5-16.4% nitrogen[129].

Most N-graphene fabrication techniques create multi-layer (6+ layers) rather than monolayer or few-layer graphene. However, in certain applications it may be beneficial to synthesize graphene in monolayer or 2-3 layer form[131]. This is hard to accomplish because reducing the number of layers tends to increase the thermodynamic driving force for transformation to other carbon allotropes such as carbon nanotubes (CNT's). Recently, however, Panchakarla et al. demonstrated that an arc discharge between two carbon electrodes in a hydrogen environment creates 2-3 layers of graphene without forming CNT's[131]. Furthermore, this process can be exploited to create N-modified graphene if the arc is deployed in a hydrogen atmosphere containing either ammonia or pyridine[131, 132]. Materials fabricated from this method contain less than 1.5 % nitrogen, but XPS results indicate the formation

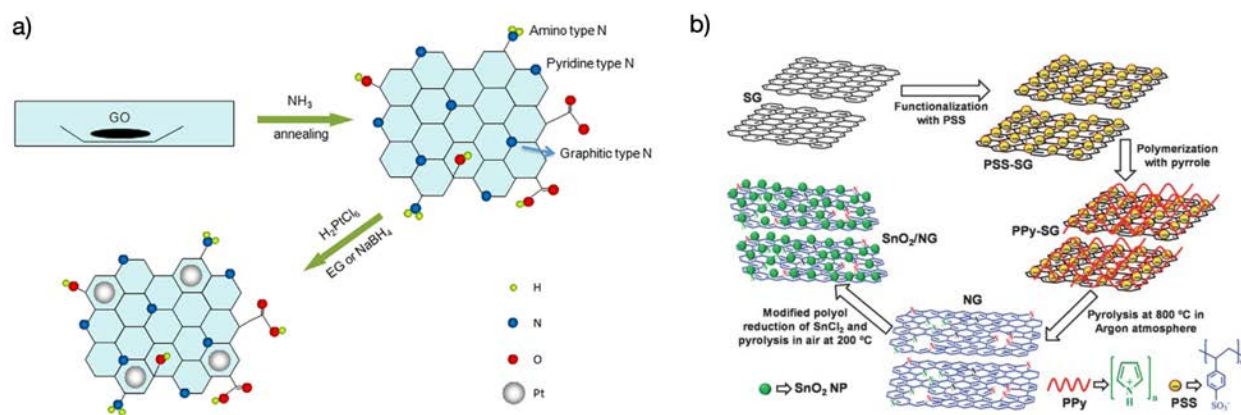


Figure A.1: a) Direct synthesis route: Illustration of the treatment of graphene oxide by NH_3 for simultaneous reduction and N-doping, followed by the loading of Pt nanoparticles (nanoparticles not-to-scale) Reprinted (adapted) with permission from Citation[40]. Copyright (2013) Elsevier. (b) Post-modification route: Schematic illustration of synthesis of N-doped graphene using the pyrolysis of polypyrrole coated functionalized graphene, with subsequent deposition of SnO_2 nanoparticles. Reprinted (adapted) with permission from Citation[130]. Copyright (2013) Royal Society of Chemistry.

of graphitic and pyridinic nitrogen functionalities directly incorporated into the graphene structure.

A.2.1.2 Post-treatment

While there are advantages to creating N-graphene through direct synthesis, post-treatment methods maybe more feasible for certain applications and are likely closer to commercialization. By far the most extensively studied method for post-modification is thermal annealing. Commonly, this is conducted in an ammonia atmosphere[58, 59, 133–137], but other environments have been studied as well[138, 139]. The ammonia thermal process results in low doping levels below 3%, typically attained by annealing between $800\text{--}900^\circ\text{C}$. Results suggest that the resulting N-functionalities are mostly pyridinic and pyrrolic. This is ascribed to the nature of thermal treatment, where dopant incorporation most readily occurs at the plane edges and on defect sites[133]. The low nitrogen level is understood because the pristine nanostructure of graphene yields a relatively small concentration of the edge and defects sites that are needed for dopant incorporation. In order to increase nitrogen content,

some researchers have instead started with graphene oxide (GO) and employed nitrogen precursors such as melamine, in combination with an ammonia heat treatment to simultaneously reduce the GO and modify it with nitrogen. Such procedures can create N levels as high as 10 at% [138]. Li et al. [140] showed that the N content achieved in this process depends strongly on temperature (decreasing N as temperature increases), likely due to reduction of the graphene oxide during the treatment. The reduction of graphene oxide (GO) in an ammonia/hydrazine environment has also been used to create nitrogen moieties [141, 142]. This is an interesting pseudo in-situ N-graphene fabrication process because hydrazine is frequently used to reduce GO to pristine graphene.

Higher dosage levels can also be achieved by physically inducing chemical defects into the graphene. This can be accomplished through energetic post-synthesis bombardment techniques like plasma treatment or ion implantation. Historically, nitrogen plasma treatments have focused on the modification of CNT's. However, graphene has recently been functionalized in this matter as well [143–147]. Nitrogen plasma treatment is attractive as a facile modification method because the plasma strength and/or exposure time can be tuned to control the level of N-doping. [146] Nitrogen contents as high as 8% have been reported; however, bombardment techniques generally lead to oxygen functionalization as well [148]. At least in one report, oxygen was incorporated to concentration levels as high as 28% [147]. Intriguingly, this unplanned oxygen co-functionalization has also proven to be beneficial for some applications. In plasma treatment, ammonia is typically the nitrogen source, but recently it has been shown that N_2 gas can also be used during ion implantation to reach dosage levels as high as $\sim 10\%$ [95]. Using plasma modification, a wide range of functionalities can be achieved. Interestingly, a survey of the literature suggests that pyrrolic nitrogen is the dominant species created by plasma modification. In contrast, nitrogen ion-beam implantation appears to produce a more balanced mix of nitrogen functionalities, although further studies are needed to clarify these issues [149].

A number of other techniques have also led to the successful incorporation of nitrogen into the graphene nanostructure. Very recently, Vinayan et al. demonstrated a novel nitrogen doping process carried out by the pyrolysis of polypyrrole (PPy) coated poly(sodium 4-styrenesulfonate) (PSS) functionalized graphene[130]. The anionic polyelectrolyte PSS introduces negatively charged SO_3^- surface groups that interact with the N^+ groups present in the PPy and gives rise to a uniform coating of the polymer on the graphene surface. The pyrolysis of the PPy/graphene, completed at 800 OC, removes the PPy, leaving behind nitrogen atoms incorporated into the graphene structure (Figure A.1b). This process leads to a nitrogen incorporation of around 7.5% with a relatively large quantity of graphitic nitrogen as well as some pyridinic nitrogen species.

A.2.2 Carbon nanotubes

After Iijima’s pioneering work in the early 1990s, carbon nanotubes (CNT’s) triggered significant interest in nanotechnology as well as a renaissance in the fundamental condensed matter physics of carbon. CNT’s continue to captivate researchers after a quarter century of study due to their attractive mechanical and chemical stability as well their high thermal and electrical conductivities. Due to the fact that the application of CNT’s relies strongly on their surface properties, surface chemistry has been a major focus of CNT research in recent years. While oxygen functionalization has been the most intensively studied, in the last decade investigations have shifted to species like nitrogen due to promising results for a variety of applications.

Previous research has shown that the addition of nitrogen into CNT’s increases the edge plane structure, creating more active sites and increasing electrochemical activity. Similarly, a combination of functionalization and CNT width can tune the electrical properties for use as an n-type semiconductor. Combining the intrinsic properties of CNT’s with the significant electrical modification provided by nitrogen functionalization, N-CNT’s have significant research appeal[118].

As with graphene, different CNT synthesis or post-treatment modification techniques can lead to variations in the concentration and range of functional species. For CNT's, CVD and pyrolysis are the most extensively studied nitrogen incorporation methods. In 1997, Sen et al. first prepared CNT's that contained small amounts of nitrogen by pyrolyzing aza-aromatics over metal nanoparticles[150]. Then in 2002, N-CNT's were grown onto substrates through a microwave plasma enhanced chemical vapor deposition (MWPECVD) process[151]. In the last 5 years, derivatives of these techniques have remained the focus of attention, with the three major functionalization approaches being CVD[50, 152–158], thermal heat treatment[159–161], and pyrolysis[52, 162–164].

Wiggins et al. used a floating catalyst CVD approach in 2009 that allowed for selective nitrogen doping and the controlled growth of CNT structures by using precursors consisting of ferrocene and either xylene or pyridine to directly control the nitrogen content. XPS analysis revealed nitrogen concentrations as high as 7.4% and Fe levels below 0.2%[157]. Chen et al also employed floating catalyst CVD using melamine precursor to synthesize the CNT's with bamboo-like structure shown in Figure A.2. Using this method, higher nitrogen concentrations result in CNT's with larger diameter and altered structure. Recently, it has been shown that metal catalysts are not required for the formation of CNT's and by utilizing the proper anisotropic carbon structures; self-catalyzed CNT's can be formed. In 2011, Wang et al. attempted to directly synthesize metal-free N-CNT's via a carbon self-catalysis process exploiting the use of a detonation-assisted CVD technique. Their results showed that nitrogen strongly promotes nanotube formation, without the need for metal atoms, and displays the ability to promote the self-assembly of tubular carbon nanostructures[156]. Their approach yielded nitrogen concentration as high as 20 at% by using melamine as a precursor. In 2012, the synthesis of large quantities of vertically aligned N-CNT's with modulated nitrogen content was reported using a spray pyrolysis CVD technique[165]. A 2009 report found that vertically aligned nitrogen carbon nanotubes (VA-NCNT's) could be fabricated through pyrolysis of a nitrogen containing metal heterocyclic molecule in either

the presence or absence of additional NH_3 vapor. Analysis revealed nitrogen in pyridinic and pyrrolic forms at concentrations as high as 6%, as well as the complete removal of the metal seed[162] . Another study reported that aligned NCNT's could also be prepared by ultrasonic spray pyrolysis from mixtures of imidazole and acetonitrile[166]. SEM and TEM images revealed that increasing the concentration of imidazole decreased the nanotube diameter and increased the nanotube length as well as the density of the bamboo-like C-N structures.

In the last few years, several groups have demonstrated heat treatment in the presence of ammonia (as well as other precursors [167]) as a route to introduce nitrogen functionalities in prefabricated CNT's. In one study, thermally treated MWCNT's were oxidized in a HNO_3 gas environment at 200°C for 2 days. After drying, the oxidized carbon nanotubes were heated under an ammonia environment at varying temperatures for 6 hours[160]. This process has been repeated[160, 161] and analysis indicates that as the ammonia treatment temperature increases, the oxygen and nitrogen contents decrease. However, at higher temperatures the ratio of N:O is much larger.

Hsu et al. used aniline to form polyaniline, which was then coated and pyrolyzed around CNT's to form a nitrogen-doped porous carbon layer that was used to stabilize precious metal sites during the reduction and pyrolysis process[52]. Similarly, polymerization of nitrogen containing organics has been shown to have a promising future for CNT post modification carbonization. An et al. showed that carbonization of polypyrrole created N-CNT's with nitrogen contents as high as 8.6 at%. In this system, BET testing showed that these nanotubes had higher specific surface areas and a pore structure consisting of micropores, mesopores and macropores[168].

Ionic liquids have been established as precursors for a variety of compounds, but just recently they have been applied as precursors for N-modification of prefabricated CNT's. Nitrogen contents as high as 10 wt% have been achieved. However, due to the expense of the ionic liquid precursor materials, only thin CNT coatings have been studied. Recently, Tuae

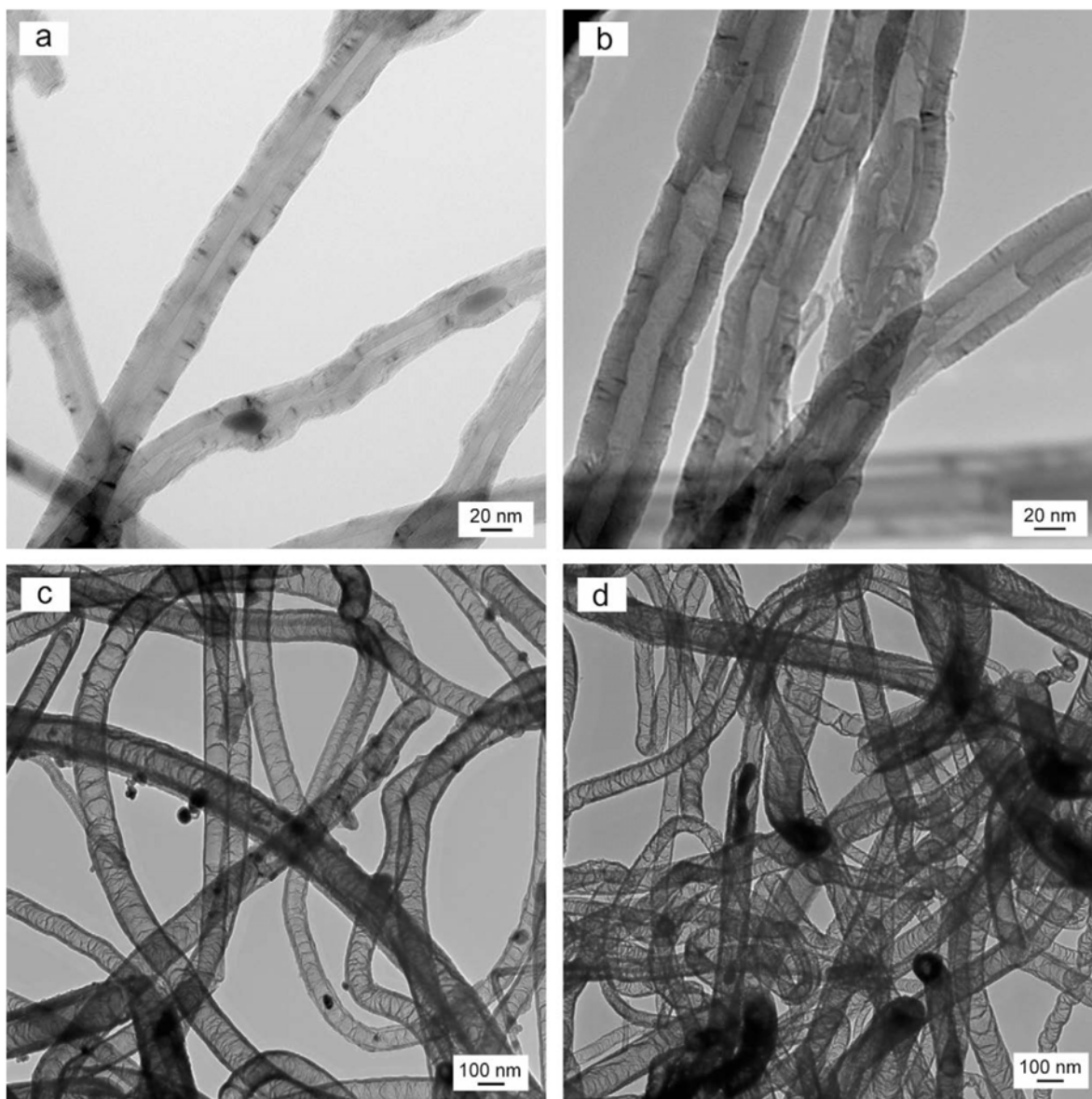


Figure A.2: TEM images of (a) CNT's, (b) CN_x (1.5 at.% N), (c) CN_x (5.4 at.% N), and (d) CN_x (8.4 at.% N) showing the effect of nitrogen on the structure of CNT's. Reprinted (adapted) with permission from Citation (Y. Chen et al., 2009). Copyright (2009) Elsevier

et al. showed that homogeneous coatings of nitrogen-doped carbon on carbon nanotubes could be achieved using ionic liquids. Their results showed modest nitrogen incorporation. The 10 wt% N-C coating on the CNT's leads to a total N concentration of $\sim 1\%$, which in this case was sufficient for its intended application[163]. These findings could lead to after-the-fact tuning of CNT's for various industries, a prospect that has already been demonstrated for pharmaceutical applications[155, 161]. However, throughout all these processes it should be appreciated that high nitrogen content is not the main metric of NCNT quality. Rather, intelligent design and targeted functional group control is most desired in order to optimize behavior for specific applications.

A.2.3 Activated Commercial Carbon Blacks

Commercial carbon blacks, which are the most widely used carbon nanomaterials, are produced by subjecting heavy residual oil feedstock to extremely high temperatures in a carefully controlled combustion reactor. These carbons can be made in various commercial grades with differing carbon structures and pore sizes, each produced through minute reactor adjustments. Researchers have used these carbon materials as inks, coatings and even in plastics for numerous applications. A large body of work has been focused on modifying commercial carbons with nitrogen through pyrolysis, annealing, bombardment or other after-the-fact techniques. Different techniques can lead to different quantities and varieties of nitrogen functional groups. There is great attraction in the potential to nitrogen-modify industry-leading carbon blacks for specific applications in order to tune the electronic structure and enhance their relative performance.

As an example, Biddinger et al. created C-N nanostructures by pyrolysis of acetonitrile over Vulcan XC-72[169]. XPS results showed overall nitrogen concentrations as high as 8.6%, which the researchers deconvoluted into pyridine, quaternary, and oxygenated pyridine functionalities. Additionally, other precursors, using nonprecious metals, were used to modify carbon blacks, such as polyaniline [67]. Jaouen et al. used an iron-based precursor and heat-treatment with ammonia to incorporate iron atoms coordinated to pyridinic nitrogen

functional groups into black pearl 2000—a well-known commercial carbon black material. This method yielded nitrogen content as high as 3.2 at %. Interestingly, the group observed some nitrogen incorporation even when the ammonia treatment was neglected[170]. Plaza et al. also used ammonia treatment to modified activated carbon materials, without metal addition. Their studies showed nitrogen incorporation up to 5 wt% and provided promising results for CO₂ capture applications[171, 172].

Commercial carbon blacks have also been modified with ion bombardment. This technique decreases the order of the graphitic structure of the carbon black and incorporates nitrogen groups into only the top ~1 to 2 nm layers (Figure A.3a) [49]. In their study, Vulcan black was ion implanted with N₂ gas in a custom implantation/sputter chamber. The material was used as a PtRu catalyst support and showed nitrogen incorporation at nearly 2 at.% after bombardment for 1hr with a nitrogen ion beam current of 14mA. Increasing the ion implantation dosage by increasing the beam current up to 45-50 mA allowed the nitrogen concentration to reach ~5 at% (Pylypenko et al., 2013). XPS analysis showed a range of nitrogen functionalities that were similar to those observed on N-doped HOPG (Figure A.3). A similar approach was used for post modification of a commercial Johnson Matthey PtRu catalyst supported on carbon black. The authors compared samples implanted for 1hr at 12mA and 45mA and found that the higher beam-current dosage led to a relative increase in the concentration of low binding energy nitrogen species such as pyridine[98]. This result suggests that it may be possible to tune the specific types of nitrogen functional groups that are created by ion implantation in order to optimize the functionalization process for specific applications.

A.2.4 Highly Porous and Mesoporous Carbon

Nitrogen-modified ordered mesoporous and highly porous carbon materials have seen considerable research because of their potential applications in areas such as adsorbents, supports, gas storage hosts, and electrode materials. Based on the size of pore diameters, carbon materials can be classified as microporous (diameter < 2 nm), mesoporous (2 nm <

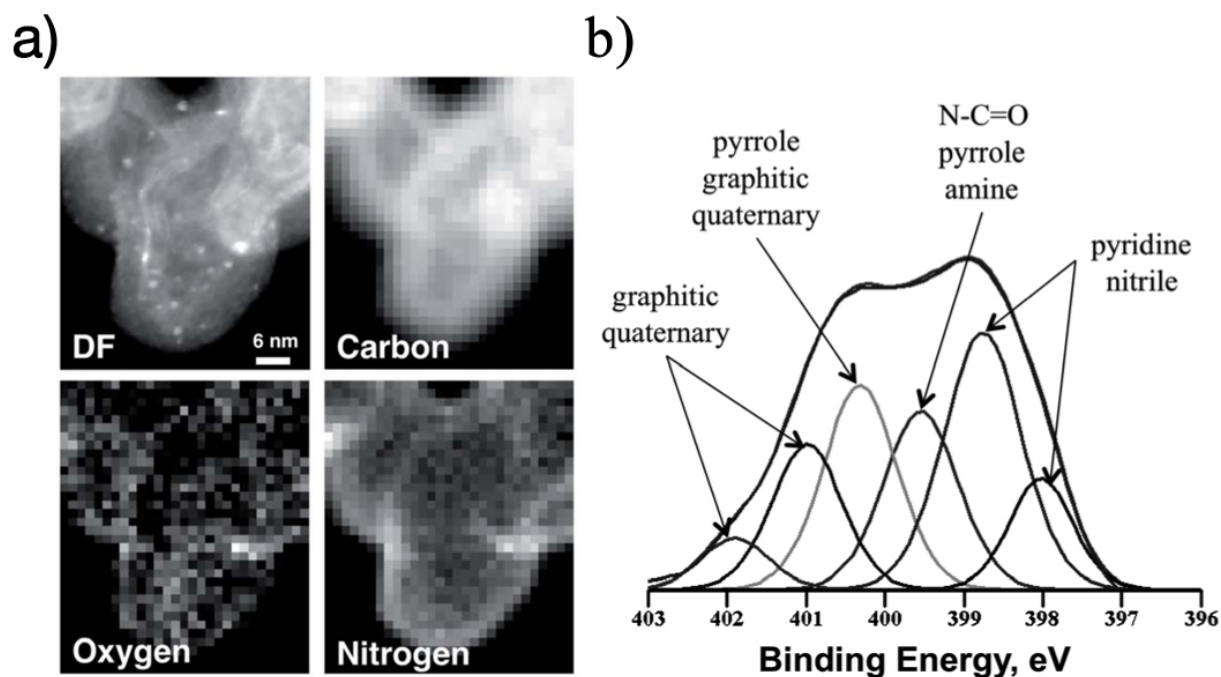


Figure A.3: (a) HAADF-STEM image and corresponding EELS oxygen, carbon, and nitrogen maps obtained from Graphitic Vulcan doped with nitrogen and decorated with Pt nanoparticles showing enrichment of the support surface with doped nitrogen. (b) XPS N1s spectrum of N-doped Graphitic Vulcan. Reprinted (adapted) with permission from Citation (Pylypenko et al., 2013). Copyright (2013) Royal Society of Chemistry.

diameter < 50 nm), and/or macroporous (diameter > 50 nm). The properties of porous carbon materials largely depend on the surface area and porosity of the carbon as well as on any heteroatom modifiers built into porous structure. Research on nitrogen incorporation into porous carbons has led to a wide variety of functionalities including amides, imides, lactames, pyrrolic and pyridinic groups. Researchers have shown that N-modification can enhance the anion adsorption capacity of meso-carbons as well as modify their pore structure and surface area. In addition, nitrogen modification has been shown to improve thermodynamic stability when meso-carbons are used as supports structures, specifically for electrocatalysis and charge collection[173].

The traditional method of obtaining ordered mesoporous carbons by nanocasting from silica is a complicated and high-cost procedure. However, the recent advent of a direct synthesis strategy using organic-organic self-assembly offers potentially lower cost and more scalable manufacturing of these materials. Although N-functionalization of ordered mesoporous carbons from the organic-organic direct strategy is still lacking, much effort has been placed on improving and understanding nitrogen modification through ionic liquid hard templating, in situ polymerization, and post-modification treatment.[173] Combining the understanding of nitrogen-containing mesoporous carbons with the creation of a facile/inexpensive, direct synthesis technique could lead to major breakthroughs in the energy harvesting and conversion fields.

Post-synthesis modification of porous carbon materials has also been widely investigated. In the typical process, an organic nitrogen-containing precursor (most frequently ammonia) is used to introduce nitrogen into the porous carbons structure. Either gaseous or aqueous environments can be employed, depending on the precursor. The carbon can be directly modified in a single step method, or oxidized prior to nitrogenation. Different precursors will yield variations in the obtained surface chemistry and porosity of the modified carbon. Porous carbon materials treated at high temperatures with ammonia show increased porosity and form surface groups such as $-NH_2$, $-CN$, pyrrolic and graphitic nitrogen due to free rad-

icals formed during the heating process. Nitrogen content and speciation is affected by the treatment temperature[174–176]. At high temperatures, pyridinic and graphitic (401.2eV) carbon become more prevalent[174]. This result is consistent with the ammonia heat treatment of other carbon structures as well. Ammonia-treated porous carbon produces nitrogen contents as high as ~4 wt.% at treatment temperatures of 973 K.

To date, porous carbon materials prepared by post-synthetic amine modification or ammonia treatment have led to materials lacking in stability and having poor performance for many applications[177, 178]. Therefore, recent efforts have been placed on direct ‘one pot’ synthesis of nitrogen functionalized porous carbon structures. Hao et al. described the fabrication of a new type of nitrogen-containing carbon monolith prepared through a direct pyrolysis technique using a copolymer of resorcinol, formaldehyde, and lysine[179]. Their results showed higher nitrogen content in the bulk rather than on the surface. They also saw that as the pyrolysis temperature was increased beyond 500°C, the total obtained nitrogen levels decreased and shifted toward higher XPS binding energies. While these results were similar to those obtained from post modification processes, their as-prepared carbon monolith was nearly crack-free. Su et al. fabricated a series of polypyrrole-derived N-containing microporous carbon spheres and demonstrated an important trend that increasing temperature leads to beneficial increase in the surface area, but results in lower nitrogen concentrations (Figure A.4) [180].

Direct polymerization of polyaniline using a template is also a well-studied method of direct synthesis[181–185]. Silva et al. have demonstrated mesoporous oxygen- and nitrogen-doped carbons synthesized from in-situ polymerized polyaniline (PANI) through carbonization in a silica SBA-15 template. The mesoporous silica template was then etched away from the structure leaving behind the PANI-derived mesoporous carbon. The obtained material exhibited remarkably active performance for oxygen reduction, challenging conventional paradigms. Moreover, it is worth emphasizing that nitrogen speciation in the PANI-derived mesoporous carbon was dominated by pyrrolic nitrogen, chemically resembling the N

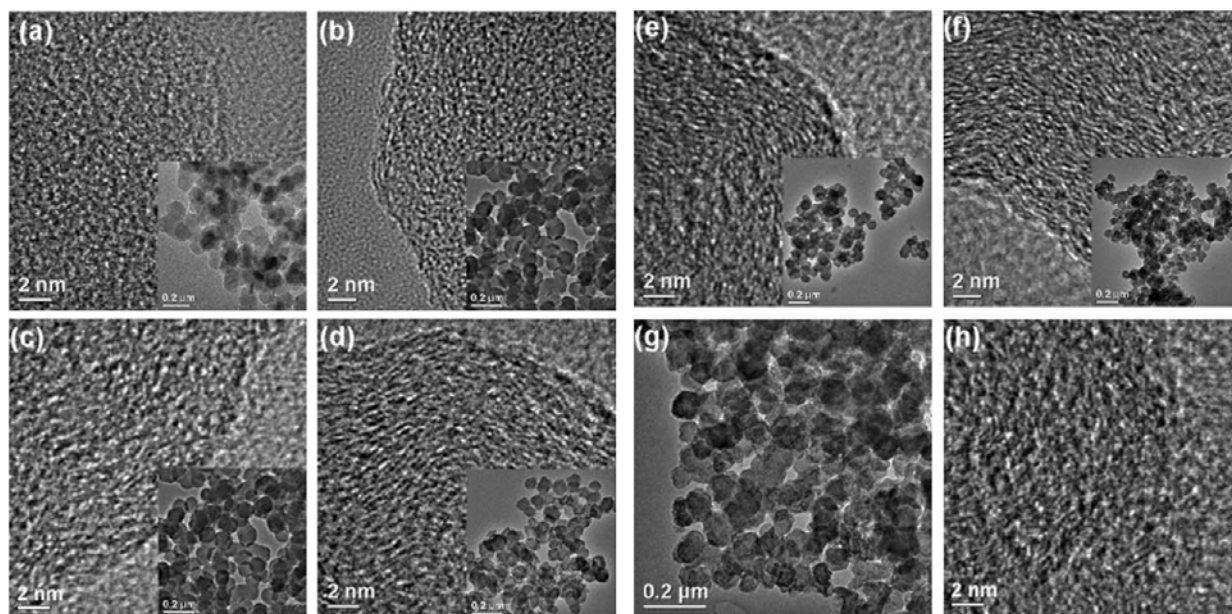


Figure A.4: TEM images (a) polypyrrole nanospheres, 14.3 at% N, and carbon nanospheres carbonized at BET 45 m²/g (b) 300°C, 14.1 at% N, BET 23 m²/g (c) 600°C, 12.5 at% N, BET 36 m²/g (d) 900°C, 7 at% N, BET 89 m²/g (e) 1100°C, 5.9 at% N, BET 20 m²/g (f) 1300°C, 4.3 at% N, BET 12 m²/g and microporous carbon nanospheres (g) and (h) 2.2 at% N BET 1080 m²/g. Reprinted (adapted) with permission from Citation(Su et al., 2011). Copyright (2011) Royal Society of Chemistry.

groups in porphyrin-like structures which have also shown good catalytic activity for oxygen reduction[184].

Recently, Ma et al. pioneered a one-step evaporation-induced self-assembly strategy focused on creating N-doped porous carbon nanostructures with large surface area. The materials were obtained through in-situ copolymerization of resorcinol and formaldehyde where HNO_3 was used as both the catalyst and the nitrogen source without involving the use of halogenides[186]. The nitrogen content and surface area could be tuned by adjusting the synthesis parameters. This one-pot method is particularly attractive because HNO_3 is inexpensive and easily accessible.

A.2.4.1 Ionic liquids

An extensive body of work has examined the use of ionic liquids (ILs) in combination with hard template structures to create controlled, porous carbon materials[176, 178, 187–192]. IL's are molten salts possessing melting temperatures generally below 100 C; in the last few decades they have attracted attention due to their low vapor pressure, high electrical conductivity, and excellent thermal stability. Due to their low vapor pressures, ILs can be used to complete the carbonization process without evaporation[178]. Unfortunately, this process leaves behind disordered structures, which have wide pores and poor surface areas if left unconfined. In addition, some reports indicate that the carbonization yield can be low[188]and the cost of these materials can be prohibitive unless small amounts are utilized effectively. Multiple recent studies have explored the possibility of using IL's without templating, some of which have resulted in materials with very poor surface areas[56, 193]. However, a 2009 report[188] demonstrated a phase separation process induced by an inorganic salt that acts as a porogen, leading to high surface area materials after water washing[194–196].

While interest in template-free synthesis continues to grow, the use of hard templating provides a beneficial avenue for expanding current knowledge and application based on improved control and understanding offered by these materials. Qui et al. demonstrated

porous carbons with nitrogen contents ranging from 8-20% using a mixture of SBA-15 and a nitrogen containing IL by first heating the mixture to 100°C and then carbonizing at a range of higher temperatures. As the carbonization temperature increases, the nitrogen content decreases. However, BET surface area and pore size increase, showing that the proper fabrication procedure is strongly application dependent.

As discussed in the CNT section, carbonization of IL's has recently been explored using CNT's as the structural host, due to their defined morphology that allows for a good control of the homogeneity of the coating. This is attractive because allows the elimination of the template material, thus potentially decreasing costs. While this novel coating idea has only led to nitrogen contents near 1 at%, it could provide a future pathway for reducing the cost and re-engineering the current templating strategy.

To this end, other creative template strategies have been explored. One such approach reported by Qui et al. explored the fabrication of nitrogen-doped carbon nanofiber webs (CNFWs) prepared by carbonization-activation of polypyrrole with KOH. The nanofiber webs were created using a reactive template solution of dissolved cetrimonium bromide and ammonium persulfate. The final materials exhibited nitrogen contents as high as 16 wt% (mostly pyrrolic N, with some pyridinic species) and BET values above 2300m²/g[197]. Results showed that the pyrolysis time affected the nitrogen content and speciation of the final structure.

A.2.4.2 Hydrothermal Carbonization

The use of plant biomass to produce carbonaceous materials is garnering interest commensurate with increased emphasis on sustainability. While biomass has been used to create carbon structures for centuries (e.g. charcoal), the recent reinvigoration of this field has led to re-exploration of a process called hydrothermal carbonization (HTC). HTC has a number of distinct advantages as it is inexpensive and can create a variety of sustainable carbonaceous materials with attractive, “built-in” functionalization possibilities and unique nanostructure that can be used in various applications. HTC can be used to create C-N structures from

sustainable nitrogen sources with appropriate co-reactivity, where the final structure is tuned using principles from colloid and polymer science. Recently, researchers have used HTC to fabricate nitrogen functionalized materials for applications such as CO₂ sequestration, and electrochemical catalyst supports for supercapacitors, fuel cells and batteries[198–203].

Natural nitrogen containing molecules such as, proteins, glucosamine or aminated saccharides can be used to fabricate carbonaceous materials with 8-10% nitrogen via HTC Figure A.4. These types of natural molecules typically form materials with higher aromatic character, which have the ability to retain greater levels of nitrogen after high temperature carbonization and achieve BET values as high as 3012 m²/g[204]. NMR used after carbonization reveals similar overall ending structures no matter the complexity of the starting molecule used, however the nitrogen functionalities may vary. In one interesting example, the sustainable preparation of a porous, nitrogen-doped high surface area carbon has been demonstrated using prawn shells as a natural nanostructured inorganic/organic composite[201].

A.2.5 Carbon nitride

For years, carbon nitride investigations have centered on understanding graphitic carbon nitride (g-C₃N₄) as a single crystal with high strength properties. However recently, polymer-derived carbon nitrides have opened up new horizons. Since 2006, when the first use of g-C₃N₄ as a metal-free heterogeneous catalyst emerged, the number of studies on polymer derived carbon nitride has steadily increased. While this branch of research is just emerging, modified carbon nitrides have already exhibited promising catalytic activity for certain reactions[205]. It has been shown that g-C₃N₄ and related allotropes have the necessary properties to catalyze oxidation and hydrogenation reactions as well as photochemical water splitting. Furthermore, it has been shown that carbon nitride is a medium-bandgap semiconductor with the HOMO and LUMO orbital's positioned in a range where it can act as a mild electron transfer agent with powerful chemical potential[206]. Since carbon nitride is metal-free, it also tolerates functional groups and is therefore suited for multipurpose

applications in biomass conversion and sustainable chemistry.

For these catalytic and energy storage applications, carbon nitride materials should possess relatively high surface areas. Unfortunately, g-C₃N₄ materials are typically made through self-condensation of organic precursors, which creates bulk materials with surface areas below $\sim 10 \text{ m}^2/\text{g}$ [205]. For the practical applications of these materials, the introduction of controlled porosity at the nanoscale must be realized—essentially the goal is to create carbon-nitride analogs of mesoporous carbon structures. Mesoporous g-C₃N₄ was first obtained through nanocasting with mesoporous silica templates[198]. Analogous to the silica-based templating of mesoporous carbons, an organic precursor is infiltrated in the silica template, and after water extraction, is heated for several hours to ensure the condensation of the precursor into polymeric C₃N₄. Utilizing this “hard template” approach provides morphological control of the mesoporous carbon nitride, giving rise to surface areas between $86 \text{ m}^2/\text{g}$ and $439 \text{ m}^2/\text{g}$, depending on the type of silica template used[207, 208]. However, these surface areas are still less than optimal due to the weak binding affinities of the basic precursors in neutral silica templates, which make it kinetically difficult to diffuse the precursors into the nanopores of the templates[209]. Recently, a SBA-15 meso-zeolite template was used in conjunction with liquid cyanamide to form a carbon nitride structure with a better 2D mesoporous hexagonal framework, resulting in a final mesoporous carbon nitride with surface area nearly identical to that of the silica template (Figure A.5)[210]. Applying the knowledge obtained from recent mesoporous carbon research could greatly impact the development of mesoporous carbon nitrides. In particular, the advent of a facile, inexpensive nanocasting strategy for mesoporous carbon nitride would provide a major impetus for the use of these materials in energy storage and capture.

As an alternative pathway, core-shell structures containing carbon nitride have been investigated as they can yield higher surface area and lower cost[211]. In these systems, metal carbon nitride materials act as the shell and are supported on electronically conductive graphite nanoparticles, the core. Both hybrid inorganic–organic polymer networks and

zeolitic inorganic–organic polymer electrolyte materials were used to impregnate an electronically conductive support (e.g. a high surface area graphite), and after a suitable pyrolysis processes, core–shell carbon nitride electrocatalysts were formed with a good dispersion of active sites for catalytic applications. Results showed that carbon nitride shells formed out of hybrid polymer networks led to higher overall nitrogen content (as high as 18%). Similar carbon nitride contents were obtained using carbon tetrachloride and ethylenediamine and a silica template. These structures contained no metal and showed promising results for Hydrogen storage[177, 209]. Continued exploration of these types of core-shell structures could lead to inexpensive high surface area materials with high concentrations of surface carbon nitride sites[211].

Finally, the formation of highly crystalline graphitic carbon nitride has been demonstrated using a simple self-condensation of dicyandiamide in a salt melt of lithium chloride and potassium chloride[212]. This synthesis route has given rise to a new type of structure, verified as poly(triazine imides), that consists of triazine structures bridged together with imide functional groups[213] (see Figure 2.4). Beneficially, it appears this type of carbon nitride material is stable in aqueous solution, allowing for potential use in applications requiring thin film coatings[214].

A.2.6 Other Carbon Structures and Synthesis Methods

A wide range of other carbon structures have been investigated, including highly ordered pyrolytic graphite[63, 65, 215], carbon nanospheres, nanoribbons[216], onion-like structures[68], fullerenes[217, 218], and covalent triazine frameworks[219, 220]. They have been developed to target various applications and/or improve basic scientific knowledge. Recently Sakaushi et al investigated amorphous covalent triazine-based frameworks (ACTFs) synthesized from p-dicyanobenzene. In their discussion they compared crystalline and amorphous CTFs, showing BET surface areas of 1140 and 792 m²/g respectively[219, 220]. The pore structure of these materials was of key interest, and was controlled by the crystallinity through the adjustment of the p-dicyanobenzene/ZnCl₂ ratio during fabrication. A pore size distribution

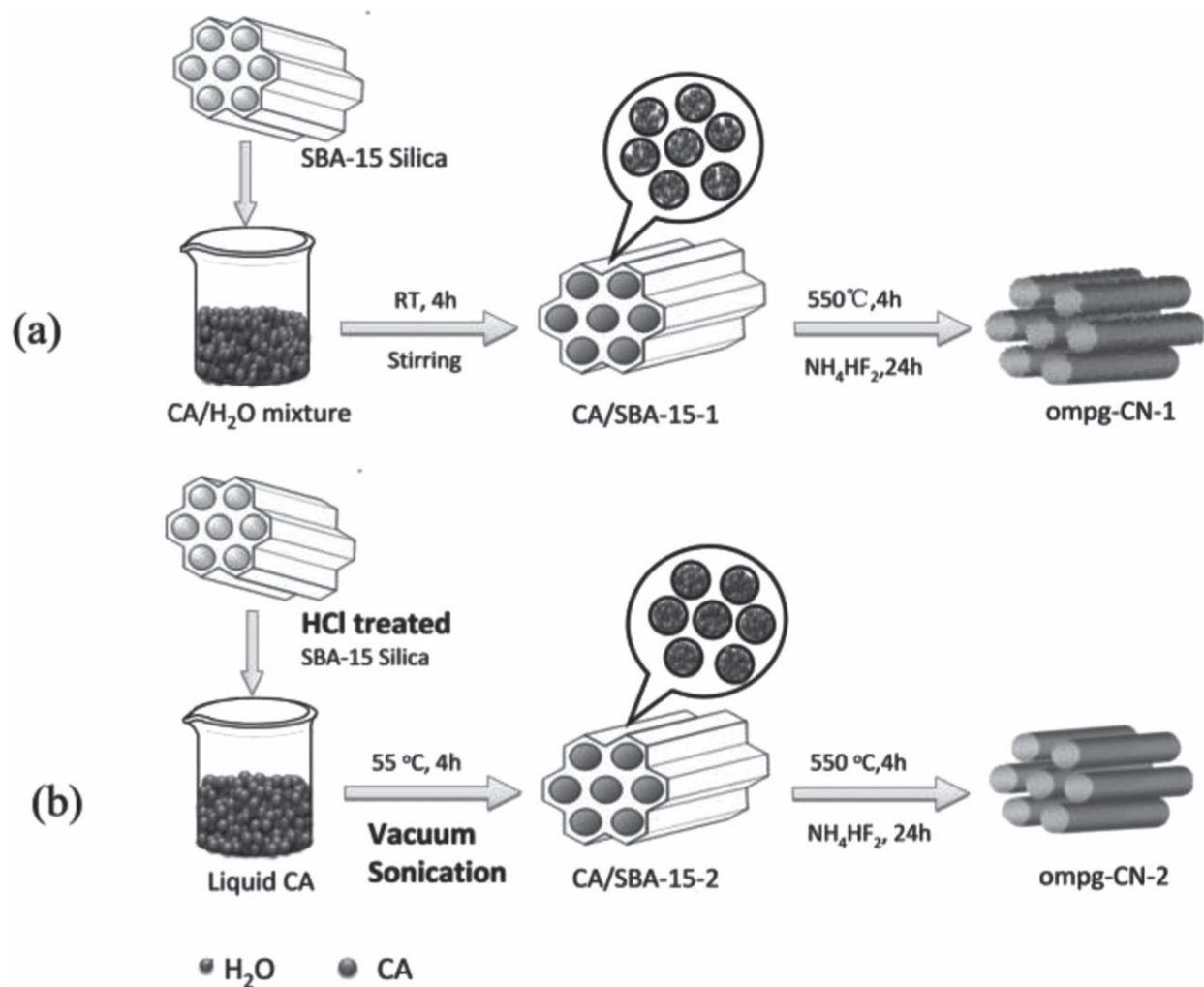


Figure A.5: Illustration for the synthesis process of ordered mesoporous-CN using (a) traditional method and (b) new method. Reprinted (adapted) with permission from Citation(Jinshui Zhang et al., 2013). Copyright (2013)Wiley-VCH.

between 1-2nm was obtained for the crystalline material vs. 0.7-0.9nm for the amorphous material. The combination of high surface area and pore structure control with the high degree of nitrogen coordination ($-\text{C}_3\text{N}_3-$) makes this an interesting material for many applications.

Onion-like carbon structures are of interest because the surface is fully accessible to ion adsorption due to an almost perfect graphite network with a high degree of curvature. Additionally, the graphitic nature of these supports provides desirable features for their use as a supporting material. Nitrogen-doped onion-like carbon materials have been synthesized by heat treatment in the presence of Co and Fe species[68]. XPS analysis reveals nitrogen contents were attained at levels near 6 at.% with slightly more sp^3 hybrid character than sp^2 , while metal species were detected at around 1 at.%.

There has also been recent interest in covalent grafting of nitrogen-containing species onto carbonaceous structures (commercial powders, nanotubes, graphene, etc.). This type of carbon modification permits organic layers to be attached to solid conducting substrates, which make them attractive (because of chemisorption) for biosensing, microelectronics, and photovoltaics. The covalent bonds in these systems are difficult to obtain, but are essential for their use in energy and sustainability applications. Unfortunately, weak physisorption bonds, detrimental toward the utility of these materials, frequently form instead of the covalent type, creating instability[221, 222]. Because these materials contain very low nitrogen amounts and frequently have high concentration of physisorbed species, we limit discussion of these materials, referring readers to an interesting review focused on this topic[221].

While all of these materials are focused on application-based integration, basic scientific studies have also been carried out using highly oriented pyrolytic graphite (HOPG). The well ordered, consistent surface structure of HOPG enables studies of the mechanism of nitrogen incorporation as well as studies of the interactions between carbon-nitrogen composites and supported ad-atoms/nanoparticles. HOPG has been modified with nitrogen by ion implantation to create C-N structures containing ~8at% nitrogen[49, 65]. High-resolution XPS scans

revealed a wide range of functionalities present after implantation ranging from $\sim 403\text{eV}$ to $\sim 397\text{eV}$ in binding energy.

A.3 Theoretical Studies

As our understanding of structures and reactions has advanced, areas stretching from synthesis to performance have become more and more theoretically grounded. Through quantum mechanical modeling, density functional theory (DFT) can provide invaluable insight into the energetic shifts of carbon as a function of nitrogen modification and help elucidate the role of specific functional groups on stability and performance for specific applications. These insights can help direct future study and give validity to current hypotheses or raise valuable questions. Herein we provide a discussion on the current revelations provided to the community through theoretical methods.

In order to increase the effectiveness of experimental research it is of great benefit to understand conceptually and mathematically the underlying chemical phenomena. To this end theory can give insight into properties such as structure, absolute and relative (interaction) energies, reactivity or other spectroscopic quantities, dipoles and higher multipole moments, vibrational frequencies, and electronic charge distributions.

Computational chemistry frequently involves a delicate dance between residual error minimization and computation time. As such, all computational chemistry approaches, including both *ab initio* and semi-empirical approaches involve approximations. These range anywhere from simplified forms of first-principle equations, which are easier/faster to solve, to approximations limiting the system size (i.e. periodic boundary conditions). Because of these limitations, among the carbon allotropes, graphene and its cylindrical analog (CNT's) are typically the best suited for computational study.

A.3.1 Electronic Effects

In 2012, Schiros et al. used x-ray adsorption spectroscopy combined with DFT to show the overall electronic effect of the different bond structures in N-doped graphene[44]. In this

study, the extra electron from the single N defect was shown to be distributed in the local network (electron donation) of carbon π -states and create an n-type effect. However, multi-defects such as pyridinic species have the opposite effect, insomuch as the two electrons fill the σ -bonds of the carbon neighbors, two electrons form a lone pair in the graphene plane, and the remaining electron occupies the N π -state. Thus, the pyridine-like defect has the equivalent occupation of a nominal carbon in graphene, however a π -electron is missing due to the vacancy site so the system is p-doped, leading to the conclusion that pyridinic nitrogen has an electron withdrawing nature. More recently, Muhich et al. studied singly and triply bound N-substituted graphene using density functional theory (DFT)[45]. Their results indicated that both n-type singly N-doped graphene and p-type triply N-doped graphene gain electron density; these results were contrary to the study by Schiros[44]. This behavior was attributed to unequal charge sharing in the C-N sp^2 sigma bond and the necessity of occupation for the orthogonal p orbital to maintain the aromaticity of graphene. This work also showed a strong enhancement in adsorption of Pt even at distances well away from the nitrogen site while revealing that migration over the nitrogen atom is unlikely due to the increased energy barrier. This phenomena has also been confirmed through experimental studies using STM mapping[46] and motivates the use of N-doped carbon materials as Pt catalyst supports to mitigate catalyst migration and agglomeration. Muhich et al. also shown that metal sites adsorbed on a pyridine ring are trapped by the strong Pt-N bonds having a greater stabilizing effect than the single N defect[45](Figure A.6).

A DFT study investigating the effects of N defects in SWCNT's discovered the interesting properties of nitrogen modification on armchair conformations versus those of a zigzag structure[223]. The results showed that zigzag like CNT's exhibit electronic shifts in the Fermi level as a result of the nitrogen adatom in pyridine-like defects. Conversely, in the same defect structure, the Fermi level shifts in armchair CNT's are due to vacancy formation. It was also shown that the resulting Fermi level shifts lead to a metallic nature of N-CNT's at N concentrations as low as 1.6 at.%. At lower concentrations N-CNT's behave

as semiconductors [223].

A.3.2 Applications

Many theoretical studies have focused on examining the effect of N-doped carbon nanostructures for specific applications, including fuel cell supports[48, 224–227], batteries[228–232], hydrogen storage[217, 233–238], supercapacitors[239], and field emission properties[33].

A.3.2.1 Fuel Cells

A 2009 study combining DFT theoretical applications with experimental results using HOPG highlighted the fact that Pt binding energy modification due to N-doping is likely the principal reason for the improved Pt catalytic activity and metal site ‘tethering’ in N-doped carbon fuel cell support systems[47, 48]. Similar studies investigating the effects of PtRu on nitrogen-modified systems reveal the complicated nature of the bi-functional system and indicate that the behavior is greatly affected by the specific nitrogen functionality employed. Simulations revealed that graphitic N defects consistently improve resistance to dissolution in all considered cases, (dissolution of Pt from Pt, dissolution of Pt from Ru_2Pt_2 and dissolution of Ru from Pt_2Ru_2). However, DFT analysis shows that the effect of pyridinic nitrogen is conflicting. It helps improve resistance to dissolution for Pt from Ru_2Pt_2 but makes dissolution of Ru from Pt_2Ru_2 more likely. Therefore the stability of PtRu catalysts can be improved through a well-balanced mix of pyrrolic, pyridinic and graphitic N[49].

DFT has also been used to investigate the full reaction path of the oxygen reduction reaction (ORR) on N-doped graphene like surfaces[217, 225–227]. These studies have summarized the effect of N-doping on different configurations. N located at sites next to the zigzag edge activates the neighboring two carbons along the zigzag edge. On the other hand, the pyridinic N located along the zigzag edge may negatively affect ORR activity, although it is abundant in most samples. Unfortunately, the pyridinic sites appear more stable and so researchers must fight the negative relation between energetic stability and the chemical reactivity [225]. Conversely, it has also been shown that higher concentrations of graphite-

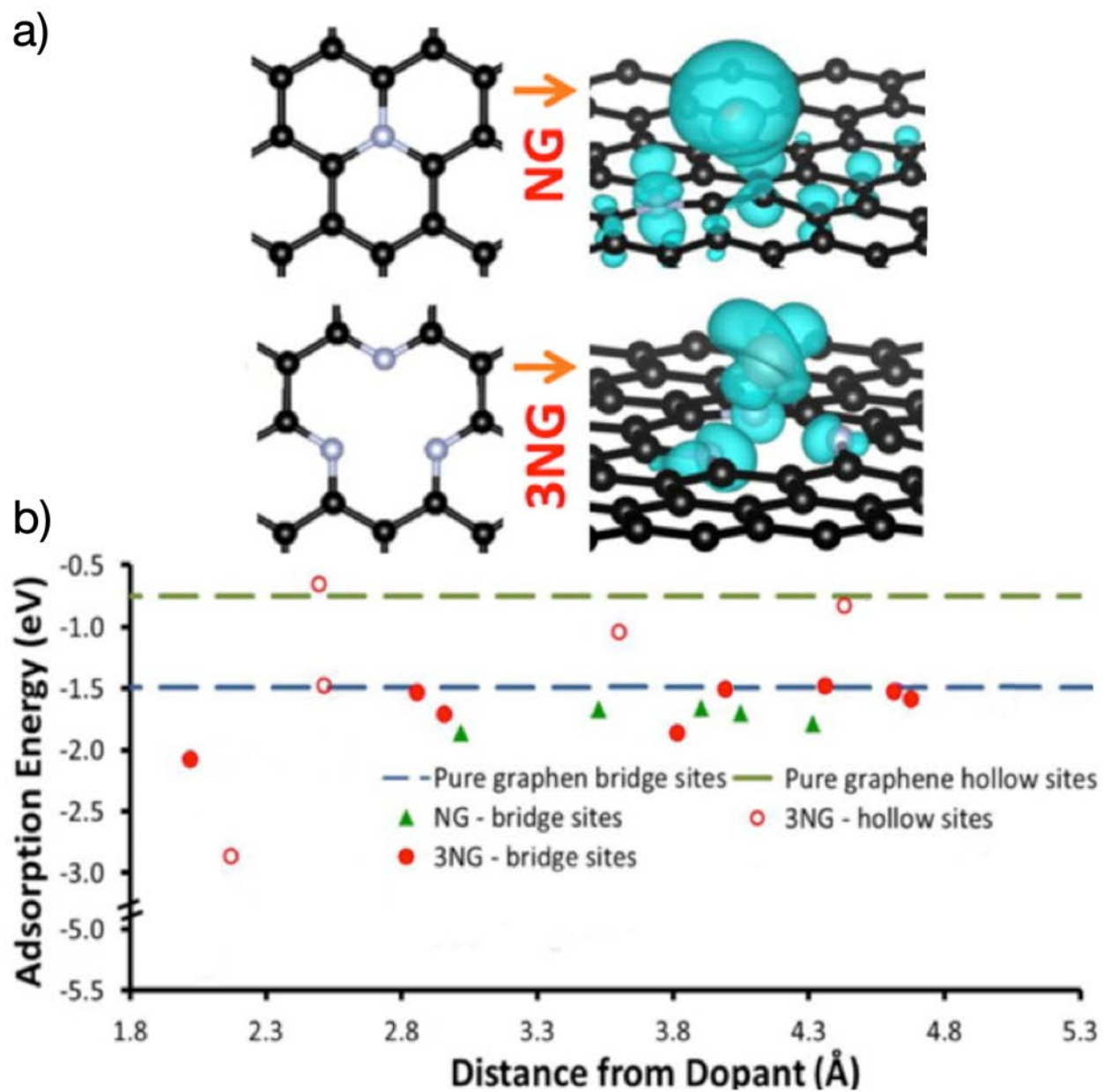


Figure A.6: (a) Electron density of singly and triple doped nitrogen sites. (b)) Pt adsorption energy as a function of distance from the dopant atom. Reprinted (adapted) with permission from Citation(Muhich et al., 2013). Copyright (2013) American Chemical Society.

like nitrogen groups reduce the energy barrier for oxygen molecule dissociation much more efficiently[226]. Recently other groups have proposed that theoretically, graphitic nitrogen on graphene will precipitate the ORR reaction via a $4e^-$ pathway[227, 240]. However, this is much debated and other studies contradict this finding[241]. It is likely specific groups such as graphitic nitrogen may reduce the energy barrier for the $4e^-$ pathway, however the $2e^-$ pathway is overall more energetically favorable (on N-graphene without metal) and a combination of two pathways is inevitable (Figure A.7)[226]. It is well documented that the rate-determining step is likely the removal of the adsorbed oxygen species, meaning that future catalysts should be designed to improve the kinetics of O_{ads} removal[227, 241].

Non precious metal group (NPMG) catalysis has been the focus of many theoretical studies. In this area it is well believed that the geometrical and electronic structures of Me-N_x clusters are the most important factors in influencing the catalytic activity of Me-N/C electrocatalysts for ORR[240, 242–245]. To date, DFT computation studies have explored the progression of ORR on Me-N_x clusters in isolated transition metal-macrocylic molecules[246, 247] and perfect graphene[242, 243]. These studies focus on understanding the geometry, stability, ORR pathway, and electronic structure of the Me-N₄ (Me=Fe, Co, or Ni) on carbon. Recent work by Kattel and Wang focused on elucidating the ORR pathway of Me-N/C electrocatalysts. Consistent with experimental findings, the DFT results suggest that Fe-N₄ and Co-N₄ clusters could promote $4e^-$ ORR on a single active site and that the ORR activity of the Me-N₄ clusters is correlated to the d-orbital electronic structure[248]. Additionally, DFT has also recently been used to predict binding energy shifts in N1s XPS spectra resulting from the Me-N_x structures present in these types of ORR catalysts. Therefore the synergy of experiment and theory could allow researchers to extract critical information from in situ high-resolution N1s spectra. This information is needed for the determination of geometry and abundance of ORR active sites in an oxidizing atmosphere, which is critical information that must be evaluated against electrochemical activity for ORR reactions[249].

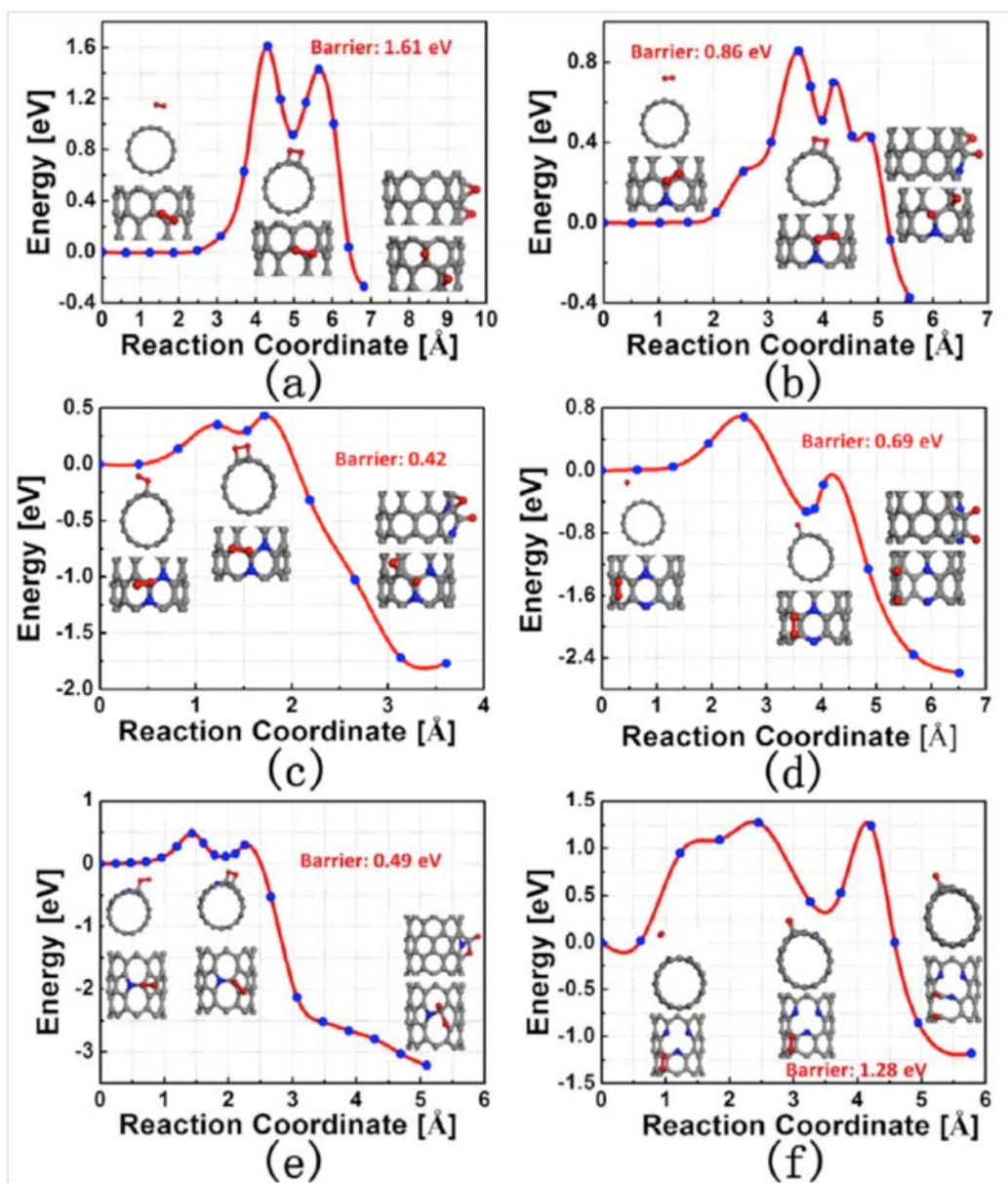


Figure A.7: Minimal energy paths of oxygen molecule dissociation on (a) a pure (8,0) SWCNT, (b) a one nitrogen atom substituted (8,0) SWCNT, (c) a two meta nitrogen atom substituted (8,0) SWCNT, (d) a two para nitrogen atom substituted (8,0) SWCNT, (e) a one nitrogen atom substituted (8,0) SWCNT with a stone-wales defect, and (f) a (8,0) SWCNT with pyridine-like nitrogen atoms. Gray dots, blue dots and red dots represent carbon, nitrogen and oxygen atoms respectively. Reprinted (adapted) with permission from Citation(Ni et al., 2012). Copyright (2013)Royal Society of Chemistry.

A.3.2.2 Batteries

Nitrogen-modified carbon-based ORR catalysts have also been studied for lithium air/oxygen batteries[228–232]. The results of these studies indicate beneficial effects similar to those observed in fuel cell studies. Results by Yan et al. show that N-doping can decrease the energy barrier of graphene from 2.39eV (undoped case) to 1.20 eV, increasing the energetic feasibility of O₂ disassociation [230]. The effect of N on lithium intercalation into carbon has also been studied. Ma et al. used first principle calculations to investigate three different nitrogen defect structures, pyridinic, pyrrolic, and graphitic, in order to study the electronic properties and adsorption mechanism of single and multiple Li atoms[250]. This work showed that pyridinic nitrogen is the most beneficial for Li intercalation and gives rise to the highest storage capacity. This was attributed to the fact that the single atom Li absorption energy on pyridinic sites was increased by ~40% (compared against pristine graphene) and was energetically more favorable than the formation of Li clusters, which tend to form on pristine graphene. Computational results indicated that N-graphene has the potential to possess reversible capacities of 1262 mAh/g[250]. A more recent theoretical study by Kong et al. studied various pyridinic clusters and found that a 4 pyridinic cluster is the best candidate for Li adsorption[231]. In this work it was also shown that this structure enhanced Li mobility and increased the strength of Li adsorption. Comparing these results with recent experimental findings shows that the steep reduction in Li capacity observed for N-modified anodes after cycling can be attributed to their enhanced Li adsorption. It can be hypothesized that the strong Li-pyridinic attractions can allow the Li atoms to stay on the surface even after multiple charge-discharge cycles. While nitrogen modification in these systems is still very beneficial, these positive effects decrease over the lifetime of the anode. As such, focus needs to be placed on maintaining Li capacity through creative means.

A.3.2.3 Hydrogen Storage

In the arena of hydrogen storage, theoretical studies have explored the effects of dispersed Li on N graphene at standard temperature and pressure. The results showed the maximum number of adsorbed H₂ molecules to be three for pyridinic and pyrrolic species, which can be adsorbed and desorbed under the same conditions[235]. Lu et al. explored a similar system by studying the effect of nitrogen on a 2-D porous polymeric network. Authors showed that the increasing number of N in an aromatic ring enhances the binding energies between hydrogen molecules and pre-adsorbed Li atoms from 1H₂ to 3H₂. While these studies have focused on the molecular adsorption of H₂, a novel strategy of applying an electric field to N-graphene allows for atomic H adsorption. Theoretically, materials used in this way could reach hydrogen uptake values of 7.23 wt% at complete hydrogenation, well above the U.S. Department of Energy (DOE) target. Hydrogen can then be released through another voltage change, adding utility and interest to this type of system because the band gap of N-doped graphene is increased to 3 eV after 2 H atoms are adsorbed. These results suggest that hydrogenated N-doped graphene could display photocatalytic activity and solve the band gap problem of graphene for nanoelectronic applications[233]. Overall, the combination of theoretical calculations with experimental observations greatly enhances the community's understanding of doping mechanisms, the effects of doping on adatom adsorption, as well as the effects of doping on the electronic properties of these materials. This enhanced understanding can be applied to a variety of systems to enable the tailoring of carbon structures to fit various specific applications.

A.4 Applications

Carbon-nitrogen nanostructures are ultimately intended for integration into important, industry-relevant applications. The goal is to determine which functionalities and properties are most beneficial for a desired application and amalgamate that knowledge into systems that improve performance and efficiency. Within the last five years, research has greatly

improved our understanding of how C-N structures can benefit applications ranging from fuel cells to batteries, hydrogen storage to CO₂ capture, and supercapacitors to photocatalysis. This section discusses recent findings related to the effects of nitrogen on these various applications and draws conclusions for future study and improved integration.

A.4.1 Fuel Cells

The following paragraphs discuss progress in N-modified carbon-supported catalyst systems for methanol electrooxidation and oxygen electroreduction, starting with carbon-supported precious metal catalysts, followed by non-precious metal catalysts (transition metal based catalysts) and finally, nitrogen-functionalized metal-free catalysts.

A.4.1.1 Precious metal N-containing catalyst systems for methanol electrooxidation

State-of-the-art methanol electrooxidation catalysts typically consist of carbon-supported Pt-Ru alloy nanoparticles. A bimetallic Pt-Ru alloy, instead of pure Pt, is generally used as it shifts the onset potential to lower values and eliminates poisoning from CO intermediates. Nitrogen functionalized carbon supports are interesting for these applications because the nitrogen modification can improve the interactions between the carbon support and the metallic nanoparticles, leading to improved catalyst activity and durability.

While a few authors have examined the role of nitrogen-doping in the enhancement of performance for carbon-supported Pt-Ru catalysts, most papers discuss the effects of nitrogen doping on carbon-supported Pt catalysts[47, 48, 51–59, 251] even though these pure Pt-based catalysts are not optimal for methanol oxidation applications. Several classes of nitrogen-doped carbon materials have been investigated in the past 5 years, including carbon blacks [49, 77, 79, 97, 98, 101, 252], carbon nanotubes[50, 52, 60], mesoporous carbons [253], carbon shells[54],porous carbon nanospheres[55, 57], carbon nitride[211], graphene[40, 59, 139]and highly oriented pyrolytic graphite (HOPG) [47, 48, 63, 65, 215].

N-doping of CNT's for fuel cell applications has been achieved by direct synthesis using chemical vapor deposition (CVD)[251], post-treatment with nitrogen plasma[60] or polymerization of aniline[52]. Carbonization of polyaniline/aniline has also been used to incorporate nitrogen into ordered mesoporous carbons [51, 53] and to synthesize nitrogen-doped carbon shells[54]. N-doped porous carbon nanospheres have been fabricated by carbonization of polypyrrole nanospheres, followed by chemical activation to introduce porosity[55, 57]. Melamine precursors have also been employed to incorporate nitrogen into the graphene nanocomposites[139].

Shao et al. explored doping of graphene using ammonia treatment and a one-pot synthesis route using N-methyl-2-pyrrolidone as nitrogen precursor[59], while Pan et al. utilized a polymerizable ionic liquid to control carbon yield, nanostructure and nitrogen concentration in nitrogen-doped carbon/Pt nanoparticle hybrids[56]. These materials showed nitrogen in the range of 8.27-15.29%. O'Hayre et al. have studied effect of nitrogen ion beam implantation onto the structural and chemical modification of highly-oriented pyrolytic graphite [47–49, 63, 65, 215] and later applied same method to incorporate nitrogen into carbon blacks[77, 79, 97, 101] and commercial catalysts [98].

A review paper published in 2010 highlighted the effects of nitrogen doping on the performance of methanol electro-oxidation catalysts, concluding that irrespective of the type of the carbon support and doping method, when compared to undoped counterparts, the N-doped systems generally show improved MOR performance [2]. Specifically, N-doped catalyst systems show improved catalyst dispersion[47, 49–51, 53–55, 57], lower onset potential[47, 53–55, 60, 61], increased current produced per catalyst surface area (specific activity)(Chetty et al., 2009; Lei, Zhao, et al., 2009) or per metal catalyst mass (mass activity)[53, 55, 57] and exhibit improved stability. The evidence that nitrogen modification improves dispersion of carbon-supported precious metal nanoparticles and enhances their durability is strong. Figure 9 a-d shows the effect of nitrogen concentration on the pre- and post-cycled Pt particle size distribution and the respective benefit to the electrochemical surface area. The evidence

that nitrogen modification enhances intrinsic catalytic activity is less clear-cut.

It is well documented that the nucleation and dispersion of metal nanoparticles on carbon materials with high graphitic content is quite poor and typically requires surface pretreatment. Incorporation of nitrogen into CNT's provides sites for preferential nucleation, without need for pretreatment [251]. Similarly, incorporation of nitrogen into the structure of graphitic Vulcan through ion beam implantation greatly enhances the nucleation of uniformly dispersed Pt nanoparticles[49]. Generally, catalyst nanoparticles supported on undoped and N-doped carbon differ in their initial density, dispersion, size and composition. It is observed that N-doping alters the nucleation and growth of nanoparticles in a beneficial way, leading to improved dispersion and smaller particle sizes[47, 49–51, 53–55]. Guo showed that incorporation of nitrogen into ordered mesoporous carbon enables dense dispersions of Pt nanoparticles at dramatically increased Pt loading[51]. Lei et al compared a series of nitrogen-containing ordered mesoporous carbons synthesized in the temperature range of 600-950 °C, and showed that the nitrogen concentration was critical to the dispersion of the Pt nanoparticles[53]. Within the set of materials produced, the authors reported BET surface areas from 988 to 1166 m²/g, pore sizes from 2.7 to 3.3 nm and nitrogen concentrations from 9.6 to 4.8 at.%. Despite relatively comparable BET surface areas, the increase in nitrogen concentration from 4.8 % to 9.6 % led to a systematic decrease in the Pt nanoparticle size from 4.0 to 2.4 nm. The authors also discussed the interplay between the N concentration and particle size in terms of their effect on the CO stripping peak. The materials synthesized at the lowest temperatures possessed the highest N contents and exhibited the highest CO tolerance, while the materials synthesized at the highest temperatures showed lower nitrogen content, but larger pore size. The materials synthesized at the highest temperatures also showed lower charge transfer resistance and demonstrated the best mass activities for methanol oxidation. Lei et al also explored the effect of nitrogen by using a series of nitrogen-doped carbon shells pyrolyzed in the temperature range of 400-950 °C; material synthesized at 900°C showed the best catalytic performance towards oxidation

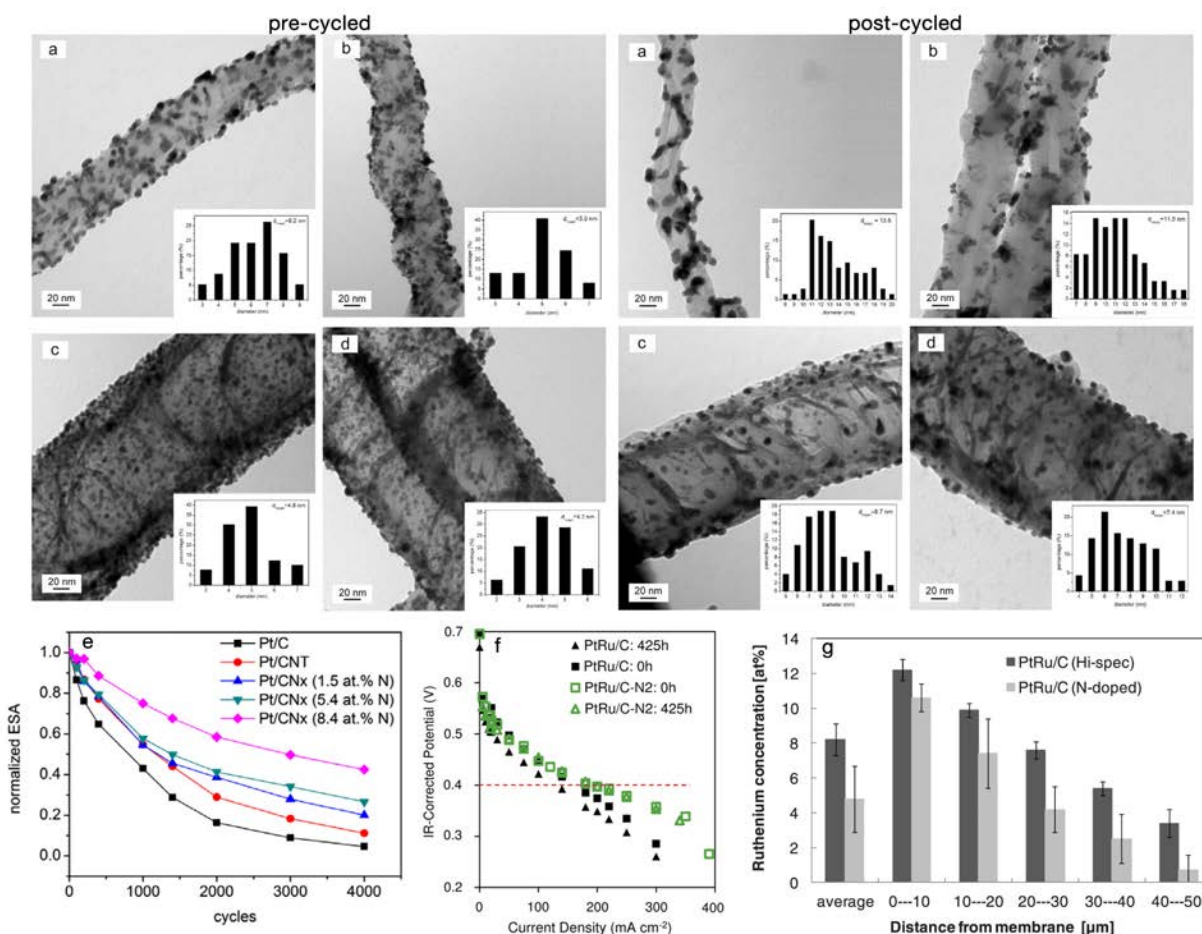


Figure A.8: TEM images and size distribution histograms (insets) of Pt electrocatalysts before and after ADT. (a) Pt/CNT's; (b) Pt/N-CNT's (1.5 at.% N); (c) Pt/N-CNT's (5.4 at.% N); (d) Pt/N-CNT's (8.4 at.% N) and (e) the comparison of the degradations of the five catalysts. on the structure of CNT's. Reprinted (adapted) with permission from Citation (Y. Chen et al., 2009). Copyright (2009) Elsevier (f) the effect of N-doping on performance of PtRu anode. Reprinted (adapted) with permission from Citation (Corpuz et al., 2014). Copyright (2014) Elsevier (g) the effect of N-doping on Ru crossover in DMFC made with PtRu anode. Reprinted (adapted) with permission from Citation (Joghee et al., 2012). Copyright (2012) The Electrochemical Society.

of methanol.

Pt and PtRu supported on N-doped porous carbon nanospheres show enhanced dispersion and particle size as well as improved onset and mass activities[55]. Authors also reported that N-supported PtRu retained better performance even after durability cycling. For bimetallic precious metal nanoparticles such as PtRu, nitrogen functionalization of the carbon support can change the Pt-to-Ru composition due to altered nucleation and growth kinetics. For example, PtRu nanoparticles grown on ammonia-treated N-containing CNT's also contained an unalloyed hexagonal Ru phase that appeared to be least partially responsible for enhanced activity[60].

In addition to the typical catalyst degradation mechanisms (i.e. dissolution/reprecipitation, migration/coalescence, support detachment) experienced by carbon-supported Pt-based catalysts, PtRu/C anode catalysts experience an additional degradation mechanism associated with the dissolution of ruthenium, which crosses over the electrolyte and contaminates the cathode. Modification of the catalyst-support interactions through nitrogen modification has been shown to improve PtRu catalyst nanoparticle stability while also mitigating Ru crossover and particle-growth mechanisms[63, 77–79, 101].

Since N-doping alters the metal nanoparticle nucleation dynamics and can therefore affect the initial particle size and dispersion of the supported metal nanoparticles, this can make it difficult to assess the effect of N-doping on subsequent catalyst durability, since the morphological starting point for doped and undoped catalyst systems will be different. In order to address this issue and isolate the effect of nitrogen functionalization on the stability of PtRu nanoparticles independent of their effect on metal nanoparticle nucleation, O'Hayre et al. conducted a series of experiments utilizing PtRu nanoparticles deposited via sputtering from a single-alloyed PtRu target [47–49, 63, 65, 215], which led to initial PtRu nanoparticle coverage, dispersion, and particle size distributions that were identical for nitrogen-modified and unmodified carbon supports. PtRu nanoparticle stability was probed by accelerated degradation testing using a series of model HOPG substrates with varying nitrogen concentrations

(controlled via ion implantation dosage) but identical starting PtRu nanoparticle composition, size and coverage [63]. It was found that low implantation dosages had an overall negative effect on catalyst stability, presumably due to the presence of implantation-induced physical defects and oxygen groups associated with the nitrogen functionalities present at low dosages. These samples were similar in their stability to those exposed to Ar⁺ irradiation, which introduced physical defects that had a beneficial effect on nucleation but a detrimental effect on durability[47]. Samples implanted at higher nitrogen dosage, however, possessed a mixture of physical defects, oxygen functionalities and significantly higher amounts of nitrogen (up to 8 at% N prior to metal deposition). The high nitrogen concentrations led to the formation of clustered multi-nitrogen defects and also led to great improvement in PtRu nanoparticle stability (specifically preventing nanoparticle agglomeration by migration/coalescence). Through analysis of datasets containing electron energy spectral images, it was demonstrated that only regions with the highest nitrogen concentration offered improved stability after accelerated degradation testing[49]. Within the areas of best stability, PtRu nanoparticles appeared to be surrounded by nitrogen defects, suggesting that the incorporation of nitrogen next to the catalyst nanoparticles is of utmost importance in preventing migration[49]. This effect was also later demonstrated by testing post-doped commercial PtRu/carbon catalysts (Corpuz et al., 2014). Further, it was shown that stability of PtRu nanoparticles on N-doped HOPG substrates could be additionally improved by the incorporation of fluorine. In this “co-functionalized” system, nitrogen is believed to mitigate migration/coalescence and fluorine is hypothesized to improve resistance to metal dissolution[215].

The beneficial effect of N-doping on the stability of PtRu nanoparticles has also been demonstrated with the N-doped carbon black supports such as Vulcan black[77, 79, 97, 101]. Investigation of catalyst stability with in situ small-angle x-ray scattering (SAXS) has revealed remarkably improved durability of PtRu nanoparticles on N-doped carbon blacks compared to an unmodified carbon blacks[77, 79, 163]. N-doped supports have shown better

retention of electrochemically active catalytic sites when compared against undoped in-house materials and commercial references [79]. Long-term stability of PtRu supported on N-doped Vulcan has also been investigated in complete direct methanol fuel cells, revealing improved fuel cell performance as well as mitigation of metal dissolution and ruthenium cross-over after durability testing (Figure A.8(f) and (g))[78, 101]. Overall the role of specific nitrogen functionalities is hard to elucidate and as seen above most studies in this application show that increasing nitrogen content, regardless of functionality, is the most important. Every work reports presence of multiple functionalities, among them nearly every study mentions pyridinic nitrogen.

A.4.1.2 Precious metal N-modified catalyst systems for oxygen electrooxidation

As previously noted, when compared to methanol electrooxidation, fewer studies have been completed on Pt and Pt-alloy supported N-doped carbons investigating oxygen electroreduction. Most studies have focused on the improved Pt nanoparticle dispersion and stability provided by N-doping, rather than on the electrocatalytic properties for ORR. Among the N-doped carbon materials studied for ORR are N-CNT's [109, 143, 163, 254–256], mesoporous carbons[62], porous carbon nanospheres [57], carbon blacks [257], graphene[66, 143] and graphene nanoplates[109, 143, 163, 254].

Chen et al. demonstrated control of nitrogen content in CVD-grown carbon nanotubes through the use of a melamine precursor[254]. Their work clearly demonstrated that with increasing nitrogen concentration, the average Pt particle size decreases and the size distribution narrows. In addition, the authors used accelerated degradation testing to demonstrate that nitrogen helps to stabilize the supported nanoparticles, evident from the analysis of nanoparticle size distributions and improved retention of active surface area (11.2 % on undoped CNT's, vs. 20.2 %, 26.6 % and 42.5 % on CNT's doped with 1.5, 5.4 and 8.4 at% nitrogen, respectively). Another work focusing on N-doped CNT's compared various nitrogen precursors and found that nitrogen-rich ethylenediamine helps incorporate more nitrogen (4.74 at%) than the less nitrogen-rich pyridine precursor (2.35 at%)[109]. Both types of N-containing

CNT's demonstrated more uniform Pt particle size and increased ORR activity compared against the unmodified catalyst material. During MEA testing, catalysts with higher nitrogen contents showed better overall performance metrics, including enhanced nanoparticle dispersion and substantial increases in the power density. Saha et al. also reported smaller nanoparticle sizes (2.6 nm) and more narrow particle size distributions on the N-doped CNT's as compared to undoped CNT's (5.89 nm); the improved particle size distribution led to a 36% improvement in active surface area and higher current density[256].

A series of nitrogen-doped ordered mesoporous carbons for use as ORR catalyst supports were prepared by pyrolysis of carbon and Pt precursors using a silica SBA-15 template functionalized with 3-[2-(2-aminoethylamino)ethylamino]propyl as the nitrogen source[62]. Nitrogen levels in the range of 0 to 3 wt% were achieved, and with exception of one test, all samples followed the trend of improved Pt nanoparticle dispersion with increasing nitrogen concentration. The dominant functionalities were graphitic and pyridinic nitrogen and the pyridinic fraction increased with increasing total nitrogen concentration. Electron energy loss spectroscopy mapping of carbon and nitrogen revealed that nitrogen was not homogeneously dispersed in these materials, displaying enrichment along the outer rims. The best electrocatalytic activity, durability and tolerance to methanol were reported for the materials with 2.2 wt% nitrogen. Methanol tolerance is important for ORR cathode catalysts in direct methanol fuel cells in order to mitigate the deleterious effects of methanol crossover at the cathode.

Ramaprabhu et al have investigated Pt and Pt₃Co alloy nanoparticles supported on N-doped graphene, where 5.9 at% N-doping was achieved by coating graphene with polypyrrole and treating it at 800°C in inert atmosphere[66]. Samples showed contributions from pyridinic, pyrrolic, graphitic and oxidized nitrogen groups, with pyridinic nitrogen being the main component. Pt and Pt₃Co were deposited onto N-doped graphene by a modified-polyol reduction method and showed higher electrochemical surface area (ECSA) than that of commercial Pt/C. The high ECSA was attributed to the uniform dispersions of nanoparticles, achieved

due to the presence of nitrogen groups. Both samples also showed maximum power densities higher than those of commercially supported Pt or PtCo catalysts and demonstrated good stability. Liu et al. demonstrated Pt supported N-doped porous carbon nanospheres with excellent dispersion and small particle size as well as improved half-wave potentials and mass activities [57]. Popov et al. developed a nitrogen-modified carbon composite (NMCC), prepared from ethylene diamine, $\text{Co}(\text{NO}_3)_2$ and carbon black[257]. The authors first compared the performance of Pt/C, Pt/NMCC and PtPd /NMCC catalysts with various Pt/Pd ratio and reported that the Pt/NMCC material showed best mass activity. Mass activities of PtPd/NMCC catalysts varied due to differences in the particle size and alloying effects. Fuel cell testing revealed that the NMCC-supported catalyst had higher initial catalytic performance and was also more stable than the unmodified carbon black support due to higher graphitization.

As discussed in the materials section, pyrolysis of ionic liquids using CNT's as a template was used to investigate the electrocatalytic performance of Pt. These materials contained low overall N concentration, but possessed a reasonable ($\sim 8\%$) concentration of surface C-N bonds. While Pt-mass based activities of the undoped and N-doped materials were very comparable, author's observed major differences in the stability of these materials, demonstrating the beneficial effect of surface nitrogen groups towards stabilization of the Pt nanoparticles. In this study, ECSA losses were reduced from 33% to 27% and more significantly, the average particle size growth was reduced from 45% to 22%, suggesting reduced dissolution/ripening and/or migration/coalescence due to nitrogen functionalization[163].

A.4.1.3 Non-precious metal N-modified catalyst systems for oxygen electroreduction

N-containing non-precious metal catalysts (NPMCs) derived from precursors of carbon, transition metals, and nitrogen by means of heat treatment have been studied for years, but the recent years have been transformational, with major advances in the oxygen reduction performance. Within the past 5 years, several detailed reviews of nonprecious metal catalysts

for ORR have appeared in the literature [108, 258–260].

In general, various precursors and synthesis routes have been explored in the search for the most active and stable catalysts. Despite this vigorous activity, however, the precise nature of the active sites in this class of materials is yet to be determined. The mechanism of oxygen reduction can follow several pathways, i.e. proceeding via two, four or two-by-two electron transfer. In these systems, identification of the active site is challenging because these materials are typically complex and possess many different species that could potentially support the different pathways. The most widely used techniques employed for investigation of the catalyst composition and structure is X-ray photoelectron spectroscopy (XPS) and transmission electron microscopy (TEM). In search of the nature of the active sites, scientists have also employed a variety of other techniques, including X-ray absorption techniques (XAS), time-of-flight secondary ion mass spectroscopy (ToF-SIMS) and Mössbauer spectroscopy[261–269]. Several studies have additionally employed sophisticated statistical analyses such as principal component analysis to determine correlation between ORR activity and parameters obtained from spectroscopic techniques[263, 270, 271].

Published in 2009, a cross-laboratory study of non-noble-metal electrocatalysts compared electrocatalysts synthesized by different groups using several routes: 1) pyrolysis of a single precursor based on a metal-N₄ chelate, 2) pyrolysis of two separate precursors for metal and nitrogen, 3) second pyrolysis of materials derived by 1 or 2 under reactive atmosphere of O₂, CO₂, NH₃ or N₂/H₂) and 4) pyrolysis of metal precursors under NH₃[272]. The conclusion of this work was that total nitrogen content appeared not to have a direct correlation with the activity, but micropores produced during heat-treatment were found to be important as they were hypothesized to host N-containing active sites. Later, the Dodelet group demonstrated significant improvement in the current and power densities by focusing on optimization of the synthesis to maximize the amount of active sites hosted between graphitic sheets within micropores, with the active site proposed to be pyridinic nitrogen coordinated to iron[170] (Figure 2.4). Pyrolysis of chloro-iron tetramethoxyphenylporphyrin (Cl-FeTMPP) supported

on a non-microporous carbon in NH_3 led to a more active and less stable catalyst than heat-treatment in argon environment[273].

In attempts to increase the density of active sites, a group from Los Alamos National Laboratory (LANL) explored materials derived from cyanamide and polyaniline. A cyanamide precursor was employed in efforts to increase the nitrogen content; however, authors reported lower than expected nitrogen concentration and additional incorporation of sulfur[274]. NPMC based on pyrolysis of polyaniline showed high selectivity for four-electron oxygen reduction when materials contained both nitrogen and metal[67]. Authors explored the effect of pyrolysis temperature in the range of 400-1000°C, finding 900°C to be the optimum temperature for maximum activity and stability. The unique characteristic of this material was the high degree of graphitization that occurred in the form of graphitized onion-like carbon shells over the metal-rich particles and graphene-like sheets. These graphitic structures were hypothesized to improve stability and host active sites[68, 269]. For the iron-based catalyst, increasing the heat-treatment temperature led to an increase in the ratio of quaternary (Figure 2.4) to pyridinic N species, but because the total nitrogen content decreased, the correlation between quaternary nitrogen species and activity could not be directly depicted[269]. In addition, the authors also investigated the effect of metal type (Fe or Co) and metal loading on the catalyst composition, morphology and resulting performance. It was noted that compared to Co-based catalysts, more active Fe-based catalysts showed higher amounts of graphitic nitrogen, but authors discussed the unlikeliness for this type of nitrogen to be the most active catalytic site; instead the apparent correlation might have been associated with beneficial morphological changes. In general, the authors didn't find strong direct correlations between activity and specific nitrogen functionality[269]. Correlations between XANES, XPS, BET and ORR activity for a polyaniline-iron-carbon catalyst revealed close correlation between ORR activity, Fe-N content, BET, and microporous surface area. The authors of this study also observed correlation of ORR activity to the total amount of graphitic and quaternary nitrogen and the ratio of pyrrolic N to

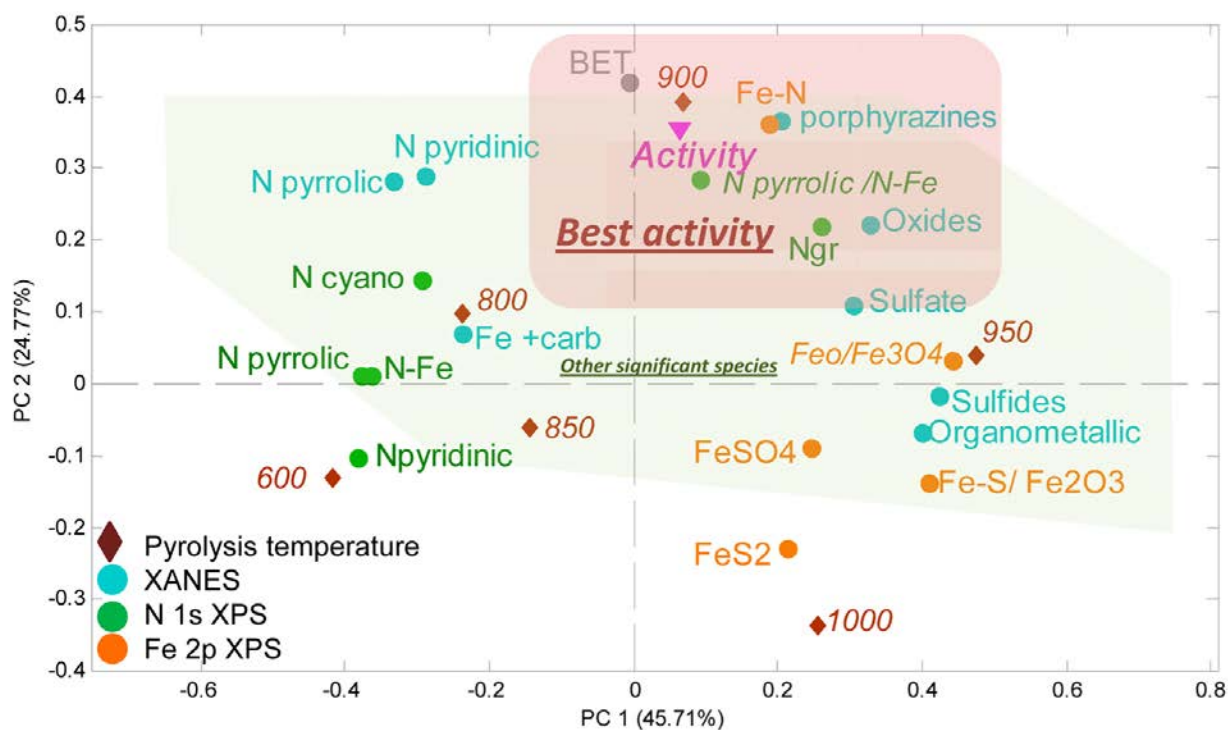


Figure A.9: Correlation between XANES, XPS, and BET data and ORR activity for PANI-Fe-C using principal component analysis. All catalysts after heat treatment, acid leach, and a second heat treatment. Reprinted (adapted) with permission from Citation(Ferrandon et al., 2012). Copyright (2012) American Chemical Society.

Fe-N species (Figure A.9). These findings showed the importance of the relative distribution of nitrogen functionalities in determining catalytic performance[263]. Aiming at improving the stability of polyaniline-derived catalysts, Wu et al. increased catalyst graphicity by using CNT's as the support[260]. Fe-N_x centers and quaternary nitrogen incorporated into carbon structures have been proposed as possible active sites in iron-imidazole-derived catalysts[275]. Ramaswamy also investigated the role of the carbon basal plane in more detail, demonstrating that changes in the transition metal redox potential are closely related to pyrolysis-induced integration of the Fe-N_x centers into the π -electron-deficient environment of the carbon[267].

Another approach to increase the density of nitrogen-containing active sites was proposed by Kothandaraman et al. through the pyrolysis of nitrogen and iron precursors, mixed with

high surface area carbon, performed at high pressure in a closed container[276]. For materials prepared using high-pressure pyrolysis, the concentration of incorporated nitrogen and the corresponding ORR activities were greatly affected by the structure and composition of the carbon support[277]. Byon investigated surface functionalization of multi-walled CNT's for incorporation of sites participating in ORR and observed higher ORR mass activity when materials possessed higher amounts of Me-N_x (where x~4) as well as greater Fe/C ratios [278]. Arechederra et al. demonstrated incorporation of nitrogen and iron or cobalt into carbon nanotubes from phthalocyanines using low temperature solvothermal synthesis[279].

Several reports have discussed self-supporting catalyst materials prepared without carbon support using sacrificial silica templates[262, 270, 280–282]. Serov et al. showed that performance of iron-aminoantipyrine-derived catalysts prepared with a sacrificial support had a greater density of active sites as compared to a carbon-supported catalyst. The best performance was obtained for the catalyst pyrolyzed at 800 °C. At higher pyrolysis temperatures the performance dropped, most likely due to decomposition of active sites. Doubling the amount of the nitrogen precursor relative to the amount of transition metal resulted in significant improvement in the catalytic activity. Further increases in the amount of the nitrogen precursor, however, led to a drop in the performance[283]. Olson et al. prepared catalysts based on pyrolyzed porphyrins with nitrogen and cobalt content of 5 at% and 1.24 at%, respectively. The catalyst was subjected to various treatments with the objective of selective removal/enrichment of catalyst with different moieties. Authors reported a decrease in the halfway potential upon removal of either Co-N_x or Co_xO_y/Co. It was hypothesized that oxygen reduction follows two-by-two electron pathway, where the first step occurs on the Co-N_x and second on Co_xO_y/Co. Materials depleted in active Co-N_x and Co_xO_y/Co showed correlation between high concentration of graphitic carbon and graphitic nitrogen and lower amounts of produced peroxide, suggesting that these species might contribute to decomposition of peroxide[270]. In the absence of transition metal, N-containing catalysts derived from poly(ethyleneimine) showed a high peroxide yield, which was significantly reduced with

the addition of iron[282]. Catalysts derived from iron and 4-aminoantipyridine, which had nitrogen and iron contents of 3.5 at% and 0.1 at% respectively, also followed the 2x2 electron transfer pathway. This material was shown to be effective in acid and alkaline media and was found to be especially good at reducing peroxide[280, 283]. Other reports also evaluated activity of the NPMC's at different pH, demonstrating the potential of these materials in alkaline media[284–286]. In these studies, iron and nitrogen-containing electrocatalysts were shown to have 7-10 times higher ORR activity in alkaline media when compared to acid media[285]. Investigation of cobalt-polypyrrole electrocatalysts in alkaline media suggested dual-site mechanism where Co-N_x acted as an active site for the 2e^- process[286].

NPMC catalysts based on graphene have been studied in acid[261] and alkaline media[266, 287, 288]. Byon reported synthesis of NPMC based on heat-treatment of chemically reduced graphene in the presence of iron salt and graphitic carbon nitride. Increased integration of Fe-N_x centers were observed for temperatures between 600 and 700°C. This material contained ~5 at% of nitrogen and 0.4 at% of iron, where on average, the Fe was coordinated to 3 nitrogen atoms (based on EXAFS analysis)[261]. Similar to observations in acid media, the ORR performance and stability of the N-doped materials was improved by incorporation of iron[288] or cobalt[266, 287]demonstrating the necessity for both nitrogen and transition metal.

In addition to non-precious metal N-containing catalysts derived from pyrolysis of transition metal and nitrogen precursors, N-functionalization was also demonstrated for catalysts based on carbon-supported high-loading transition metal oxides[253, 289–293]. Liang et al. reported on the effects of nitrogen doping on the nucleation and growth of Co_3O_4 ; demonstrating the reduction of particle size from ~12-25 nm to ~4-8 nm. Additionally, incorporation of nitrogen resulted in positive ORR peak potentials, higher peak currents and more positive halfway potentials as well as lower peroxide yields. Authors reported the results of XANES analysis indicating a bond formation between Co_3O_4 and N-doped graphene[289–292]. Later, authors also described electrocatalysts based on manganese-cobalt oxide and

graphene[294] and reported high-performance hybrid catalysts based on cobalt oxide and N-doped carbon nanotubes[292]. He et al. also reported narrow nanoparticle size and synergistic effects between N-doped graphene and cobalt oxide. Authors reported that addition of nitrogen and cobalt oxide improved ORR activity and four-electron selectivity, while the addition of nitrogen only improved the onset and half-wave potentials. Spectroscopic analysis, paired with DFT, were used to hypothesize that pyridinic nitrogen species in N-doped graphene might be coordinated to cobalt ions[290]. Impressive ORR performance in alkaline media was demonstrated for carbon-nanotube/carbon nanoparticle composites synthesized from iron acetate and cyanamide[289]. Nitrogen surface groups were also shown to improved stability of iron nanoparticles, decreasing their sintering[295].

A.4.1.4 Metal-free N-containing catalyst systems for oxygen electroreduction

Many groups report that ORR performance of carbon material could be significantly improved upon doping with nitrogen even in the absence of nitrogen-coordinated transitional metal complexes. Increases in the current densities and decrease in the overpotential are observed for metal-free N-doped systems when compared to undoped references. Most of the studies focus on N-doped CNT's and graphene, but a few also report on carbon blacks[296, 297], porous carbons[184, 298] carbon nanoshells[299] and carbon nitrides[300]. Some groups also investigated composite structures made with both CNT's and graphene[301, 302]. Based on the fact that many studies use iron during the synthesis, and treatments utilized to remove the iron might not be 100% efficient, most "metal-free" materials might actually still have some trace transition metal sites that might be responsible for the observed effects. Therefore there is a debate among researchers whether truly "metal-free" N-doped carbons are as active as reported.

Vertically aligned CNT's showed significant improvement in kinetics of ORR in both acid and alkaline media[303]. Gong et al. evaluated vertically aligned N-doped CNT's in alkaline media and reported high electrocatalytic activity, a four-electron pathway and good stability after potential cycling. Authors synthesized vertically aligned N-doped CNT's using pyro-

lysis of iron and nitrogen containing precursor, iron (II) phthalocyanine, with and without NH_3 , followed by removal of residual iron[162]. Vertically aligned N-doped CNT's produced from ferrocene under ammonia [304]also showed improved onset and peak potential, but due to lower amount of doped nitrogen underperformed as compared to the phthalocyanine-based materials. The same work also discussed vertically aligned CNT's doped with boron and demonstrated that CNT's co-doped with nitrogen and boron show synergistic effect on ORR performance, meanwhile CNT's doped with boron only are less effective than N-doped material [304]. Good ORR activity was demonstrated for N-doped CNT's and N-doped graphene obtained from melamine with and without assistance from metal atoms [69, 138, 156, 305]. McClure et al. synthesized N-doped carbon nanowall electrodes without a metal catalyst and observed an increase in kinetic current density and the number of electrons transferred per O_2 as total nitrogen concentration increased, specifically graphitic nitrogen and pyridine-N-oxides[306]. Investigation of CNT's doped with nitrogen by ammonia treatment revealed a gradual positive shift in onset potential and an increase in the limiting current when the temperature increased from 200°C to 800°C . The increase in the temperature associated with reduction of the total amount of nitrogen and oxygen functionalities, was, however, accompanied by a relative increase in quaternary nitrogen with respect to pyridinic and pyrrolic groups, suggesting the importance of the formation of quaternary nitrogen for the improvement in the ORR performance[160]. Higher temperature treatment (which decreases the amount of nitrogen) and higher loading of polypyridine precursor on the surface of the carbon black (which increases the amount of nitrogen) were beneficial for ORR activity[307]. Higher temperature was also shown to be beneficial to ORR activity of nitrogen-rich mesoporous carbon materials[308]. Surface coatings rich in pyridinic and quaternary nitrogen groups obtained by pyrolysis of cyanamide result in improved onset potential and ORR kinetics [309]. Likewise, Liu also reported pyridinic and quaternary nitrogen as proposed ORR sites [310].

Improvements in ORR activity as a function of nitrogen concentration were reported for CNT's synthesized from pyridine[311], diamine[312] and melamine[69] precursors. Interesting findings in regard importance of clustering of nitrogen atoms were reported by Zhang et al. Authors discussed that the number of active sites per dopant atom is maximum when clusters consist of two nitrogen atoms. Further increase in the cluster size reduces the number of active sites[238]. For the pyridine-based materials, a small increase in the nitrogen concentration had a large effect on the limiting current density and H₂O selectivity and a smaller effect on the onset and half-wave potential[313]. Similarly, an increase in nitrogen concentration had no effect on onset potential, but led to an increase in the current density for the melamine-derived graphene[138]. Materials derived from diamine with different nitrogen to carbon ratios showed a larger range of nitrogen concentrations (1.2-4.74 at.%), which was associated with a higher degree of edge plane defects arising from pyridinic species[312]. N-doped CNT's synthesized with ethylenediamine showed improvements in onset and half-wave potential, limiting current density, number of electrons transferred, and H₂O selectivity when compared to CNT's made with pyridine. This effect was attributed to the higher nitrogen concentration and surface defects[314]. Chen et al. also compared CNT's synthesized from ferrocene and iron (II) phthalocyanine, and concluded that when the nitrogen concentration is similar, CNT's with more surface defects perform better. In this work, the authors employed an acid treatment process to remove iron seed atoms, but reported that about 0.2-0.27 at% of the iron remained, which is near the same level as previously discussed in the NPMC catalysts section([311]. Zhao correlated ORR activity to the concentration of species at binding energies of 398.3 and 401.5 eV rather than the total nitrogen content[315]. Singh et al. reported correlation between pyridinic N and ORR activity of CN_x grown on two different substrates[316]. Biddinger suggested that the total amount of nitrogen or nanostructure on its own are not so important; rather it is the amount of nitrogen incorporated into graphitic structure that matters [317]. Taking into account these observations, it is clear that there is a need for systematic studies aimed at understanding the importance of specific functionalities,

in addition to total nitrogen content.

Since a lot of N-doped materials do contain small amounts of metal, investigations aimed at evaluating the effect of nitrogen vs. the effect of residual metal/metal oxide phase are important. Masa et al. compared the performance of catalysts made without metal precursor, with metal precursor and with addition of trace amounts of metal and showed that the performance of the metal-free materials was the lowest and was significantly effected by the addition of iron even at very low concentrations (0.05%) [318]. A mechanistic study by Wiggins-Camacho et al. concluded that both nitrogen groups and residual surface metal oxide/metal phase participate in the ORR on N-doped CNT's. The authors correlated the gradual shift in ORR on-set potential with the increase in the nitrogen content. In addition, reduction potential was correlated with an increase in the amount of pyridinic species and a decrease in the pyrrolic species. This work suggested that on N-doped CNT's, the reaction undergoes a "pseudo"-four electron pathway, where the first step of two-electron electrochemical reduction of O_2 is followed by chemical disproportionation. The last step occurs faster on the CNT's with larger concentrations of nitrogen and involves the iron oxide/iron sites stabilized by the pyridinic nitrogen groups (See Figure A.10)[319]. The mechanistic investigation of ORR on N-doped CNT's in alkaline media conducted by Vazquez-Arenas proposed parallel two and four electrochemical electron pathways of ORR on N-doped CNT's in alkaline media[320]. N-doped CNT's were also investigated in neutral pH phosphate buffer solution suggesting a four-electron pathway[321]. Deak et al. used carbon monoxide and cyanide to probe the active sites in CN_x , suggesting that metal centers are not involved. In contrast, Li observed more than 100 mV decrease in the onset potential and changes to the diffusion-limiting current in the presence of cyanide ions, indicating the involvement of iron in the ORR. Moreover, aberration-corrected STEM-ADF and EELS mapping of graphene sheets that were active for the ORR showed the presence of iron and nitrogen atoms in close proximity to each other [322].

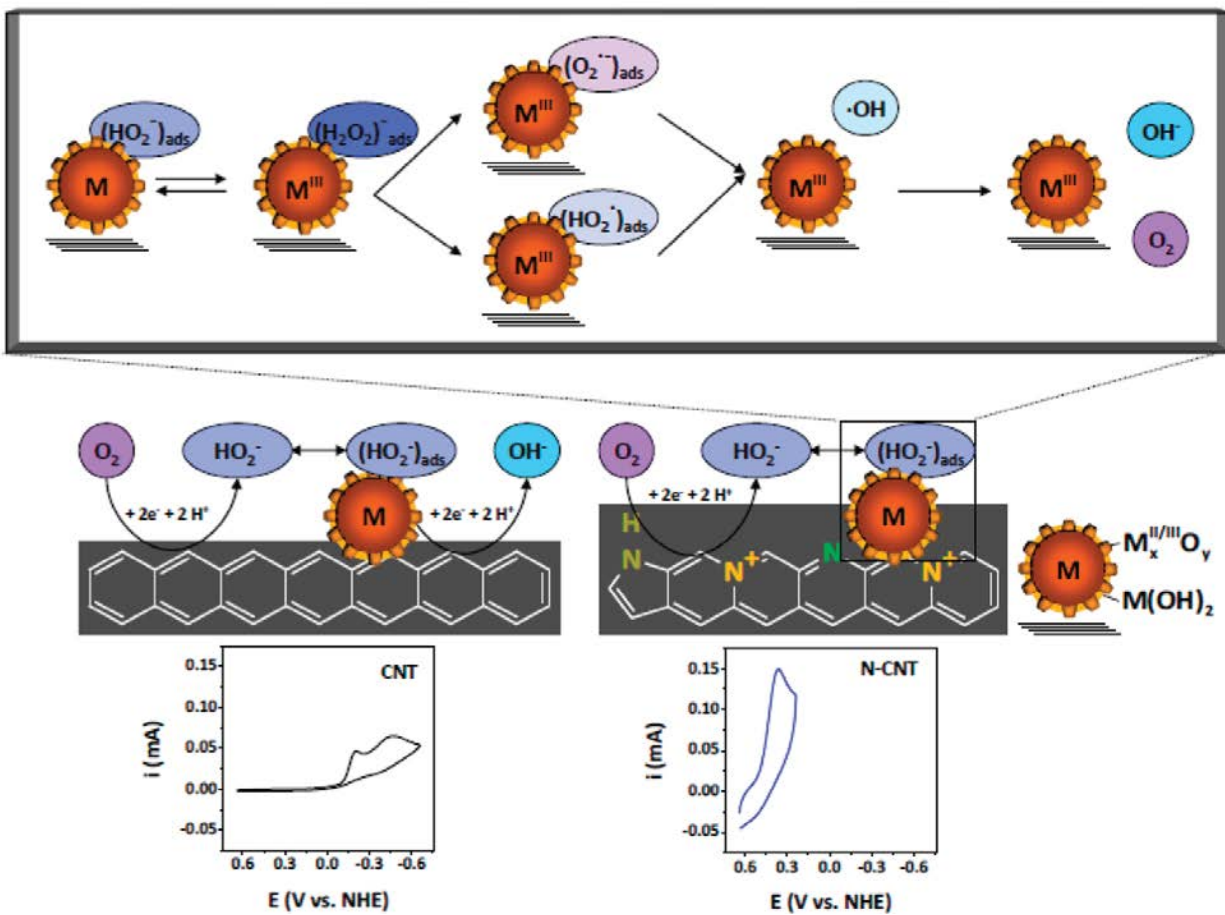


Figure A.10: Graphical Representation of Proposed ORR Mechanism at CNT versus N-CNT Electrodes with Representative Cyclic Voltammograms for CNT's and 6.3 at. % N-CNT's in 1 M Na_2HPO_4 (V vs. NHE). Reprinted (adapted) with permission from Citation(Wiggins-Camacho & Stevenson, 2011). Copyright (2011) American Chemical Society.

Beyond CNT's, metal-free N-modified mesoporous carbons have also been investigated as ORR electrocatalysts. Silva et al. investigated mesoporous carbons derived from polyaniline and concluded that high catalytic activity of metal-free materials was most likely due to synergistic effect of nitrogen and oxygen functionalities[184]. Another class of N-doped porous carbons that showed promising ORR activities was derived using porous organic framework as sacrificial template[298].

In recent years, many groups have studied N-doped graphene as an efficient catalyst for ORR in alkaline media with performance comparable to that of commercial Pt/C catalysts[37, 70, 133]. Qu et al. reported large area synthesis of N-doped graphene using ammonia. This material showed great catalytic activity via a four-electron pathway and long-term stability[37]. Geng et al. employed an ammonia treatment at temperatures of 800-1000 °C to incorporate 2-2.8 at% of nitrogen. The authors suggested that nitrogen species located at binding energy of 401.3 eV might be responsible for the improvement in onset potential. The largest shift in the onset potential and close to four-electron reduction process was reported for the material pyrolyzed at 900°C (Geng, Chen, et al., 2011). Niwa analyzed three sets of materials using XAS to propose the importance of graphitic nitrogen over the pyridinic nitrogen[323]. To facilitate the formation of graphitic nitrogen species (at 401-401.2 eV), Lin et al. reported pyrolysis of graphene oxide with polypyrrole[324] or polyaniline[325] being the N source[324]. Another approach using a thermal annealing process with urea resulted in nitrogen concentrations close to 2-3 at % [326]. High levels of nitrogen (~10.6%) were achieved using a solvothermal method employing ammonia as both the nitrogen source and the reducing agent[327]. Investigation by Luo et al. showed a two-electron reduction mechanism on graphene doped with pyridinic nitrogen, suggesting that these species may not be as beneficial for ORR as other functionalities[32]. In contrast, the activity of hollow mesoporous carbon with graphene-like structure was attributed to the availability of pyridinic nitrogen[328]. This could be explained using a study by Brun et al. which discussed the fact that selectivity for the $2e^-$ vs. $4e^-$ electron pathways can be controlled by tuning the

pyrrolic/pyridinic nitrogen ratio[329]. More recently, Guo et al. reported that the pyrrolic nitrogen species present in materials pyrolyzed from blood protein in the presence of carbon black are possible catalytic sites for four-electron transfer [330]. Lai et al. compared ammonia treatment vs. pyrolysis of polyaniline and polypyrrole and reported preferential formation of graphitic and pyridinic N via the first route and pyridinic and pyrrolic N via the second [331]. Authors also reported positive effects from graphitic N on the limiting current density and from pyridinic N on the onset potential.

A.4.2 Batteries

Carbonaceous materials doped with nitrogen have been vigorously explored for application in non-aqueous Lithium-air batteries. In these applications, the oxygen reduction reaction at the cathode is similar to the ORR reaction at the fuel cell cathode and therefore many of the advantages discussed in the previous sections also apply to this field of research.

Li et al. evaluated the performance of N-doped graphene nanosheets with 2.8 at% nitrogen and demonstrated several improvements over undoped material: First, the N-doped material showed higher discharge plateaus at various discharge current densities and specifically demonstrated 40% higher discharge capacity at a current density of 75 mA/g. Secondly, the onset potential, current densities and the number of transferred electrons were also improved. Analysis of discharge products revealed more uniform distribution of the particles, indicating a larger number of active sites[332]. N-doped CNT's with nitrogen concentration of 10.2 at% showed 1.5 times higher specific discharge capacity as compared to undoped CNT's. N-doped CNT' were also employed in binder-free Li-air batteries[333]. The performance of exfoliated N-doped graphene showed a shift in the onset potential and a predominant four-electron transfer clearly attributed to nitrogen-doping. These promising results were demonstrated in Lithium-oxygen and Zinc-air battery single cells [334]. N-doped CNT's and N-doped carbon fibers have been investigated as efficient catalysts for Zn-air batteries[335, 336]. For example, electrocatalytic activity of carbon fibers produced from polystyrene and polyacrylonitrile was attributed to developed porosity and enrichment with nitrogen[335].

Wu et al. discussed graphene-rich nanocomposites prepared from polyaniline and a cobalt precursor, which were supported on commercial MWCNT's. The temperature of the heat-treatment was shown to be an important factor that affected the nitrogen speciation and in turn improved ORR performance. The authors discussed the formation of desirable functionalities located at 398.6 eV and 401.3 eV (assigned to pyridinic and quaternary nitrogen groups respectively), which they suggest may have been preferentially formed due to the addition of cobalt [337].

Recently, Park et al. reported on a bi-functional nanocomposite made of N-doped CNT's and graphene. The role of the N-doped CNT's is two-fold; in addition to providing catalytic sites, they also connect the graphene sheets and compensate for the loss of conductivity in the graphene resulting from the synthesis via the thermal annealing route. The material was also highlighted for its excellent oxygen evolution reaction (OER) performance [338].

Kichambare et al. investigated mesoporous carbons made with a mix of N-doped Ketjen black and Calgon black[339, 340]. A two times higher cell discharge capacity of the N-doped material was attributed to higher electrocatalytic activity and increased porosity of the N-doped material, thereby leading to higher oxygen diffusivity[339]. The importance of pore structure, in conjunction with high nitrogen content (~ 6.59 at%), was also discussed by Nie[341]. Excellent electrocatalytic activity observed in molybdenum nitride/N-doped carbon nanospheres was attributed to the nanostructure and the synergy between the molybdenum nitride and the N-doped carbon nanospheres[342]. Hybrid catalysts based on MnO_2 nanotubes and N-doped exfoliated graphene have been shown to have increased ORR activity because of defect sites introduced by doping[343].

Various N-doped carbonaceous materials were also explored for application as efficient anode materials in lithium-ion batteries (LIBs) and emerging sodium ion batteries (NIBs). In these systems the purpose of nitrogen doping is to improve the intercalation properties and increase specific capacity. Here it is beneficial to grow N-doped materials directly on the current collector substrate to improve the adherence and electron transport. Due to their

modified electron transport, however, the N-doped carbons often display non-ideal voltage versus capacity plateaus. The capacitor-like sloping V vs. capacity profile of N-rich carbon anodes for both lithium ion and sodium ion applications reduce the total energy density of the cell by limiting the working voltage window and making it difficult to design devices that behave analogously to commercial LIB technology. In fact, where N-rich carbons may have the highest use is in Li ion and Na ion capacitors[344].

A 2010 report published by Reddy et al. examined the benefits of N-doping for graphene films. The addition of nitrogen dopants led to a nearly two times increase in the reversible discharge capacity (Figure A.11a). N-doped films contained about 9 at% nitrogen, with pyridinic nitrogen as the predominant functionality. The effect of nitrogen on performance was explained by the presence of a large number of surface defects associated with nitrogen doping[34]. Several groups discussed that N-doping improves the reversible capacity, rate capability and long-term cycling stability related to enhanced kinetics, as well as the number of active sites, and contributes to more stable interfaces[136, 345, 346]. Materials with higher levels of nitrogen demonstrate higher reversible specific capacity and rate capacity[347]. Li et al. didn't detect a noticeable change in the initial Li⁺ intercalation/de-intercalation associated with doping of ~2.8 at% nitrogen into graphene nanosheets, but reported a remarkable difference in the cycle performance of undoped and N-doped materials[348]. In the N-doped material an increase in the specific capacity was observed starting at 17th cycle and continuing until it reached a maximum at around 501st cycle. Conversely, the undoped graphene demonstrated a typical decrease in the specific capacity (Figure 12b). The authors attributed this effect to the gradual increase in the defects of the already disordered structure of N-doped material. The benefits of the surface defects introduced by N-doping can be effectively combined with benefits of sandwich structures, in which nanoparticles or arrays are sandwiched between graphene sheets[127].

Dispersion and stability of active nanoparticles in graphene-based hybrid anodes can be greatly enhanced via modification of graphene with nitrogen. These properties of N-

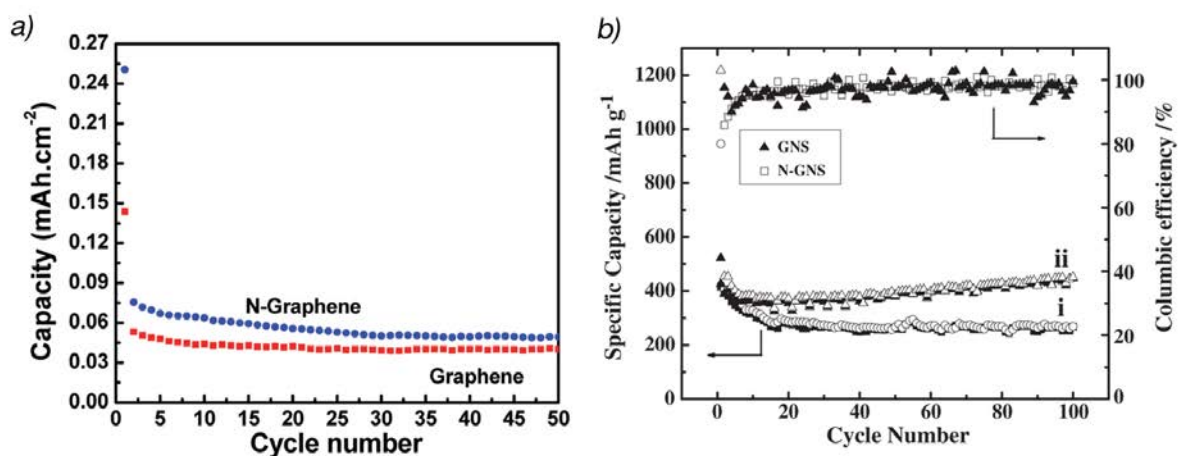


Figure A.11: a) Electrochemical performance of graphene films grown on Cu foil, galvanostatically cycled in Li half cells. Variation in discharge capacity vs. cycle number for the pristine graphene and N-doped graphene cycled at a rate of 5 mA/cm² between 3.2 and 0.02 V vs. Li/Li⁺ in 1 M solution of LiPF₆ in 1:1 (v/v) mixture of ethylene carbonate (EC) and dimethyl carbonate (DMC) as the electrolyte. Reprinted (adapted) with permission from Citation (Reddy et al., 2010). Copyright (2010) American Chemical Society. b) Reversible charge/discharge capacity verse cycle number of (i) graphene-nanosheets and (ii) N-graphene-nanosheets Reprinted (adapted) with permission from Citation (Xifei Li et al., 2011). Copyright (2011) Elsevier.

doped graphene were explored in the hybrid materials with nanoparticles of SnO_2 [127, 130, 349], Fe_2O_3 [350], Fe_3O_4 [351], TiO_2 [352, 353], MnO [354] and NiS [355] demonstrating synergy between the N-doped support and the nanoparticles.

Increase in the specific charge capacities and improvement in rate capability of carbon nanotubes[332, 356, 357]carbon nanofibers[197, 358] and mesoporous carbon materials[359, 360] upon nitrogen doping has been reported by several groups. CNT's with 16.4 at % of nitrogen showed better rate capability and about a two times higher reversible capacity when compared against undoped CNT's[332]. Characterization of a series of N-doped CNT's with nitrogen content ranging from 1.23 to 2.89 at % produced with an acetonitrile precursor revealed that higher nitrogen levels lead to an increase in the first-cycle discharge capacity. The authors suggested that the irreversible capacity is related to the amount of pyridinic nitrogen. The best electrochemical performance was observed for material with the lowest N-content that had the highest relative amount of graphitic nitrogen[356]. Ren et al. investigated CNT's doped with similar amount of nitrogen (1.21-2.83 at %) using melamine as a nitrogen precursor and found that higher nitrogen concentrations not only increase the first discharge/charge capacity, but also increase reversible capacity[357]. A storage capacity of 1780 uAhg⁻¹ was reported for N-doped mesoporous carbons obtained from biomass-derived proteins, the result of an efficient combination of high surface area, graphitization and high nitrogen content (up to 10.1 at%)[360]. Porous nanostructure and high nitrogen content (~13 %) of N-doped carbon capsules resulted in high rate capacity and good cycling performance[361].

The performance of electrode materials (e.g. oxides) with low conductivity can be improved by carbon-coating, where N-doped carbon coatings provide additional benefits as compared to undoped coatings. For example, N-doped carbon coatings were used to improve rate capability and cycling performance of Li_4TiO (LTO)[362, 363]and LiFePO_4 [364]. Using experimental and theoretical studies, Ding et al. suggested that doping nitrogen into carbon coatings improves interfacial stability and electric conductivity[365]. Improvements

in storage capacity, rate capability and/or cyclic performance were also reported for other nitrogen-doped carbon-coated anode materials, including SiO, TiO₂ and CoSnO₃[251, 366, 367]. In addition to the battery applications discussed above, N-doped materials have also been evaluated for vanadium redox flow batteries[38, 368, 369], and lithium-sulfur batteries [164, 370, 371] with promising results. The benefit of N-doping towards improving capacitance of various types of batteries had been clearly demonstrated and further improvements in the performance are expected as the field advances fundamental understanding of N-doping.

A.4.3 Supercapacitors

Carbon materials have been used for decades in capacitor applications. The capacitance of high-surface area carbon-based materials with good conductivity and fast electron transfer rate can be further improved through functionalization with heteroatoms such as nitrogen or oxygen groups. Functionalization is believed to increase the capacitance through pseudocapacitance effects, i.e. via additional Faradaic reactions.

Comprehensive analysis of the pore structure in conjunction with deconvolution of the type of functional groups present is critical to understand the contributions to capacitive performance. This is particularly essential for highly porous materials, where pseudocapacitance is superimposed onto a more significant contribution from double-layer capacitance. In organic electrolytes, the pore size plays a particularly important role. In aqueous electrolytes, the porous structure still greatly controls capacitance, but the pseudocapacitive effects of heteroatom functionalization are more clearly resolved. Capacitive enhancement due to nitrogen functionalization has been shown by comparing highly-porous nitrogen-containing carbons and porous carbons with no nitrogen, but similar textural characteristics[372]. Furthermore, significant (e.g. 2X) capacitive enhancement has been observed upon the addition of surface nitrogen to porous carbon already containing nitrogen in the bulk[373]. In addition to increased capacitance due to pseudocapacitive effects, the enhancement in the electrochemical properties of N-containing carbon supercapacitor materials has also been attributed at least in part to improved wettability[373–376].

Hulicova-Jurcakova et al. synthesized ammonia-treated low surface-area non-porous carbon materials prepared from melamine-mica composites which demonstrate excellent cycleability and three times higher gravimetric capacitance than untreated composites. Materials pre-oxidized prior to ammonia treatment exhibited higher nitrogen content, larger concentration of pyrrole-like nitrogen groups and showed improved pseudocapacitance[377]. Others also reported pseudocapacitive effects in the presence of positively-charged pyrrole species detected at XPS binding energies of 400.0-400.3 eV[378–380]. In another study, Hulicova-Jurcakova et al. modified coconut-shell-based microporous carbons with nitrogen functional groups from urea and melamine precursors to investigate the combined effect of nitrogen and oxygen functional groups[377]. Pyridinic and pyrrolic nitrogen groups (along with quinone oxygen groups) had the largest effect on capacitance, meanwhile the positive charge of quaternary and pyridinic-N-oxides also improved capacitance, particularly at high current loads. Amino-functionalization of carbon nanotubes was also shown to enhance capacitance[381]. Lai et al. compared the effect of various surface functionalities on the capacitance of graphene/polyaniline composites and found that among chemically-reduced (RG-O), nitrogen-doped RG-O and amine-modified RG-O, the latter had the highest capacitance, reaching up to 500 F/g (in acid electrolyte)[382] (see Figure A.12). Researchers also examined supercapacitor performance for surface-functionalized graphene/polypyrrole composites. In this study, an amine-modified graphene/polypyrrole composite showed higher capacitance than unmodified graphite oxide, but both were clearly outperformed by composites made with N-doped graphene, which demonstrated a high specific capacitance of 393.67 F/g.[375] This performance was attributed to improved electron transfer efficiency and surface wettability. In a similar vein, composites of polyaniline and graphene functionalized with oxygen groups outperformed nanocomposites made with oxygen functionalized graphene and metal oxides such as RuO_2 , TiO_2 and Fe_3O_4 [383]. About 4 times higher capacitance was observed for the nitrogen-plasma modified graphene as compared to pristine graphene; the enhancement was linked to nitrogen sites at the basal planes of the graphene[144]. In 2012,

a report used direct synthesis to fabricate C_3N_4 coated graphene, which had a surface area of $465\text{ m}^2/\text{g}$, large pore volume, and 10.8 at.% N. This material performed well in electrochemical testing because of easy ion transport as well as good conductivity. The resulting material showed a capacity of 302 F/g in a 6M KOH electrolyte[384].

The effect of carbonization temperature on the nitrogen content, speciation, pore structure, and their respective contributions toward capacitance have been studied by many[373, 376, 378, 385]. N-containing porous carbon nanofiber papers with moderate to low surface areas, carbonized at temperatures 700-1000°C, demonstrated the effect of pyridinic and pyrrolic functionalities on activity in aqueous media[385]. Evaluation of nitrogen-doped porous carbon derived by pyrolysis of nitrogen-containing salts in the 600-900°C temperature range revealed maximal pseudocapacitance for the 600°C pyrolysis temperature, which was correlated to a large amount of pyridinic and pyrrolic groups. Samples pyrolyzed at 800 and 900°C showed decreased capacitance despite higher surface areas; authors attributed this to poor functionalization. The sample pyrolyzed at 700 °C showed the highest overall capacitance (245 F/g, alkaline electrolyte), the result of a good balance between surface area and nitrogen content. In a similar vein, the effect of synthesis temperature on the performance of terephthalonitrile-derived nitrogen-rich networks was studied, identifying important differences between materials produced below 550°C vs. those synthesized at temperatures above 550°C. While it is typically reported that nitrogen content decreases with increasing carbonization temperature, in general, nitrogen-doped porous carbons synthesized from ionic liquid precursors have allowed researchers to obtain higher nitrogen content even at high carbonization temperatures [178, 189, 386].

Motivated by a focus on sustainability, nitrogen-doped porous carbons have been prepared from gelatin using an activation process involving NaOH[204] as well as via a dual carbonization method without physical/chemical activation[387]. Xu et al. reported capacitance in the range of 172-385 F/g (alkaline electrolyte) for materials with nitrogen concentrations ranging from 9.26% to 0.88 at% and BET surface areas from 323-3012 m^2/g .

The highest capacitance was observed for the samples with highest BET surface area and lowest N content. Nevertheless, pseudocapacitive effects were obtained in the samples with the highest nitrogen content, and despite much lower BET surface area, these samples still demonstrated capacitance reaching 172 F/g. Carbon spheres derived from polypyrrole nanospheres by carbonization showed poor capacitance despite their high nitrogen content (up to 14.3 %), although the materials had surface areas below 100 m²/g. The authors reported much improved capacitance once the carbon nanospheres were chemically activated using potassium hydroxide to obtain microporous carbon spheres with higher BET surface area (1080 m²/g) and significantly lower nitrogen content (around 2.2 %)[180]. A similar trend was observed for templated porous carbon treated either with potassium hydroxide or carbon dioxide: after treatment, the nitrogen content decreased while porosity increased[388]. In general, the synthesis and treatment approaches that lead to high nitrogen content tend to favor low surface area, while procedures to enhance surface area tend to also decrease nitrogen content. It is clear that there is still significant need for further innovations in synthesis so that materials can be obtained with high nitrogen concentration while also achieving high porosity.

Wu et al. reported that graphene aerogels show enhanced pseudocapacitive contribution upon doping with either nitrogen or boron. Moreover, the authors reported that materials co-doped with nitrogen and boron demonstrate a synergistic effect[389]. Generally, carbon materials doped with nitrogen and boron show higher specific capacitance than their undoped counterparts. For example, Konno et al. reported specific capacitance for a B/C/N composite measured in sulfuric acid that exceeded 300 F/g[390]. Guo et al. reported specific capacitance values for boron and nitrogen co-doped porous carbons of up to 268 F/g in potassium hydroxide electrolyte[374]. Comparable specific capacitance values were achieved for boron and nitrogen substituted carbons synthesized using a combination of polyborazine as the nitrogen/boron precursor and coal tar pitch as the graphitizing precursor. This method allowed for the simultaneous incorporation of N and B at high concentrations (10 and 14 at

%, respectively) and it was suggested that boron aided the stabilization of nitrogen during the pyrolysis[391]. Increasing the pyrolysis temperature during the growth of boron and nitrogen-doped aligned nanotubes synthesized from melamine diborate enhanced the incorporation of both dopants. Promising electrochemical performance and pseudocapacitance has also been shown for glucose-derived microporous carbon co-doped with nitrogen and phosphorus using ammonium phosphate as a phosphorus and nitrogen precursor[392]. Table A.1 compares some advances made in the supercapacitor field, using nitrogen doping, over the last 5 years.

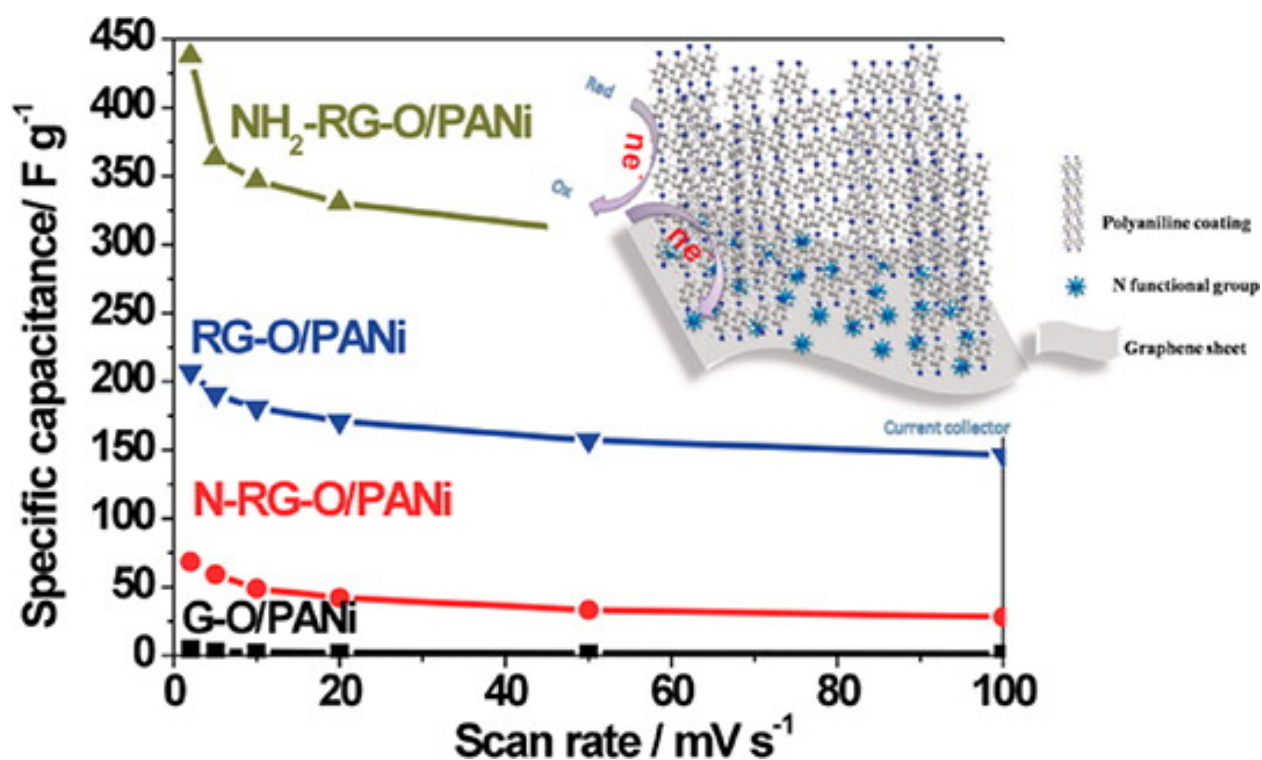


Figure A.12: Performance of 10 wt% PANi as a function of scan rate (from 2 to 100 mV/s) in 1M H₂SO₄ electrolyte. Reprinted (adapted) with permission from Citation (Lai, Yang, et al., 2012). Copyright (2012) American Chemical Society.

Table A.1: Recent reports on progress of supercapacitors

Carbon structure	Technique	N-content	Functional groups	Surface area m^2g^{-1}	Conditions	Capacitance (Fg^{-1})	Cycling Retention	Reference
Mesoporous carbon	Ionic Liquid	~ 8.2 at%	Pyridinic, quaternary, oxidized	931	6 M KOH @1 A/g	210	91% (1000 cycles)	(Qiu et al., 2013)
Porous carbon	Gelatin via activation with NaOH	$\sim .9$ at%	pyrrolic/pyridone, quaternary	3012	6 M KOH @1A/g @50A/g	385 281	96% (2500 cycles)	(Xu, Hou, Cao, Wu, & Yang, 2012)
Mesoporous carbon	Ethylene diamine and carbon tetrachloride w/NaOH Activation	$\sim .8$ at%	NR	2833	6M KOH @2 mV/s	318	NR	(Jiang, Gao, Xia, & Hu, 2009)
Porous carbon	Solvent exchange	~ 2.6 at%	NR	~ 515	TEATFB in Saturated PC/DMC @.5mA	18.6 10.1 (no N sample)	NR	(Candelaria, Garcia, Liu, & Cao, 2012)

Table A.1: Continued.

Carbon structure	Technique	N-content	Functional groups	Surface area m^2g^{-1}	Conditions	Capacitance (Fg^{-1})	Cycling Retention	Reference
Graphene	PECVD	1.5-2.5 at%	Graphitic, Pyridinic, pyrrolic	NR Theory Value: ~ 2600	6 M KOH @.1 A/g	280	NR	(Jeong et al., 2011)
Porous carbon	Heating with ammonium phosphate	4.8%	Pyridinic, pyrrolic, quaternary, pyridic-N-oxides	445.1	6 M KOH @.05A/g	183.8	NR	(C. Wang et al., 2013)
Mesoporous carbon	Carbonization of polyacrylonitrile-based carbon	15.5 wt%	pyrrolic/pyridone, quaternary, pyridinic	635	1M H_2SO_4 @1A/g	191	NR	(Yang, Wu, Chen, & Fu, 2010)
Graphene	Chemical polymerization of pyrrole	10 wt% (Not measured by XPS)	Assumed Pyrrolic not examined in XPS	NR	6 M KOH @.26A/g	296.9	90% (540 cycles)	(Lai et al., 2012)
Porous carbon	Pyrolysis and carbonization of gels	7.1 at%	C-B-N	894	6 M KOH @.1A/g	268	NR	(Guo & Gao, 2009)

Table A.1: Continued.

Carbon structure	Technique	N-content	Functional groups	Surface area m^2g^{-1}	Conditions	Capacitance (Fg^{-1})	Cycling Retention	Reference
Graphene	PECVD	1.5-2.5 at%	Graphitic, Pyridinic, pyrrolic	NR Theory Value: ~ 2600	6 M KOH @.1 A/g	280	NR	(Jeong et al., 2011)
Porous carbon	Heating with ammonium phosphate	4.8%	Pyridinic, pyrrolic, quaternary, pyridic-N-oxides	445.1	6 M KOH @.05A/g	183.8	NR	(C. Wang et al., 2013)
Graphene	Poly-condensation of aniline	NR	C-N	NR	1M H_2SO_4 @10A/g	355	NR	(Mishra & Ramaprabhu, 2011)
Mesoporous carbon	Carbonization with quinoline	5.4 wt.%	Pyridinic, Pyrrolic, Quaternary, Oxidized-N	1428	1M H_2SO_4 @ 1mV/s	108	NR	(Kim et al., 2010)AM
Porous carbon	Chemical activation of novolac resin	7.8 wt%	NR	2679	1 M TEABF_4/PC @ 1mA/ cm^2	180.4	NR	(Y. J. Kim et al., 2010)
Microporous carbon	Melamine and urea treatment	.8%	Pyridinic, pyrrolic, quinone	804	1M H_2SO_4 @1A/g	~ 210	NR	(Hulicova-Jurcakova, Seredych, Lu, & Bandosz, 2009)

Table A.1: Continued.

Carbon structure	Technique	N-content	Functional groups	Surface area m^2g^{-1}	Conditions	Capacitance (Fg^{-1})	Cycling Retention	Reference
Graphene	PECVD	1.5-2.5 at%	Graphitic, Pyridinic, pyrrolic	NR Theory Value: ~ 2600	6 M KOH @.1 A/g	280	NR	(Jeong et al., 2011)
Porous carbon	Heating with ammonium phosphate	4.8%	Pyridinic, pyrrolic, quaternary, pyridic-N-oxides	445.1	6 M KOH @.05A/g	183.8	NR	(C. Wang et al., 2013)
Carbon nanotubes	Amidation reaction	17.7 at%	C-N, N-C=O	166	1M H_2SO_4 @1 mV/s	180.5	NR	(Hsieh, Teng, Chen, & Cheng, 2010)
Graphene	Amine functionalization with PANi	9.6 at%	Pyridinic, amine, admide	320	1 M H_2SO_4 @1A/g	388	119% (after 640 cycles)	(Lai, Yang, et al., 2012)
Carbon nanofibers	Carbonization activation of PAN (PAN-900)	6.9 at%	pyridinic, pyridonic and pyrrolic	~ 375	6 M KOH @1A/g	~ 205 No data reported	>95% After 5000 cycles (no numbers reported)	(Ra, Raymundo-Piñero, Lee, & Béguin, 2009)

Table A.1: Continued.

Carbon structure	Technique	N-content	Functional groups	Surface area m^2g^{-1}	Conditions	Capacitance (Fg^{-1})	Cycling Retention	Reference
Graphene	PECVD	1.5-2.5 at%	Graphitic, Pyridinic, pyrrolic	NR Theory Value: ~ 2600	6 M KOH @.1 A/g	280	NR	(Jeong et al., 2011)
Porous carbon	Heating with ammonium phosphate	4.8%	Pyridinic, pyrrolic, quaternary, pyridic-N-oxides	445.1	6 M KOH @.05A/g	183.8	NR	(C. Wang et al., 2013)
Porous carbon	Carbonization of gelatin -Mg-Zn-1	2.12 at%	Pyridine, pyrrolic/pyridone, quaternary	1518	6 M KOH @1A/g	284.1	96.1% (10000 cycles @ 20A/g)	(Chen, Chen, Zhang, & Xie, 2013)
Carbon nano-spheres	Carbonizing polypyrrole	2.2 at%	Quaternary	1080	0.5M H_2SO_4 @100mV/s	237.9	98.7% (3000 Cycles)	(Su et al., 2011)
Porous carbon	Poly-merization of $\text{C}_2\text{H}_4(\text{NH}_2)_2$ and CCl_4	1.72	Assumed graphitic	2970	6 M KOH @1A/g 1.5M TEABF_4 @1A/g	259 165	93% (900 cycles) 83% (900 Cycles)	(Wang, Gao, & Hu, 2010)
Graphene	Hydrothermal reaction of NH_3BF_3	3.0%	Pyridinic, pyrrolic, graphitic, C-N-B	249	1 M H_2SO_4 @1 mV/s	239	$\sim 100\%$ (1000 cycles)	(Wu et al., 2012)

Table A.1: Continued.

Carbon structure	Technique	N-content	Functional groups	Surface area m^2g^{-1}	Conditions	Capacitance (Fg^{-1})	Cycling Retention	Reference
Graphene	PECVD	1.5-2.5 at%	Graphitic, Pyridinic, pyrrolic	NR Theory Value: ~ 2600	6 M KOH @.1 A/g	280	NR	(Jeong et al., 2011)
Porous carbon	Heating with ammonium phosphate	4.8%	Pyridinic, pyrrolic, quaternary, pyridic-N-oxides	445.1	6 M KOH @.05A/g	183.8	NR	(C. Wang et al., 2013)
Porous carbon	Carbonization of polyacrylamide and boric acid	8.1%	Pyridinic N, pyrrolic N, quaternary N	420	1mol/dm^3 H_2SO_4 @2 mV/s	234	NR	(Konno, Ito, Ushiro, Fushimi, & Azumi, 2010)

A.4.4 Hydrogen Storage

High surface area carbon materials such as CNT's and graphene continue to see interest as physisorption materials for hydrogen storage applications. Surface properties of the support, such as surface area, nanostructure and composition are well known to have dramatic effects on the hydrogen storage properties of these materials. Altering the composition and nanostructure through targeted functionalization of the support and design of the pores that promote two-wall interactions[393] have proven to be beneficial approaches to increase the hydrogen binding energy. Direct effects from functionalization, however, are debated, as it is hard to separate their influence from the effects of porosity/texture. The microporosity of the support is believed to be the major player, while functionalization is believed to play a more minor role.

Giraudet et al. created and compared the physical adsorption properties of two classes of nitrogen containing carbon materials. Mesoporous carbon was enriched with nitrogen through ammonia treatment, maintaining a surface area above 1300 m²/g while enabling 1.2-3.9 wt% nitrogen doping levels. A variety of nitrogen functionalities were observed depending on the treatment temperature, yielding hydrogen uptake values from 0.18-0.24 wt% H₂, at 298 K and 4.5 MPa. For the second set of materials, the authors used a hard silica template to synthesize carbon nitrides with up to 20 wt% nitrogen content, consisting of pyridinic and pyrrolic functionalities with high pyridine to pyrrole ratios. This set of materials showed hydrogen uptake values of 0.03-0.05 wt%, at 298 K and 4.5 MPa. The authors concluded that physical characteristics, such as the specific surface area, determined the amount of adsorbed hydrogen, and that the nitrogen groups had no impact. However, the authors did report that nitrogen groups participate in the oxidation reaction during electrochemical adsorption of hydrogen. Later, Giraudet et al. reported on the improved hydrogen-storage properties of nitrogen-enriched mesoporous carbons doped with nickel nanoparticles. Electrosorption of hydrogen benefited from incorporation of nickel, but the combined effect of nitrogen and nickel was negative[209].

Jiang et al. have combined a doping and activation approach that changes the textural characteristics of the carbon[394]. First, the authors showed that pristine ordered mesoporous carbon nitride, despite having half the surface area of ordered mesoporous carbon CMK3, gave similar hydrogen storage performance. This result suggested that the nitrogen dopants may have somehow compensated for the difference in the specific surface area. Second, they demonstrated activated nitrogen-containing carbon spheres with a unique hollow structure that yielded a hydrogen uptake of 2.21 wt.% at 298K and 8 MPa. The authors concluded that hydrogen physical adsorption is facilitated through the unique structure and texture of the material, while nitrogen activates the absorbent and increases defect site density and the binding strength of hydrogen to the carbon.

Activation of hydrogen near the nitrogen sites was also suggested by the work of Parambath et al., who employed nitrogen plasma treatment to dope exfoliated graphene, leading to a 66% increase in the hydrogen uptake[148]. A further 272% increase in the hydrogen uptake was achieved by depositing Pd nanoparticles over the nitrogen-doped graphene, where uniform metal dispersion was facilitated by the modification of graphene with nitrogen heteroatoms (Figure A.13). Moreover, the addition of nitrogen strengthened the binding between the Pd nanoparticles and the graphene support, preventing the detachment of Pd nanoparticles and thus facilitating continuous migration and diffusion of hydrogen to the adsorbate surface. Authors reported hydrogen uptake capacities of 1.97 and 4.4 wt% at 25°C using 2 and 4 MPa respectively. Later, the same group reported similar hydrogen uptake capacity (4.3 wt% at 25°C and 4 MPa hydrogen pressure) for Pd nanoparticle decorated nitrogen-doped graphene synthesized using a one-step green approach. The in-situ process uses solar radiation and combines the formation of graphene nanosheets, nitrogen doping, and the reduction of the Pd nanoparticles in one step[395]. The graphene materials reported in these two papers had similar concentrations of nitrogen, ~7 at% (Figure A.13).

Nitrogen dopants, along with vacancies and other dopants including P and B, can adjust the binding energy between the hydrogen and Pt atoms without inducing a negative effect

on hydrogen storage capacity[237]. The binding energy between N and Pt is rather strong, and thus the binding energy of the second hydrogen increases such that release occurs only when the pressure is reduced to ambient conditions [237]. This is contrary to sidewall vacancies where two hydrogen molecules can adsorb and desorb easily, and thus have the potential to improve hydrogen storage capacities at higher pressures. It is important to note that this study was limited to single defects and authors suggested that clustered defects should be further investigated. Liu et al. have explored the effect of substitutional nitrogen, ranging from 1 to three N atoms in the aromatic ring, on hydrogen adsorption in Li-decorated porous graphene. They observed a clear trend for multiple hydrogen adsorptions, where increasing the number of substitutional nitrogen atoms leads to stronger adsorption energies[396]. Comparing graphitic, pyridinic and pyrrolic nitrogen defects in the Li-decorated graphene system, Lee concluded that as compared to pristine and graphitic structures, pyridinic and pyrrolic structures are more stable, leading to better dispersions of Li atoms without clustering. The pyridinic and pyrrolic graphitic structures were also shown to adsorb and desorb up to a maximum of three H_2 molecules under ambient conditions[235]. A recent theoretical study of four-nitrogen divacancy defects in CNT's suggests that these defects may be more favorable than pyridine-like defects, as they have strong, agglomeration-preventing interactions with Ca atoms and meet the requirements for hydrogen adsorption energy[236]). A first-principles study conducted on graphitic carbon-nitride nanotubes ($g-C_3N_4$), assuming a heptazine-like structure, reported a configuration where hydrogen atoms chemisorbed to each alternate nitrogen atom. The authors predicted fast uptake rates due to easy access to the interior of the tube and a storage capacity close to 5.45 wt% H_2 [234].

Ao et al. have proposed a novel approach to lower the energy barrier for the dissociative adsorption of hydrogen on graphene based on N-doping and the application of an electric field normal to the graphene surface[397]. Further study suggests that the electric field facilitates the dissociative adsorption and diffusion of hydrogen while removal of electric field can be used to release hydrogen[233]. N-doped graphene was also reported to be an

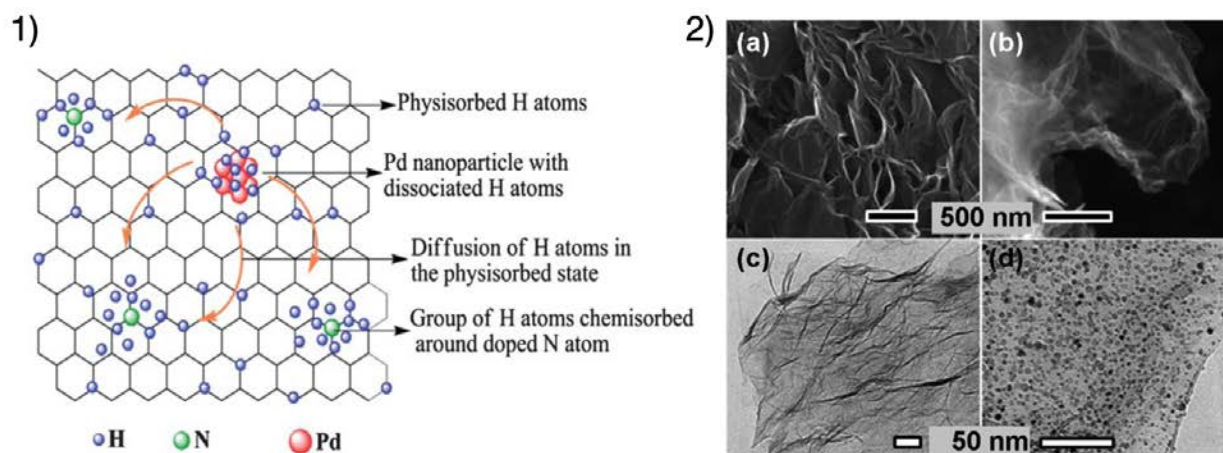


Figure A.13: (1) Hydrogen adsorption mechanism schematic on Pd/N-graphene Reprinted (adapted) with permission from Citation(Z M Ao et al., 2012). Copyright (2013) Royal Society of Chemistry. (2) Scanning electron micrographs of (a) N-HEG and (b) Pd-N-HEG depicting the folds in graphene layers. Transmission electron micrographs of (c) N-HEG and (d) Pd-N-HEG. A uniform dispersion of Pd NPs on N-HEG support is clearly visible. Reprinted (adapted) with permission from Citation (Parambath et al., 2012). Copyright (2012) American Chemical Society.

effective additive to NaAlH_4 to assist with hydrogenation and dehydrogenation reactions. The research team demonstrated that the addition of N-doped CNT or N-doped graphene to NaAlH_4 promotes rehydrogenation as hydrogen molecules are more easily activated on the nitrogen sites [398]. In contrast, the addition of undoped carbon materials doesn't improve rehydrogenation, whose benefit is limited only to dehydrogenation[399–402]. Table A.2 helps show the recent advances in hydrogen storage.

Table A.2: Research in the last 5 years on hydrogen storage

Cabon Structure	Technique	N-Content	Functionalities	Surface area m^2/g	Temp $^{\circ}\text{C}/$ Pressure	Adsorption (wt%)	Reference
Mesoporous carbon	Carbonization with N_2 gas	3.9 wt%	Pyridinic, pyrrolic	984	25/ \sim 3 MPa	0.26	(Giraudet & Zhu, 2011)
Graphene	Plasma treatment	7.0 at%	Graphitic, pyrrolic, pyridinic	NR	25/ \sim 4 MPa	4.4	(Parambath, Nagar, & Ramaprabhu, 2012)
Graphene	GO melamine solar exfoliation	7.0 at%	pyridinic, pyrrolic, graphitic	NR	25/ \sim 4MPa	4.3	(Vinayan, Nagar, & Ramaprabhu, 2013)
Graphene	PPy Poly-merization	6.5 at%	Pyridinic, pyrrolic, graphitic	146.4	25/ \sim 2MPa	1.9	(Vinayan, Sethu-pathi, & Ramaprabhu, 2013)
Graphene nanoflake	Direct synthesis	28.1 at%	Melamine	\sim 180	-196/ \sim 2MPa	1.1	(Jin et al., 2010)
Graphene/CNT's	Ammonia Annealing/ Direct synthesis	\sim 5 at%	NR	NR	180/ \sim 6.5 MPa	1.8	(Kumar, Rao, & Viswanathan, 2013)

A.4.5 CO₂ Capture

Carbon-based materials considered for CO₂ capture must meet several requirements including large adsorption capacity, fast adsorption and desorption kinetics, high selectivity and facile regeneration. It has been previously established that adsorption of CO₂, which is acidic in nature, can be improved using nitrogen sites that are basic in nature[403]. Carbonaceous materials with amine groups were produced from biomass in a two-step process consisting of hydrothermal carbonization of glucose and modification with branched tetramine. These sorbent materials possessed high nitrogen content (5.27 and 10.75 wt%) but very low specific surface areas (less than 20 m²/g) and authors suggested that these materials would benefit from further optimization of the channels and surface area[404]. Low cost soybean was used to synthesize carbon with a surface area 811 m²/g, enriched with pyridinic and amide nitrogen groups[405].

Development of sorbent materials used for CO₂ capture, similar to those used for hydrogen storage, requires consideration of the interplay between textural characteristics and functional groups. Jones et al., in their recent review of sorbents for CO₂ capture, highlighted conflicting trends for the adsorption capacities of activated carbons treated with ammonia at higher temperatures, with one group reporting an increase in the CO₂ uptake and another group demonstrating a decrease[403]. The decrease in the hydrogen uptake was related to the blockage of pores. Results across the field suggest that if the surface area and pore structure are equivalent, N-doped materials provide better characteristics than undoped counterparts. However, it appears difficult to incorporate significant quantities of nitrogen and maintain high surface area and pore structure at the same time.

Hao et al. studied the effect of temperature for a series of nitrogen-doped porous carbon monoliths pyrolyzed at 400-800°C. Despite a low BET surface area of 42 m²/g, the sample treated at 400°C showed a moderate CO₂ absorption capacity of 1.87 mmol/g. Samples synthesized at 500-800°C had an order magnitude higher BET, with the sample pyrolyzed at 500°C demonstrating the highest CO₂ capacity of 3.13 mmol/g. In this group of samples,

nitrogen content slightly decreased but surface area slightly increased, thereby leading to relatively similar CO₂ adsorption capacities [179]. Hierarchically structured porous N-doped carbon structures synthesized with deep eutectic solvents have allowed for the incorporation of relatively high nitrogen concentrations despite relatively high synthesis temperatures. For example, N content of 8-12 at% and 5 at% were reported for 600°C and 800°C synthesis temperatures, respectively. The best CO₂ uptake was obtained for the sample treated at 800°C (3.29 mmol/g at 25 °C and 1 atm). Lower uptake for the sample treated at 600°C was attributed to lower micropore surface area. Authors estimated the isosteric heat values, which decreased with the amount of adsorbed CO₂, and concluded that the materials exhibited two coexisting mechanisms for CO₂ absorption: one occurring on nitrogen sites and the other on undoped carbon sites.

Sevilla et al. have reported CO₂ adsorption uptake of 3.9 mmol CO₂ ·g⁻¹ (at 25°C and 1 atm) in a microporous carbon derived from polypyrrole and activated using KOH agent. The carbon exhibited narrow microporosity and a high concentration of nitrogen groups (~10 wt%)[406]. In addition to a high CO₂ adsorption rate, the authors highlighted the excellent selectivity and regeneration properties of their material. Good selectivity, stability and CO₂ capacities were similarly reported for nanostructured templated carbons synthesized using acetonitrile and post treated with ammonia [406]. These materials exhibited a range of BET surface areas (1361-3840 m²/g) and possessed slightly lower N content (~6-7 wt %) than those reported by Sevilla. The authors observed a linear relationship for CO₂ adsorption capacity vs. BET surface area within a series of undoped carbons. A linear trend was also observed for the series of N-doped carbons, but an increased slope indicated an approximate doubling in capacity for a given surface area (Figure A.14) [407]. Despite dramatic differences in surface area between the N-doped (1762 m²/g) and undoped (3840 m²/g) samples, they both showed similar CO₂ capacities (3.2 mmol/g at 298 K and 1 atm), demonstrating 2.2 improvement related to N-doping. Moreover, optimization of the synthesis procedure allowed for the N-doped, microporous carbons to attain a BET value of 2559 m²/g with a 4.0 mmol/g CO₂

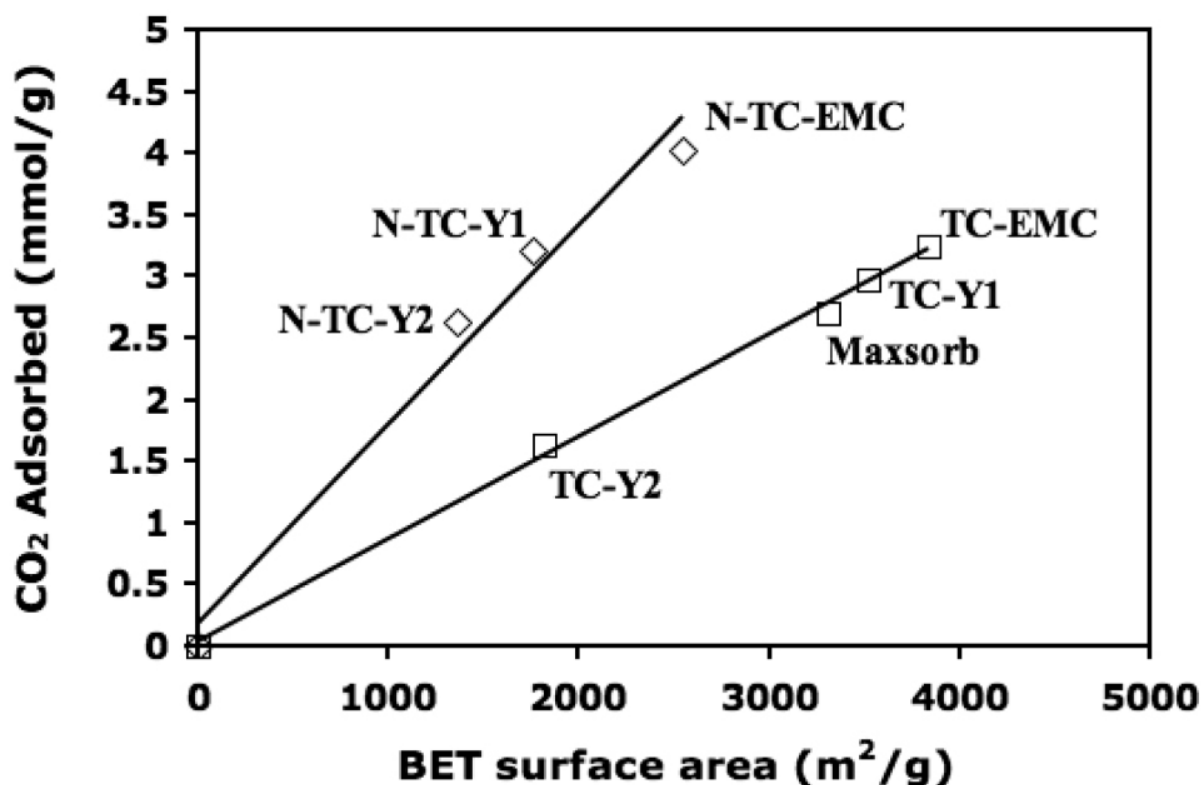


Figure A.14: Relationships between the CO₂ adsorption capacities (at 298 K and 1 atm) and BET surface area of nitrogen-doped carbons and undoped carbons. The N-doped carbons contain 6-7 wt % nitrogen. Reprinted (adapted) with permission from Citation (L. Wang & Yang, 2011). Copyright (2011) American Chemical Society.

uptake[407]. This work provides a clear demonstration that both surface area and N-doping are important factors leading to increased CO₂ capacities. The interplay between these parameters was thoroughly investigated for ordered mesoporous carbons doped with nitrogen using ammonia treatment at 650-1000°C. Samples treated with ammonia at 650 and 800 °C produced relatively lower porosity, but higher capacities per pore. Meanwhile, the sample treated with ammonia at 1000 °C had the highest BET surface area, but the lowest capacity per pore. These results indicate that surface nitrogen functionalities produced at lower temperatures improve CO₂ adsorption, while those produced at high temperature reduce CO₂ adsorption. The authors also established that higher microporosity was beneficial, whereas mesoporosity didn't matter as much[407].

Recently, Wang et al. have studied nitrogen-doped microporous carbons derived from porous polyimine. Their first report examined nitrogen-doped materials produced by calcination at 600-800 °C under argon gas flow. The reported materials had surface areas in the range 263-366 m²/g and nitrogen content ranging from 8.74-5.58 wt%. Interestingly, materials prepared at 800°C had the lowest surface area and the lowest nitrogen content among the calcined samples, but demonstrated the highest CO₂ capacity of 1.955 mmol/g[408]. Their second report examined nitrogen-doped materials also fabricated from polyimine, but chemically activated in KOH at temperatures from 600-750°C[409]. Nitrogen content ranged from 5.05-1.52 wt%, which was lower than the nitrogen content of the calcined materials, but surface areas were significantly improved and reached 1033-3195 m²/g. In this case, the materials prepared at 600 and 650 C showed better performance than the materials prepared at 700 and 750 C, mainly due to their single narrower pore size and higher nitrogen content, although they had lower surface area. The highest CO₂ capacity so far reported for a N-doped porous carbon material (4.3 mmol/g at 1 atm and 298 K) was obtained via a facile one-pot evaporation induced self-assembly process, where HNO₃ was used as a nitrogen source and catalyst, promoting polymerization. The resulting material had 4.32 wt.% nitrogen and a surface area of 1979 m²/g[186]. ?? compares recent publications and their figures of merit for CO₂ capture.

A.4.6 Other Applications

As the field of nitrogen-modified carbon structures continues to grow, its use has expanded to a wide range of other applications. Below we provide a brief discussion on some of these less researched topics.

A.4.6.1 Chemical Production (H₂O₂, butyronitrile, oxidized-cyclohexane)

As of 2007, the annual world production of hydrogen peroxide was about 2.5 million tons, making hydrogen peroxide number 47 on a list of the 100 most important chemicals in the

Table A.3: Recent Progress on CO₂ Capture

Carbon Structure	Technique	N-Content	Functionalities	Surface Area m ² /g	Temp °C	Capacity (mmol/g)	Reference
Porous Carbon	Direct pyrolysis	1.92 wt%	Pyrrolic/amine, quaternary, pyridine-N-oxide	467	25/ ~1 atm	3.13	(Hao, Li, Qian, & Lu, 2010)
Graphene	Chemical modification w/ PANI	NR	C=N, C-N (Raman)	~450 (Mishra & Ramaprabhu, 2011)	25/~11 atm	75	(Mishra & Ramaprabhu, 2012)
Sustainable biomass	Condensation reactions w/ tetramine	10.75 wt%	Amides, tertiary amines, primary amines	<20	-20/~1 atm	4.3	(Zhao et al., 2010)
Sustainable biomass	Heat treatment with N ₂	0.64 wt%	C=N, C-N, N-H	811	30/~1atm	.93	(Thote et al., 2010)
Templated Carbon	CVD	~7 wt%	Pyrrolic, pyridinic, quaternary, pyridonic, Oxidized-N	2559	25/ ~1 atm	4.0	(Wang & Yang, 2011)
Microporous Carbon	Direct Synthesis w/ m-phenylene-diamine	5.58 wt%	Pyridine, quaternary	263	25/~1atm	1.05	(J. Wang et al., 2013)

world[410]. The need for efficient and inexpensive H_2O_2 production is therefore essential; however, direct reactions via H and O are dangerous. To mitigate these risks, attention has been drawn to the idea of reaction separation using an electrochemical flow reactor. With significant current research in improving ORR reaction kinetics, mechanistic analysis of the electrochemical reduction of oxygen on nitrogen modified carbon structures has led to a better understanding of electron reaction pathways. As was previously discussed in the ORR section of this review, the reduction of oxygen with hydrogen does not always proceed through the direct transfer of 4 electrons. Instead, 2 electron or combined electron pathways are typical, which lead to the formation of H_2O_2 instead of H_2O [411].

Fellinger et al. used N-doped mesoporous carbons derived from an ionic liquid to explore the effects of electrocatalytic hydrogen peroxide production. The high-resolution N 1s XPS spectra showed high levels of pyridinic and quaternary nitrogen species in addition too pyrrolic and nitrogen-oxide functionalities (see Figure 2.4). A Koutecky-Levich plot derived from polarization curves obtained at various rotation rates during electrochemical testing clearly revealed a two-electron process[187]. Quantum calculations by Sidik et al. further validated these results, indicating that carbon radical sites formed adjacent to substitutional nitrogen dopants are essential for the reduction of O_2 to hydrogen peroxide in an acid electrolyte[412]. The authors also hypothesized that pyrrolic nitrogen might be a contributing factor in the two-electron nature of the samples; however, the true dependence of the structure on the reactivity remains unclear and further investigations are needed. Photometric determination of a flow reactor using N-doped carbon as the catalyst was able to produce H_2O_2 at .241 Wh/g, corresponding to >65% efficiency. The true utility of this approach lies in its flexibility, relatively low cost, and the ability to synthesize H_2O_2 “on-demand” in specific locations without the need for transport and storage[412].

For similar reasons, the hydrogenation of nitrilic-based species bear industrial interest because the commercial production of amines has a wide range of industrial applications including the fabrication of fungicides, chelating agents, surfactants and fine chemicals. Using

nickel supported on nitrogen-doped carbon nanospheres Nieto-Marquez et al. investigated the hydrogenation of butyronitrile [413]. They hypothesized that nitrogen doping strongly affects the electronic properties of the nickel support, facilitating hydrogenation and enhanced metal sintering through electron surface enrichment.

Within the last year, Cao et al. have explored the aerobic oxidation of cyclohexane (CyH) through a myriad of functionalizations (N,P,B)[152]. Using CVD of aniline-NH₃, N-CNT's were fabricated with ~4 at% N, mostly in the form of pyridinic and substitutional nitrogen defects. N-modified structures had the best mass normalized activity for the oxidation of cyclohexane in the liquid phase with molecular oxygen as the oxidant. Electron transfer between graphene sheets and the reactive radicals was determined to play an important role in the oxidation. The current industrial process for the oxidation of CyH is only about 4% efficient and uses unrecyclable catalysts[414]. Creating an improved and reusable method for this oxidation process would be extremely important for the modern chemical industry, because oxidized CyH is used in the synthesis of adipic acid and caprolactam, which are then used to create various nylon polymers.

Taken together, these recent studies on peroxide, butyronitrile, and oxidized-cyclohexane synthesis using nitrogen-functionalized carbon catalysts suggests that the nitrogen modification approach can play an important role in improving the catalytic processes needed to form a variety of important chemicals.

A.4.6.2 Photocatalysis

Due to environmental concerns arising from global energy demands, problems such as pollution and fossil fuel depletion have inspired the search for ways to convert waste and pollutants into environmentally friendly by-products. To this end, Photocatalysis is touted as a future 'green technology' for the degradation of pollutants, purification of various chemicals (including water), as well as water splitting to form hydrogen. It has been reported that nanoparticles, such as Pt, Au, Ag, ZnO, CdS, TiO₂, CeO₂, and MnO₂, incorporated with structured carbon supports can demonstrate enhanced activity for various catalytic applic-

ations including fuel cells, capacitors, photocatalytic degradation, and photovoltaic devices. However, only a few studies have examined the photocatalytic properties of such catalysts (particularly the semiconducting catalysts) on N-doped modified carbon nanocomposites [415].

Support systems like N-modified graphene can significantly promote charge transfer from semiconductor nanoparticles (like CdS or ZnSe) due to an electron density shift caused by a change in sp² to sp³ bonding configuration[416, 417]. This shift can also accelerate the transfer of electrons between the reactants and the electrode, thereby creating a possible intermediate pathway for chemical transformations during the reaction.

Recently, Min et al. reported on the photoactivity of carbon-supported TiO₂ catalysts, demonstrating a significant increase in activity through the use of nitrogen modified graphene supports[418]. XPS results show that hydrothermal treatment in urea produced an N-graphene structure mostly consisting of sp² bound graphitic nitrogen. To explore the photocatalytic properties, the degradation of benzoic acid (BA) was studied. Adding N-graphene to the TiO₂ catalyst assists the charge separation and surface affinity. It was suggested that N-graphene/ TiO_{2-x}N₂ exhibits improved degradation for BA because the nitrogen-doped graphene facilitates stronger interactions between the organic molecules and the carbon structure through enhanced $\pi - \pi$ interactions, leading to longer electron lifetimes. It was shown that the graphene content must be differently optimized depending on the surface chemistry of the organic being degraded (i.e., BA vs. Methyl Orange). Impedance measurements also showed enhanced conductivity for the graphene supports modified with nitrogen, especially under solar irradiation, which can be an additional factor for the improved performance.

Jia et al. studied the photocatalytic activity of hydrogen evolution on N-graphene/CdS nanocomposites[417]. Their results clearly showed that the hydrogen evolution rate from the CdS catalyst was significantly enhanced by incorporating N-doped graphene. Adding 2 wt% of N-graphene resulted in the most significant increase in H₂ production rate, exceeding

that of pure CdS by more than 5 times and generating 210 $\mu\text{mol/h}$ (0.2g of catalyst). The enhancement in H_2 evolution activity was attributed to the electrical conductivity of the N-graphene. The authors suggested that the larger work function of N-graphene vs. the conduction band minimum of CdS created a thermodynamic driving force for charge transfer, thereby reducing the recombination of photogenerated electron-hole pairs.

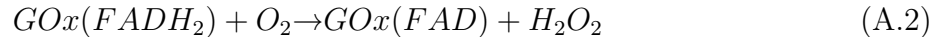
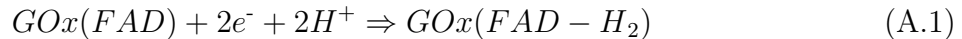
Interestingly, a metal-free graphitic carbon nitride (g-C₃N₄) polymeric photocatalyst has also been tested for hydrogen and oxygen production. Results showed good photocatalytic performance due to a 2.7 eV bandgap straddling the electrolytic oxidation ($\text{O}^2/\text{H}_2\text{O}$) and reduction (H^+/H_2) potentials[419]. By combining g-C₃N₄ with graphene sheets to improve conductivity and charge carrier separation, catalytic performance was increased, resulting in a 3X increase in the H_2 evolution rate. These studies show that C-N structures can be used to create semiconducting materials with beneficial properties for energy applications and/or to enhance other semiconductors by reducing charge recombination. These materials are therefore interesting for potential direct application in photocatalysis.

A.4.6.3 Biosensing

Biosensors have become an important component of both scientific and commercial interest. For a typical application, a material is designed to facilitate the identification of a specific target molecule and assist in a direct electron transfer process needed to access the redox active sites. Recently, researchers have focused on nitrogen-modified carbon materials for glucose sensors, where the oxidation of glucose produces hydrogen peroxide, which is then detected by the electrode (See ORR application above).

In 2005, it was shown that electrocatalytic C-N architectures have beneficial effects on the immobilization of glucose oxidase (GOx), leading to novel “third-generation” designs for glucose sensing[420]. More recently, a novel glucose biosensor was prepared by the immobilization of GOx on a nitrogen-doped carbon nanotube electrode[421]. The results showed that nitrogen doping accelerated the electron transfer process, leading to the direct electrochemical reaction of GOx and its cofactor (flavin adenine dinucleotide = FAD) through a

two-electron redox process (shown in A.1 and A.2)



This approach yielded sensitive amperometric biosensing for glucose levels ranging from 0.02 to 1.02mM with a detection limit of 0.01mM (signal to noise ratio of 3), demonstrating high affinity and excellent selectivity. In a similar approach, Xu et al. designed N-CNT-based electrochemical biosensors and obtained good analytical results with an even more sensitive detection limit, but a smaller linear detection range (from 2-140 μ M) [158].

Wang et al. fabricated an analogous glucose sensor using N-graphene rather than N-CNTs[147]. Their results showed that the GOx redox peak current was greatly improved on N-doped graphene compared to pristine graphene, which was attributed to the enhanced electron transfer efficiency attained by nitrogen doping. Their biosensor shows glucose detection at concentrations ranging from 0.01 to 0.5 mM in the presence of other molecules. This was also confirmed by a study on nitrogen-doped pyrolytic carbon films using cyclic voltammetry with a ferri/ferro-cyanide redox probe[422]. Results showed significantly enhanced electron transfer kinetics for the nitrogen-doped pyrolytic carbon films as compared with unmodified carbon films. EIS measurements confirmed that the N-PyC films yielded lower resistance to charge transfer.

Recently, Goran et al. demonstrated CVD-fabricated N-CNT's containing 7.4at% N that displayed a detection limit of 24 μ M with a linear range of 6.5 mM. It was suggested that the N-CNT's outperformed unmodified CNT's due to a more positive ORR onset potential[423]. There have been several studies exploring similar effects for nitrogen modified carbons applied to other biosensing applications including ascorbic acid[424], dopamine[424], uric acid[424], proteins[425], and thioridazine[426]. Collectively, the results strongly indicate that N-modified carbons show great promise for the construction of highly selective and efficient, third-generation enzyme biosensors that possess less cytotoxicity and better

biophilicity[427].

A.5 Outlook and Conclusions

In this work we have discussed a wide breadth of recent findings in nitrogen modified carbon architectures, ranging from materials synthesis to theory to applications. The review of current literature indicates that nitrogen doping is beneficial in many areas, as it allows for the tailoring and tuning of carbon materials for various applications of interest.

Recent cost-effective and creative strategies for the synthesis of a variety of N-doped carbon materials have yielded promising results; continued research in this field is focused on creating inexpensive, high surface area materials with high N contents. In general, synthesis/treatment approaches that lead to high nitrogen content tend to favor low surface areas, while procedures that enhance surface area tend to decrease nitrogen content. Unfortunately, for many applications, including hydrogen storage, CO adsorption, and supercapacitors, both high nitrogen content and high surface area are essential for improved performance. This fact makes it clear that there is a significant need for further innovations in synthesis of materials that contain high nitrogen concentration in addition to high surface area and developed porosity.

Among the potential N-doped materials systems, N-doped graphene possesses particularly intriguing intrinsic properties. The future utility of this material will greatly depend on the ability to design new fabrication methods, specifically those that create well-dispersed 1 to 2 graphene layer materials rather than multi-layer clumps. Templated carbon structures also show promise, as they combine the benefits of functionalization and nanoconfinement. Novel concepts and strategies toward synthesis of N-doped materials will create a positive ripple effect through out the community as they can be directed to a variety of important applications.

The application of carbon nitride like films onto high surface area materials is an interesting area of increasing interest. Creative strategies and applications of such “core-shell” materials will likely become a more widely studied area of research. These types of materials

have already show excelent performance and durability in areas such as supercapacitors, hydrogen adsorption, and photocatalytic applications and we expect it see their utility continue to increase.

For many applications, nitrogen functionalized carbon materials are interesting because the nitrogen sites improve performance by influencing important properties such as catalytic activity, sorption, conductivity, and the general interactions between components. Of the three most dominant nitrogen functionalities (graphitic, pyridinic and pyrrolic), pyridinic and graphitic nitrogen are the most frequently reported as beneficial. While nitrogen has been proven to be an import player in many applications, the observed beneficial effects vary depending on the type of N-doped materials. Furthermore, studies of N-doped carbon materials for certain applications have sometimes shown contradictory results. Therefore, continued progress in mechanistic understanding is necessary.

Possibly the most beneficial property of nitrogen, as it has been demonstrated across a wide range of applications, is its ability to stabilize catalytically active metal sites. Additionally, when used as a catalyst support, a general increase in nitrogen content leads to improvement in nucleation, dispersion and stability of metal nanoparticles. For example, it has been well documented both theoretically and experimentally that clustered nitrogen defects have a greater stabilizing effect than single N defects. In addition, it has been demonstrated that stabilization can be achieved by the incorporation of nitrogen either beneath or around nanoparticles. DFT studies have also provided insight into the effect nitrogen has on various systems. These results provide mechanistic explanations for the modified electronic properties, catalytic activity, reaction mechanisms and improved stability observed in N-doped carbon materials when used as catalytic supports. Further investigations combining theoretical and experimental work are critically needed to add further depth to our understanding of N-doped systems and the functionalities most important for specific applications.

Acknowledgements: This work was supported by the Army Research Office under grant #W911NF-09-1-0528

APPENDIX B - MEA TESTING EXPERIMENTAL/SUPPLEMENTARY INFORMATION

B.1 Acid Testing Information

Before measuring the initial DMFC performance, the MEAs were broken-in at 70 °C, using 1 M methanol at flow rate of 0.7 mL min⁻¹ and 60 sccm air with 100% relative humidity and back-pressure of 3 psi. After allowing the open circuit voltage (OCV) to rise above 0.75 V, the fuel cell was set at 0.35 V for 10 minutes with a 3.3 stoichiometric air-flow. It was then subjected to a series of potential cycles. Each potential cycle began held at 0.35 V for 30 min, after which the potential was increased in 0.05 V increments up to 0.7 V at 10 second intervals. This procedure was repeated for a total of six cycles. The cell was then brought to OCV and cooled to 50 °C with continuous reactant flow, followed by termination of the air-flow, then the methanol flow, in that order. The cell was then allowed to sit overnight at room temperature to continue hydration of the Nafion.

A variety of electrochemical tests (anode CO stripping, cathode CO stripping, methanol/H₂ polarization (also called methanol oxidation reaction, or MOR) on the anode, and methanol/air polarization) were conducted after break-in as well as intermittently during the long term performance durability testing. This durability test was carried out for both MEAs for 425h. CO stripping was performed at 25 °C by flowing 300 sccm of 1% CO in Ar at 100% relative humidity (RH) for 30 minutes to the electrode of interest (either in the anode or in the cathode), followed by flowing 300 sccm 100% RH N₂ for 30 min. During that time, H₂ was flowed at 100 sccm and 100%RH on the other electrode. This CO stripping was carried out on the respective electrodes (either anode or cathode) by holding a constant potential of 0.1 V vs. DHE. Cyclic voltammetry (CV) was then performed between 0.05 and 0.90 V vs. DHE for three cycles at a scan rate of 5 mV s⁻¹. During CV measurement, no gases were passed over the electrode of interest (either anode or cathode) while 50 sccm

of 100% H₂ was fed to the opposite electrode (the DHE). MOR polarization curves were collected at 70 °C by flowing 1 mL min⁻¹ of 1 M methanol on the anode and 50 sccm of 100% RH H₂ on the cathode. A linear-sweep voltammogram was performed from 0 to 0.7 V vs DHE at a scan rate of 2 mV s⁻¹. Data between 0.2 and 0.5 V was used. Methanol/air polarization curves were acquired by feeding 1 M methanol at a flow rate of 0.7 mL min⁻¹ to the anode and 3.3 stoichiometric air flow (100% RH) to the cathode side (minimum flow of 60 sccm) at 80 °C. Constant current steps, 15 min in duration, were used to generate the polarization curve, with the last 5 minutes of data averaged to produce each voltage point for the polarization curve.

DMFC durability testing was carried out at 80 °C by feeding 1 M methanol at a flow rate of 0.7 mL min⁻¹ to the anode and 3.3 stoichiometric oxidant flow of 100% RH air on the cathode side (minimum flow of 60 sccm). Each fuel cell was then held at 0.4 V for a total of 425 hours. Durability testing was stopped intermittently for electrochemical testing.

B.2 Alkaline Testing Information

The alkaline DMFC performance (140 mW cm⁻², 80 °C) described in this thesis was done using 3 mg cm⁻² loading of commercial PtRu/C catalyst (JM Hi-spec 10000) that has been post-doped with nitrogen. Post-doping is accomplished by nitrogen ion-implantation of the commercial carbon supported PtRu/C catalyst after it has already been synthesized and supplied by the company. The obtained performance from the N-doped catalyst is significantly higher than that of an otherwise identical MEA made from the same commercial catalyst without N-doping. Electrochemical and micro-structural evidence suggests that the nitrogen post-doping process improves performance in part by increasing the electrochemical surface area (ECSA) of the catalyst, likely by catalyst re-sputtering and refinement caused by the doping process. While the performance of the MEA fabricated from the N-doped catalyst is considerably better than that of the undoped control, both MEAs yield maximum power densities that are among the highest reported for ADMFCs.

The MEAs were fabricated by coating the PtRu/C (3 mg cm^{-2}), N-doped PtRu/C (3 mg cm^{-2}), and Pt/C (2 mg cm^{-2}) catalyst inks directly on the alkaline membrane (Tokuyama A-201) using the same direct-membrane coating protocols (which is supposed to be the best protocol for making high performance DMFC MEAs) as have been previously used for the fabrication of Nafion-based acid DMFCs.

REFERENCES CITED

- [1] J. Zhang and H. Liu, *Electrocatalysis of Direct Methanol Fuel Cells: From Fundamentals to Applications*, Wiley-VCH, 2009, p. 606.
- [2] Y. Zhou, K. Neyerlin, T. S. Olson, S. Pylypenko, J. Bult, H. N. Dinh, T. Gennett, Z. Shao and R. O'Hayre, *Energy & Environmental Science*, 2010, **3**, 1437.
- [3] S.-W. C. W. P. F. B. O'Hayre, Ryan Cha, *Fuel Cell Fundamentals*, Wiley, Second Edition, 2009.
- [4] E. Müller, *Zeitschrift für Angewandte Chemie*, 1922, **35**, 503–503.
- [5] B. George, A. Sri and E. Johnson, 2004, 12–17.
- [6] K. Kordesch and G. R. Simader, *Fuel Cells and Their Applications*, Wiley-VCH, 1996, p. 375.
- [7] T. O. Pavela, *The low potential Oxidation of methanol at a platinised platinum anode*, Suomalainen Tiedeakatemia, 1954, p. 45.
- [8] M. Janssen and J. Moolhuysen, *Electrochimica Acta*, 1976, **21**, 861–868.
- [9] M. Watanabe and S. Motoo, *Journal of Electroanalytical Chemistry and Interfacial Electrochemistry*, 1975, **60**, 275–283.
- [10] V. Bagotzky and Y. Vassilyev, *Electrochimica Acta*, 1967, **12**, 1323–1343.
- [11] B. Beden, F. Kadirgan, C. Lamy and J. Leger, *Journal of Electroanalytical Chemistry and Interfacial Electrochemistry*, 1981, **127**, 75–85.
- [12] K. Chandrasekaran, *Journal of The Electrochemical Society*, 1990, **137**, 518.
- [13] P. Christensen, A. Hamnett and G. Troughton, *Journal of Electroanalytical Chemistry*, 1993, **362**, 207–218.
- [14] J. Goodenough, A. Hamnett, B. Kennedy, R. Manoharan and S. Weeks, *Journal of Electroanalytical Chemistry and Interfacial Electrochemistry*, 1988, **240**, 133–145.
- [15] N. Markovic, A. Widelöv, P. Ross, O. Monteiro and I. Brown, *Catalysis Letters*, 1997, **43**, 161–166.

- [16] J. McBreen, *Journal of The Electrochemical Society*, 1995, **142**, 3399.
- [17] M. K. Ravikumar, *Journal of The Electrochemical Society*, 1996, **143**, 2601.
- [18] B. Gurau, R. Viswanathan, R. Liu, T. J. Lafrenz, K. L. Ley, E. S. Smotkin, E. Reddington, A. Sapienza, B. C. Chan, T. E. Mallouk and S. Sarangapani, *The Journal of Physical Chemistry B*, 1998, **102**, 9997–10003.
- [19] P. Piela, C. Eickes, E. Broscha, F. Garzon and P. Zelenay, *Journal of The Electrochemical Society*, 2004, **151**, A2053.
- [20] A. S. Aricò, S. Srinivasan and V. Antonucci, *Fuel Cells*, 2001, **1**, 133–161.
- [21] S. Wasmus and A. Küver, *Journal of Electroanalytical Chemistry*, 1999, **461**, 14–31.
- [22] A. Arico, A. Shukla, H. Kim and S. Park, *Applied Surface . . .*, 2001, **172**, 33–40.
- [23] H. A. Gasteiger, *Journal of The Electrochemical Society*, 1994, **141**, 1795.
- [24] A. Aricò, V. Baglio, A. Di Blasi, E. Modica, P. Antonucci and V. Antonucci, *Journal of Electroanalytical Chemistry*, 2003, **557**, 167–176.
- [25] R. O’Hayre, *Ph.D. thesis*, Stanford, 2004.
- [26] W. Vielstich, H. Yokokawa and H. A. Gasteiger, *Handbook of fuel cells: fundamentals technology and applications. Advances in electrocatalysis, materials, diagnostics and durability : Part 1, Volume 5*, John Wiley & Sons, 2009, p. 1038.
- [27] M. S. Wilson, *Journal of The Electrochemical Society*, 1993, **140**, 2872.
- [28] P. Bindra, *Journal of The Electrochemical Society*, 1979, **126**, 1631.
- [29] Y. Shao-Horn, W. C. Sheng, S. Chen, P. J. Ferreira, E. F. Holby and D. Morgan, *Topics in Catalysis*, 2007, **46**, 285–305.
- [30] a. K. Shukla, *Journal of The Electrochemical Society*, 1994, **141**, 1517.
- [31] Z. Jin, J. Yao, C. Kittrell and J. M. Tour, *ACS nano*, 2011, **5**, 4112–7.
- [32] Z. Luo, S. Lim, Z. Tian, J. Shang, L. Lai, B. MacDonald, C. Fu, Z. Shen, T. Yu and J. Lin, *Journal of Materials Chemistry*, 2011, **21**, 8038.
- [33] C. Qu, L. Qiao, C. Wang, S. Yu, Q. Jiang and W. Zheng, *Physics Letters A*, 2010, **374**, 782–787.

- [34] A. L. M. Reddy, A. Srivastava, S. R. Gowda, H. Gullapalli, M. Dubey and P. M. Ajayan, *ACS nano*, 2010, **4**, 6337–42.
- [35] D. Wei, Y. Liu, Y. Wang, H. Zhang, L. Huang and G. Yu, *Nano letters*, 2009, **9**, 1752–8.
- [36] Y.-F. Lu, S.-T. Lo, J.-C. Lin, W. Zhang, J.-Y. Lu, F.-H. Liu, C.-M. Tseng, Y.-H. Lee, C.-T. Liang and L.-J. Li, *ACS nano*, 2013, **7**, 6522–32.
- [37] L. Qu, Y. Liu, J.-B. Baek and L. Dai, *ACS nano*, 2010, **4**, 1321–6.
- [38] S. Wang, X. Zhao, T. Cochell and A. Manthiram, *The Journal of Physical Chemistry Letters*, 2012, **3**, 2164–2167.
- [39] H. Wang, T. Maiyalagan and X. Wang, *ACS Catalysis*, 2012, **2**, 781–794.
- [40] B. Xiong, Y. Zhou, R. O’Hayre and Z. Shao, *Applied Surface Science*, 2013, **266**, 433–439.
- [41] J. F. Evans and T. Kuwana, *Analytical Chemistry*, 1979, **51**, 358–365.
- [42] C. W. Miller, D. H. Karweik and T. Kuwana, *Analytical Chemistry*, 1981, **53**, 2319–2323.
- [43] K. N. Wood, R. O’Hayre and S. Pylypenko, *Energy & Environmental Science*, 2014.
- [44] T. Schiros, D. Nordlund, L. Pálová, D. Prezzi, L. Zhao, K. S. Kim, U. Wurstbauer, C. Gutiérrez, D. Delongchamp, C. Jaye, D. Fischer, H. Ogasawara, L. G. M. Pettersson, D. R. Reichman, P. Kim, M. S. Hybertsen and A. N. Pasupathy, *Nano letters*, 2012, **12**, 4025–31.
- [45] C. L. Muhich, J. Y. Westcott, T. C. Morris, A. W. Weimer and C. B. Musgrave, *The Journal of Physical Chemistry C*, 2013, **117**, 10523–10535.
- [46] L. Zhao, R. He, K. T. Rim, T. Schiros, K. S. Kim, H. Zhou, C. Gutiérrez, S. P. Chockalingam, C. J. Arguello, L. Pálová, D. Nordlund, M. S. Hybertsen, D. R. Reichman, T. F. Heinz, P. Kim, A. Pinczuk, G. W. Flynn and A. N. Pasupathy, *Science (New York, N.Y.)*, 2011, **333**, 999–1003.
- [47] Y. Zhou, R. Pasquarelli, T. Holme, J. Berry, D. Ginley and R. O’Hayre, *Journal of Materials Chemistry*, 2009, **19**, 7830.
- [48] Y. Zhou, T. Holme, J. Berry, T. R. Ohno, D. Ginley and R. O’Hayre, *The Journal of Physical Chemistry C*, 2010, **114**, 506–515.

- [49] S. Pylypenko, A. Borisevich, K. L. More, A. R. Corpuz, T. Holme, A. a. Dameron, T. S. Olson, H. N. Dinh, T. Gennett and R. O’Hayre, *Energy & Environmental Science*, 2013, **6**, 2957.
- [50] W.-C. Fang, *Nanoscale research letters*, 2009, **5**, 68–73.
- [51] Y. Guo, J. He, T. Wang, H. Xue, Y. Hu, G. Li, J. Tang and X. Sun, *Journal of Power Sources*, 2011, **196**, 9299–9307.
- [52] C.-H. Hsu and P.-L. Kuo, *Journal of Power Sources*, 2012, **198**, 83–89.
- [53] Z. Lei, L. An, L. Dang, M. Zhao, J. Shi, S. Bai and Y. Cao, *Microporous and Mesoporous Materials*, 2009, **119**, 30–38.
- [54] Z. Lei, M. Zhao, L. Dang, L. An, M. Lu, A.-Y. Lo, N. Yu and S.-B. Liu, *Journal of Materials Chemistry*, 2009, **19**, 5985.
- [55] Z. Liu, F. Su, X. Zhang and S. W. Tay, *ACS applied materials & interfaces*, 2011, **3**, 3824–30.
- [56] C. Pan, L. Qiu, Y. Peng and F. Yan, *Journal of Materials Chemistry*, 2012, **22**, 13578.
- [57] F. Su, Z. Tian, C. K. Poh, Z. Wang, S. H. Lim, Z. Liu and J. Lin, *Chemistry of Materials*, 2010, **22**, 832–839.
- [58] B. Xiong, Y. Zhou, Y. Zhao, J. Wang, X. Chen, R. O’Hayre and Z. Shao, *Carbon*, 2013, **52**, 181–192.
- [59] Y. Zhao, Y. Zhou, B. Xiong, J. Wang, X. Chen, R. O’Hayre and Z. Shao, *Journal of Solid State Electrochemistry*, 2012, **17**, 1089–1098.
- [60] R. Chetty, S. Kundu, W. Xia, M. Bron, W. Schuhmann, V. Chirila, W. Brandl, T. Reinecke and M. Muhler, *Electrochimica Acta*, 2009, **54**, 4208–4215.
- [61] S. Suthirakun, T. Sarakonsri, S. Aukkaravittayapun and T. Vilaithong, 2009, **10**, 502–506.
- [62] S.-H. Liu, M.-T. Wu, Y.-H. Lai, C.-C. Chiang, N. Yu and S.-B. Liu, *Journal of Materials Chemistry*, 2011, **21**, 12489.
- [63] S. Pylypenko, A. Queen, T. S. Olson, A. Dameron, K. O’Neill, K. Neyerlin, B. Pivovarov, H. N. Dinh, D. S. Ginley, T. Gennett and R. O’Hayre, *The Journal of Physical Chemistry C*, 2011, **115**, 13676–13684.

- [64] A. A. Dameron, T. S. Olson, S. T. Christensen, J. E. Leisch, K. E. Hurst, S. Pylypenko, J. B. Bult, D. S. Ginley, R. P. O. Hayre, H. N. Dinh, T. Gennett and R. P. O'Hayre, *ACS Catalysis*, 2011, **1**, 1307–1315.
- [65] S. Pylypenko, A. Queen, T. S. Olson, A. Dameron, K. O'Neill, K. C. Neyerlin, B. Pivovarov, H. N. Dinh, D. S. Ginley, T. Gennett and R. O'Hayre, *The Journal of Physical Chemistry C*, 2011, **115**, 13667–13675.
- [66] B. P. Vinayan, R. Nagar, N. Rajalakshmi and S. Ramaprabhu, *Advanced Functional Materials*, 2012, **22**, 3519–3526.
- [67] G. Wu, K. L. More, C. M. Johnston and P. Zelenay, *Science (New York, N.Y.)*, 2011, **332**, 443–7.
- [68] G. Wu, M. Nelson, S. Ma, H. Meng, G. Cui and P. K. Shen, *Carbon*, 2011, **49**, 3972–3982.
- [69] D. Geng, H. Liu, Y. Chen, R. Li, X. Sun, S. Ye and S. Knights, *Journal of Power Sources*, 2011, **196**, 1795–1801.
- [70] Z. Mo, R. Zheng, H. Peng, H. Liang and S. Liao, *Journal of Power Sources*, 2014, **245**, 801–807.
- [71] J. P. Paraknowitsch and A. Thomas, *Energy & Environmental Science*, 2013, **6**, 2839.
- [72] Z. Yao, H. Nie, Z. Yang, X. Zhou, Z. Liu and S. Huang, *Chemical communications (Cambridge, England)*, 2012, **48**, 1027–9.
- [73] G. Kalita, K. Wakita, M. Takahashi and M. Umeno, *Journal of Materials Chemistry*, 2011, **21**, 15209.
- [74] T. T. Cheng, N. Jia, V. Colbow, S. Wessel and M. Dutta, *Journal of Power Sources*, 2010, **195**, 4622–4627.
- [75] T. T. H. Cheng, N. Jia and P. He, *Journal of The Electrochemical Society*, 2010, **157**, B714.
- [76] T. Maiyalagan, *Applied Catalysis B: Environmental*, 2008, **80**, 286–295.
- [77] K. N. Wood, S. T. Christensen, S. Pylypenko, T. S. Olson, A. A. Dameron, K. E. Hurst, H. N. Dinh, T. Gennett and R. O'Hayre, *MRS Communications*, 2012, **2**, 85–89.

- [78] P. Joghee, S. Pylypenko, T. Olson, A. A. Dameron, A. R. Corpuz, H. N. N. Dinh, K. Wood, K. O'Neill, K. E. Hurst, G. Bender, K. J. O'Neill, T. Gennett, B. S. Pivovar and R. P. O'Hayre, *Journal of the Electrochemical Society*, 2012, **159**, F768–F778.
- [79] T. S. Olson, A. a. Dameron, K. Wood, S. Pylypenko, K. E. Hurst, S. Christensen, J. B. Bult, D. S. Ginley, R. O'Hayre, H. Dinh, T. Gennett and R. O'Hayre, *Journal of the Electrochemical Society*, 2013, **160**, F389–F394.
- [80] C. Yu, 2011, **DAI/B 72-1**, year.
- [81] J. Ilavsky and P. R. Jemian, *Journal of Applied Crystallography*, 2009, **42**, 347–353.
- [82] S. Pylypenko, B. B. Blizanac, T. S. Olson, D. Konopka and P. Atanasov, *ACS applied materials & interfaces*, 2009, **1**, 604–11.
- [83] N. Wongyao, A. Therdthianwong and S. Therdthianwong, *Fuel*, 2010, **89**, 971–977.
- [84] K.-H. Chang and C.-C. Hu, *Journal of The Electrochemical Society*, 2004, **151**, A958.
- [85] M. K. Jeon, J. Y. Won and S. I. Woo, *Electrochemical and Solid-State Letters*, 2007, **10**, B23.
- [86] C.-M. Lai, J.-C. Lin, K.-L. Hsueh, C.-P. Hwang, K.-C. Tsay, L.-D. Tsai and Y.-M. Peng, *Journal of The Electrochemical Society*, 2008, **155**, B843.
- [87] Q. Lu, B. Yang, L. Zhuang and J. Lu, *The journal of physical chemistry. B*, 2005, **109**, 1715–22.
- [88] A. J. Allen, S. Krueger, G. Skandan, G. G. Long, H. Hahn, H. M. Kerch, J. C. Parker and M. N. All, *Journal of the American Ceramic Society*, 1996, **79**, 1201–1212.
- [89] L. C. Gontard, R. E. Dunin-Borkowski, D. Ozkaya, T. Hyde, P. A. Midgley and P. Ash, *Journal of Physics: Conference Series*, 2006, **26**, 367–370.
- [90] T. Hyde, *Platinum Metals Review*, 2008, **52**, 129–130.
- [91] T. Holme, Y. Zhou, R. Pasquarelli and R. O'Hayre, *Physical chemistry chemical physics : PCCP*, 2010, **12**, 9461–8.
- [92] T. Kondo, T. Suzuki and J. Nakamura, *The Journal of Physical . . .*, 2011, **2**, 577–580.
- [93] S. Pylypenko, T. Olson, A. Dameron, A. Borisevich, K. More, T. Holme, K. N. Wood, K. O'Neill, K. E. Hurst, S. T. Christensen, D. S. Ginley, H. N. Dinh, T. Gennett and R. O'Hayre, *Meeting Abstracts*, 2011, 1191.

- [94] S. Pylypenko, A. Corpuz, T. Olson, A. Dameron, K. Wood, P. Joghee, K. Hurst, S. Christensen, D. Ginley and B. S. Pivovar, *Meeting Abstracts*, 2012, 1340.
- [95] S. Pylypenko, K. N. Wood, A. Serov, P. Atanassov and R. O'Hayre, *Meeting Abstracts*, 2013, 1603.
- [96] K. N. Wood, S. Pylypenko, A. Corpuz, P. Joghee, A. Dameron, H. N. Dinh, T. Gennett and R. O'Hayre, *Meeting Abstracts*, 2013, 1576.
- [97] P. Joghee, S. Pylypenko, K. Wood, A. Corpuz, G. Bender, H. N. Dinh and R. O'Hayre, *Journal of Power Sources*, 2014, **245**, 37–47.
- [98] A. R. Corpuz, K. N. Wood, S. Pylypenko, A. a. Dameron, P. Joghee, T. S. Olson, G. Bender, H. N. Dinh, T. Gennett, M. Ryan, R. M. Richards and R. O'Hayre, *Journal of Power Sources*, 2014, **248**, 296–306.
- [99] T. S. Olson, a. a. Dameron, K. Wood, S. Pylypenko, K. E. Hurst, S. Christensen, J. B. Bult, D. S. Ginley, R. O'Hayre, H. Dinh and T. Gennett, *Journal of the Electrochemical Society*, 2013, **160**, F389–F394.
- [100] S. Pylypenko, K. Wood, A. Queen, R. O'Hayre, A. A. Dameron, T. S. Olson, K. Hurst, S. Christensen, K. Bult, K. O'Neill, D. S. Ginley, T. Gennett and H. N. Dinh, *Preprints of Papers – American Chemical Society, Division of Fuel Chemistry.*, 2011, **56**, 264–265.
- [101] A. R. Corpuz, T. T. Olson, P. Joghee, S. Pylypenko, A. A. A. Dameron, H. H. N. Dinh, K. J. K. O'Neill, K. K. E. Hurst, G. Bender, T. Gennett, B. B. S. Pivovar, R. R. M. Richards and R. P. R. O'Hayre, *Journal of Power Sources*, 2012, **217**, 142–151.
- [102] S. Pylypenko, A. Queen, K. C. Neyerlin, T. Olson, A. Dameron, K. O'Neill, D. Ginley, B. Gorman, S. Kocha, H. N. Dinh, T. Gennett and R. O'Hayre, *ECS Transactions*, 2010, pp. 351–357.
- [103] H. N. Dinh, X. Ren, F. H. Garzon and S. Gottesfeld, *Journal of Electroanalytical Chemistry*, 2000, **491**, 222–233.
- [104] H. A. Gasteiger, N. Markovic, P. N. Ross and E. J. Cairns, *The Journal of Physical Chemistry*, 1994, **98**, 617–625.
- [105] R. Dillon, S. Srinivasan, A. Aricò and V. Antonucci, *Journal of Power Sources*, 2004, **127**, 112–126.
- [106] W. Li, C. Liang, W. Zhou and J. Qiu, *The Journal of . . .*, 2003, **107**, 6292–6299.

- [107] Z. Liu, X. Ling, X. Su and J. Lee, *The Journal of Physical Chemistry . . .*, 2004, **108**, 8234–8240.
- [108] Z. Chen, D. Higgins, A. Yu, L. Zhang and J. Zhang, *Energy & Environmental Science*, 2011, **4**, 3167.
- [109] D. C. Higgins, D. Meza and Z. Chen, *The Journal of Physical Chemistry C*, 2010, **114**, 21982–21988.
- [110] P. Roy, R. Soc, J. I. Met, W. Vernon, E. Akeroyd, J. Desmaison, M. Billy, C. R. A. Sci, S. Dominique, B. Devillers, J. Bardoll, M. Froman, R. Bell, C. Roy, S. Roy and A. Harding, *Journal of the . . .*, 1997.
- [111] B. Yue, Y. Ma, H. Tao, L. Yu, G. Jian, X. Wang, X. Wang, Y. Lu and Z. Hu, *Journal of Materials Chemistry*, 2008, **18**, 1747.
- [112] Y. Shao, J. Sui, G. Yin and Y. Gao, *Applied Catalysis B: Environmental*, 2008, **79**, 89–99.
- [113] K. S. Novoselov, a. K. Geim, S. V. Morozov, D. Jiang, Y. Zhang, S. V. Dubonos, I. V. Grigorieva and a. a. Firsov, *Science (New York, N.Y.)*, 2004, **306**, 666–9.
- [114] D. Chen, L. Tang and J. Li, *Chemical Society reviews*, 2010, **39**, 3157–80.
- [115] W. S. Hummers and R. E. Offeman, *Journal of the American Chemical Society*, 1958, **80**, 1339–1339.
- [116] P. Matter, L. Zhang and U. Ozkan, *Journal of Catalysis*, 2006, **239**, 83–96.
- [117] P. Ayala, R. Arenal, M. Rummeli, a. Rubio and T. Pichler, *Carbon*, 2010, **48**, 575–586.
- [118] D. Jana, C.-L. Sun, L.-C. Chen and K.-H. Chen, *Progress in Materials Science*, 2013, **58**, 565–635.
- [119] K. Kinoshita, *Angewandte Chemie International Edition in English*, 1988, **27**, 1218–1219.
- [120] S. Maldonado, S. Morin and K. J. Stevenson, *Carbon*, 2006, **44**, 1429–1437.
- [121] S. Maldonado and K. J. Stevenson, *The journal of physical chemistry. B*, 2005, **109**, 4707–16.
- [122] M. Cohen, *Physical Review B*, 1985, **32**, 7988–7991.

- [123] a. Y. Liu and M. L. Cohen, *Science (New York, N.Y.)*, 1989, **245**, 841–2.
- [124] D. Teter and R. Hemley, *Science*, 1996, **271**, 1–3.
- [125] S.-K. Lee, J.-H. Kim, M.-G. Jeong, M.-J. Song and D.-S. Lim, *Nanotechnology*, 2010, **21**, 505302.
- [126] A. Lherbier, X. Blase, Y.-M. Niquet, F. Triozon and S. Roche, *Physical Review Letters*, 2008, **101**, 036808.
- [127] X. Wang, X. Cao, L. Bourgeois, H. Guan, S. Chen, Y. Zhong, D.-M. Tang, H. Li, T. Zhai, L. Li, Y. Bando and D. Golberg, *Advanced Functional Materials*, 2012, **22**, 2682–2690.
- [128] C. H. Choi, S. H. Park, M. W. Chung and S. I. Woo, *Carbon*, 2013, **55**, 98–107.
- [129] D. Deng, X. Pan, L. Yu, Y. Cui, Y. Jiang, J. Qi, W.-x. Li, Q. Fu, X. Ma, Q. Xue, G. Sun and X. Bao, 2011, 1188–1193.
- [130] B. P. Vinayan and S. Ramaprabhu, *Journal of Materials Chemistry A*, 2013, **1**, 3865.
- [131] L. S. Panchakarla, K. S. Subrahmanyam, S. K. Saha, A. Govindaraj, H. R. Krishnamurthy, U. V. Waghmare and C. N. R. Rao, *Advanced Materials*, 2009, **560012**, NA–NA.
- [132] L. Panchakarla, a. Govindaraj and C. Rao, *Inorganica Chimica Acta*, 2010, **363**, 4163–4174.
- [133] D. Geng, Y. Y. Chen, Y. Li, R. Li, X. Sun, S. Ye and S. Knights, *Energy & Environmental Science*, 2011, **4**, 760.
- [134] B. Guo, Q. Liu, E. Chen, H. Zhu, L. Fang and J. R. Gong, *Nano letters*, 2010, 4975–4980.
- [135] X. Wang, X. Li, L. Zhang, Y. Yoon, P. K. Weber, H. Wang, J. Guo and H. Dai, *Science (New York, N.Y.)*, 2009, **324**, 768–71.
- [136] Y. Li, J. Wang, X. Li, D. Geng, M. N. Banis, R. Li and X. Sun, *Electrochemistry Communications*, 2012, **18**, 12–15.
- [137] L.-S. Zhang, X.-Q. Liang, W.-G. Song and Z.-Y. Wu, *Physical chemistry chemical physics : PCCP*, 2010, **12**, 12055–9.
- [138] Z.-h. Sheng, L. Shao, J. Chen and W. Bao, *ACS ...*, 2011, 4350–4358.

- [139] G. Yang, Y. Li, R. K. Rana and J.-J. Zhu, *Journal of Materials Chemistry A*, 2013, **1**, 1754.
- [140] X. Li, H. Wang, J. T. Robinson, H. Sanchez, G. Diankov and H. Dai, *Journal of the American Chemical Society*, 2009, **131**, 15939–44.
- [141] D. Long, W. Li, L. Ling, J. Miyawaki, I. Mochida and S.-H. Yoon, *Langmuir : the ACS journal of surfaces and colloids*, 2010, **26**, 16096–102.
- [142] D.-W. Wang, I. R. Gentle and G. Q. M. Lu, *Electrochemistry Communications*, 2010, **12**, 1423–1427.
- [143] R. I. Jafri, N. Rajalakshmi and S. Ramaprabhu, *Journal of Power Sources*, 2010, **195**, 8080–8083.
- [144] H. M. Jeong, J. W. Lee, W. H. Shin, Y. J. Choi, H. J. Shin, J. K. Kang and J. W. Choi, *Nano letters*, 2011, **11**, 2472–7.
- [145] Y.-C. Lin, C.-Y. Lin and P.-W. Chiu, *Applied Physics Letters*, 2010, **96**, 133110.
- [146] Y. Shao, S. Zhang, M. H. Engelhard, G. Li, G. Shao, Y. Wang, J. Liu, I. a. Aksay and Y. Lin, *Journal of Materials Chemistry*, 2010, **20**, 7491.
- [147] Y. Wang, Y. Shao, D. W. D. Matson, J. Li and Y. Lin, *Acs Nano*, 2010, **4**, year.
- [148] V. B. Parambath, R. Nagar and S. Ramaprabhu, *Langmuir : the ACS journal of surfaces and colloids*, 2012, **28**, 7826–33.
- [149] U. Bangert, a. Bleloch, M. Gass, a. Seepujak and J. van den Berg, *Physical Review B*, 2010, **81**, 1–11.
- [150] R. Sen, B. C. Satishkumar, a. Govindaraj, K. R. Harikumar, M. K. Renganathan and C. N. R. Rao, *Journal of Materials Chemistry*, 1997, **7**, 2335–2337.
- [151] L. Chen, C. Wen, C. Liang, W. Hong, K. Chen, H. Cheng, C. Shen, C. Wu and K. Chen, *Advanced Functional Materials*, 2002, **12**, 687–692.
- [152] Y. Cao, H. Yu, J. Tan, F. Peng, H. Wang, J. Li, W. Zheng and N.-B. Wong, *Carbon*, 2013, **57**, 433–442.
- [153] K. Ghosh, M. Kumar, T. Maruyama and Y. Ando, *Carbon*, 2010, **48**, 191–200.
- [154] H. Liu, Y. Zhang, R. Li, X. Sun, S. Désilets, H. Abou-Rachid, M. Jaidann and L.-S. Lussier, *Carbon*, 2010, **48**, 1498–1507.

- [155] T. Thomas, R. J. Mascarenhas, B. E. K. Swamy, P. Martis, Z. Mekhalif and B. S. Sherigara, *Colloids and surfaces. B, Biointerfaces*, 2013, **110**, 458–65.
- [156] Z. Wang, R. Jia, J. Zheng, J. Zhao, L. Li, J. Song and Z. Zhu, *ACS nano*, 2011, **5**, 1677–84.
- [157] J. D. Wiggins-Camacho and K. J. Stevenson, *The Journal of Physical Chemistry C*, 2009, **113**, 19082–19090.
- [158] X. Xu, S. Jiang, Z. Hu and S. Liu, *ACS nano*, 2010, **4**, 4292–8.
- [159] S. Kundu, W. Xia, W. Busser, M. Becker, D. A. Schmidt, M. Havenith and M. Muhler, *Physical chemistry chemical physics : PCCP*, 2010, **12**, 4351–9.
- [160] T. C. Nagaiah, S. Kundu, M. Bron, M. Muhler and W. Schuhmann, *Electrochemistry Communications*, 2010, **12**, 338–341.
- [161] V. G. Ramu, A. Bordoloi, T. C. Nagaiah, W. Schuhmann, M. Muhler and C. Cabrele, *Applied Catalysis A: General*, 2012, **431-432**, 88–94.
- [162] K. Gong, F. Du, Z. Xia, M. Durstock and L. Dai, *Science (New York, N.Y.)*, 2009, **323**, 760–4.
- [163] X. Tuaev, J. P. Paraknowitsch, R. Illgen, A. Thomas and P. Strasser, *Physical chemistry chemical physics : PCCP*, 2012, **14**, 6444–7.
- [164] G. Xu, B. Ding, P. Nie, L. Shen, J. Wang and X. Zhang, *Chemistry (Weinheim an der Bergstrasse, Germany)*, 2013, **19**, 12306–12.
- [165] M. I. Ionescu, Y. Zhang, R. Li, H. Abou-Rachid and X. Sun, *Applied Surface Science*, 2012, **258**, 4563–4568.
- [166] J. Liu, Y. Zhang, M. I. Ionescu, R. Li and X. Sun, *Applied Surface Science*, 2011, **257**, 7837–7844.
- [167] A. Morozan, P. Jégou, M. Pinault, S. Campidelli, B. Joussetme and S. Palacin, *ChemSusChem*, 2012, **5**, 647–51.
- [168] B. An, S. Xu, L. Li, J. Tao, F. Huang and X. Geng, *Journal of Materials Chemistry A*, 2013, **1**, 7222.
- [169] E. J. Biddinger, D. Deak and U. S. Ozkan, *Topics in Catalysis*, 2009, **52**, 1566–1574.

- [170] M. Lefèvre, E. Proietti, F. Jaouen and J.-P. J. Dodelet, *Science (New York, N.Y.)*, 2009, **324**, 71–4.
- [171] M. Plaza, C. Pevida, B. Arias, J. Feroso, M. Casal, C. Martín, F. Rubiera and J. Pis, *Fuel*, 2009, **88**, 2442–2447.
- [172] M. Plaza, C. Pevida, B. Arias, J. Feroso, F. Rubiera and J. Pis, *Energy Procedia*, 2009, **1**, 1107–1113.
- [173] T.-Y. Ma, L. Liu and Z.-Y. Yuan, *Chemical Society Reviews*, 2013, **42**, 3977–4003.
- [174] D. Hulicova-Jurcakova, M. Kodama, S. Shiraishi, H. Hatori, Z. H. Zhu and G. Q. Lu, *Advanced Functional Materials*, 2009, **19**, 1800–1809.
- [175] M. S. Shafeeyan, W. M. A. W. Daud, A. Houshmand and A. Shamiri, *Journal of Analytical and Applied Pyrolysis*, 2010, **89**, 143–151.
- [176] W. Shen and W. Fan, *Journal of Materials Chemistry A*, 2013, **1**, 999.
- [177] S. Giraudet, Z. Zhu, X. Yao and G. Lu, *The Journal of Physical Chemistry C*, 2010, **114**, 8639–8645.
- [178] J. P. Paraknowitsch, A. Thomas and M. Antonietti, *Journal of Materials Chemistry*, 2010, **20**, 6746.
- [179] G.-P. Hao, W.-C. Li, D. Qian and A.-H. Lu, *Advanced materials (Deerfield Beach, Fla.)*, 2010, **22**, 853–7.
- [180] F. Su, C. K. Poh, J. S. Chen, G. Xu, D. Wang, Q. Li, J. Lin and X. W. Lou, *Energy & Environmental Science*, 2011, **4**, 717.
- [181] Z. Jin, Z. Sun, L. J. Simpson, K. J. O'Neill, P. A. Parilla, Y. Li, N. P. Stadie, C. C. Ahn, C. Kittrell and J. M. Tour, *Journal of the American Chemical Society*, 2010, **132**, 15246–51.
- [182] A. K. Mishra and S. Ramaprabhu, *Journal of Materials Chemistry*, 2012, **22**, 3708.
- [183] Z. Rozlívková, M. Trchová, M. Exnerová and J. Stejskal, *Synthetic Metals*, 2011, **161**, 1122–1129.
- [184] R. Silva, D. Voiry, M. Chhowalla and T. Asefa, *Journal of the American Chemical Society*, 2013, **135**, 7823–6.
- [185] L. L. Zhang and X. S. Zhao, *Chemical Society reviews*, 2009, **38**, 2520–31.

- [186] X. Ma, M. Cao and C. Hu, *Journal of Materials Chemistry A*, 2013, **1**, 913.
- [187] T.-P. Fellingner, F. Hasché, P. Strasser and M. Antonietti, *Journal of the American Chemical Society*, 2012, **134**, 4072–5.
- [188] J. S. Lee, X. Wang, H. Luo, G. a. Baker and S. Dai, *Journal of the American Chemical Society*, 2009, **131**, 4596–7.
- [189] B. Qiu, C. Pan, W. Qian, Y. Peng, L. Qiu and F. Yan, *Journal of Materials Chemistry A*, 2013, **1**, 6373.
- [190] X. Wang and S. Dai, *Angewandte Chemie (International ed. in English)*, 2010, **49**, 6664–8.
- [191] B. Xu, D. Zheng, M. Jia, G. Cao and Y. Yang, *Electrochimica Acta*, 2013, **98**, 176–182.
- [192] W. Yang, T.-P. Fellingner and M. Antonietti, *Journal of the American Chemical Society*, 2011, **133**, 206–9.
- [193] X. Duan, D. Li, H. Zhang, J. Ma and W. Zheng, *Chemistry (Weinheim an der Bergstrasse, Germany)*, 2013, **19**, 7231–42.
- [194] N. Fechler, T.-P. Fellingner and M. Antonietti, *Advanced materials (Deerfield Beach, Fla.)*, 2013, **25**, 75–9.
- [195] D.-C. Guo, J. Mi, G.-P. Hao, W. Dong, G. Xiong, W.-C. Li and A.-H. Lu, *Energy & Environmental Science*, 2013, **6**, 652.
- [196] T.-P. Fellingner, D. S. Su, M. Engenhorst, D. Gautam, R. Schlögl and M. Antonietti, *Journal of Materials Chemistry*, 2012, **22**, 23996.
- [197] L. Qie, W.-M. Chen, Z.-H. Wang, Q.-G. Shao, X. Li, L.-X. Yuan, X.-L. Hu, W.-X. Zhang and Y.-H. Huang, *Advanced materials (Deerfield Beach, Fla.)*, 2012, **24**, 2047–50.
- [198] A. Thomas, F. Goettmann and M. Antonietti, *Chemistry of Materials*, 2008, **20**, 738–755.
- [199] M.-M. Titirici and M. Antonietti, *Chemical Society reviews*, 2010, **39**, 103–16.
- [200] M.-M. Titirici, A. Thomas and M. Antonietti, *Journal of Materials Chemistry*, 2007, **17**, 3412.

- [201] R. J. White, M. Antonietti and M.-M. Titirici, *Journal of Materials Chemistry*, 2009, **19**, 8645.
- [202] L. Zhao, N. Baccile, S. Gross, Y. Zhang, W. Wei, Y. Sun, M. Antonietti and M.-M. Titirici, *Carbon*, 2010, **48**, 3778–3787.
- [203] L. Zhao, R. Crombez, F. P. Caballero, M. Antonietti, J. Texter and M.-M. Titirici, *Polymer*, 2010, **51**, 4540–4546.
- [204] B. Xu, S. Hou, G. Cao, F. Wu and Y. Yang, *Journal of Materials Chemistry*, 2012, **22**, 19088.
- [205] Y. Wang, X. Wang and M. Antonietti, *Angewandte Chemie (International ed. in English)*, 2012, **51**, 68–89.
- [206] Y. Zhang and M. Antonietti, *Chemistry, an Asian journal*, 2010, **5**, 1307–11.
- [207] A. Thomas, A. Fischer, F. Goettmann, M. Antonietti, J.-O. Müller, R. Schlögl and J. M. Carlsson, *Journal of Materials Chemistry*, 2008, **18**, 4893.
- [208] F. Goettmann, A. Fischer, M. Antonietti and A. Thomas, *Chemical Communications*, 2006, 4530.
- [209] S. Giraudet and Z. Zhu, *Carbon*, 2011, **49**, 398–405.
- [210] J. Zhang, F. Guo and X. Wang, *Advanced Functional Materials*, 2013, **23**, 3008–3014.
- [211] K. K. R. Datta, V. V. Balasubramanian, K. Ariga, T. Mori and A. Vinu, *Chemistry (Weinheim an der Bergstrasse, Germany)*, 2011, **17**, 3390–7.
- [212] Y. Ham, K. Maeda, D. Cha, K. Takanabe and K. Domen, *Chemistry, an Asian journal*, 2013, **8**, 218–24.
- [213] M. J. Bojdys, N. Severin, J. P. Rabe, A. I. Cooper, A. Thomas and M. Antonietti, *Macromolecular rapid communications*, 2013, **34**, 850–4.
- [214] M. J. Bojdys, J.-O. Müller, M. Antonietti and A. Thomas, *Chemistry (Weinheim an der Bergstrasse, Germany)*, 2008, **14**, 8177–82.
- [215] K. N. Wood, S. Pylypenko, T. S. Olson, A. A. Dameron, K. O'Neill, S. T. Christensen, H. N. Dinh, T. Gennett, R. O'Hayre, K. O'Neill and R. O'Hayre, *ACS applied materials & interfaces*, 2012, **4**, 6728–34.
- [216] E. F. Holby and C. D. Taylor, *Applied Physics Letters*, 2012, **101**, 064102.

- [217] F. Gao, G.-L. Zhao, S. Yang and J. J. Spivey, *Journal of the American Chemical Society*, 2013, **135**, 3315–8.
- [218] N. Roy, R. Sengupta and A. K. Bhowmick, *Progress in Polymer Science*, 2012, **37**, 781–819.
- [219] L. Hao, B. Luo, X. Li, M. Jin, Y. Fang, Z. Tang, Y. Jia, M. Liang, A. Thomas, J. Yang and L. Zhi, *Energy & Environmental Science*, 2012, **5**, 9747.
- [220] K. Sakaushi and G. Nickerl, *Angewandte Chemie . . .*, 2012, 7850–7854.
- [221] D. Bélanger and J. Pinson, *Chemical Society reviews*, 2011, **40**, 3995–4048.
- [222] A. Grondein and D. Bélanger, *Carbon*, 2012, **50**, 4335–4342.
- [223] M. Mananghaya, E. Rodulfo, G. N. Santos, A. R. Villagrancia and A. N. Ladines, *Journal of Nanomaterials*, 2012, **2012**, 1–14.
- [224] M. Groves, a.S.W. Chan, C. Malardier-Jugroot and M. Jugroot, *Chemical Physics Letters*, 2009, **481**, 214–219.
- [225] S.-F. Huang, K. Terakura, T. Ozaki, T. Ikeda, M. Boero, M. Oshima, J.-i. Ozaki and S. Miyata, *Physical Review B*, 2009, **80**, 235410.
- [226] S. Ni, Z. Li and J. Yang, *Nanoscale*, 2012, **4**, 1184–9.
- [227] L. Yu, X. Pan, X. Cao, P. Hu and X. Bao, *Journal of Catalysis*, 2011, **282**, 183–190.
- [228] X. Bao, X. Nie, D. Deak, E. J. Biddinger, W. Luo, A. Asthagiri, U. S. Ozkan and C. M. Hadad, *Topics in Catalysis*, 2013, **56**, 1623–1633.
- [229] C. H. San and C. W. Hong, *Journal of The Electrochemical Society*, 2012, **159**, K116.
- [230] H. J. Yan, B. Xu, S. Q. Shi and C. Y. Ouyang, *Journal of Applied Physics*, 2012, **112**, 104316.
- [231] X.-k. Kong and Q.-w. Chen, *Physical chemistry chemical physics : PCCP*, 2013, **15**, 12982–7.
- [232] Y.-X. Yu, *Physical chemistry chemical physics : PCCP*, 2013, **15**, 16819–27.
- [233] Z. M. Ao, a. D. Hernández-Nieves, F. M. Peeters and S. Li, *Physical chemistry chemical physics : PCCP*, 2012, **14**, 1463–7.

- [234] G. Koh, Y.-W. Zhang and H. Pan, *International Journal of Hydrogen Energy*, 2012, **37**, 4170–4178.
- [235] S. Lee, M. Lee, H. Choi, D. S. Yoo and Y.-C. Chung, *International Journal of Hydrogen Energy*, 2013, **38**, 4611–4617.
- [236] J.-x. Zhao, Y.-h. Ding, X.-g. Wang, Q.-h. Cai and X.-z. Wang, *Diamond and Related Materials*, 2011, **20**, 36–41.
- [237] J. G. Zhou and Q. L. Williams, *Journal of Nano Research*, 2011, **15**, 29–40.
- [238] L. Zhang, J. Niu, L. Dai and Z. Xia, *Langmuir : the ACS journal of surfaces and colloids*, 2012, **28**, 7542–50.
- [239] G. Luo, L. Liu, J. Zhang, G. Li, B. Wang and J. Zhao, *ACS applied materials & interfaces*, 2013, **5**, 11184–93.
- [240] L. Zhang and Z. Xia, *The Journal of Physical Chemistry C*, 2011, **115**, 11170–11176.
- [241] J. Zhang, Z. Wang and Z. Zhu, *Journal of molecular modeling*, 2013, 5515–5521.
- [242] S. Kattel, P. Atanassov and B. Kiefer, *Physical chemistry chemical physics : PCCP*, 2013, **15**, 148–53.
- [243] S. Kattel, P. Atanassov and B. Kiefer, *The Journal of Physical Chemistry C*, 2012, **116**, 17378–17383.
- [244] D. H. Lee, W. J. Lee, W. J. Lee, S. O. Kim and Y.-H. Kim, *Physical Review Letters*, 2011, **106**, 175502.
- [245] A. Titov, P. Zapol, P. Král, D.-j. Liu, H. Iddir, K. Baishya and L. A. Curtiss, *The Journal of Physical Chemistry C*, 2009, **113**, 21629–21634.
- [246] R. Chen, H. Li, D. Chu and G. Wang, *The Journal of Physical Chemistry C*, 2009, **113**, 20689–20697.
- [247] H. He, Y. Lei, C. Xiao, D. Chu, R. Chen and G. Wang, *The Journal of Physical Chemistry C*, 2012, **116**, 16038–16046.
- [248] S. Kattel and G. Wang, *Journal of Materials Chemistry A*, 2013, **1**, 10790.
- [249] K. Artyushkova, B. Kiefer, B. Halevi, a. Knop-Gericke, R. Schlogl and P. Atanassov, *Chemical communications (Cambridge, England)*, 2013, **49**, 2539–41.

- [250] C. Ma, X. Shao and D. Cao, *Journal of Materials Chemistry*, 2012, **22**, 8911.
- [251] G. Fang, S. Kaneko, W. Liu, B. Xia, H. Sun, R. Zhang, J. Zheng and D. Li, *Applied Surface Science*, 2013, **283**, 963–967.
- [252] J. Chang, X. Sun, L. Feng, W. Xing, X. Qin and G. Shao, *Journal of Power Sources*, 2013, **239**, 94–102.
- [253] J. Duan, Y. Zheng, S. Chen, Y. Tang, M. Jaroniec and S. Qiao, *Chemical communications (Cambridge, England)*, 2013, **49**, 7705–7.
- [254] Y. Chen, J. Wang, H. Liu, R. Li, X. Sun, S. Ye and S. Knights, *Electrochemistry Communications*, 2009, **11**, 2071–2076.
- [255] Y. Liu, Z. Jin, J. Wang, R. Cui, H. Sun, F. Peng, L. Wei, Z. Wang, X. Liang, L. Peng and Y. Li, *Advanced Functional Materials*, 2011, **21**, 986–992.
- [256] M. S. Saha, R. Li, X. Sun and S. Ye, *Electrochemistry Communications*, 2009, **11**, 438–441.
- [257] X. Li, S. Park and B. N. Popov, *Journal of Power Sources*, 2010, **195**, 445–452.
- [258] F. Jaouen, E. Proietti, M. Lefèvre, R. Chenitz, J.-P. Dodelet, G. Wu, H. T. Chung, C. M. Johnston and P. Zelenay, *Energy & Environmental Science*, 2011, **4**, 114.
- [259] N. Karim and S. Kamarudin, *Applied Energy*, 2013, **103**, 212–220.
- [260] G. Wu and P. Zelenay, *Accounts of chemical research*, 2013, **46**, 1878–89.
- [261] H. R. Byon, J. Suntivich and Y. Shao-Horn, *Chemistry of Materials*, 2011, **23**, 3421–3428.
- [262] J. Y. J. Cheon, T. Kim, Y. Y. Choi, H. Y. H. Jeong, M. G. Kim, Y. J. Sa, J. Kim, Z. Lee, T.-H. Yang, K. Kwon, O. Terasaki, G.-G. Park, R. R. Adzic and S. H. Joo, *Scientific reports*, 2013, **3**, 2715.
- [263] M. Ferrandon, A. J. Kropf, D. J. Myers, K. Artyushkova, U. Kramm, P. Bogdanoff, G. Wu, C. M. Johnston and P. Zelenay, *The Journal of Physical Chemistry C*, 2012, **116**, 16001–16013.
- [264] J. Herranz, F. Jaouen, M. Lefèvre, U. I. Kramm, E. Proietti, J.-P. Dodelet, P. Bogdanoff, S. Fiechter, I. Abs-Wurmbach, P. Bertrand, T. M. Arruda and S. Mukerjee, *The journal of physical chemistry. C, Nanomaterials and interfaces*, 2011, **115**, 16087–16097.

- [265] U. Kramm, J. Herranz and N. Larouche, *Physical Chemistry ...*, 2012, **14**, 11673–11688.
- [266] K. Niu, B. Yang, J. Cui, J. Jin, X. Fu, Q. Zhao and J. Zhang, *Journal of Power Sources*, 2013, **243**, 65–71.
- [267] N. Ramaswamy, U. Tylus, Q. Jia and S. Mukerjee, *Journal of the American Chemical Society*, 2013, **135**, 15443–9.
- [268] C. Walter, K. Kummer, D. Vyalikh, V. Bruser and K.-D. Weltmann, *Journal of the Electrochemical Society*, 2013, **160**, F1088–F1095.
- [269] G. Wu, C. M. Johnston, N. H. Mack, K. Artyushkova, M. Ferrandon, M. Nelson, J. S. Lezama-Pacheco, S. D. Conradson, K. L. More, D. J. Myers and P. Zelenay, *Journal of Materials Chemistry*, 2011, **21**, 11392.
- [270] T. S. Olson, S. Pylypenko, J. E. Fulghum and P. Atanassov, *Journal of The Electrochemical Society*, 2010, **157**, B54.
- [271] T. S. Olson, S. Pylypenko, S. Kattel, P. Atanassov and B. Kiefer, *The Journal of Physical Chemistry C*, 2010, **114**, 15190–15195.
- [272] F. Jaouen, J. Herranz, M. Lefèvre, J.-P. Dodelet, U. I. Kramm, I. Herrmann, P. Bogdanoff, J. Maruyama, T. Nagaoka, A. Garsuch, J. R. Dahn, T. Olson, S. Pylypenko, P. Atanassov and E. a. Ustinov, *ACS applied materials & interfaces*, 2009, **1**, 1623–39.
- [273] F. Charretier, F. Jaouen and J.-P. Dodelet, *Electrochimica Acta*, 2009, **54**, 6622–6630.
- [274] H. T. Chung, C. M. Johnston, K. Artyushkova, M. Ferrandon, D. J. Myers and P. Zelenay, *Electrochemistry Communications*, 2010, **12**, 1792–1795.
- [275] H. Xiao, Z.-G. Shao, G. Zhang, Y. Gao, W. Lu and B. Yi, *Carbon*, 2013, **57**, 443–451.
- [276] R. Kothandaraman, V. Nallathambi, K. Artyushkova and S. C. Barton, *Applied Catalysis B: Environmental*, 2009, **92**, 209–216.
- [277] N. Leonard, V. Nallathambi and S. C. Barton, *Journal of the Electrochemical Society*, 2013, **160**, F788–F792.
- [278] H. Byon and J. Suntivich, *Physical Chemistry ...*, 2011, 21437–21445.
- [279] R. L. Arechederra, K. Artyushkova, P. Atanassov and S. D. Minteer, *ACS applied materials & interfaces*, 2010, **2**, 3295–302.

- [280] M. H. Robson, A. Serov, K. Artyushkova and P. Atanasov, *Electrochimica Acta*, 2013, **90**, 656–665.
- [281] A. Serov, M. H. Robson, M. Smolnik and P. Atanasov, *Electrochimica Acta*, 2012, **80**, 213–218.
- [282] A. Serov, M. H. Robson, K. Artyushkova and P. Atanasov, *Applied Catalysis B: Environmental*, 2012, **127**, 300–306.
- [283] A. Serov, M. H. Robson, B. Halevi, K. Artyushkova and P. Atanasov, *Electrochemistry Communications*, 2012, **22**, 53–56.
- [284] S. Brocato, A. Serov and P. Atanasov, *Electrochimica Acta*, 2013, **87**, 361–365.
- [285] H. Meng, F. Jaouen, E. Proietti, M. Lefèvre and J.-P. Dodelet, *Electrochemistry Communications*, 2009, **11**, 1986–1989.
- [286] T. Olson and S. Pylypenko, *The Journal of . . .*, 2010, 5049–5059.
- [287] S. Jiang, C. Zhu and S. Dong, *Journal of Materials Chemistry A*, 2013, **1**, 3593.
- [288] K. Parvez, S. Yang, Y. Hernandez, A. Winter, A. Turchanin, X. Feng and K. Müllen, *ACS nano*, 2012, **6**, 9541–50.
- [289] H. T. Chung, J. H. Won and P. Zelenay, *Nature communications*, 2013, **4**, 1922.
- [290] Q. He, Q. Li, S. Khene, X. Ren, F. E. López-Suárez, D. Lozano-Castelló, A. Bueno-López and G. Wu, *The Journal of . . .*, 2013, **117**, 8697–8707.
- [291] Y. Liang, Y. Li, H. Wang, J. Zhou, J. Wang, T. Regier and H. Dai, *Nature materials*, 2011, **10**, 780–6.
- [292] Y. Liang, H. Wang, P. Diao, W. Chang, G. Hong, Y. Li, M. Gong, L. Xie, J. Zhou, J. Wang, T. Z. Regier, F. Wei and H. Dai, *Journal of the American Chemical Society*, 2012, **134**, 15849–57.
- [293] Y. Zhang, K. Fugane, T. Mori, L. Niu and J. Ye, *Journal of Materials Chemistry*, 2012, **22**, 6575.
- [294] Y. Liang, H. Wang, J. Zhou, Y. Li, J. Wang, T. Regier and H. Dai, *Journal of the American Chemical Society*, 2012, **134**, 3517–23.
- [295] M. D. Sánchez, P. Chen, T. Reinecke, M. Muhler and W. Xia, *ChemCatChem*, 2012, **4**, 1997–2004.

- [296] M. Chisaka, T. Iijima and A. Tomita, *Journal of The ...*, 2010, 1701–1706.
- [297] A. Zahoor, M. Christy, Y. J. Hwang, Y. R. Lim, P. Kim and K. S. Nahm, *Applied Catalysis B: Environmental*, 2014, **147**, 633–641.
- [298] P. Pachfule, V. M. Dhavale, S. Kandambeth, S. Kurungot and R. Banerjee, *Chemistry (Weinheim an der Bergstrasse, Germany)*, 2013, **19**, 974–80.
- [299] J.-i. Ozaki, S.-i. Tanifuji, A. Furuichi and K. Yabutsuka, *Electrochimica Acta*, 2010, **55**, 1864–1871.
- [300] S. Lyth, Y. Nabae and N. Islam, *... of The Electrochemical ...*, 2011, 194–201.
- [301] Y. Li, W. Zhou, H. Wang, L. Xie, Y. Liang, F. Wei, J.-C. Idrobo, S. J. Pennycook and H. Dai, *Nature nanotechnology*, 2012, **7**, 394–400.
- [302] Y. Ma, L. Sun, W. Huang, L. Zhang, J. Zhao, Q. Fan and W. Huang, *The Journal of Physical Chemistry C*, 2011, **115**, 24592–24597.
- [303] N. Alexeyeva, E. Shulga, V. Kisand, I. Kink and K. Tammeveski, *Journal of Electroanalytical Chemistry*, 2010, **648**, 169–175.
- [304] S. Wang, E. Iyyamperumal, A. Roy, Y. Xue, D. Yu and L. Dai, *Angewandte Chemie (International ed. in English)*, 2011, **50**, 11756–60.
- [305] H. Li, H. Liu, Z. Jong, W. Qu, D. Geng, X. Sun and H. Wang, *International Journal of Hydrogen Energy*, 2011, **36**, 2258–2265.
- [306] J. P. McClure, J. D. Thornton, R. Jiang, D. Chu, J. J. Cuomo and P. S. Fedkiw, *Journal of the Electrochemical Society*, 2012, **159**, F733–F742.
- [307] W. Xia, J. Masa, M. Bron, W. Schuhmann and M. Muhler, *Electrochemistry Communications*, 2011, **13**, 593–596.
- [308] T. C. Nagaiah, A. Bordoloi, M. D. Sánchez, M. Muhler and W. Schuhmann, *ChemSusChem*, 2012, **5**, 637–41.
- [309] D. C. Higgins, J. Wu, W. Li and Z. Chen, *Electrochimica Acta*, 2012, **59**, 8–13.
- [310] G. Liu, X. Li, P. Ganesan and B. N. Popov, *Electrochimica Acta*, 2010, **55**, 2853–2858.
- [311] Z. Chen, D. Higgins and Z. Chen, *Electrochimica Acta*, 2010, **55**, 4799–4804.
- [312] D. Higgins, Z. Chen and Z. Chen, *Electrochimica Acta*, 2011, **56**, 1570–1575.

- [313] Z. Chen, D. Higgins and Z. Chen, *Carbon*, 2010, **48**, 3057–3065.
- [314] Z. Chen, D. Higgins, H. Tao, R. S. Hsu and Z. Chen, *The Journal of Physical Chemistry C*, 2009, **113**, 21008–21013.
- [315] A. Zhao, J. Masa, M. Muhler, W. Schuhmann and W. Xia, *Electrochimica Acta*, 2013, **98**, 139–145.
- [316] D. Singh, I. I. Soykal, J. Tian, D. von Deak, J. King, J. T. Miller and U. S. Ozkan, *Journal of Catalysis*, 2013, **304**, 100–111.
- [317] E. J. Biddinger and U. S. Ozkan, *The Journal of Physical Chemistry C*, 2010, **114**, 15306–15314.
- [318] J. Masa, A. Zhao, W. Xia, Z. Sun, B. Mei, M. Muhler and W. Schuhmann.
- [319] J. D. Wiggins-Camacho and K. J. Stevenson, *The Journal of Physical Chemistry C*, 2011, **115**, 20002–20010.
- [320] J. Vazquez-Arenas, D. Higgins, Z. Chen, M. Fowler and Z. Chen, *Journal of Power Sources*, 2012, **205**, 215–221.
- [321] L. Feng, Y. Yan, Y. Chen and L. Wang, *Energy & Environmental Science*, 2011, **4**, 1892.
- [322] D. C. Mirodatos, D. Y. Schuurman, D. D. Duprez, D. F. Luck, D. von Deak, D. Singh, J. C. King and U. S. Ozkan, *Applied Catalysis B: Environmental*, 2012, **113**, 126–133.
- [323] H. Niwa, K. Horiba, Y. Harada, M. Oshima, T. Ikeda, K. Terakura, J.-i. Ozaki and S. Miyata, *Journal of Power Sources*, 2009, **187**, 93–97.
- [324] Z. Lin, G. H. Waller, Y. Liu, M. Liu and C.-p. Wong, *Carbon*, 2013, **53**, 130–136.
- [325] Z. Lin, G. H. Waller, Y. Liu, M. Liu and C.-p. Wong, *Nano Energy*, 2013, **2**, 241–248.
- [326] Z.-J. Lu, M.-W. Xu, S.-J. Bao, K. Tan, H. Chai, C.-J. Cai, C.-C. Ji and Q. Zhang, *Journal of Materials Science*, 2013, **48**, 8101–8107.
- [327] C. Zhang, R. Hao, H. Liao and Y. Hou, *Nano Energy*, 2013, **2**, 88–97.
- [328] J. Yan, H. Meng, F. Xie, X. Yuan, W. Yu, W. Lin, W. Ouyang and D. Yuan, *Journal of Power Sources*, 2014, **245**, 772–778.

- [329] N. Brun, S. a. Wohlgemuth, P. Osiceanu and M. M. Titirici, *Green Chemistry*, 2013, **15**, 2514.
- [330] C.-Z. Guo, C.-G. Chen and Z.-L. Luo, *Journal of Power Sources*, 2014, **245**, 841–845.
- [331] L. Lai, J. R. Potts, D. Zhan, L. Wang, C. K. Poh, C. Tang, H. Gong, Z. Shen, J. Lin and R. S. Ruoff, *Energy & Environmental Science*, 2012, **5**, 7936.
- [332] X. Li, J. Liu, Y. Zhang, Y. Li, H. Liu, X. Meng, J. Yang, D. Geng, D. Wang, R. Li and X. Sun, *Journal of Power Sources*, 2012, **197**, 238–245.
- [333] X. Lin, X. Lu, T. Huang, Z. Liu and A. Yu, *Journal of Power Sources*, 2013, **242**, 855–859.
- [334] D. Higgins, Z. Chen, D. U. Lee and Z. Chen, *Journal of Materials Chemistry A*, 2013, **1**, 2639.
- [335] G. S. Park, J.-S. Lee, S. T. Kim, S. Park and J. Cho, *Journal of Power Sources*, 2013, **243**, 267–273.
- [336] S. Zhu, Z. Chen, B. Li, D. Higgins, H. Wang, H. Li and Z. Chen, *Electrochimica Acta*, 2011, **56**, 5080–5084.
- [337] G. Wu, N. Mack, W. Gao, S. Ma and R. Zhong, *ACS . . .*, 2012, 9764–9776.
- [338] H. W. Park, D. U. Lee, Y. Liu, J. Wu, L. F. Nazar and Z. Chen, *Journal of the Electrochemical Society*, 2013, **160**, A2244–A2250.
- [339] P. Kichambare, J. Kumar, S. Rodrigues and B. Kumar, *Journal of Power Sources*, 2011, **196**, 3310–3316.
- [340] P. Kichambare, S. Rodrigues and J. Kumar, *ACS applied materials & interfaces*, 2012, **4**, 49–52.
- [341] H. Nie, H. Zhang, Y. Zhang, T. Liu, J. Li and Q. Lai, *Nanoscale*, 2013, **5**, 8484–7.
- [342] K. Zhang, L. Zhang, X. Chen, X. He, X. Wang, S. Dong, L. Gu, Z. Liu, C. Huang and G. Cui, *ACS applied materials & interfaces*, 2013, **5**, 3677–82.
- [343] H. W. Park, D. U. Lee, L. F. Nazar and Z. Chen, *Journal of the Electrochemical Society*, 2012, **160**, A344–A350.
- [344] H.-g. Wang, Z. Wu, F.-l. Meng, D.-l. Ma, X.-l. Huang, L.-m. Wang and X.-b. Zhang, *ChemSusChem*, 2013, **6**, 56–60.

- [345] C. He, R. Wang, H. Fu and P. K. Shen, *Journal of Materials Chemistry A*, 2013, **1**, 14586.
- [346] Z.-S. Wu, W. Ren, L. Xu, F. Li and H.-M. Cheng, *ACS nano*, 2011, **5**, 5463–71.
- [347] D. Cai, S. Wang, P. Lian, X. Zhu, D. Li, W. Yang and H. Wang, *Electrochimica Acta*, 2013, **90**, 492–497.
- [348] X. Li, D. Geng, Y. Zhang, X. Meng, R. Li and X. Sun, *Electrochemistry Communications*, 2011, **13**, 822–825.
- [349] X. Zhou, L.-J. Wan and Y.-G. Guo, *Advanced materials (Deerfield Beach, Fla.)*, 2013, **25**, 2152–7.
- [350] M. Du, C. Xu, J. Sun and L. Gao, *Electrochimica Acta*, 2012, **80**, 302–307.
- [351] Y. Chang, J. Li, B. Wang, H. Luo, H. He, Q. Song and L. Zhi, *Journal of Materials Chemistry A*, 2013, **1**, 14658.
- [352] D. Cai, D. Li, S. Wang, X. Zhu, W. Yang, S. Zhang and H. Wang, *Journal of Alloys and Compounds*, 2013, **561**, 54–58.
- [353] D. Li, D. Shi, Z. Liu, H. Liu and Z. Guo, *Journal of Nanoparticle Research*, 2013, **15**, 1674.
- [354] K. Zhang, P. Han, L. Gu, L. Zhang, Z. Liu, Q. Kong, C. Zhang, S. Dong, Z. Zhang, J. Yao, H. Xu, G. Cui and L. Chen, *ACS applied materials & interfaces*, 2012, **4**, 658–64.
- [355] N. Mahmood, C. Zhang and Y. Hou, *Small (Weinheim an der Bergstrasse, Germany)*, 2013, **9**, 1321–8.
- [356] L. Bulusheva, a.V. Okotrub, a.G. Kurennya, H. Zhang, H. Zhang, X. Chen and H. Song, *Carbon*, 2011, **49**, 4013–4023.
- [357] W. Ren, D. Li, H. Liu, R. Mi, Y. Zhang and L. Dong, *Electrochimica Acta*, 2013, **105**, 75–82.
- [358] Z. Wang, X. Xiong, L. Qie and Y. Huang, *Electrochimica Acta*, 2013, **106**, 320–326.
- [359] P. Han, Y. Yue, L. Zhang, H. Xu, Z. Liu, K. Zhang, C. Zhang, S. Dong, W. Ma and G. Cui, *Carbon*, 2011, **50**, 1355–1362.

- [360] Z. Li, Z. Xu, X. Tan, H. Wang, C. M. B. Holt, T. Stephenson, B. C. Olsen and D. Mitlin, *Energy & Environmental Science*, 2013, **6**, 871.
- [361] C. Hu, Y. Xiao, Y. Zhao, N. Chen, Z. Zhang, M. Cao and L. Qu, *Nanoscale*, 2013, **5**, 2726–33.
- [362] J. Ding, H. Wang, Z. Li, A. Kohandehghan, K. Cui and Z. Xu, 2013, 11004–11015.
- [363] H. Li, L. Shen, X. Zhang, J. Wang, P. Nie, Q. Che and B. Ding, *Journal of Power Sources*, 2013, **221**, 122–127.
- [364] S. Yoon, C. Liao, X.-G. Sun, C. a. Bridges, R. R. Unocic, J. Nanda, S. Dai and M. P. Paranthaman, *Journal of Materials Chemistry*, 2012, **22**, 4611.
- [365] Z. Ding, L. Zhao, L. Suo, Y. Jiao, S. Meng, Y.-S. Hu, Z. Wang and L. Chen, *Physical chemistry chemical physics : PCCP*, 2011, **13**, 15127–33.
- [366] D. J. Lee, M.-H. Ryou, J.-N. Lee, B. G. Kim, Y. M. Lee, H.-W. Kim, B.-S. Kong, J.-K. Park and J. W. Choi, *Electrochemistry Communications*, 2013, **34**, 98–101.
- [367] L. Tan, C. Cao, H. Yang, B. Wang and L. Li, *Materials Letters*, 2013, **109**, 195–198.
- [368] H. Lee and H. Kim, *Journal of Applied Electrochemistry*, 2013, **43**, 553–557.
- [369] Y. Shao, X. Wang, M. Engelhard, C. Wang, S. Dai, J. Liu, Z. Yang and Y. Lin, *Journal of Power Sources*, 2010, **195**, 4375–4379.
- [370] F. Sun, J. Wang, H. Chen, W. Li, W. Qiao, D. Long and L. Ling, *ACS applied materials & interfaces*, 2013, **5**, 5630–8.
- [371] F. Sun, J. Wang, D. Long, W. Qiao, L. Ling, C. Lv and R. Cai, *Journal of Materials Chemistry A*, 2013, **1**, 13283.
- [372] J. Jiang, Q. Gao, K. Xia and J. Hu, *Microporous and Mesoporous Materials*, 2009, **118**, 28–34.
- [373] S. L. Candelaria, B. B. Garcia, D. Liu and G. Cao, *Journal of Materials Chemistry*, 2012, **22**, 9884.
- [374] H. Guo and Q. Gao, *Journal of Power Sources*, 2009, **186**, 551–556.
- [375] L. Lai, L. Wang, H. Yang, N. G. Sahoo, Q. X. Tam, J. Liu, C. K. Poh, S. H. Lim, Z. Shen and J. Lin, *Nano Energy*, 2012, **1**, 723–731.

- [376] X. Yang, D. Wu, X. Chen and R. Fu, *The Journal of Physical Chemistry C*, 2010, **114**, 8581–8586.
- [377] D. Hulicova-Jurcakova, M. Seredych, G. Q. Lu and T. J. Bandosz, *Advanced Functional Materials*, 2009, **19**, 438–447.
- [378] W. Kim, M. Y. Kang, J. B. Joo, N. D. Kim, I. K. Song, P. Kim, J. R. Yoon and J. Yi, *Journal of Power Sources*, 2010, **195**, 2125–2129.
- [379] Y. J. Kim, I. Y. Jang, K. C. Park, Y. C. Jung, T. Oka, S. Iinou, Y. Komori, T. Kozutsumi, T. Hashiba, Y. A. Kim and M. Endo, *Electrochimica Acta*, 2010, **55**, 5624–5628.
- [380] Z. Li, L. Zhang, B. S. Amirkhiz, X. Tan, Z. Xu, H. Wang, B. C. Olsen, C. M. B. Holt and D. Mitlin, *Advanced Energy Materials*, 2012, **2**, 431–437.
- [381] C.-T. Hsieh, H. Teng, W.-Y. Chen and Y.-S. Cheng, *Carbon*, 2010, **48**, 4219–4229.
- [382] L. Lai, H. Yang, L. Wang, B. K. Teh, J. Zhong, H. Chou, L. Chen, W. Chen, Z. Shen, R. S. Ruoff and J. Lin, *ACS nano*, 2012, **6**, 5941–51.
- [383] A. K. Mishra and S. Ramaprabhu, *AIP Advances*, 2011, **1**, 032152.
- [384] Z. Wen, X. Wang, S. Mao, Z. Bo, H. Kim, S. Cui, G. Lu, X. Feng and J. Chen, *Advanced materials (Deerfield Beach, Fla.)*, 2012, **24**, 5610–6.
- [385] E. Ra, E. Raymundo-Piñero, Y. Lee and F. Béguin, *Carbon*, 2009, **47**, 2984–2992.
- [386] J. P. Paraknowitsch, J. Zhang, D. Su, A. Thomas and M. Antonietti, *Advanced materials (Deerfield Beach, Fla.)*, 2010, **22**, 87–92.
- [387] X. Y. Chen, C. Chen, Z. J. Zhang and D. H. Xie, *Journal of Materials Chemistry A*, 2013, **1**, 10903.
- [388] H. Wang, Q. Gao and J. Hu, *Microporous and Mesoporous Materials*, 2010, **131**, 89–96.
- [389] Z.-S. Wu, A. Winter, L. Chen, Y. Sun, A. Turchanin, X. Feng and K. Müllen, *Advanced materials (Deerfield Beach, Fla.)*, 2012, **24**, 5130–5.
- [390] H. Konno, T. Ito, M. Ushiro, K. Fushimi and K. Azumi, *Journal of Power Sources*, 2010, **195**, 1739–1746.
- [391] T. Tomko, R. Rajagopalan, P. Aksoy and H. C. Foley, *Electrochimica Acta*, 2011, **56**, 5369–5375.

- [392] C. Wang, Y. Zhou, L. Sun, P. Wan, X. Zhang and J. Qiu, *Journal of Power Sources*, 2013, **239**, 81–88.
- [393] J. Burrell, M. Kraus, M. Beckner, R. Cepel, G. Suppes, C. Wexler and P. Pfeifer, *Nanotechnology*, 2009, **20**, 204026.
- [394] J. Jiang, Q. Gao, Z. Zheng, K. Xia and J. Hu, *International Journal of Hydrogen Energy*, 2010, **35**, 210–216.
- [395] B. P. Vinayan, R. Nagar and S. Ramaprabhu, *Journal of Materials Chemistry A*, 2013, **1**, 11192.
- [396] R. Lu, Z. Meng, E. Kan, F. Li, D. Rao, Z. Lu, J. Qian, C. Xiao, H. Wu and K. Deng, *Physical chemistry chemical physics : PCCP*, 2013, **15**, 666–70.
- [397] Z. M. Ao and F. M. Peeters, *The Journal of Physical Chemistry C*, 2010, **114**, 14503–14509.
- [398] L. H. Kumar, C. V. Rao and B. Viswanathan, *Journal of Materials Chemistry A*, 2013, **1**, 3355.
- [399] P. A. Berseth, A. G. Harter, R. Zidan, A. Blomqvist, C. M. Araújo, R. H. Scheicher, R. Ahuja and P. Jena, *Nano letters*, 2009, **9**, 1501–5.
- [400] M. S. L. Hudson, H. Raghubanshi, D. Pukazhselvan and O. Srivastava, *International Journal of Hydrogen Energy*, 2012, **37**, 2750–2755.
- [401] M. Ismail, Y. Zhao, X. Yu, a. Ranjbar and S. Dou, *International Journal of Hydrogen Energy*, 2011, **36**, 3593–3599.
- [402] R. D. Stephens, A. F. Gross, S. L. Van Atta, J. J. Vajo and F. E. Pinkerton, *Nanotechnology*, 2009, **20**, 204018.
- [403] S. Choi, J. H. Drese and C. W. Jones, *ChemSusChem*, 2009, **2**, 796–854.
- [404] L. Zhao, Z. Bacsik, N. Hedin, W. Wei, Y. Sun, M. Antonietti and M.-M. Titirici, *ChemSusChem*, 2010, **3**, 840–5.
- [405] J. a. Thote, K. S. Iyer, R. Chatti, N. K. Labhsetwar, R. B. Biniwale and S. S. Rayalu, *Carbon*, 2010, **48**, 396–402.
- [406] M. Sevilla, P. Valle-Vigón and A. B. Fuertes, *Advanced Functional Materials*, 2011, **21**, 2781–2787.

- [407] L. Wang and R. Yang, *The Journal of Physical Chemistry C*, 2011, 1099–1106.
- [408] J. Wang, I. Senkovska, M. Oschatz, M. R. Lohe, L. Borchardt, A. Heerwig, Q. Liu and S. Kaskel, *ACS applied materials & interfaces*, 2013, **5**, 3160–7.
- [409] J. Wang, I. Senkovska, M. Oschatz, M. R. Lohe, L. Borchardt, A. Heerwig, Q. Liu and S. Kaskel, *Journal of Materials Chemistry A*, 2013, **1**, 10951.
- [410] R. Myers, *Addiction biology*, 2001, **6**, 189–193.
- [411] A. Morozan, B. Jousselme and S. Palacin, *Energy & Environmental Science*, 2011, **4**, 1238.
- [412] R. a. Sidik, A. B. Anderson, N. P. Subramanian, S. P. Kumaraguru and B. N. Popov, *The journal of physical chemistry. B*, 2006, **110**, 1787–93.
- [413] A. Nieto-Márquez, D. Toledano, P. Sánchez, A. Romero and J. L. Valverde, *Journal of Catalysis*, 2010, **269**, 242–251.
- [414] J. Kochi and R. Sheldon, 1981, 1981.
- [415] G. Palmisano, E. García-López, G. Marcì, V. Loddo, S. Yurdakal, V. Augugliaro and L. Palmisano, *Chemical communications (Cambridge, England)*, 2010, **46**, 7074–89.
- [416] J. Xiao, D. Mei, X. Li, W. Xu, D. Wang, G. L. Graff, W. D. Bennett, Z. Nie, L. V. Saraf, I. a. Aksay, J. Liu and J.-G. Zhang, *Nano letters*, 2011, **11**, 5071–8.
- [417] L. Jia, D.-H. Wang, Y.-X. Huang, A.-W. Xu and H.-Q. Yu, *The Journal of Physical Chemistry C*, 2011, **115**, 11466–11473.
- [418] Y. Min, G. He, R. Li, W. Zhao, Y. Chen and Y. Zhang, *Separation and Purification Technology*, 2013, **106**, 97–104.
- [419] X. Wang, K. Maeda, A. Thomas, K. Takanabe, G. Xin, J. M. Carlsson, K. Domen and M. Antonietti, *Nature materials*, 2009, **8**, 76–80.
- [420] N. Jia, L. Liu, Q. Zhou, L. Wang, M. Yan and Z. Jiang, *Electrochimica Acta*, 2005, **51**, 611–618.
- [421] S. Deng, G. Jian, J. Lei, Z. Hu and H. Ju, *Biosensors & bioelectronics*, 2009, **25**, 373–7.
- [422] H. Nolan, N. McEvoy, G. P. Keeley, S. D. Callaghan, C. McGuinness and G. S. Duesberg, *Physical chemistry chemical physics : PCCP*, 2013, **15**, 18688–93.

- [423] J. M. Goran, S. M. Mantilla and K. J. Stevenson, *Analytical chemistry*, 2013, **85**, 1571–81.
- [424] P. Gai, H. Zhang, Y. Zhang, W. Liu, G. Zhu, X. Zhang and J. Chen, *Journal of Materials Chemistry B*, 2013, **1**, 2742.
- [425] Z. Zhang, R. Zhang, C. Li, L. Yuan, P. Li, L. Yao and S. Liu, *Electroanalysis*, 2012, **24**, 1424–1430.
- [426] X. Feng, C. Wang, R. Cui, X. Yang and W. Hou, *Journal of Solid State Electrochemistry*, 2012, **16**, 2691–2698.
- [427] J. C. Carrero-Sanchez, a. L. Elías, R. Mancilla, G. Arrellín, H. Terrones, J. P. Laclette and M. Terrones, *Nano letters*, 2006, **6**, 1609–16.